THÈSE POUR OBTENIR LE GRADE DE DOCTEUR
DE L'UNIVERSITÉ DE MONTPELLIER

En Géosciences

École doctorale GAIA

Unité de recherche Géosciences Montpellier UMR 5243

Development of a Numerical Tool for Gravimetry and Gradiometry Data Processing and Interpretation Application to GOCE Observations

Présentée par Anita Thea SARASWATI
Le 27 novembre 2018

Sous la direction de
Rodolphe Cattin et Stéphane Mazzotti

Devant le jury composé de

Michel DIAMENT, Physicien, IPGP	Rapporteur
Guillaume RAMILLIEN, Directeur de Recherche, GET	Rapporteur
Olivier FRANCIS, Professeur, Université du Luxembourg	Examinateur
Mioara MANDEA, Physicienne, CNES	Président du Jury
Cécilia CADIO, Maître de conférences, Université de Montpellier	Invité
Rodolphe CATTIN, Professeur, Université de Montpellier	Directeur
Stéphane MAZZOTTI, Professeur, Université de Montpellier	Directeur

UNIVERSITÉ
DE MONTPELLIER

To know that we know what we know, and to know that we do not know what we do not know, that is true knowledge.

— *Nicolaus Copernicus*

Acknowledgments

Firstly, I would like to express my sincere gratitude to Rodolphe Cattin, Stéphane Mazzotti, and Cécilia Cadio, who took part in the supervision of my thesis, for the continuous support of my PhD study and related research, for their patience, motivation, and immense knowledge. Their guidance helped me in all the time of research and writing of this thesis. I could not have imagined having better advisors for my PhD study. I would like to thank also about the trust that they gave me to continue working in this subject as the continuation of my tasks during my *stage du M2* in Géosciences Montpellier.

Pour Rodolphe et Stéphane, merci d'avoir supporter mes compléxités pendant cette thèse. Les heures de discussion avec vous m'ont permis d'apprendre beaucoup sur l'importance de la simplicité dans les démarches scientifiques. Pour Cécilia, merci d'avoir être toujours là pour me convaincre de tous mes doutes. Merci.

Besides my supervisors, I would like to thank the rest of my thesis committee: Michel Diament, Guillaume Ramillien, Mioara Mandea, and Olivier Francis, for your willingness to participate in this thesis committee.

This thesis is financed by Beasiswa Unggulan (BU) of the Ministry of Education and Culture Indonesia, les bourses du gouvernement français (BGF), ANR DefDyCor, and Project CNES TOSCA. I would like to extend my gratitude to Bapak Mat Syai'in, Ibu Ria Asih Aryani Soemitro, dan Mbak Aini who helped me throughout the scholarship (BU) management process. I would like to thank again to Rodolphe and Stéphane for involving me in the CNES TOSCA and ANR projects. Thanks to you, this thesis can be realized.

I would like to thank also to Nicolas Le Moigne. I think the story after this thesis would be different without your help. Thank you.

Many thanks also to the other scientific members that helps me during this thesis: Isabelle Panet who enlighten me about gravity gradients, particularly with GOCE datasets; Gwendoline Pajot-Métivier and Laurent Metívier about the discussions and suggestions about how to deal with my data; Christel Tiberi and Matthieu Plasman for our interesting discussion about GOCE; Serge Lallemand with our discussions about subduction zones; Diane Arcay and Nicolas Baghdadi about their participation in my thesis committee; and for *l'équipe AT*, thanks for those exciting field trips, meetings, and discussions.

In the lab, thanks to Benoît, José, Dominique, Hélènne, and Bernadette about your helps in the administrative procedures; Fabrice and Stéphane for the helps and suggestions about informatics; Anne for your enthusiasms and helps when I need anything related to posters; and the others who I cannot mention one by one. Thank you so much.

So many thanks to my fellow labmates for the stimulating discussions, for the gallons of coffee we were drinking together, for *les blagues noires* that will be unforgettable, and for all the experiences and the fun we have had in the last three years. Grâce à vous je connais beaucoup de mots bizarres et avoir passé des moments extraordinaire pendant mon sejour à Montpellier. Thank you to Robin as my super co-bureau and because of you I progressed a lot in speaking French. Ça jouerges!! For my second co-bureau(s), Oswald and Toogii, merci de m'avoir supportée pendant les mois où je n'étais pas très agréable. Merci á Sam pour le partage de la souffrance pour ces derniere semaines. Many thanks to Alizia, Anaïs, Romain, Sven, Anneka, Elenora, Barbara, Manuel, La Gaine, Agathe, Pierre, Tim, Sylvain, Asma, Sofia, Manar, Enora, Gaëtan, Maxime H., Christine, Lise, Maxime B., Laure, and the others that I cannot mention one by one. Bowie and Pistou, please be more calm. Benou for those scuba diving and badminton experiences (et aussi pour tes blagues pourries). Sév for you infinity helps and happiness that we share together during these years. Ottax, thanks for being always there, even when you are not here. Merci énormément pour votre présence, votre sourire, et votre bonheur. Merci aussi d'avoir me nourrit à la fois pour le midi et pour les soirées ce qu'on a. Audrey and Olivier, thanks a lot for your wise advise during these years. Et Cyp, je ne sais pas comment je peux te remercier. Merci d'être toujours là. Merci d'avoir supporté tous les conneries ce que j'ai balancé. Et un grand merci pour avoir m'aidé de trouver le nom du logiciel. GEEC would never be born without you.

Other many thanks to the members of PPI Montpellier. Walaupun kalian terkadang menyebalkan, tapi kalian tetap di hati. Thank you for every single lunch or dinner that we had together and how we support each other when we are away from home. Special thanks to Wika and Andon for being there like my parents, who always care about my thesis and my health. Kalian sangat berarti.

And for dear MIAE X PIAE, Gaby, Made, Gumi. AGU would not be the same without you. Thanks for those random conversations. Made, thanks for being there when I need confidence. Gaby, our random discussions about anything, both random and serious, have enlighten my days. We have to make sure that we will *nge-bolang* again someday. For Gumi, even I just got to know you, but honestly, you gave me so much inspiration with your hard work and your calmness in living this life.

Last but not the least, to my family, I know that I am away. But I want you to know that you are always in every prayer that I have. And thank you, for always being weird and exceptional.

Thank you to all of you who were being there during my adventure.

Abstract

Nowadays, the scientific community has at its disposal gravity and gravity gradient datasets with unprecedented accuracy and spatial resolution that enhances our knowledge of Earth gravitational field at various scales and wavelengths, obtained from ground to satellite measurements. In parallel with gravimetry, the advancement of satellite observations provides the community with more detailed digital elevation models to reflect the Earth's structure geometry. Together, these novel datasets provide a great opportunity to better understand the Earth's structures and dynamics at local, regional, and global scales. The use and interpretation of these high-quality data require refinement of standard approaches in gravity-related data processing and analysis. This thesis consists of a series of studies aiming to improve the precision in the chain of gravity and gravity gradient data processing for geodynamic studies. To that aim, we develop a tool, named GEEC (Gal Eötvös Earth Calculator) to compute precisely the gravity and gravity gradients effects due to any mass body regardless of its geometry and its distance from measurements (Saraswati et al, submitted). The gravity and gravity gradients effects are computed analytically using the line integral solution of an irregular polyhedron. The validations at local, regional, and global scales confirm the robustness of GEEC's performance, where the resolution of the model, that depends on both size of the body mass and its distance from the measurement point, control strongly the accuracy of the results. We present an application for assessing the optimum parameters in the computation of gravity and gravity gradients due to topography variations. Topography has a major contribution in Earth gravitational attraction, therefore the estimation of topography effects must be carefully considered in the processing of gravity data, especially in areas of rugged topography or in large-scale studies. For high-accuracy gravity studies at a global scale, the topography correction process must consider the topography effect of the entire Earth. But for local to regional applications based on relative variations within the zone, we show that truncated topography at a specific distance can be adequate. When using a truncation distance that equals with the dimension of the study area, errors 1-10 mGal are obtained. The use of 15° ensure a precision of 1 mGal. For gravity gradient, to obtain 1 E of precision, a truncation distance of 8.5° is required. To obtain 0.01 E of precision, the truncation distance must be set at 40°. Lastly, we approach the issue: Are GOCE measurements relevant to obtain a detailed image of the structure of a subducting plate, including its geometry and lateral variation? The results of gravity gradients forward modelling using synthetic slab models demonstrate that the detailed structures of slab geometry are detectable by gravity gradients at GOCE mean altitude (255 km). However, in the application to the real case of Izu-Bonin-Mariana subduction zone, the second-order geometric features of the subducting plate (e.g., slab tear) are difficult to be detected due to poor spatial resolution and accuracy of the currently available global crustal model. We show that to be able to assess the geometry of a slab in the second-order, the estimation of crustal effect using a global crustal model with an accuracy better than 1 km is mandatory.

Keywords: *gravity field, space gradiometry (GOCE), numerical development, forward modelling, optimization, geodynamics*

Résumé

La communauté scientifique dispose aujourd'hui de jeux de données gravimétriques et gradiométriques d'une précision et d'une résolution spatiale sans précédent. Ces données obtenues à partir de mesures au sol, d'acquisitions aériennes et d'observations satellitaires permettent d'améliorer notre connaissance du champ gravitationnel de la Terre à diverses échelles et longueurs d'onde. Les observations satellitaires fournissent également à la communauté des modèles numériques de terrain globaux de plus en plus détaillés qui permettent une meilleure prise en compte de la géométrie fine des structures géologiques. Ensemble, ces nouveaux jeux de données offrent une opportunité unique de mieux comprendre les structures et la dynamique terrestre aux échelles locale, régionale et globale. L'utilisation et l'interprétation de ces données de haute qualité nécessitent d'aller au-delà des approches standards en matière de traitement et d'analyse des données gravimétriques et gradiométriques. Focalisée sur des applications géodynamiques, cette thèse consiste en une série d'études visant à améliorer la précision dans la chaine de traitement et d'interprétation de ces données. Pour cela, un nouvel outil a été développé. Intitulé GEEC (Gal Eötvös Earth Calculator), il permet de calculer précisément les effets gravimétriques et gradiométriques dus à un corps massique, quelles que soient sa géométrie et sa distance aux mesures (Saraswati et al, submitted). Ces effets sont calculés analytiquement en utilisant la solution intégrale le long des arrêtes d'un polyèdre irrégulier. Les validations aux échelles locale, régionale et globale ont permis de quantifier les performances et la robustesse de GEEC. Nous montrons qu'il est possible de définir une emprise optimale assurant rapidité de calcul et précision des résultats, qui dépend à la fois de la taille du corps massique et de sa distance aux points de mesure. L'estimation de l'effet de la topographie doit être soigneusement pris en compte dans le traitement des données gravimétriques et gradiométriques, en particulier dans les zones de topographie accidentée ou dans les études à grande échelle. Dans un premier temps, nous montrons que, pour les études gravimétriques de haute précision, la correction des effets topographiques sur les données satellitaires nécessite d'utiliser une emprise globale. A l'inverse, une topographie tronquée sur une distance égale à la dimension de la zone étudiée peut être adéquate dans l'analyse de variations relatives à des échelles locales et régionales, générant des erreurs de 1 à 10 mGal sur les mesures relatives. Plus généralement, une distance de troncature de 15° assure une précision de 1 mGal. Dans le cas de données de gradient de gravité, une distance de troncature de 8,5° (resp. 40 °) est requise pour obtenir une précision relative d'environ 1 E (resp. 0,01 E). Dans la troisième partie de cette thèse, nous abordons le problème suivant : les données du satellite GOCE sont-elles pertinentes pour obtenir une image détaillée de la structure d'une plaque de subduction (slab), y compris de sa géométrie et des variations latérales ? L'analyse d'une série de modèles synthétiques de slab montre que les structures détaillées de la géométrie sont détectables par les données de gradient de gravité à l'altitude moyenne de GOCE (255 km). Cependant, l'application au cas réel de la zone de subduction d'Izu-Bonin-Mariannes montre que la détection des caractéristiques géométriques de second ordre (par ex. déchirure de slab) reste difficile, en raison de la faible résolution spatiale des données et, principalement, de la mauvaise qualité des modèles d'épaisseur de croûte actuellement disponible. Nous montrons que, pour pouvoir étudier les détails de géométrie d'un slab, modèle régional ou global d'épaisseur de croûte est nécessaire avec une précision supérieure à environ 1 km.

Mots-clefs : *champ de pesanteur, gradiométrie spatiale (GOCE), développement numérique, modèle directe, optimisation, géodynamique*

Table of Contents

Introduction

The figure and the gravity field of the Earth

The question of the figure of the Earth was pondered in antiquity. The first conception of the figure of the Earth is Earth's shape as a planar disk. This concept was believed in many ancient cultures. However, with advancements in geodesy together with astronomy and geography, the definition of the figure of the Earth progressed.

The concept of a spherical shape of the Earth was firstly proposed by Pythagoras around 500 B.C. This spherical concept was accepted in the time of Aristotle (around 300 B.C.) and reinforced by astronomical observations of the round shadow of the Earth during lunar eclipses and the noticeable rising of an approaching ship on the horizon. Around 240 B.C., Eratosthenes calculated the radius of the Earth using the principle of the arc-measurement method by measuring the angle of the sunrays in Syene and Alexandria and obtained about 10% of error.

In the XVIth and XVIIth centuries, new observations and ideas from physics and astronomy resulted in new ideas about the figure of the Earth, starting with the ellipsoidal Earth model. In 1666, J. D. Cassini observed the flattening of the poles of Jupiter. Later, the astronomer J. Richer discovered that a one-second pendulum regulated in Paris had to be shortened to regain oscillations of one-second for measurements in Cayenne (1672-1673). This observation was confirmed by E. Halley when comparing pendulum measurements in St. Helena to those taken in London (1677-1678). Based on the law of gravitation, Isaac Newton proposed a rotational ellipsoid as the equilibrium figure for a homogeneous, fluid, rotating Earth with a flattening f. This result by Newton was also confirmed by other astronomers and physicists, such as C. Huygens, Maupertuis, and Clairaut.

In the end of XIXth century, P. S. Laplace, C. F. Gauss, and others recognized that the assumption of an ellipsoidal Earth model was no longer tenable at a high level of accuracy. The deflection of the vertical, to which new measurements referred, from the ellipsoidal normal could no longer be ignored. This led Gauss to improve the definition of the figure of the Earth and propose the definition of the geoid as the mathematical surface of the Earth that corresponds to the surface of gravity equipotential.

Nowadays, the concept of planar approximation of the Earth surface is still utilized. For example in plane surveying (e.g., cadastral survey, engineering survey, topography survey), the details of the Earth's surface are determined at a local scale, thus the curvature of the Earth can be generally ignored. For precise geodetic and global-scale applications, a geodetic reference Earth (normal Earth model, geoid, mean-Earth ellipsoid) is required.

The Earth gravity field for Earth dynamics studies

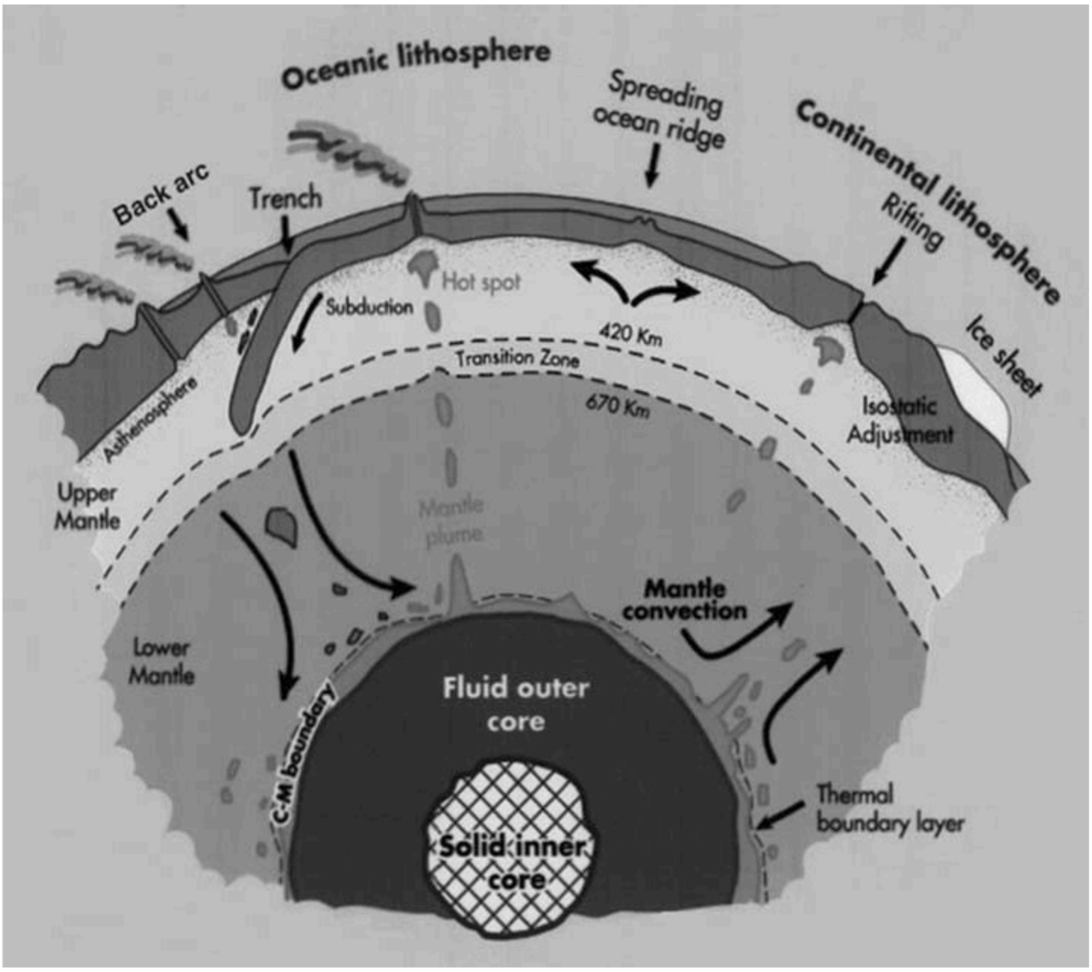

Figure 1: Major dynamic processes in solid Earth studies and layers in which the Earth is differentiated, extracted from Johannessen (1999).

The gravity field of the Earth is an essential quantity for probing the interior structure of the Earth and for modelling its dynamical behaviour under various circumstances from the core up to the outer lithosphere layer. Understanding the Earth gravity field also provides information about the interior structure of the Earth (Figure 1). For example, understanding the geoid at a large scale has brought important constraints on the viscosity of the mantle (Hager et al., 1985; Forte and Mitrovica, 2001). In this case, density anomalies in the mantle deform its upper and lower interfaces as a function of the viscosity in the middle, and the related geoid is sensitive to this effect. Additional examples are the joint analysis with seismic tomograph, topography, and analytical models that allows a better characterization of the origin of intraplate volcanism (Panet et al., 2006; Cadio et al., 2012; Adam et al., 2014). The relationship between gravity and topography can also highlight the properties of convection in the upper mantle (Morgan, 1972) and mechanisms of swell support (Cadio et al., 2012). Joint analysis of the gravitational field with topography and other geophysical information is also capable of constraining the thermo-mechanical behavior of the lithosphere (Burov and Diament, 1995, 1996; Cattin et al., 2001; Berthet et al., 2013). The sensibility of the gravity field to the mass variations also allows to study mass redistribution at depth (Tiberi et al., 2003; Panet et al., 2014) and at the surface (Ramillien et al., 2004; Kusche and Schrama, 2005; Chanard et al., 2014).

Accurate determination of the Earth's gravity field over wide spatial scales is of fundamental importance for understanding the structure and dynamics of the Earth, including to resolve the compositional, mechanical, or thermal structure of the deep crust and upper mantle, and to explain the fundamental aspects of tectonic processes (Figure 1). Together with the accuracy of gravity datasets, the spatial resolution of the gravity field is also a key to better understand those geodynamical processes.

In solid-Earth physics, the gravity field model is utilized to elucidate mass variations in several domains, such as in oceanic and continental lithosphere, ice, and mantle. These variations can be well-constrained by knowledge of the gravity field that potentially have significant contributions to the understanding of the occurrence of tectonic motions or quantification of seismic hazards (Johannessen, 1999). This type of application can be achieved with adequate accuracy and spatial resolution. The requirements for measuring the static gravity field as it relates to understanding the solid Earth are schematically illustrated in Figure 2. For example, in order to observe the mechanical and properties of a swell, we require gravity data with a precision better than 5 mGal and a spatial accuracy that is higher than ∼200 km. This necessity can be fulfilled by using the GOCE (Gravity field and steady-state Ocean Circulation Explorer) dataset. In contrast, mapping bedrock layers in deep oceanic basins, where the reliefs remain unmapped due to thick sediment cover, is difficult using satellite data resolution; it requires a spatial resolution higher than today's highest resolution of satellite gravimetry data, but it is still observable using airborne surveys. As an alternative to gravimetry measurement, Sandwell et al. (2014) constructed a marine gravity model from satellite altimetry datasets (Jason-1 and Cryosat-2).

Unprecedented measurement techniques in gravimetry, from ground to airborne and satellite acquisitions, have significantly improved the accuracy, spatial resolution, and spatial scale of gravity-related datasets. The local gravity field is normally determined with ground surveys, where the accuracy can reach up to 1 μgal (e.g., Niebauer, 2015). Regional-scale gravity measurements are mostly accomplished by airborne gravity surveys that can reach an accuracy up to 1 mGal and a spatial resolution up to 2 km (Lane, 2004). The Earth's gravity field at a global scale is commonly acquired by satellite measurements. Starting with the launch of Sputnik in 1957, the techniques of gravity data acquisition from space are continuously enhanced. The GRACE (Gravity Recovery and Climate Experiment) mission, continued by GRACE Follow-On, is capable of measuring the Earth

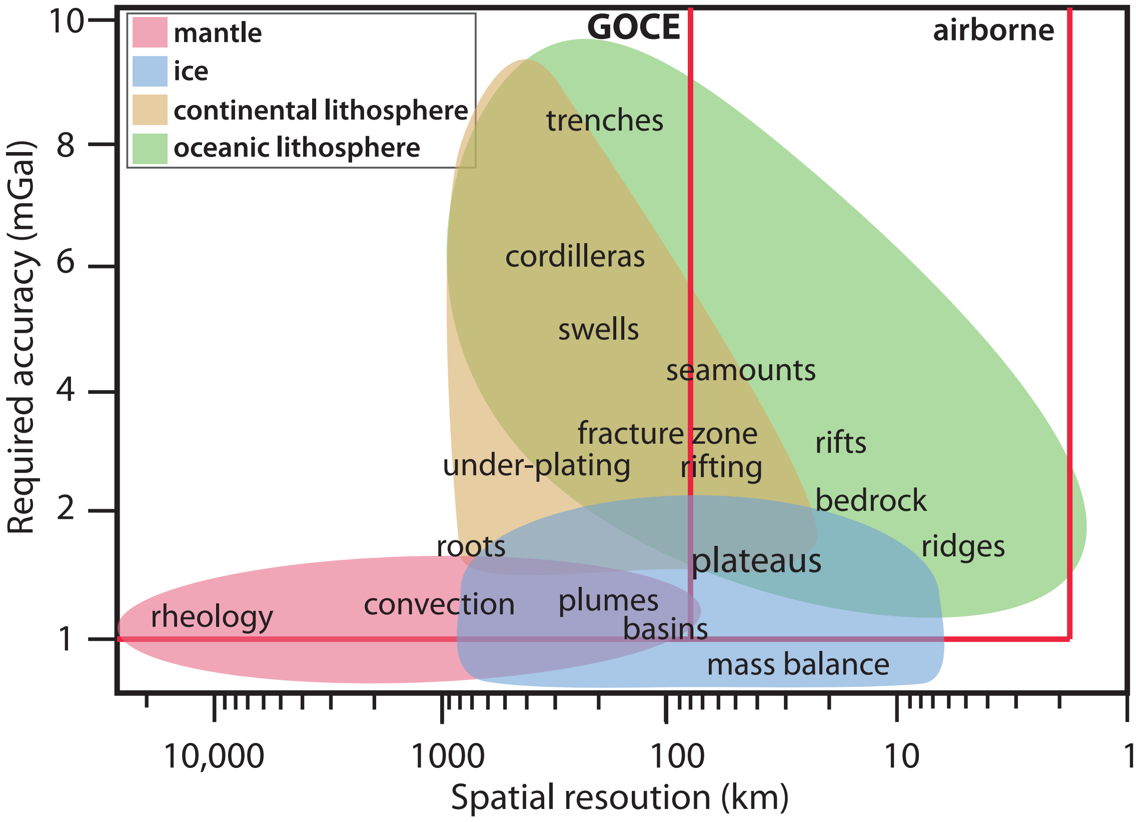

Figure 2: Summary of accuracy requirements for gravity measurements to study divers geodynamical processes as function of wavelength, modified from NASA (1987) and Johannessen (1999). Red lines indicate the maximum gravity accuracy and spatial resolution that can be attained by recent gravimetry advances at satellite and airborne acquisition altitudes.

gravity field with an accuracy of 5 mGal with spatial resolution of 300-400 km. Satellite data accuracy and spatial resolution were improved by the launch of the GOCE mission in 2009. Placed on a lower orbit, it enhanced the spatial resolution of satellite measurement up to ∼100 km (Rummel et al., 2011) with an accuracy up to ∼1 mGal and 10 mE.

In the solid Earth, gravity is commonly used in combination with topography at a commensurate resolution to elucidate the structures and dynamics of the Earth at depth. Topography effect estimation in gravity data processing is thus essential because of its major effect in the Earth's gravity field. Traditionally, gravitational contribution of the topography at local and regional scales is calculated using the Bullard (1936) approach, firstly initiated by Hayford and Bowie (1912), where the topography effect is calculated using a Hammer (1939) template mass subdivision (Figure 3). It takes into account the effect of local topography within a distance of 1.5° (∼167 km) from measurements, and the topography masses in the vicinity are approximated in the planar field. However, for regional and global scale applications, topography masses have to be considered to distances larger than 1.5° (cf. Mikuška et al., 2006; Szwillus et al., 2016) and the sphericity of the Earth must be taken into account in order to obtain a high precision (not less than the accuracy of the gravity measurements).

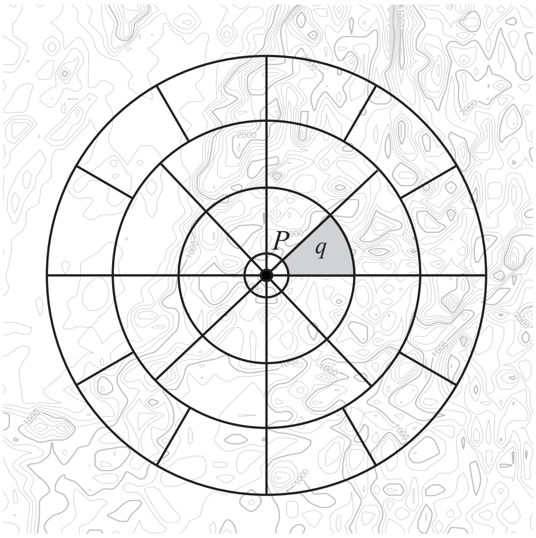

Figure 3: Hammer (1939) template for mass subdivision to estimate the gravity signature of the surrounding topography. Topography masses around the observation point P are divided into several mass compartments q by concentric circles of increasing radii.

The availability of satellite imagery, such as the one associated with the Pléiades mission, allows obtaining Digital Elevation Models (DEM) and Digital Terrain Models (DTM) at a very high resolution. For example, these DEMs are used for morpho-tectonic studies that allow constraining slip rates along seismogenic faults or to define erosion and fluvial incision by mapping river terraces (e.g., Berthet et al., 2014; Ferry et al., 2014). Although such high-precision data have not been used to calculate the gravitational effect of topography, it opens a possibility to improve the accuracy of topography effect estimations, notably for microgravity studies or other precise analyses of ground gravity surveys.

Figure 4 illustrates the typical workflow of gravity-related data processing from the data collection to data processing and interpretation. The use of gravity-related data at a high accuracy must be followed by meticulous data processing in order to maintain the precision of the results. These processes consist in gravity corrections and, if required, gravity reductions of known sources. This requires definition of the normal figure of the Earth, the topography, as well as other known sources with a high accuracy and an adequate spatial resolution. In parallel, these high-quality datasets must be processed by effective and precise approaches and computation tools. Such computation tools that allow gravity forward modelling are also needed in the interpretation steps, for example in performing stochastic analysis, and, when the gravity residual is properly extracted, to obtain well-constrained information on the geometry and dynamics of anomalous deep masses.

The availability of these new datasets, i.e. gravity-field related data and Earth topography model, provides a better spatial coverage and more accurate observations of the gravity field. The use and the interpretation of these higher quality data require re-

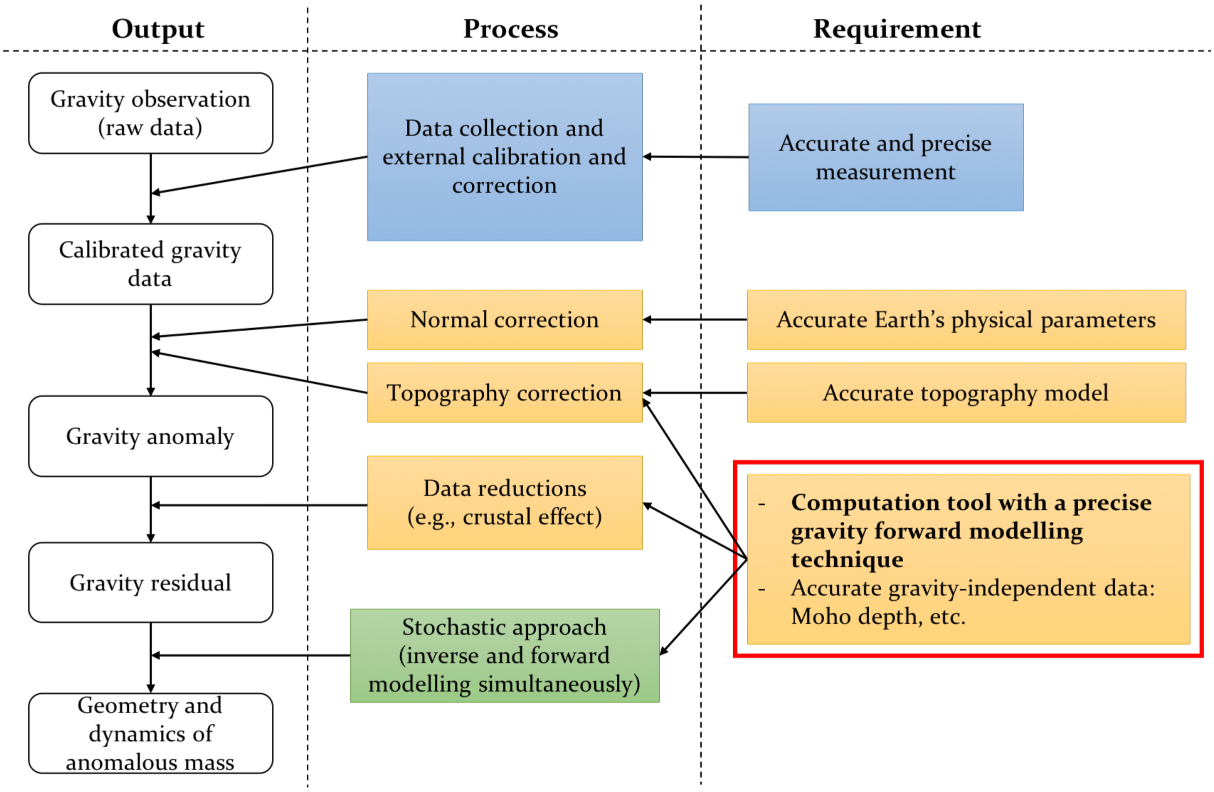

Figure 4: Gravity-related data processing workflow. The blue box indicates the data acquisition process, yellow boxes are related to the data correction and reduction, and green box is related to the interpretation process. The major part of work during this thesis is marked with the red box.

finements of the standard approaches. In particular, joint approaches combining ground, airborne, and satellite measurements are now needed to tackle many open questions, such as:

- What is the most efficient approach to estimate the gravitational attraction of a known mass body at multi-scale applications and for multi-altitude gravity observations?
- In the topography correction, how far must topography be taken into account, as a function of the dimension of the study zone and the altitude of the gravity and gravity gradients used in the study?
- Can the sensibility of satellite gravity gradient data allow the detection of second-order geometrical properties of subducting plates, i.e., more detailed geometry properties, for geodynamic application at a regional scale?

In this thesis, my work is focused on the development of a new computation tool that is adaptable for processing of all gravity datasets, including gravity reductions and forward modeling as a part of interpretation. This tool development is followed by an application on the analysis of the optimum topography truncation distance, as an important factor in topography correction and assessment. Next, in a second application, I attempt to understand and evaluate GOCE gravity gradients in relation with the second-order geometry properties of subducting plates, i.e. the lateral variations of subduction angles.

Structure of the manuscript

In this thesis manuscript, **the first chapter** presents the state of the art and basic theories of gravity field of the Earth that are used during this thesis. In this chapter, a review of the advancements in gravimetry and gradiometry up to today is also included.

The developed tool to calculate the gravity and gravity gradient effect of a mass body is presented in **Chapter 2**. This section is mostly presented in a scientific article submitted to Journal of Geodesy. Complementary information about the tool development and additional information that are not reported in the submitted paper are also presented.

Thereafter, this tool development is followed by the application on topography correction that is presented in **Chapter 3**. In this section, we quantify the relative error produced by variations in the topography truncation distance. We discuss the optimum truncation distance for local- and regional-scale applications to obtain a given precision in relative gravity and gravity gradient surveys. To highlight the importance of the precision in topography effect estimation and its implication to assess the compensation degree of topography in continental domain, I include the scientific paper by Cadio et al. (2016) (published in GJI) to which I participated during my thesis. This paper can be found in Appendix A.

Chapter 4 presents an application of GOCE gravity gradients to estimate the geometry of a subducting plate, including lateral variations of the subduction angle and its border. A preliminary analysis using synthetic slab models is presented, followed by an application to the Izu-Bonin-Mariana subduction zone. Finally, I conclude the work in this thesis by summarizing the results and proposing some perspectives for improvements in future works.

Chapter 1

Gravity and the Earth's Shape

> *La gravité est un mystère du corps inventé pour cacher les défauts de l'ésprit.*
> *[Gravity is a mystery of the body invented to conceal the defects of the mind.]*
> — *La Rochefoucauld*

The purpose of this chapter is to present the fundamentals of geopotential theory, including its spatial derivations, in sufficient details to assure a full understanding of the later chapters. Summaries about current gravity data acquisitions are also presented in this chapter. A simple forward modelling in gravity and gravity gradients is presented as a guide to interpret the gravity and gravity gradients distributions on the later chapters. Solutions to estimate the normal gravity field and its spatial derivations are presented in the end of this chapter, that is used later in the gravity and gravity gradients data processing.

1.1. Gravity

A mass rotating with Earth experiences the gravitational force of the Earth's masses and the centrifugal force due to the Earth's rotation. The sum of these forces is called gravity. If the Earth is a sphere, non rotational, and only consists of a homogeneous density, the gravitational acceleration will be constant on its surface. However, due to the rotation, the Earth topography, and lateral variations of density, the gravitational acceleration varies. As a result, the rotation deforms the Earth: it is flattened on the poles and bulged on the equator. It implies to the variation of gravitational as a function of latitude, where it is more important on the poles than along the equator. The gravitational field of this spheroid (or ellipsoid of revolution) is called the reference of gravitational field. Consequently, the local variations of the gravitational field produced by the topography and the density heterogeneities inside the Earth constitute gravimetric anomalies with respect to this model.

1.1.1. Gravitational Potential and Its Spatial Derivations

According to Newton's gravitational law, two point masses m_1 and m_2 separated by a distance r attract each other with an attractive force

$$\vec{F} = -G\frac{m_1 m_2}{\vec{r}^2} \tag{1.1}$$

where G is the gravitational constant,

$$G = 6.67408 \times 10^{-11} m^3 kg^{-1} s{-}2 \tag{1.2}$$

The minus sign in the force equation indicates that the force is attractive.

The masses m_1 and m_2 attract each other in a symmetrical way. However, it is convenient to call one of them as the attracting mass and the attracted mass for the other. Where the attracted mass is equal to unity and denote the attracting mass by m, the Eq. (1.1) becomes

$$F = -G\frac{m}{r^2} \tag{1.3}$$

This force is derived from a scalar gravitational potential function V, such as $F = -\nabla V$, where

$$V = G\frac{m}{r} \tag{1.4}$$

If we have a system of several point masses $m_1, m_2, \ldots, m_n$ instead of only one mass m, the potential of the system is the sum of the individual contributions

$$V = G\sum_{i=1}^{n}\frac{m_i}{r_i} \tag{1.5}$$

The gravitational acceleration $\vec{a}$ may be presented as the gradient of the potential V,

$$\vec{a} = -\nabla V = \left[\frac{\partial V}{\partial x}, \frac{\partial V}{\partial y}, \frac{\partial V}{\partial z}\right] \tag{1.6}$$

and the magnitude of the gravitational acceleration a can be defined as

$$a = G\sum_{i=1}^{n}\frac{m_i}{r_i^2} \tag{1.7}$$

1.1.2. Centrifugal Attraction

The centrifugal force arises as a result of the Earth's rotation about its axis. This force acts on an object that is affected by the rotation. In the case of satellite gravimetry, the satellite does not rotate with the Earth, thus only gravitation acts on the satellite (Torge, 2001).

Assuming a rotation of constant angular velocity ω around the fixed rotational axis. The centrifugal acceleration on a unit mass is given by

$$\vec{z} = \omega^2 \vec{p} \tag{1.8}$$

where p is the distance from the axis of rotation. With the geocentric latitude φ, we have

$$p = r\, cos\varphi \tag{1.9}$$

thus the magnitude of the centrifugal acceleration is

$$z = \omega^2 r\, cos\varphi \tag{1.10}$$

With

$$\vec{z} = \nabla Z \tag{1.11}$$

and Z, the centrifugal potential can be obtained with

$$Z = \frac{1}{2}\omega^2 \left(r\, cos\varphi\right)^2 \tag{1.12}$$

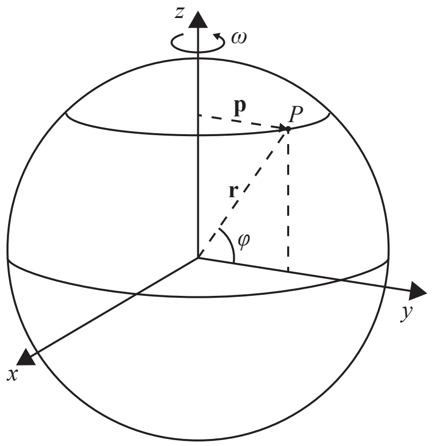

Figure 1.1: The centrifugal force of the point P that is located on the (r, φ) with the angular velocity ω. $\vec{p}$ is the direction vector of the point P from the centrifugal axis z.

1.1.3. Gravity Attraction

The gravity acceleration, or *gravity* $\vec{g}$, is the result of gravitation $\vec{a}$ and centrifugal acceleration $\vec{z}$,

$$\vec{g} = \vec{a} + \vec{z} \tag{1.13}$$

Similar with the gravity acceleration, the gravity potential W is also the sum if the potential gravitational V and centrifugal Z

$$W = V + Z \tag{1.14}$$

and thus the gravity acceleration also can be derived from the potential

$$\vec{g} = \nabla W \tag{1.15}$$

The magnitude g is simply called gravity. The direction of gravity vector $\vec{g}$ is parallel to the plumb line, and hence defined the local vertical direction.

1.1.4. Second Spatial Potential Derivation and Its mathematical Properties

The acceleration is the first spatial derivative of the potential in three independent orthogonal axes. The second order partial derivatives of the potential, which is also the first order spatial derivatives of the acceleration, is called *gravity gradients*, denoted as $\vec{T}$. In vector notation, it can be written as

$$\vec{T} = \nabla\vec{g} = \nabla\nabla W \tag{1.16}$$

For example, in a Cartesian coordinate system x, y, z, the tensor components of $\vec{T}$ can be written as

$$\vec{T} = \begin{bmatrix} T_{xx} & T_{xy} & T_{xz} \\ T_{yx} & T_{yy} & T_{yz} \\ T_{zx} & T_{zy} & T_{zz} \end{bmatrix} = \begin{bmatrix} \frac{\partial^2 W}{\partial x^2} & \frac{\partial^2 W}{\partial x \partial y} & \frac{\partial^2 W}{\partial x \partial z} \\ \frac{\partial^2 W}{\partial y \partial x} & \frac{\partial^2 W}{\partial y^2} & \frac{\partial^2 W}{\partial y \partial z} \\ \frac{\partial^2 W}{\partial z \partial x} & \frac{\partial^2 W}{\partial z \partial y} & \frac{\partial^2 W}{\partial z^2} \end{bmatrix} \tag{1.17}$$

In SI unit (Système International d'unités), the acceleration is expressed in m.s^{-2} and the gravity gradient is in s^{-2}. Other accepted and more convenient units for these parameters are:

- for the gravity g, in milligal or mGal, where 1 mGal = 10^{-5} m s^{-2},
- for the gravity gradients, in Eötvös, where 1 E = 10^{-9} s^{-2},
- thus, 1 E = 10^{-4} mGal m^{-1}.

The gravity acceleration has property

$$curl\,\vec{g} = curl\,\nabla W = 0 \tag{1.18}$$

follows from the corresponding properties of gravitation and centrifugal acceleration. In other words, $\vec{g}$ is an irrotational field. Therefore, for any orthogonal coordinate system, the operator of bi-gradient $\nabla\nabla$ is symmetric, thus

$$T_{ij} = T_{ji} \ \forall(i,j) \subset \{x,y,z\} \tag{1.19}$$

Outside the attracting bodies, the gravitational potential satisfies Laplace's equation (Blakely, 1996),

$$\Delta V = \frac{\partial^2 V}{\partial x^2} + \frac{\partial^2 V}{\partial y^2} + \frac{\partial^2 V}{\partial z^2} = 0 \tag{1.20}$$

This solution is called harmonic functions (Hofmann-Wellenhof and Moritz, 2005). For the gravity potential outside the attracting bodies, there is the influence of the centrifugal force. As consequence,

$$\Delta W = 2\omega^2 \tag{1.21}$$

In this study, we are only interested in the gravitational part. Therefore, the gravity gradients that will be discussed in this study is the result of the spatial derivative of the gravitational potential. According to Eq. 1.20, the trace of gravity gradients $\vec{T}$ in the orthogonal coordinate system becomes

$$tr(\vec{T}) = \sum T_{ii} = 0 \ \forall i \subset x,y,z \tag{1.22}$$

In consequence of the Eq. (1.19) and (1.22), has only five independent components at any observation point.

1.2. Gravity Data Acquisition

Gravimetry deals with the measurement of the gravity acceleration (hereinafter called gravity) and the gravity gradients. In general, gravimetry is divided into two type of measurements, absolute and relative measurements. While absolute gravimeters measure the absolute gravity, relative type of gravimeters measure the variations of the gravity field with time and space. A global gravity reference system is required to refer local and regional gravity network to a common standard (Torge, 2001).

Mass density inhomogeneities as well as mass displacement over time causes spatial and temporal variations on the gravitational attraction measured by the gravimeter or gravity gradiometer. In this context, gravity observations can be used to derive information in various domains, including mineral exploration, solid earth applications, water storage estimation, or global water current mapping.

Nowadays, the advancement of technologies allows us to measure the gravity field with unprecedented accuracy at various levels of measurement. Currently, gravity measurements are performed using terrestrial, airborne, or satellite platforms (Figure 1.2). Those levels of measurements provide different spatial resolutions of gravity attractions, the further from the Earth surface, a lower spatial resolution it gives. From the point of view of the survey coverage, ground surveys normally performed in a relatively smaller network than airborne and satellite missions due to the limitation of terrain accessibility. The combination of those three level datasets can be useful for the construction of Earth gravity field models, e.g. Earth Gravitational Model 1996 (EGM96) (Lemoine et al., 1997), EGM2008 (Pavlis et al., 2008), and Word Gravity Map 2012 (WGM2012) (Balmino et al., 2012). Together, these datasets can also be used to build global gravity field models and to assess mass distributions at depth in order to provide information at various scales from regional lithospheric structures to a very local and shallow anomalous bodies.

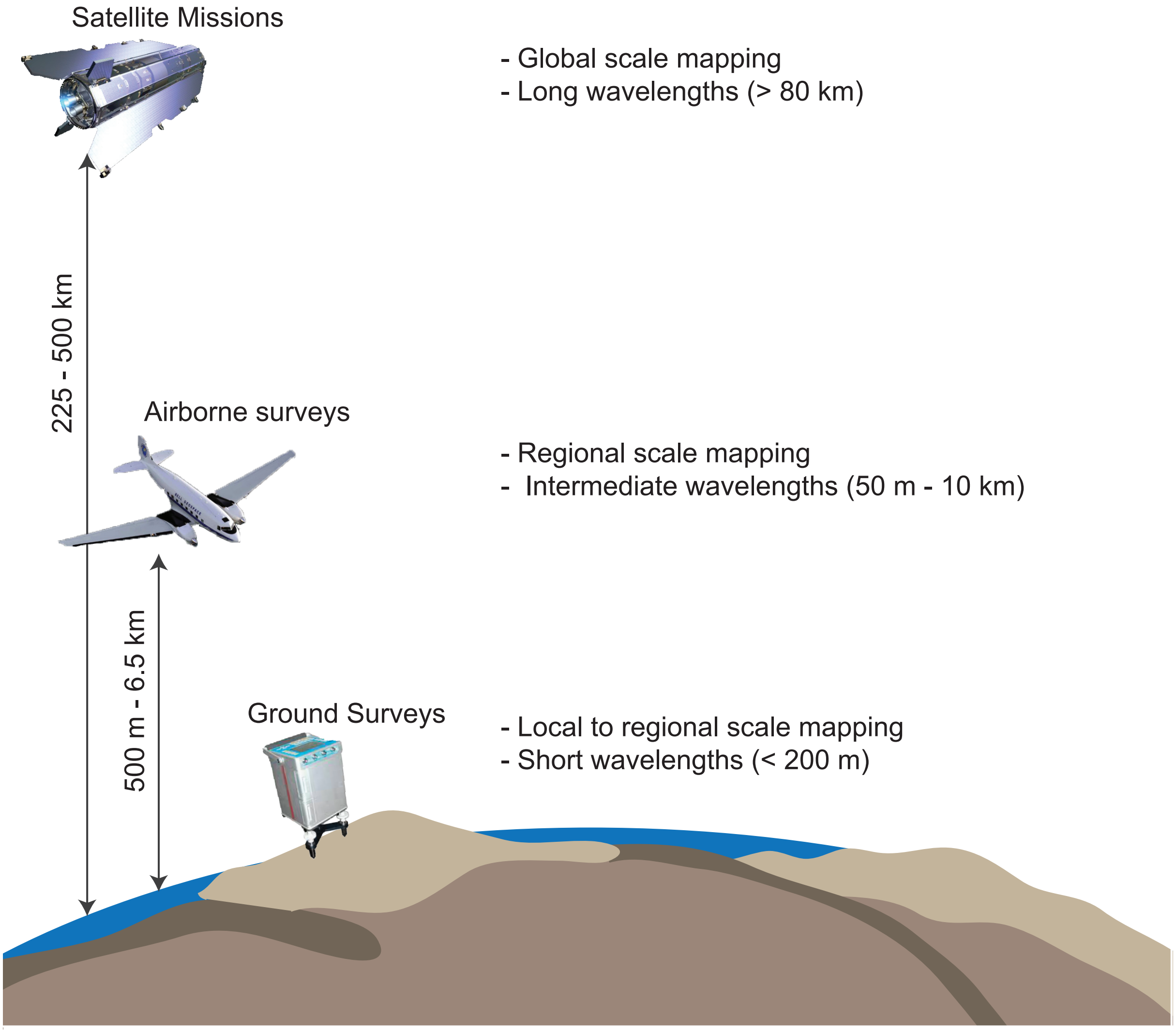

Figure 1.2: A simplified scheme showing the present-day available gravity data-sets, which include measurements from satellite missions as well as airborne or ground surveys.

Recent conventional gravimeters provide the measurement of the vertical component of gravity (g_z). Yet the use of accelerometers, especially on the moving platforms like airborne of satellite, provide us with gravity in three directions in orthogonal system

(g_x, g_y, g_z).

When measuring the gravity gradients, the gradients are obtained by calculating the difference between pairs of measured accelerations that are separated by a known distance. It can be written in a mathematical notation,

$$T_{ij} = \frac{\partial g_i}{\partial j} = \lim_{d_j \to 0} \frac{g_i\left(j + \frac{d_j}{2}\right) - g_i\left(j - \frac{d_j}{2}\right)}{d_j} \tag{1.23}$$

where g_i is the gravity acceleration in the i-direction, d_j is the distance in the axes j, and $i, j \subset x, y, z$ (cf. Figure 1.5 that visualize the gradiometer configuration of GOCE as an example).

1.2.1. Terrestrial Gravity Measurements

The first terrestrial gravity measurement was performed by using the pendulum method, that is based on the measurement of the period and the length of a freely swinging pendulum (Torge, 2001). However, this method is no longer used due to its limitation in accuracy. Nowadays, gravity instrumentation has been driven by the need of a better precision, shorter time for each measurement, and the ease of use (Torge, 1989; Dubois et al., 2011; Crossley et al., 2013). In terrestrial gravimetry, there are two domains of measurement type that are widely used, absolute and relative measurements.

Absolute gravimeters are based on the measure of time and distance of a free-falling object, as conceptualized by Galileo Galilei. To obtain a high precision, the time and distance measurements of the free fall object should be done in a very accurate way (Van Camp et al., 2017). Essentially, recent absolute gravimeters are equipped with an atomic clock to measure the time precisely, a laser interferometer to measure the distance, a vacuum chamber where the tested mass travels vertically, and computing unit for data acquisition and the calculation of gravity. The absolute gravimeter, such as Micro-g LaCoste FG5, can obtain an accuracy of 1-2 µgal (Sasagawa et al., 1995; Niebauer et al., 1995). The A10 portable absolute gravimeter, which is smaller than an FG5 is 10 times less precise and accurate than an FG5 gravimeter (Van Camp et al., 2017). Beside those classical free-fall gravimeters, quantum free-fall gravimeters are recently developed (Debs et al., 2013; Bonvalot et al., 2016). One of them is the Absolute Quatum Gravimeter (AQG), developed by Muquans. In this type of instrument, the classical free-fall mass is replaced by cold atoms where the position and the time of their motions are observed precisely. Absolute gravimeters are widely used for measuring temporal variations of gravity field, for example for observing postglacial rebound and tectonic activities (e.g., Larson and Van Dam, 2000; Francis et al., 2004) and hydrological variations (Jacob et al., 2008).

For relative gravimeters, there are two instrument types that are widely used, spring gravimeters and superconducting gravimeters. In spring gravimeters, a proof mass is suspended by using a mechanical spring. Some widely used instruments such as Micro-g LaCoste gPhone, Scintrex CG-5, and recent Scintrex CG-6 Autograph with an accuracy up to 5 µgal (Niebauer, 2015). When gravity changes, the force acting on the proof mass

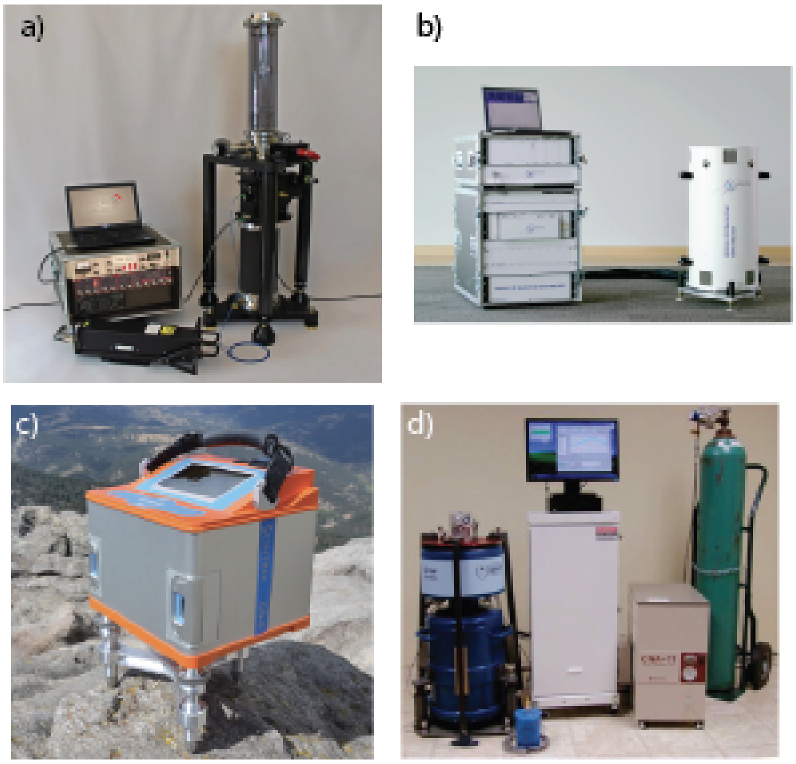

Figure 1.3: FG5 (a) Micro-g LaCoste absolute gravimeters, the Absolute Quantum Gravimetry (AQG) from Muquans (b), Scintrex CG-6 Autograph (c) by Scintrex Ltd., and iGrav superconducting gravimeter (d) (Hinderer et al., 2015).

will change, and it affects in a change in the length of the supporting spring. Because it is easy to transport, the spring instruments are mostly used for regional gravity mapping.

Superconducting gravimeter is the most precise relative instrument, approximately 0.01 µgal (Hinderer et al., 2015). Instead of a mechanical spring, it consists of a hollow superconducting sphere as a proof mass that levitates in a constant magnetic field generated by currents in a pair of superconducting coils (Hinderer et al., 2015; Van Camp et al., 2017). Because of its complexity of the supporting instruments and materials, this superconducting gravimeter is not easily moved. It is mostly used to measure temporal variations.

To obtain the related absolute gravity value from relative measurements, the stations of the relative measurements should be tied into one or more absolute gravity bases (Torge, 1989; Seigel, 1995).

1.2.2. Airborne

Located in the mid-altitude (Figure 1.2), airborne gravimeters bring valuable information on static and dynamic geophysical phenomena and bridge the gap between terrestrial and satellite measurements of the static gravity field. Airborne systems became an alternative for a rapid regional gravity mapping for several applications, especially for exploration reconnaissance and geodetic applications.

Since the first era of airborne gravimetry, gravimeters and also gradiometers have been developed in various measurement techniques, such as using zero-spring length (e.g. LaCoste Romberg and TAGS-7 dynamic gravimeter from Micro-g LaCoste, GT-1A and GT-2A by Gravimetric Technologies) and using accelerometer measurement (e.g. Air-Grav System by Sander Geophysics Ltd. (Sander et al., 2005), Falcon Airborne Gravimeter (AG) and Airborne Gravity Gradiometer (AGG) by CGG). The instrument is gyro-stabilized gimbals platform to maintain direction in space and to provide vertical stability.

The precision of recent airborne surveys datasets varies between 0.1 - 5 mGal in term of gravity acceleration and 3 - 6 E in term of gravity gradient. The spatial resolution of airborne surveys also varies depending of the survey altitude, varies from 500 m up to 6.5 km above sea level with the resulting spatial resolution approximately 5 - 10 km (Forsberg and Olesen, 2007) and can reach up to 50 m in Helifalcon system (Chen and Dransfield, 2016). Some reports and evaluations about previous airborne survey can be found in Christensen et al. (2015); Chen and Dransfield (2016); Dransfield (2010); Dransfield and Lee (2004); H. P. Elieff and Sander (2015); Damiani and Youngman (2011); Forsberg and Olesen (2007); Hannah (2001); Sander et al. (2005); Seigel (1995); Verdun et al. (2003).

1.2.3. Satellite Mission

Since the launch of Sputnik I in 1957, artificial satellites have been used for geodetic purposes, including the determination of Earth's gravity field and rotation parameters. In the beginning of satellite launch, the knowledge of the very long-wavelength of gravity signal was obtained by the analysis of the orbit perturbations of the artificial satellite, which is caused by the flattening of the Earth and also the irregular distribution of masses inside and on the Earth. By accurately measuring the deviations of the satellite track from its designed orbit, it can be used to compute the forces it undergoes, among them is the gravity force. For this purpose, the satellites are equipped with rectoflectors to obtain telemetric data for positioning. Some examples of the satellites built for this purpose are Starlette (1975) and LAGEOS (1976).

On higher resolution, gravity field over oceanic domain also can be obtained from satellites altimetry, among them are Topex-Poseidon, Jason, Geosat, ERS, and Cryosat (Sandwell and Smith, 1997; Andersen and Knudsen, 1997; Sandwell and Smith, 2009). Satellite altimetry measures the altitude of the satellite above the closest point of sea surface, which is the approximation of the geoid surface, using a pulse-limited radar (Sandwell and Smith, 1997). Global precise tracking along with orbit dynamic calculations allow to obtain the geoid with an accuracy of tens of centimeters. The geoid obtained from this measurement then is processed using Meinesz (1928) or Stokes (1849) method to obtain gravity anomaly.

The advancement of the gravity field measurement on global scale coverage with an unprecedented accuracy was importantly improved after the launch of satellite gravimetry missions CHAMP (CHAllenging Minisatellite Payload, 2000 to 2010), GRACE (Gravity Recovery and Climate Experiment, launched 2002) and GOCE (Gravity Field and

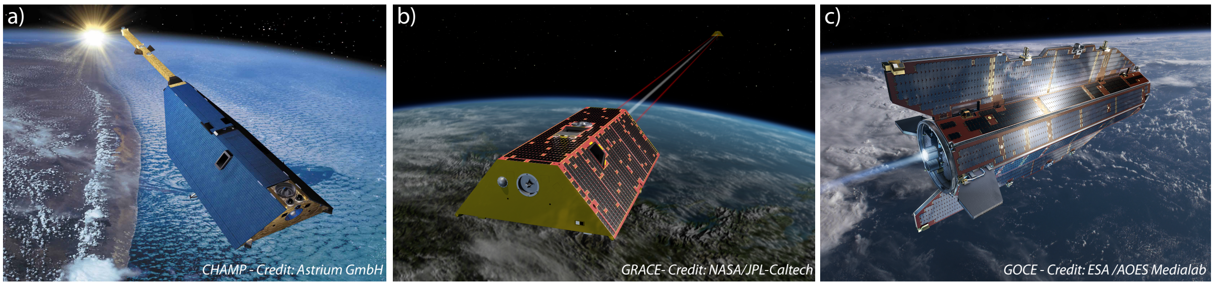

Figure 1.4: CHAMP, GRACE, and GOCE satellite missions.

Steady-State Ocean Circulation Explorer, 2009 to 2013) (Figure 1.4). Satellite gravimetry normally occupies the low Earth orbit (LOE) (Hofmann-Wellenhof and Moritz, 2005), with altitude is lower than 2000 km.

One of the objectives of the CHAMP mission was to accurately determine the long-wavelength features of the static Earth gravity field. It flied at the altitude of 400 km in average. The gravity field is also deducted from the analysis of the orbit perturbation, but this time it was measured continuously and accurately using Global Navigational Satellite System (GNSS) and it was completed with the measurements of a three-axial accelerometer at the center of mass of CHAMP. It allowed to separate the forces acting on the satellite surface (e.g. satellite drag or radiation pressure) from the gravitational forces (Barthelmes, 2018; Hofmann-Wellenhof and Moritz, 2005). The best global gravity field model (GGM) from CHAMP spatial datasets has a precision up to 0.5 mGal in term of gravity anomaly and 5 cm in term of geoid with a spatial resolution of 400 km (Reigber et al., 2005).

After CHAMP, there was GRACE, the twin satellite mission. The main objectives of GRACE are to determine the global high-resolution of the Earth gravity field in temporal variations. The initial altitude of this mission is between 485 and 500 km with a track repetition is approximately 15 days. Because GRACE measures continuously, GRACE datasets are widely used for spatio-temporal variations in global scale. The two GRACE satellites are separated on 220 km apart. The satellites are equipped with GNSS receivers and accelerometers to track the orbit and measure the non-gravitational forces. The spatio-temporal variations of the gravity modify the distance between the satellites, measured by the microwave K-band range system between the tandem satellites. The GRACE concept can be regarded as a one-dimensional gradiometer with a very long distance (Seeber, 2003). The geoid precision from GRACE is about 2-3 mm with 300-400 km of spatial resolution (Tapley et al., 2004). GRACE mission orbited Earth from 2002-2017. At May 22, 2018, GRACE-Follow On (GRACE-FO) was launched to continue the work of GRACE to monitor hydrological changes of the Earth.

GOCE mission becomes the first satellite mission that uses a gravity gradiometer to obtain the gravity field in a high-resolution and accuracy (Rummel et al., 2011; Drinkwater et al., 2003). It flied at ∼255 km of altitude height, the lowest altitude satellite gravimetry ever launched .The gradiometer is mounted in the satellite, composed with six accelerometers that were put in three spatial orthogonal axis, where the baseline between accelerometers at each axes is 50 cm. The scheme of the GOCE's gravity gradiometer construction can be seen on Figure 1.5. The mathematical principle to obtain the gravity gradient observed by GOCE is explained in the Eq. (1.23).

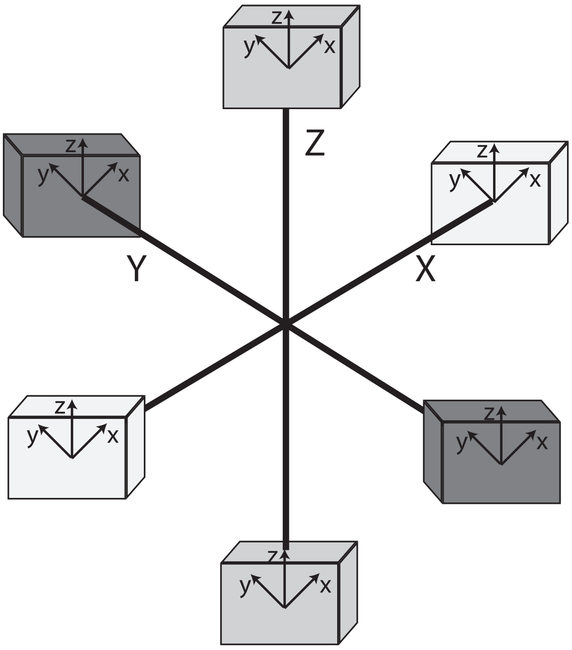

Figure 1.5: A simplified scheme of a gradiometer embarked in GOCE satellite. It consists of three pairs of accelerometers mounted orthogonaly, separated with certain 50 cm length of baseline on each axes. Each accelerometer measures the gravitational acceleration in three orthogonal axis, therefore this gradiometer construction allows in providing gravity gradients in full tensors.

GOCE datasets has enhanced the determination of the global gravity field model (Gruber et al., 2011). The mean global accuracy achieved by GOCE observation in EGM_TIM_RL05 Earth gravity model is 2.4 cm in terms of geoid heights, 0.7 mGal for gravity anomalies with 100 km of spatial resolution (Brockmann et al., 2014). In GOCE level 2 datasets, the accuracy in gravity gradients term is better than 10 mE. Various types of GOCE datasets can be downloaded in GOCE virtual online archive (http://eo-virtual-archive1.esa.int/Index.html).

1.3. Gravity Forward Modeling

Gravity Forward Modeling (GFM) denotes the computation of the gravitational field generated by any given mass distribution (Hirt, 2016). The basic technique of GFM refers to Newton's law of universal gravitation (see Section 1.1.1.). GFM is relevant for the context of geoid determination (Sansò and Sideris, 2013), gravity prediction, interpolation, and reduction, and for the investigation of the interior structure of the Earth (Álvarez et al., 2012).

The Earth's topography, given in form of Digital Terrain Model (DTM), is the most frequently used mass distribution in GFM (Grombein et al., 2014; Hirt et al., 2012). The details for the estimation of topography effect will be discussed in the Chapter 3.

Several solutions exists to calculate the gravitational effect associated to specific simple source mass, among them are point source (cf. Blakely, 1996) and prism (cf. Mader, 1951). However, the implementation of GFM in the real geophysical or geodetic case normally involves a complicated geometry of source mass. Decomposing such geometry into smaller simple bodies and sum their contributions could be a solution (Barnett, 1976; Singh and Guptasarma, 2001). But using a GFM method that can better approach the modelled mass geometry can be an ideal one. This method is further discussed in the Chapter 2.

For the further discussion in this dissertation report, the acceleration will be simply called gravity and its gradient will be called gravity gradients.

1.3.1. Understanding Gravity and Gravity Gradient of a Simple Body Mass

The gravity field of the Earth is resulted from the integration of various sources, including topography, volcanoes, mantle plume, etc. Moreover, almost all of those effecting mass are irregularly shaped. Therefore, sometimes it is difficult to interpret the corresponding gravity field signal.

To better understand the gravity field signal, it is better to start from the gravity field signal associated to a simple geometry. In this part, a cube with a dimension of 100 m×100 m×100 m is used as the source mass, with a tested density of 300 kg m^{-3}. The calculation is performed at 5 m above the prism.

The spatial derivative of gravitational potential in three orthogonal directions result the gravity in three directions (Figure 1.6). The resulted gravity fields are different among those directions,

- g_x, is the gravity attraction in the direction x. The corresponding signal is sensitive on the x direction, with a pair of positive-negative signal at the mass borders along the x axes, located at the border of the mass.
- g_y, is the gravity attraction in the direction y, sensitive on the direction y. Like g_x, a pair of positive-negative signal are located at the mass' borders along the y direction.
- g_z, is the gravity attraction in vertical direction (z). This is the direction of the gravity that is used in most at geophysical related applications.The highest magnitude of the signal is located at the center of the mass. In this case, the direction of z-axis is upward, thus it produces a negative sign in the g_z.

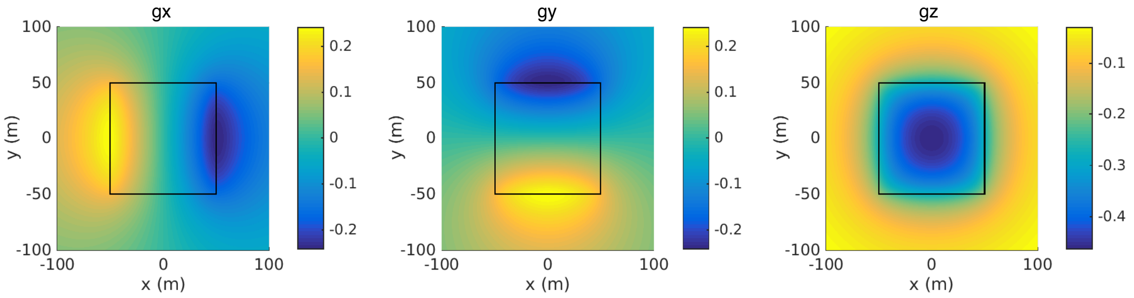

Figure 1.6: Gravity signal of a cube (in mGal) in three spatial directions. For the scheme of the cube, see Figure 1.7.

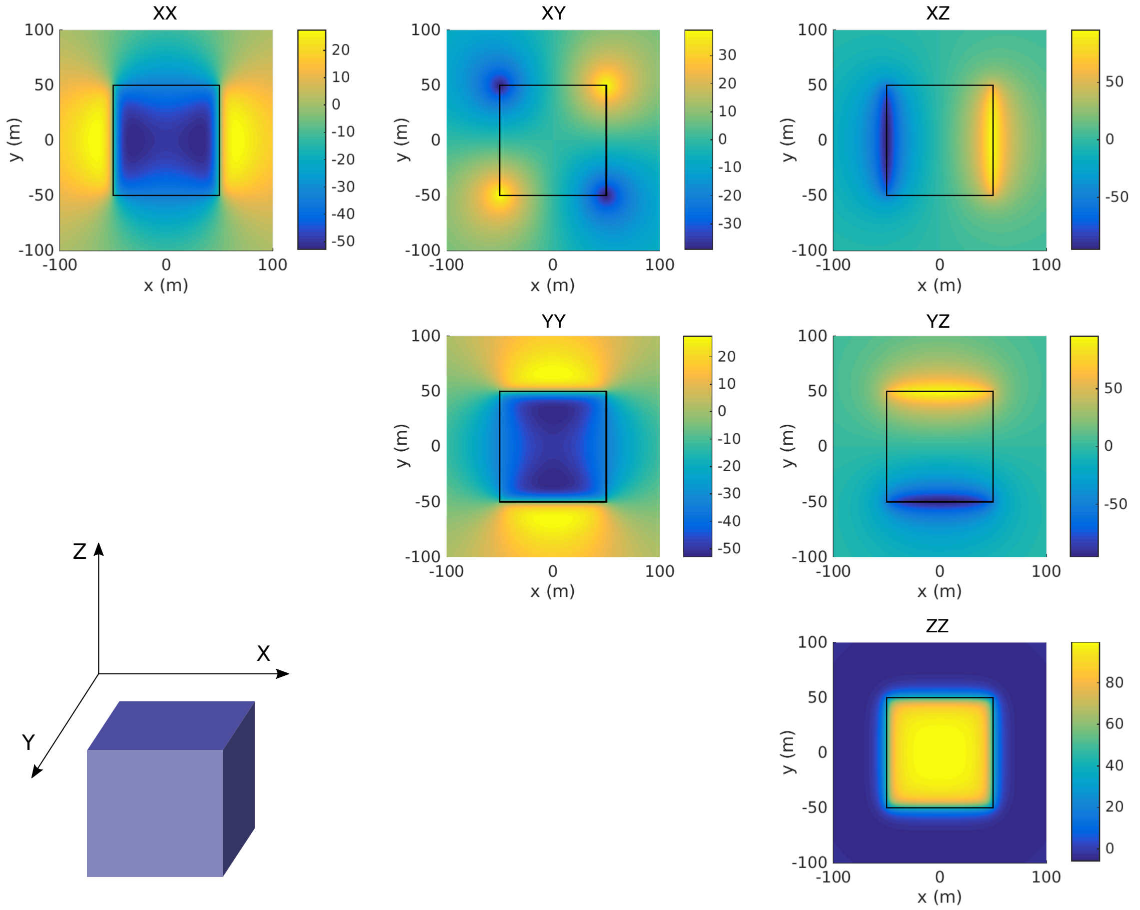

Figure 1.7: Gravity gradient signal of a cube (in E). The scheme of the cube and the orientation of x, y, z-axes of gravity gradients are shown on the bottom-left.

The gravity gradient components are computed by deriving each of three gravity components on the x, y, and z directions (see Section 1.1.4.). Figure 1.7 shows six tensors of gravity gradients of a prism. As seen on Figure 1.7, the wavelength of gravity gradient signals are shorter and more constrained than gravity.

For each component of gravity gradients,

- T_{xx} is the derivative of g_x in the x direction (cf. Figure 1.6), resulting into a "positive-negative-positive" anomaly along the x-axes for an anomaly with positive density and inversely for a negative one. The borders of the prism along the x direction are close to the zero.
- T_{yy} has a same characteristic as T_{xx} but along the y direction.
- T_{zz} is the most used component other than other gravity gradient tensors. It has a similar characteristic with g_z, yet the signal is more constrained following the geometry of the mass. The highest magnitude of the signal is located at the center of the mass, positive for a positive anomalous mass body and inversely.
- T_{xy} is computed by taking the derivative of the g_x in the y direction or by taking the derivative of the g_y in the x direction. This results a "negative-positive-negative-positive" pair. The peaks of those signals are located on the approximately corners of the anomalous mass.
- T_{xz} is sensitive to the mass variation along x axes, resulting in a positive-negative anomalies. It has a similar signal pattern as the g_x yet it is more constrained.
- T_{yz} is sensitive to the mass variation along y axes. Like T_{xz}, it results in a positive-negative anomalies on the y direction. The resulted signal is more constrained than the horizontal gravity g_y.

The magnitude and the wavelength of the signal depend strongly on the size of the anomalous mass, its density, and also its distance to the measurement point. Beside the magnitude, the noise in the measured signal could be also augmented due to the decrease of the distance between the measurement point and the mass source.

In general, the tensors of gravity gradient in horizontal directions are helpful to detect the lateral variation of the observed mass. Nevertheless, they are less used than the vertical tensor due to the difficulties in the signal interpretation. This simple example illustrates the complementary of gravity and gravity gradients datatasets to better assess geometry of body mass at depth.

1.4. Normal Gravity

The observed gravity and gravity gradients is the total attraction of the gravitational and the centrifugal force of the Earth (see Section 1.1.). The magnitude of the observed gravity and gravity gradient is thus very large (cf. Figure 1.8). The majority part of the measured gravity signal is due to the shape of the Earth. This large signal tends to "conceal" the detectable anomalous gravity due to the anomalous mass. To handle this, the signal due to the "normal" shape of the Earth is normally removed.

Approximation to obtain the disturbing potential (or also anomalous potential) A at the point P is

$$A_P = W_P - U_P \tag{1.24}$$

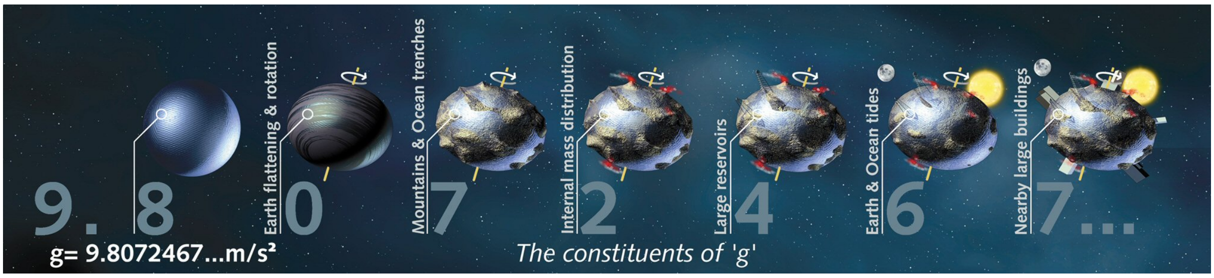

Figure 1.8: The constituents that make up the force of gravitational acceleration g at Earth's surface (ESA, 2008).

where W_P is the actual gravity potential and U_P is the normal gravity potential. The method to obtain the normal potential is described in this section.

In geodesy, the best representative of the Earth shape is the geoid (Figure 1.9), which is an equipotential surface of the Earth's gravity field, that coincides with the steady sea level. However, due to its irregularity, it is not straightforward to handle this geoid form mathematically.

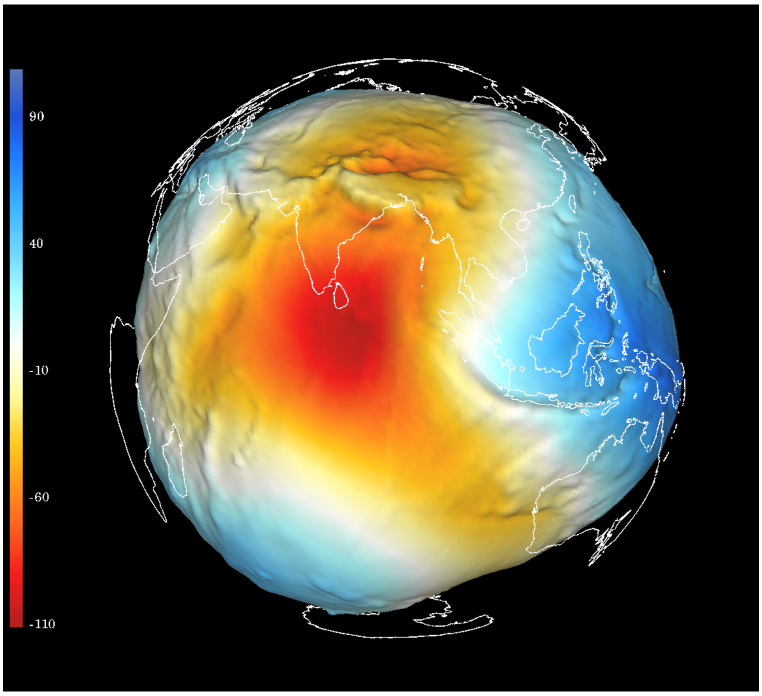

Figure 1.9: Geoid as the "true" shape of the Earth. The color scale represents the geoid height. Source: (unavco.org)

As the first estimation, the Earth is a sphere. As a further approximation, the normal figure of the Earth can be considered as an ellipsoid of revolution, a geometric surface produced by rotating an ellipse about its rotation axis.

The normal gravity potential is resulted from the gravitational potential of the normal reference, here is ellipsoid of revolution, and the centrifugal potential around its rotation axis. Hence, the normal potential function is determined by the shape of the ellipsoid of revolution, the total Earth mass M, and the angular velocity ω. Mathematically, the normal gravity potential U at the radius r from the center of the Earth and latitude φ and can be written as following,

$$U(r, \varphi) = V_u(r, \varphi) + Z(r, \varphi) \tag{1.25}$$

where V_u is the gravitational potential due to the Earth model geometry and Z is the potential due to the Earth rotation (cf. Eq. (1.12)).

Due to the ellipticity of the Earth, the magnitude of the normal gravitational potential V_u strongly depends on the geocentric radius and latitude of the measurement, r and φ respectively. Replacing $t = sin\varphi$ and $u = cos\varphi$, the Clairaut's theorem to obtain the normal gravitational potential V_u can be written as following,

$$V_u(r, \varphi) = \frac{GM}{r}\left(1 - J_2\left(\frac{a}{r}\right)^2 P_2(t) - J_4\left(\frac{a}{r}\right)^4 P_4(t)\right) \tag{1.26}$$

where a is the length of the semi-major axis of the Earth. J_n is the dynamic form factor of the normal ellipsoid which is related to the flattening of the Earth geometry at the poles. P_n are the Legendre polynomia of degree n, that is (Hofmann-Wellenhof and Moritz, 2005),

$$P_2(t) = \frac{1}{2}3t^2 - 1 \tag{1.27}$$

and

$$P_4(t) = \frac{1}{8}\left(35t^4 - 30t^2 + 3\right) \tag{1.28}$$

One of the known reference ellipsoid that is widely used is Geodetic Reference System 1980 (GRS80). It is defined based on the theory of the geocentric equipotential ellipsoid The constants that define this ellipsoid of revolution are written in Table 1.1 (Moritz, 1980).

Table 1.1: Numerical Parameters of the GRS 1980

Parameter	**Value**	**Unit**
a : equatorial radius of the Earth	6378137	m
$1/f$: invers flattening	298.257222101	
GM : geocentric gravitational constant of the earth (including the atmosphere)	398 600.5×10^9	m^3 s^{-2}
J_2 : dynamical form factor of the Earth	1 082.63×10^{-6}	-
J_4 : dynamical form factor of the Earth (higher degree)	- 2.37091222×10^{-6}	-
ω : angular velocity of the Earth	7.29211501×10^{-5}	rad s^{-1}

Spatial Derivative of The Normal Gravity

For various purposes, partial derivatives of the normal potential U are required. This potential is resulted as a function of the variables r and t, where $t = sin\varphi$. Since the equipotential ellipsoid is rotationally symmetric, there would be no derivatives with respect to longitude λ. From the Eq. (1.25), the partial derivatives of the normal potential with the respect to polar coordinates are

$$\frac{\partial U}{\partial i} = \frac{\partial V_u}{\partial i} + \frac{\partial Z}{\partial i} \text{and} \frac{\partial^2 U}{\partial i \partial j} = \frac{\partial^2 V_u}{\partial i \partial j} + \frac{\partial^2 Z}{\partial i \partial j} \tag{1.29}$$

where $\forall (i, j) \subset \{r, t\}$.

The following partial derivatives of the normal gravitational potential V_u are obtained by differenting Eq. (1.26),

$$\frac{\partial V_u}{\partial r} = -\frac{GM}{r^2}\left(1 - 3J_2\left(\frac{a}{r}\right)^2 P_2(t) - 5J_4\left(\frac{a}{r}\right)^4 P_4(t)\right) \tag{1.30}$$

$$\frac{\partial V_u}{\partial t} = -\frac{GM}{r}\left(J_2\left(\frac{a}{r}\right)^2 \frac{\partial P_2(t)}{\partial t} - J_4\left(\frac{a}{r}\right)^4 \frac{\partial P_4(t)}{\partial t}\right) \tag{1.31}$$

$$\frac{\partial^2 V_u}{\partial r^2} = 2\frac{GM}{r^3}\left(1 - 6J_2\left(\frac{a}{r}\right)^2 P_2(t) - 15J_4\left(\frac{a}{r}\right)^4 P_4(t)\right) \tag{1.32}$$

$$\frac{\partial^2 V_u}{\partial t^2} = -\frac{GM}{r}\left(J_2\left(\frac{a}{r}\right)^2 \frac{\partial^2 P_2(t)}{\partial t^2} - J_4\left(\frac{a}{r}\right)^4 \frac{\partial^2 P_4(t)}{\partial t^2}\right) \tag{1.33}$$

$$\frac{\partial^2 V_u}{\partial r \partial t} = \frac{GM}{r^2}\left(3J_2\left(\frac{a}{r}\right)^2 \frac{\partial P_2(t)}{\partial t} - 5J_4\left(\frac{a}{r}\right)^4 \frac{\partial P_4(t)}{\partial t}\right) \tag{1.34}$$

where the partial derivatives of the Legendre polynomia of the Eq. (1.27) and (1.28) are

$$\frac{\partial P_2(t)}{\partial t} = 3t \tag{1.35}$$

$$\frac{\partial^2 P_2(t)}{\partial t^2} = 3 \tag{1.36}$$

$$\frac{\partial P_4(t)}{\partial t} = \frac{1}{2}\left(35t^3 - 15t\right) \tag{1.37}$$

$$\frac{\partial P_4^2(t)}{\partial t^2} = \frac{1}{2}\left(105t^2 - 15\right) \tag{1.38}$$

The partial derivatives of the centrifugal potential Z are obtained by differenting Eq. (1.12). Remembering that $t = sin\varphi$, and $u = cos\varphi = \sqrt{1 - t^2}$, the spatial derivatives of Z with respect to polar coordinates can be written as

$$\frac{\partial Z}{\partial r} = \omega^2 \ r \ u^2 \tag{1.39}$$

$$\frac{\partial Z}{\partial t} = -\omega^2 \; r^2 \; t \tag{1.40}$$

$$\frac{\partial^2 Z}{\partial r^2} = \omega^2 \; u^2 \tag{1.41}$$

$$\frac{\partial^2 Z}{\partial t^2} = -\omega^2 \; r^2 \tag{1.42}$$

$$\frac{\partial^2 Z}{\partial r \partial t} = -2\omega^2 \; r \; t \tag{1.43}$$

1.5. Derivatives of the Potentials with Respect to the Local Cartesian Coordinates

The origin of polar coordinates latitude, longitude, and geocentric radius (φ, λ, r) lies at the center of the reference ellipsoid. While the origin of a local Cartesian coodinates x, y, z lies at the point $P_0(\varphi_0, \lambda_0, r_0)$. The positive z-axis direction is in the direction of increasing geocentric radius r (up), the $x - z$ plane lies in the meridian passing though P_0 with the positive x-axis pointing north, and the positive y-axis pointing west.

Defining the Cartesian component $x_i = [x, y, z]$, transforming the first-order spatial derivatives from polar coordinates to the local Cartesian of the Eq. (1.30) until (1.43) can be done using following matrix (Tscherning, 1976)

$$\frac{\partial V}{\partial x_i} = \begin{bmatrix} \dfrac{u}{r}\dfrac{\partial V}{\partial t} \\ \dfrac{1}{ur}\dfrac{\partial V}{\partial \lambda} \\ \dfrac{\partial V}{\partial r} \end{bmatrix} \tag{1.44}$$

The symmetric matrix of second-order derivatives is

$$\frac{\partial^2 V}{\partial x_i \partial x_j} = \begin{bmatrix} \dfrac{1}{r}\dfrac{\partial V}{\partial r} - \dfrac{t}{r^2}\dfrac{\partial V}{\partial t} + \dfrac{u^2}{r^2}\dfrac{\partial^2 V}{\partial t^2} & \dots & \dots \\ -\dfrac{1}{r}\left(\dfrac{\partial^2 V}{\partial t \partial \lambda} + \dfrac{t}{u^2}\dfrac{\partial V}{\partial \lambda}\right) & -\dfrac{1}{r}\dfrac{\partial V}{\partial r} - \dfrac{t}{r^2}\dfrac{\partial V}{\partial t} + \dfrac{1}{u^2 r^2}\dfrac{\partial^2 V}{\partial \lambda^2} & \dots \\ \dfrac{u}{r}\left(\dfrac{\partial^2 V}{\partial t \partial r} - \dfrac{1}{r}\dfrac{\partial V}{\partial t}\right) & -\dfrac{1}{ur}\left(\dfrac{\partial^2 V}{\partial r \partial \lambda} - \dfrac{1}{r}\dfrac{\partial V}{\partial \lambda}\right) & \dfrac{\partial^2 V}{\partial r^2} \end{bmatrix} \tag{1.45}$$

By replacing V in Eq. (1.44) and (1.45) with V_u or Z in Eq. (1.30) - (1.43), the partial derivatives of the normal potential U can be obtained. This process can be applied to derivatives of other potential, e.g. W or A which may be useful for other applications.

Chapter 2

GEEC: An Effective Tool for Gravity and Gravity Gradients Forward Modelling

2.1. Introduction

As described in the Chapter 1, gravity and gravity gradients datasets are nowadays available in various altitudes of acquisition, from ground measurements to airborne surveys, and satellite missions. The joint interpretation of these datasets will lead to a better image of the geometry of a body mass in depth. To bring the observation data into a state where we can characterize the geometry of a body mass, we have to pass trough the step of the computation of specific masses which geometry is well known, e.g. topography and bathymetry, or partially known, i.e. the expected mass in depth.

Various approaches and codes to calculate the gravity or gravity gradients effect of a body mass have been developed, including the solution using spherical harmonic decomposition (Lee and Kaula, 1967; Balmino et al., 2012; Hirt et al., 2012) and wavelet decomposition (Chambodut et al., 2005; Panet et al., 2011), thin spherical layer (Tsoulis and Stary, 2005), rectangular prisms (Mader, 1951), tesseroids (Grombein et al., 2013; Uieda et al., 2016), or polyhedron (cf. Okabe, 1979; Singh and Guptasarma, 2001; Cattin et al., 2015; Tsoulis, 2012). However, most of the available approaches are made for a very specific spatial scale and application, hence it could encounter limitations if it is used for other application, for example:

- The spherical harmonic method is very efficient for calculation of a uniform and global data coverage but becomes ineffective when measurements are not regularly distributed. This method is widely used for application of satellite gravimetry, how-

ever for terrestrial gravimetry, this method suffers from omission error, i.e., because the spherical harmonic coefficients cannot represent short-scale gravity effects (Hirt et al., 2012).
- The prism approach is very effective for a local application with planar approximation but not for a global one where the curvature of the Earth has to be taken into account. This method is also reported in Grombein et al. (2013) as a method that is time consuming due to the logarithmic and arctan functions that must be evaluated during the process.
- In the tesseroid approach, mass body has to be given in a uniform geographical grid. The precision of tesseroid approach decreases towards the poles due to tesseroids degenerating into an approximately triangular shape at the poles (Uieda et al., 2016; Grombein et al., 2013). In this method, the Newton's integral can not be solved analytically, instead of that, approximation solutions are applied. This leads to the occurrence of errors in the use of tesseroids solution in the very near zone around the computation point (Heck and Seitz, 2007; Grombein et al., 2013), therefore it is less convenient to be utilized for local application with that demand a high precision.

As mentioned, most of the existing methods demand a gridded model dataset in geographical coordinates. It could cause difficulties in combining several datasets as the input mass geometry, for example in combining a detailed local terrain model from ground measurement in the vicinity of gravity station and an available global DTM. Besides those limitations, some of those tools are not freely available for the public.

In order to address those problems, we need a all-in-one tool that is free and open source to forward model gravity and gravity gradients that is (1) suitable to compute gravitational attraction of various scales or size of a body mass, from the small scale up to the scale of a planet, (2) capable to calculate any geometry of a body mass and preserve the complexity of its geometry, (3) adaptable for the computation at any measurement points regardless of the extent, the altitude, and the irregularity of its spatial distribution, (4) robust, and (5) time-saving. The compliance to those mentioned points allow us to use one single tool for the processing of all available gravity and gravity gradients datasets.

In this chapter, I present an open-source code named GEEC (Gal Eötvös Earth Calculator) which has been developed during this thesis to do those tasks mentioned above. It is Matlab-based tool and user friendly, from the computation process to the visualization of the result. With a high numerical precision of Matlab, the tool is robust. The integration of the Matlab Parallel Toolbox allows us to do the computation in parallel, thus the computation time can become more efficient.

This chapter will present the following items:

- The modifications made during the creation and the development of GEEC during this dissertation.
- The submitted paper containing the description and implementation of GEEC, the new developed analytical solution to obtain gravity gradients, and the validation and results comparison.
- Some additional information about GEEC that is not included in the submitted paper.

2.2. GEEC Publication

GEEC: A Matlab-based software for computing ground, aerial and satellite gravity and gravity gradients due to an irregularly shaped body

Anita Thea Saraswati[1], Rodolphe Cattin[1], Stéphane Mazzotti[1], and Cécilia Cadio[1]

[1] Géosciences Montpellier, UMR 5243, Université de Montpellier, CNRS. Place E. Bataillon, 34095 Montpellier Cedex 05, France

Corresponding author: Anita Thea Saraswati (anita.saraswati@gm.univ-montp2.fr)

Key Points:

- We report a novel method using polyhedron approach to compute gravity gradients due to a body mass with an arbitrary shape.
- We validate this method using applications from a very local ground survey to global satellite missions.
- We assess the optimum resolution of global model for satellite missions and airborne surveys.

Abstract

We present *GEEC* (Gal Eötvös Earth Calculator), a set of Matlab routines to compute both gravity and gravity gradients due to a body mass of uniform density with arbitrary geometry. This software is based on polyhedron modelling, for which the surface integral over each polygonal facet is converted into line integrals around its boundaries. We give new formulas for gravity gradients and show that they can be computed using the same simple procedure as the gravity. We perform a case study for various measurement heights and body mass sizes from local geophysical prospecting applications to global topographic effect on satellite data. Compared to existing methods, we show that our approach provides high accuracy and great computational efficiency. *GEEC* is thus well suited to jointly interpret all types of gravity measurements regardless of the extent and irregularity of their spatial distribution.

1. **Introduction**

Nowadays, the availability of gravity and gravity gradient datasets from ground measurements, airborne surveys and satellite missions allows the study of many phenomena such as water resource availability (Van Camp et al., 2017), volcanic activity (Jousset et al., 2003) or lithosphere dynamics (Cadio et al., 2016). Due to their different measurement heights (Fig. 1), these various datasets are commonly interpreted separately: the higher the measurement altitude, the larger the spatial scale and the deeper the sources. On local and regional scales, ground gravity measurements are typically used to assess the geometry of subsurface bodies (less than a few hundred meter depth) and crustal structures whereas, on global scales, satellite data give information for lithosphere processes.

A joint interpretation of these datasets requires modelling taking into account the complex geometry of body masses, the curvature of the Earth and calculating gravity and gravity gradients from local to global scales. Several methods exist. At a global scale, spectral analysis is classically performed using spherical decomposition (Lee & Kaula, 1967). This method is very efficient for uniform and global data coverage but becomes ineffective when measurements are not regularly distributed or for regional application. These shortcomings can partly be overcome using wavelet decomposition, although it still requires refinements at resolution below 15 km (Chambodut et al., 2005; Panet et al., 2011). A second set of methods consists in dividing the anomalous body masses into a succession of thin spherical layers (Tsoulis & Stary, 2005) or a distribution of simple volume elements such as rectangular prisms or tesseroids (Uieda et al., 2016). Analytical solutions exist for rectangular prisms (Mader, 1951; Nagy et al., 2000) and can be used to calculate near-field gravity, whereas, due to the Earth's curvature, tesseroidal modelling is more suitable for larger scales. Combined models of prismatic and tesseroidal methods are also developed to take advantage of these two approaches (e.g. Tsoulis et al., 2009).

Here, we investigate a third approach based on polyhedron modelling that allows computing gravity and gravity gradients due an arbitrary body mass at any point of measurement, at local to global scales, and at ground to satellite heights. Since the pioneer approaches developed by Hubbert (1948) or Talwani & Ewing (1960), many workers have proposed formulations to calculate the gravity field due to an arbitrary polyhedron of uniform density (e.g. Okabe, 1979; Pohanka, 1988; Tsoulis, 2012). Among them Singh & Guptasarma (2001) developed optimized formulation for the gravitational field of a polyhedron using Stoke's theorem, in which the surface integral over each polygonal facet of the polyhedron is converted into line integrals around its boundaries. Compared to previous approaches, these formulas are faster to compute because they do not require coordinate transformations and avoid the need to discriminate between observation points located outside, on the surface, and inside the solid body.

We expand the approach of the Singh & Guptasarma (2001) in the open-source code *GEEC* (Gal Eötvös Earth Calculator) extending the line-integral formulations to compute gravity and gravity gradients at the same time. After a reminder of this previous work, we present the new formulations to compute the gravity gradients. Next we describe the software design and we validate our approach by comparing our results with simple analytical solutions and those obtained from tesseroid modelling (Uieda et al., 2016). We present a numerical investigation of the errors due to a body mass discretization and assess the dependency between optimum mesh size and the height of measurements.

2. Theory

GEEC carries out the calculation of gravity $\boldsymbol{g_\alpha}$ **with** $\boldsymbol{\alpha} \in \{\boldsymbol{x}, \boldsymbol{y}, \boldsymbol{z}\}$ and gravity gradients $\boldsymbol{T_{\alpha\beta}} = \frac{\partial g_\alpha}{\partial \beta}$ **with** $\boldsymbol{\beta} \in \{\boldsymbol{x}, \boldsymbol{y}, \boldsymbol{z}\}$ due to an irregular polyhedron body in a right-handed 3-D Cartesian system. The computation process uses analytical solutions that are described in details in the two following sections. The first one is a reminder of the main formulations obtained by Singh and Guptasarma (2001) to calculate the gravity field. The second one is an extension of this previous work, in which we present formulas providing a new technique for computing all the components of both gravity and gravity gradient at the same time.

1.1. Line-integral approach to calculate gravity from a polyhedron

The component of gravitational field $\vec{g}$ in the given direction $\alpha \in \{x, y, z\}$ due to an arbitrary polyhedron with constant density can be written as the surface integral (Singh & Guptasarma, 2001)

$$\boldsymbol{g_\alpha = G\rho \oiint_S \frac{\alpha}{r^3} \vec{r}.\overrightarrow{u_n}\, ds}, \tag{1}$$

where G is the gravitational constant, ρ is the density of the body, r is the Euclidean distance from the observation point P to a surface element of area ds on the surface of the body, $\vec{r}$ is the vector from P to ds, and $\overrightarrow{\mathrm{u_n}}$ is the unit outward normal vector at the surface element ds (Fig. 2).

The polyhedron is bounded by a number of plane facets, thus the integration can be done separately on each facets. Summing the integration result over all the facets to obtain the attraction of the whole body, we get

$$\boldsymbol{g_\alpha = G\rho \sum_i \vec{r}\cdot\vec{u_i} \iint_{Si} \frac{\alpha}{r^3} ds} \tag{2}$$

where $\vec{u_i}$ is the outward normal vector of the i-th facet. It can be obtained by,

$$\vec{\mathbf{u_i}} = \frac{\vec{\mathbf{n_i}}}{\|\vec{\mathbf{n_i}}\|} \tag{3}$$

where $\vec{n_i} = \overrightarrow{S_1S_2} \times \overrightarrow{S_1S_3}$ as illustrated in figure 2.

As described in Guptasarma & Singh (1999), the surface integrals in equation (2) can be evaluated for each facet by converting them into line integrals of the edges that construct that facet. The approach is done by comparing the solution for the magnetic field from a polyhedron. Using the fact that, for the unit pole density, the solid angle Ω subtended at the computation point by that facet is numerically equal to the component of the magnetic field H_α parallel to the outward normal $\vec{u_i}$, we have

$$\boldsymbol{\Omega = lH_x + mH_y + nH_z} \tag{4}$$

where (l, m, n) are the Cartesian coordinates of $\vec{u_i}$. For a positive pole density, the field normal to the facet is away from the facet. As a consequence, the sign of Ω would be the opposite of the sign of the scalar product of the outward vector $\vec{u_i}$ and the vector position $\vec{r}$ of any corner of the polygon ($\vec{e_1}$ to $\vec{e_3}$, Fig. 2).

For unit pole density on the surface, the scalar integrals of the Cartesian component of the field over the polygon can be written as

$$\boldsymbol{H_\alpha = \iint_S -\frac{\alpha}{r^3} ds} \tag{5}$$

Note that the surface integrals of the outward normal components of the curl are linearly related to the component of the field at the computation point. Taking the each component of the unit vector $\vec{e_x}, \vec{e_y}, \vec{e_z}$ in the x, y, z directions, we have

$$
\begin{aligned}
\overrightarrow{\mathbf{u_i}} \cdot \overrightarrow{\mathbf{curl}}\left(\frac{\overrightarrow{\mathbf{e_x}}}{\boldsymbol{r}}\right) &= \frac{\boldsymbol{ny - mz}}{\boldsymbol{r^3}}, \\
\overrightarrow{\mathbf{u_i}} \cdot \overrightarrow{\mathbf{curl}}\left(\frac{\overrightarrow{\mathbf{e_y}}}{\boldsymbol{r}}\right) &= \frac{\boldsymbol{lz - nx}}{\boldsymbol{r^3}}, \\
\overrightarrow{\mathbf{u_i}} \cdot \overrightarrow{\mathbf{curl}}\left(\frac{\overrightarrow{\mathbf{e_z}}}{\boldsymbol{r}}\right) &= \boldsymbol{mx} - \frac{\boldsymbol{ly}}{\boldsymbol{r^3}}
\end{aligned}
\tag{6}
$$

Integrating these equations over the surface and combining with equations (5), we get

$$
\begin{aligned}
\boldsymbol{P} &= \iint_{S} \overrightarrow{\mathbf{u_i}} \cdot \overrightarrow{\mathbf{curl}}(\overrightarrow{\mathbf{e_x}}/\boldsymbol{r})\, \boldsymbol{ds} = \boldsymbol{nH_y - mH_z}, \\
\boldsymbol{Q} &= \iint_{S} \overrightarrow{\mathbf{u_i}} \cdot \overrightarrow{\mathbf{curl}}(\overrightarrow{\mathbf{e_y}}/\boldsymbol{r})\, \boldsymbol{ds} = \boldsymbol{lH_z - nH_x}, \\
\boldsymbol{R} &= \iint_{S} \overrightarrow{\mathbf{u_i}} \cdot \overrightarrow{\mathbf{curl}}(\overrightarrow{\mathbf{e_z}}/\boldsymbol{r})\, \boldsymbol{ds} = \boldsymbol{mH_x - lH_y}
\end{aligned}
\tag{7}
$$

By combining equations (7) and equation (4) and notice that $l^2 + m^2 + n^2 = 1$, we obtain

$$
\begin{aligned}
\boldsymbol{H_x} &= \boldsymbol{l\Omega + nQ - mR}, \\
\boldsymbol{H_y} &= \boldsymbol{m\Omega + lR - nP}, \\
\boldsymbol{H_z} &= \boldsymbol{n\Omega + mP - lQ}
\end{aligned}
\tag{8}
$$

Inserting the combination of equation (5) and (8) into equation (2), the solution of gravitational field using line integrals can be written

$$
\begin{aligned}
\boldsymbol{g_x} &= -\boldsymbol{G\rho} \sum_{i} \vec{\mathbf{r}} \cdot \overrightarrow{\mathbf{u_i}}\, (\boldsymbol{l_i\Omega_i + n_iQ_i - m_iR_i}), \\
\boldsymbol{g_y} &= -\boldsymbol{G\rho} \sum_{i} \vec{\mathbf{r}} \cdot \overrightarrow{\mathbf{u_i}}\, (\boldsymbol{m_i\Omega_i + l_iR_i - n_iP_i}), \\
\boldsymbol{g_z} &= -\boldsymbol{G\rho} \sum_{i} \vec{\mathbf{r}} \cdot \overrightarrow{\mathbf{u_i}}\, (\boldsymbol{n_i\Omega_i + m_iP_i - l_iQ_i}).
\end{aligned}
\tag{9}
$$

According to Stokes' theorem, the surface integral of the normal component of $\overrightarrow{curl}(\overrightarrow{e_x}/r)$, $\overrightarrow{curl}(\overrightarrow{e_y}/r)$, $\overrightarrow{curl}(\overrightarrow{e_z}/r)$ are equal to the line integral of vector $(\overrightarrow{\mathrm{e_x}}/r)$, $(\overrightarrow{\mathrm{e_y}}/r)$, and $(\overrightarrow{\mathrm{e_z}}/r)$, taken along the edges of the surface polygon in a counterclockwise direction as seen from the outside of the polyhedron. The detail of the integration of the line integrals of $(\overrightarrow{\mathrm{e_x}}/r)$, $(\overrightarrow{\mathrm{e_y}}/r)$, and $(\overrightarrow{\mathrm{e_z}}/r)$ of each edge of a polygon is described in Guptasarma & Singh (1999).

In the solution using line integrals, the contributions of the j-th edge P_{ij}, Q_{ij}, R_{ij} for the integration along the j-th edge of the i-th facet can be obtained from

$$\boldsymbol{P_{ij} = \left(I_j L_{jx}\right)_i, Q_{ij} = \left(I_j L_{jy}\right)_i, \textbf{and } R_{ij} = \left(I_j L_{jz}\right)_i} \tag{10}$$

where $\left(L_{jx}, L_{jy}, L_{jz}\right)$ are the Cartesian coordinates of the vector $\overrightarrow{\mathrm{L_j}}$ along the j-th edge. The length of the j-th edge is $L_j = \left\|\overrightarrow{\mathrm{L_j}}\right\|$. The line integral along edge I_j can be written as

$$\begin{gathered}\boldsymbol{I_j = \left(\frac{1}{L_j}\right)\ln\left[\frac{\left(\sqrt{\mathbf{L}_j^2 + b_j + r1_j^2} + L_j + \dfrac{b_j}{2L_j}\right)}{\left(r1_j + \dfrac{b_j}{2L_j}\right)}\right], \textbf{if } \left(r1_j + \frac{b_j}{2L_j}\right) \neq 0} \\ \boldsymbol{\textbf{and } I_j = \left(\frac{1}{L_j}\right)\ln\left[\frac{\left|L_j - r1_j\right|}{r1_j}\right], \textbf{if } \left(r1_j + \frac{b_j}{2L_j}\right) = 0.}\end{gathered} \tag{11}$$

where

$$\boldsymbol{b_j = 2\left(\overrightarrow{\mathbf{r1_j}} \cdot \overrightarrow{\mathbf{L_j}}\right)} \tag{12}$$

and $r1_j$ is the Euclidean distance from the computation point to the beginning of j-th edge. $\overrightarrow{\mathrm{r1_j}}$ is the position vector of the beginning of the j-th edge from the computation point P, thus $\left(r1_{jx}, r1_{jy}, r1_{jz}\right)$ are the Cartesian coordinates of the vector $\overrightarrow{\mathrm{r1_j}}$. The beginning and the end of each edge is evaluated in a counter-clockwise direction, seen from the point of observation as the origin point.

Thus, the total boundary contribution for each facet is the sum of the integral contribution of its edges

$$\boldsymbol{P_i = \sum_j P_{ij}, Q_i = \sum_j Q_{ij}, R_i = \sum_j R_{ij}} \tag{13}$$

The solid angle Ω_i subtended by the computation point as the apex and each surface of the polygon is negative $(-\Omega_\mathrm{i})$ if it is seen from the inside of the polyhedron. To make it seen from the outside, we have to inverse the order of the vertices that construct that facet.

The solid angle of each facet can be obtained by

$$\boldsymbol{\Omega_\mathrm{i} = \left(\sum_k \psi_k\right) - (n-2)\pi} \tag{14}$$

where ψ_k is the angle between the planes forming the adjacent edge of the pyramid and n is the number of the side of the i-the facet. Using the position vector of each corner of the facet to the computation point,

$$\overrightarrow{\mathbf{nn}_1} = \frac{\overrightarrow{\mathbf{v}_1}}{\|\overrightarrow{\mathbf{v}_1}\|} \text{ and } \overrightarrow{\mathbf{nn}_2} = \frac{\overrightarrow{\mathbf{v}_2}}{\|\overrightarrow{\mathbf{v}_2}\|} \tag{15}$$

where $\overrightarrow{\mathrm{v}_1} = \overrightarrow{\mathrm{e}_k} \times \overrightarrow{\mathrm{e}_{k-1}}$ and $\overrightarrow{\mathrm{v}_2} = \overrightarrow{\mathrm{e}_{k+1}} \times \overrightarrow{\mathrm{e}_k}$. $\overrightarrow{\mathrm{e}_\mathrm{k}} = \overrightarrow{\mathrm{PS}_\mathrm{k}}$ is the position vector of the corner of the polygon from the computation point P. Thus we have

$$\begin{cases} \boldsymbol{\psi_k = \cos^{-1}(\overrightarrow{\mathbf{nn}_1} \cdot \overrightarrow{\mathbf{nn}_2}) \text{ if } \overrightarrow{\mathbf{e}_{k+1}} \cdot \overrightarrow{\mathbf{nn}_1} > 0} \\ \boldsymbol{\psi_k = 2\pi - \cos^{-1}(\overrightarrow{\mathbf{nn}_1} \cdot \overrightarrow{\mathbf{nn}_2}) \text{ if } \overrightarrow{\mathbf{e}_{k+1}} \cdot \overrightarrow{\mathbf{nn}_1} < 0} \end{cases} \tag{16}$$

The sign of $\overrightarrow{\mathrm{e}_{k+1}} \cdot \overrightarrow{\mathrm{nn}_1}$ can indicate whether this internal angle exceeds π or not. If the sign is negative, the internal angle at the j-th corner exceeds π.

1.2. Analytical solution for the gravity gradients due to an arbitrary polyhedron

Following the approach described in the previous paragraph, here we extent the Guptasarma & Singh (1999)'s formulations to calculate all components of the gravity gradients. The partial derivatives of the gravity g_α, known as the gravitational gradients, in direction $\beta \in \{x, y, z\}$ can be written as

$$\boldsymbol{T_{\alpha\beta} = \frac{\partial g_\alpha}{\partial \beta}} \tag{17}$$

Thus, the partial derivatives of the equation (9) are

$$\begin{aligned} \boldsymbol{\frac{\partial g_x}{\partial \beta}} &= \boldsymbol{-G\rho \sum_i \frac{\partial}{\partial \beta} \{\vec{\mathbf{r}} \cdot \overrightarrow{\mathbf{u}_i}\, (l_i\Omega_i + n_iQ_i - m_iR_i)\}}, \\ \boldsymbol{\frac{\partial g_y}{\partial \beta}} &= \boldsymbol{-G\rho \sum_i \frac{\partial}{\partial \beta} \{\vec{\mathbf{r}} \cdot \overrightarrow{\mathbf{u}_i}\, (m_i\Omega_i + l_iR_i - n_iP_i)\}}, \\ \boldsymbol{\frac{\partial g_z}{\partial \beta}} &= \boldsymbol{-G\rho \sum_i \frac{\partial}{\partial \beta} \{\vec{\mathbf{r}} \cdot \overrightarrow{\mathbf{u}_i}\, (n_i\Omega_i + m_iP_i - l_iQ_i)\}}. \end{aligned} \tag{18}$$

The results of the partial derivative of the scalar product $\vec{\mathrm{r}}$ and $\overrightarrow{\mathrm{u}_\mathrm{i}}$ is

$$\boldsymbol{\frac{\partial}{\partial \beta}(\vec{\mathbf{r}} \cdot \overrightarrow{\mathbf{u}_i}) = -u_{i\beta}} \tag{19}$$

where $u_{i\beta}$ is the scalar of the outward vector $\overrightarrow{\mathrm{u}_\mathrm{i}}$ in the coordinate β. Combined with equation (19), the equation (18) can be therefore expanded into

$$\begin{aligned}
\frac{\partial \boldsymbol{g_x}}{\partial \boldsymbol{\beta}} &= -\boldsymbol{G\rho} \sum_{i} \left[\left\{ \vec{\mathbf{r}} \cdot \overrightarrow{\mathbf{u_\imath}} \left(\boldsymbol{l_i} \frac{\partial \boldsymbol{\Omega}_\mathbf{i}}{\partial \boldsymbol{\beta}} + \boldsymbol{n_i} \frac{\partial \boldsymbol{Q_i}}{\partial \boldsymbol{\beta}} - \boldsymbol{m_i} \frac{\partial \boldsymbol{R_i}}{\partial \boldsymbol{\beta}} \right) \right\} - \left\{ \boldsymbol{u_{i\beta}} (\boldsymbol{l_i} \boldsymbol{\Omega}_\mathbf{i} + \boldsymbol{n_i Q_i} - \boldsymbol{m_i R_i}) \right\} \right] \\
\frac{\partial \boldsymbol{g_y}}{\partial \boldsymbol{\beta}} &= -\boldsymbol{G\rho} \sum_{i} \left[\left\{ \vec{\mathbf{r}} \cdot \overrightarrow{\mathbf{u_\imath}} \left(\boldsymbol{m_i} \frac{\partial \boldsymbol{\Omega}_\mathbf{i}}{\partial \boldsymbol{\beta}} + \boldsymbol{l_i} \frac{\partial \boldsymbol{R_i}}{\partial \boldsymbol{\beta}} - \boldsymbol{n_i} \frac{\partial \boldsymbol{P_i}}{\partial \boldsymbol{\beta}} \right) \right\} - \left\{ \boldsymbol{u_{i\beta}} (\boldsymbol{m_i \Omega_i} + \boldsymbol{l_i R_i} - \boldsymbol{n_i P_i}) \right\} \right] \qquad (20) \\
\frac{\partial \boldsymbol{g_z}}{\partial \boldsymbol{\beta}} &= -\boldsymbol{G\rho} \sum_{i} \left[\left\{ \vec{\mathbf{r}} \cdot \overrightarrow{\mathbf{u_\imath}} \left(\boldsymbol{n_i} \frac{\partial \boldsymbol{\Omega}_\mathbf{i}}{\partial \boldsymbol{\beta}} + \boldsymbol{m_i} \frac{\partial \boldsymbol{P_i}}{\partial \boldsymbol{\beta}} - \boldsymbol{l_i} \frac{\partial \boldsymbol{Q_i}}{\partial \boldsymbol{\beta}} \right) \right\} + \left\{ \boldsymbol{u_{i\beta}} (\boldsymbol{n_i \Omega_i} + \boldsymbol{m_i P_i} - \boldsymbol{l_i Q_i}) \right\} \right]
\end{aligned}$$

The partial derivatives of P, Q, R and the solid angle Ω are expanded in the two following steps.

<u>Partial derivative of the solution of the line integral</u>

Replacing $t = \left(\sqrt{\mathrm{L}_j^2 + b_j + r1_j^2} + L_j + \frac{b_j}{2L_j}\right) / \left(r1_j + \frac{b_j}{2L_j}\right)$ for $\left(r1_j + \frac{b_j}{2L_j}\right) \neq 0$ and $t = \left|L_j - r1_j\right| / r1_j$ for $\left(r1_j + \frac{b_j}{2L_j}\right) = 0$ of the equation (11), the partial derivatives of the solution of the line integral P, Q, R on each polygon edge of the equation (10) are

$$\begin{aligned}
\frac{\partial \boldsymbol{P_j}}{\partial \boldsymbol{\beta}} &= \frac{\boldsymbol{L_{jx}}}{\boldsymbol{L_j}} \frac{\mathbf{1}}{\boldsymbol{t}} \frac{\partial \boldsymbol{t}}{\partial \boldsymbol{\beta}} \\
\frac{\partial \boldsymbol{Q_j}}{\partial \boldsymbol{\beta}} &= \frac{\boldsymbol{L_{jy}}}{\boldsymbol{L_j}} \frac{\mathbf{1}}{\boldsymbol{t}} \frac{\partial \boldsymbol{t}}{\partial \boldsymbol{\beta}} \qquad (21) \\
\frac{\partial \boldsymbol{R_j}}{\partial \boldsymbol{\beta}} &= \frac{\boldsymbol{L_{jz}}}{\boldsymbol{L_j}} \frac{\mathbf{1}}{\boldsymbol{t}} \frac{\partial \boldsymbol{t}}{\partial \boldsymbol{\beta}}
\end{aligned}$$

To obtain $\frac{\partial t}{\partial \beta}$, we use the product rule

$$\frac{\partial \boldsymbol{t}}{\partial \boldsymbol{\beta}} = \frac{\left(\frac{\partial \boldsymbol{u}}{\partial \boldsymbol{\beta}} \boldsymbol{v} - \boldsymbol{u} \frac{\partial \boldsymbol{v}}{\partial \boldsymbol{\beta}} \right)}{\boldsymbol{v}^2} \qquad (22)$$

with $u = \sqrt{\mathrm{L}_j^2 + b_j + r1_j^2} + L_j + \frac{b_j}{2L_j}$ and $v = r1_j + \frac{b_j}{2L_j}$ for $\left(r1_j + \frac{b_j}{2L_j}\right) \neq 0$. We have

$$\frac{\partial \boldsymbol{u}}{\partial \boldsymbol{\beta}} = \frac{\mathbf{1}}{\mathbf{2}} \frac{\mathbf{1}}{\sqrt{\boldsymbol{L_j^2} + \boldsymbol{b_j} + \boldsymbol{r1_j^2}}} \frac{\partial}{\partial \boldsymbol{\beta}} \left(\boldsymbol{L_j^2} + \boldsymbol{b_j} + \boldsymbol{r1_j^2} \right) + \frac{\mathbf{1}}{\mathbf{2}\boldsymbol{L}} \frac{\partial \boldsymbol{b}}{\partial \boldsymbol{\beta}} \qquad (23)$$

and

$$\frac{\partial \boldsymbol{v}}{\partial \boldsymbol{\beta}} = \frac{\partial \boldsymbol{r1_j}}{\partial \boldsymbol{\beta}} + \frac{\mathbf{1}}{\mathbf{2}\boldsymbol{L}} \frac{\partial \boldsymbol{b_j}}{\partial \boldsymbol{\beta}} \qquad (24)$$

The derivative of b_j in equation (12) is

$$\frac{\partial \boldsymbol{b}}{\partial \boldsymbol{\beta}} = \frac{\partial}{\partial \boldsymbol{\beta}}\left(2\left(\overrightarrow{\mathbf{r1_j}} \cdot \overrightarrow{\mathbf{L_j}}\right)\right) = -2\boldsymbol{L_{j\beta}} \tag{25}$$

and the derivative of $r1_j$ is

$$\frac{\partial \boldsymbol{r1_j}}{\partial \boldsymbol{\beta}} = \frac{\partial}{\partial \boldsymbol{\beta}}\left(\sqrt{\boldsymbol{r1_{jx}^2} + \boldsymbol{r1_{jy}^2} + \boldsymbol{r1_{jz}^2}}\right) = \frac{\mathbf{1}}{\mathbf{2}}\frac{\mathbf{1}}{\boldsymbol{r1_j}}\left(-\mathbf{2}\boldsymbol{r1_{j\beta}}\right) = -\frac{\boldsymbol{r1_{j\beta}}}{\boldsymbol{r1_j}} \tag{26}$$

thus we have

$$\frac{\partial \boldsymbol{r1_j^2}}{\partial \boldsymbol{\beta}} = \mathbf{2}\boldsymbol{r1_j}\frac{\partial \boldsymbol{r1_j}}{\partial \boldsymbol{\beta}} = -\mathbf{2}\,\boldsymbol{r1_{j\beta}} \tag{27}$$

Substituting equation (25), (26), and (27) in equations (23) and (24),

$$\frac{\partial \boldsymbol{u}}{\partial \boldsymbol{\beta}} = -\left(\frac{\boldsymbol{L_{j\beta}} + \boldsymbol{r1_{j\beta}}}{\sqrt{\mathbf{L_j^2} + \boldsymbol{b_j} + \boldsymbol{r1_j^2}}} + \frac{\boldsymbol{L_{j\beta}}}{\boldsymbol{L_j}}\right) \tag{28}$$

and

$$\frac{\partial \boldsymbol{v}}{\partial \boldsymbol{\beta}} = -\left(\frac{\boldsymbol{r1_{j\beta}}}{\boldsymbol{r1_j}} + \frac{\boldsymbol{L_{j\beta}}}{\boldsymbol{L_j}}\right) \tag{29}$$

While if $\left(r1_j + \frac{b_j}{2L_j}\right) = 0$, we substitute $u = \left|L_j - r1_j\right|$ and $v = r1_j$, thus we obtain

$$\frac{\partial \boldsymbol{u}}{\partial \boldsymbol{\beta}} = \frac{\left(\boldsymbol{L_j} - \boldsymbol{r1_j}\right)}{\left|\boldsymbol{L_j} - \boldsymbol{r1_j}\right|}\frac{\partial}{\partial \boldsymbol{\beta}}\left(\boldsymbol{L_j} - \boldsymbol{r1_j}\right) = \frac{\left(\boldsymbol{L_j} - \boldsymbol{r1_j}\right)}{\left|\boldsymbol{L_j} - \boldsymbol{r1_j}\right|}\frac{\boldsymbol{L_{j\beta}}}{\boldsymbol{L_j}} \tag{30}$$

and

$$\frac{\partial \boldsymbol{v}}{\partial \boldsymbol{\beta}} = -\frac{\boldsymbol{r1_{j\beta}}}{\boldsymbol{r1_j}} \tag{31}$$

<u>Partial derivative of the solid angle</u>

Replacing $\overrightarrow{\mathrm{nn_1}} \cdot \overrightarrow{\mathrm{nn_2}}$ with a of the equation (16), the derivative of the angle at the adjacent edge can be written

$$\begin{cases} \dfrac{\partial \psi_k}{\partial \beta} = \dfrac{\partial}{\partial \beta}\cos^{-1} a = -\dfrac{1}{\sqrt{1-a^2}}\dfrac{\partial a}{\partial \beta} \text{ if } \overrightarrow{\mathbf{e}_{k+1}} \cdot \overrightarrow{\mathbf{nn}_1} > 0 \\ \dfrac{\partial \psi_k}{\partial \beta} = \dfrac{1}{\sqrt{1-a^2}}\dfrac{\partial a}{\partial \beta} \text{ if } \overrightarrow{e_{k+1}} \cdot \overrightarrow{nn_1} < 0 \end{cases} \tag{32}$$

where

$$\frac{\partial a}{\partial \beta} = \left(\frac{\partial \overrightarrow{\mathbf{nn}_1}}{\partial \beta} \cdot \overrightarrow{\mathbf{nn}_2}\right) + \left(\overrightarrow{\mathbf{nn}_1} \cdot \frac{\partial \overrightarrow{\mathbf{nn}_2}}{\partial \beta}\right) \tag{33}$$

To obtain the derivative of $\overrightarrow{\mathrm{nn}_1}$ and $\overrightarrow{\mathrm{nn}_2}$, first we calculate the derivative of $\overrightarrow{\mathrm{v}_1}, \overrightarrow{\mathrm{v}_2}$ and its magnitude $\|\overrightarrow{\mathrm{v}_1}\|$, $\|\overrightarrow{\mathrm{v}_2}\|$.

$$\overrightarrow{\mathbf{v}_1} \cdot \begin{Bmatrix} \dfrac{\partial}{\partial x} \\ \dfrac{\partial}{\partial y} \\ \dfrac{\partial}{\partial z} \end{Bmatrix} = \begin{Bmatrix} [0 \quad -(e_{kz} - e_{k-1z}) \quad (e_{ky} - e_{k-1y})] \\ [(e_{kz} - e_{k-1z}) \quad 0 \quad -(e_{kx} - e_{k-1x})] \\ [-(e_{ky} - e_{k-1y}) \quad (e_{kx} - e_{k-1x}) \quad 0] \end{Bmatrix} \tag{34}$$

$$\overrightarrow{\mathbf{v}_2} \cdot \begin{Bmatrix} \dfrac{\partial}{\partial x} \\ \dfrac{\partial}{\partial y} \\ \dfrac{\partial}{\partial z} \end{Bmatrix} = \begin{Bmatrix} [0 \quad -(e_{k+1z} - e_{kz}) \quad (e_{k+1y} - e_{ky})] \\ [(e_{k+1z} - e_{kz}) \quad 0 \quad -(e_{k+1x} - e_{kx})] \\ [-(e_{k+1y} - e_{ky}) \quad (e_{k+1x} - e_{kx}) \quad 0] \end{Bmatrix} \tag{35}$$

and

$$\begin{aligned} \frac{\partial}{\partial \beta}\|\overrightarrow{\mathrm{v}_1}\| &= \frac{\partial}{\partial \beta}\left(\sqrt{v_{1x}^2 + v_{1y}^2 + v_{1z}^2}\right) \\ &= \frac{1}{2}\frac{1}{\sqrt{v_{1x}^2 + v_{1y}^2 + v_{1z}^2}}\frac{\partial}{\partial \beta}\left(v_{1x}^2 + v_{1y}^2 + v_{1z}^2\right) \\ &= \frac{1}{2}\frac{1}{\|\overrightarrow{\mathrm{v}_1}\|}\left(2v_{1x}\frac{\partial v_{1x}}{\partial \beta} + 2v_{1y}\frac{\partial v_{1y}}{\partial \beta} + 2v_{1z}\frac{\partial v_{1z}}{\partial \beta}\right) \\ &= \frac{1}{\|\overrightarrow{\mathrm{v}_1}\|}\left(\overrightarrow{\mathrm{v}_1} \cdot \frac{\partial \overrightarrow{\mathrm{v}_1}}{\partial \beta}\right) \end{aligned} \tag{36}$$

Similarly for the derivative of $\|\overrightarrow{\mathrm{v}_2}\|$

$$\frac{\partial}{\partial\beta}\|\overrightarrow{\mathrm{v}_2}\| = \frac{\partial}{\partial\beta}\left(\sqrt{v_{2x}^2 + v_{2y}^2 + v_{2z}^2}\right) = \frac{1}{\|\overrightarrow{\mathrm{v}_2}\|}\left(\overrightarrow{\mathrm{v}_2}\cdot\frac{\partial\overrightarrow{\mathrm{v}_2}}{\partial\beta}\right) \tag{37}$$

Using equations (34) to (37) to obtain the derivatives of $\overrightarrow{\mathrm{nn}_1}$ and $\overrightarrow{\mathrm{nn}_2}$, we have

$$\frac{\partial\overrightarrow{\mathbf{nn}_1}}{\partial\boldsymbol{\beta}} = \frac{\boldsymbol{\partial}}{\partial\boldsymbol{\beta}}\left(\frac{\overrightarrow{\mathbf{v}_1}}{\|\overrightarrow{\mathbf{v}_1}\|}\right) = \frac{\mathbf{1}}{\|\overrightarrow{\mathbf{v}_1}\|^2}\left(\frac{\partial\overrightarrow{\mathbf{v}_1}}{\partial\boldsymbol{\beta}}\|\overrightarrow{\mathbf{v}_1}\| - \overrightarrow{\mathbf{v}_1}\frac{\boldsymbol{\partial}}{\partial\boldsymbol{\beta}}\|\overrightarrow{\mathbf{v}_1}\|\right) \tag{38}$$

and

$$\frac{\partial\overrightarrow{\mathbf{nn}_2}}{\partial\boldsymbol{\beta}} = \frac{\boldsymbol{\partial}}{\partial\boldsymbol{\beta}}\left(\frac{\overrightarrow{\mathbf{v}_2}}{\|\overrightarrow{\mathbf{v}_2}\|}\right) = \frac{\mathbf{1}}{\|\overrightarrow{\mathbf{v}_2}\|^2}\left(\frac{\partial\overrightarrow{\mathbf{v}_2}}{\partial\boldsymbol{\beta}}\|\overrightarrow{\mathbf{v}_2}\| - \overrightarrow{\mathbf{v}_2}\frac{\boldsymbol{\partial}}{\partial\boldsymbol{\beta}}\|\overrightarrow{\mathbf{v}_2}\|\right) \tag{39}$$

Finally, using the result of equation (32), the derivative of the solid angle of the i-th edge can be obtain with

$$\frac{\partial\boldsymbol{\Omega}_i}{\partial\boldsymbol{\beta}} = \sum\frac{\partial\boldsymbol{\psi}_k}{\partial\boldsymbol{\beta}} \tag{40}$$

3. **Implementation**

Based on the formulas given in the previous section, we have implemented the line-integral approach to compute both the gravity and gravity gradients in the open-source software *GEEC*. It is freely available online on the web page of Geosciences Montpellier laboratory (http://www.gm.univ-montp2.fr). An archived version of the source code is also available as part of this paper.

GEEC is written in Matlab version 2014, but can be also used with a more recent version. Taking advantage of the Matlab Parallel Computing Toolbox, this software includes programs developed to enhance the computation time. The main program “launch_geec.m” manages input and output files and launches the function “geec.m” with correct variable formats. Input files include (1) the locations, *i.e.* longitude, latitude and altitude (in meters), of measurement points, which can be distributed non-uniformly, (2) the geometry of the body mass, *i.e.* longitude, latitude and altitude (in meters) of the polyhedron corners and their counter clockwise triangulation.

Commonly, ground gravity measurements as well as satellite and airborne observation track points are spatially unevenly distributed. We allow for this type of data in *GEEC* with computation points that can be defined at any location without any interpolation in the calculation process. Computation points can be defined either as gridded or scattered locations given in a geographic coordinate system (longitude, latitude, and altitude) that are transformed in the local ENU (East, North, and Up) Cartesian coordinate system using a predefined reference ellipsoid (major axis and eccentricity). The body mass is modelled using polyhedra with triangular facets. This enables a robust representation of any specific geometry.

Additional information has to be given, such as the density of the body mass in kg.m^{-3} and the type of computation, *i.e.* either gravity only or both gravity and gravity gradients. An ellipsoidal approximation is used to avoid any unacceptable error due to the neglected Earth's curvature (Tsoulis et al., 2009). An option to define the vertical datum, geoid or ellipsoid reference, is also provided in order to avoid the indirect effect caused by different vertical reference level (Talwani, 1998). All computation results are saved in an output file, which includes longitude, latitude and altitude (in meters) of measurement points, the three components of gravity in mGal (10^{-5} m.s^{-2}) and the nine components of gravity gradient in Eötvös (10^{-9} s^{-2}). The combined effect of several bodies is simply the sum of gravity and gradients due to each polyhedron.

4. Applications

4.1. Anomaly due to a buried sphere

A first application of the developed polyhedron approach consists in modelling the gravity and gravity gradients due to a buried body. Such a computation is very common to interpret gravity anomalies in geophysical prospecting, which requires forward modelling to image oil pockets, ore veins or water reservoirs. The scale associated with these local studies is often small, less than a few kilometres. Here, to validate our approach we compare the computed *GEEC* gravity and gravity gradients due to a buried sphere (Fig. 3) with the classical analytical solution

$$\boldsymbol{g_x} = \frac{\boldsymbol{\alpha x}}{(\boldsymbol{x^2 + z^2})^{\frac{3}{2}}} \textbf{ and } \boldsymbol{g_z} = \frac{\boldsymbol{\alpha z}}{(\boldsymbol{x^2 + z^2})^{\frac{3}{2}}}$$
$$\textbf{with } \boldsymbol{\alpha} = \frac{-\boldsymbol{4\pi G\, R^3 \Delta\rho}}{\mathbf{3}}, \tag{41}$$

and

$$\boldsymbol{T_{xx}} = \frac{\partial \boldsymbol{g_x}}{\partial \boldsymbol{x}} = \frac{\boldsymbol{\alpha}}{(\boldsymbol{x^2 + z^2})^{\frac{3}{2}}}\left(\mathbf{1} - \frac{\mathbf{3}\boldsymbol{x^2}}{\boldsymbol{x^2 + z^2}}\right),$$
$$\boldsymbol{T_{zz}} = \frac{\partial \boldsymbol{g_z}}{\partial \boldsymbol{z}} = \frac{\boldsymbol{\alpha}}{(\boldsymbol{x^2 + z^2})^{\frac{3}{2}}}\left(\mathbf{1} - \frac{\mathbf{3}\boldsymbol{z^2}}{\boldsymbol{x^2 + z^2}}\right), \tag{42}$$
$$\boldsymbol{T_{xz}} = \frac{\partial \boldsymbol{g_x}}{\partial \boldsymbol{z}} = -\mathbf{3}\boldsymbol{\alpha}\frac{\boldsymbol{xz}}{(\boldsymbol{x^2 + z^2})^{\frac{5}{2}}},$$

where $\boldsymbol{x}$ and $\boldsymbol{z}$ are the horizontal and vertical distance from the sphere centre. $\boldsymbol{z}$ is positive upward. **G** = 6.67408 x 10^{-11} $m^3.kg^{-1}.s^{-2}$, $\boldsymbol{R}$ is the sphere radius and $\boldsymbol{\Delta\,\rho}$ the density contrast. We assume a sphere with a radius of 10 m, a density contrast of -200 km/m^3, centred at 20 m depth. For the *GEEC* computation, the surface of the sphere is discretized using a mesh size of 0.3 m.

Compared with the standard deviations of both ground gravity and gravity gradient measurements (Van Camp et al., 2017), our computation results are in very good agreement with the theoretical values obtained along a surface profile (Fig. 3). The maximum differences are less than 7.5 x 10^{-5} mGal and 0.06 E for the gravity and gravity gradients, respectively. This very simple application demonstrates the robustness of our approach at a local scale and its relevance to assess the geometry and density contrast of a buried body using forward modelling. In the following application, we test our approach at a global scale, for which the curvature of Earth must be taken into account.

4.2. Effect of a superficial Earth’s shell at various measurement heights

In the previous application, the mesh size is small enough to ensure the robustness of the results, but is not optimal for large computations due to time and memory limitations. Since the computation is performed using planar facets to discretise the surface of the arbitrary mass body, the smaller the mesh size, the better the geometry, but the longer the computation time and memory requirements, preventing calculations at too high a resolution. To overcome this limitation, one can define an optimum mesh size as the model resolution required to achieve a given accuracy. This optimum mesh size depends on both the size of the body mass and its distance to the measurement points (ground, airborne or satellite surveys).

To evaluate the relationship between model resolution, computation time and height of measurements, we compute the gravity due to a spherical shell with a mass density $\rho = 2670$ kg m^{-3} and a constant thickness of 1 km above a reference sphere with a mean radius R = 6378.137 km. This simple example represents a test case of a standard Bouguer Plateau correction of the topography in gravity studies. We test heights of observation points between the ground surface and 255 km of altitude. The accuracy of *GEEC* results is defined as the absolute difference with the theoretical values obtained from equations (41) and (42) for two concentric spheres of differing radii:

$$\begin{cases} \boldsymbol{\Delta g_i = g_i(R + 1km) - g_i(R)} \\ \boldsymbol{T_{ij} = T_{ij}(R + 1km) - T_{ij}(R)} \end{cases} \tag{43}$$

where $\boldsymbol{i} \in \{\boldsymbol{x}, \boldsymbol{y}, \boldsymbol{z}\}$ and $\boldsymbol{j} \in \{\boldsymbol{x}, \boldsymbol{y}, \boldsymbol{z}\}$.

Here, we only compute the vertical attractions $\boldsymbol{g_z}$ and $\boldsymbol{T_{zz}}$. The reference values for the spherical shell at each computation altitude $\boldsymbol{h}$ are indicated in Table 1. As expected, for any computation altitude, our results show that the error is inversely proportional to the resolution of the model (Table 1 and Figure 4). For instance, the ground-based $\boldsymbol{g_z}$ errors are 15 µGal and 859 µGal for a mesh size of 5 km and 150 km, respectively. The error also depends on the considered altitude (Figure 4). Assuming a low-resolution sphere model (i.e. mesh size of 150 km), the $\boldsymbol{g_z}$ error decreases from 859 µGal to 47 µGal with an increase of altitude from 0 km to 255 km (Table 1).

In order to achieve an accuracy (approximation of the exact analytical values) of 99.9%, a resolution *ca.* 35 km is required for near surface gravity calculations, whereas a resolution *ca.*

80 km is sufficient at 10 km altitude, and all tested resolutions (up to 150 km) are adequate for satellite altitude (Figure 4a). For the gravity gradient signal (Figure 4b), an accuracy of 99.9% requires a minimum resolution *ca.* 15 km for airborne surveys (10 km altitude) and is always achieved for satellite altitudes. In contrast with the gravity signal, a 99.9% accuracy error in the gradient is not achieved using any tested resolution for any altitude below 10 km. These results are consistent with those obtained by Uieda et al. (2016) showing that $\boldsymbol{T_{ZZ}}$ requires higher surface resolution than $\boldsymbol{g_z}$ to obtain the same percentage of error.

The detail of the computational effort can be found in table 2 and figure 5. Computation time increases very strongly from 20 seconds to 9 minutes for tested mesh sizes ranging between 25 km and 5 km. These results demonstrate the efficiency of *GEEC* to compute both gravity and gravity gradients at 255 km, allowing a comparison with the dense and global GOCE dataset. The presented approach is also suitable for studying regional airborne surveys (5-10 km altitude). In contrast, ground or low altitude airborne surveys (<2 km) require the use of a mode resolution higher than ca. 5 km, for which a global-scale computation can be impractical. If the extent of surveys is local (few 10s km), our approach remains relevant. As the previous buried sphere application, a small network extent makes it possible to improve the resolution without increasing computing times too much. For larger extent, we have developed an adaptive discretization, in which the surface of mass bodies is meshed into triangles with higher density near the measurement points. This local grid refinement improves the computation accuracy, without a large increase in computation resources and time.

4.3. Global and regional topographic effect

The last presented application consists in the computation of the topography contribution in the gravity field, which is an important step to assess deep sources from gravitational data. We compare the computed *GEEC* gravity and gravity gradients due to topography and bathymetry with results obtained from the software *Tesseroids* (Uieda et al., 2016), in which the Earth topography is discretized in tesseroids.

We use the DTM2006.0 topographic data defined on a grid of 5' × 5' (Pavlis et al., 2007). Based on the results obtained in the previous section, we recompose DTM2006.0 in a 10 km equidistant mesh, providing a uniform resolution over the entire Earth. For the computation using *Tesseroids*, we deactivate the adaptive discretization to keep the original grid size. In both cases, we decompose the topographic model in two parts: a rock layer for masses above sea level with a density $\boldsymbol{\rho_c}$=2670 kg.m^{-3}, and a water layer for masses below sea level with a density $\boldsymbol{\rho_w}$=1000 kg.m^{-3}. Using the crustal density as the reference density, this gives a density contrast for the ocean of -1670 kg.m^{-3}. For simplicity, the ice layer above sea level is considered as a rock layer. We set the computation points at 255 km of ellipsoid height, which corresponds to the mean altitude of the GOCE mission (Rummel et al., 2011).

Figure 6 shows the gravity $\boldsymbol{g_z}$ and gradient $\boldsymbol{T_{zz}}$ topographic effects computed with *GEEC* (Fig. 6a and 6c) and their respective differences with the *Tesseroids* computation (Fig. 6b and 6d). *GEEC* and *Tesseroids* give very consistent results. Their differences are in the range of GOCE measurements uncertainties, i.e. 1 mGal and 10-60 mE for gravity and gravity gradient, respectively (Brusima et al., 2014; Panet et al., 2014). For $\boldsymbol{g_z}$, maximum differences are *ca.* ±1.3 mGal, less than 0.25% of the topographic effect. For $\boldsymbol{T_{ZZ}}$, the maximum differences are ±21 mE with an overall standard deviation of 3.6 mE. Considering all components of both gravity and gravity gradients, 90% of the differences between *GEEC* and *Tesseroids* are below ±0.38 mGal and ±4.5 mE, respectively (Fig. 7).

Most of the large discrepancies are located in high latitudes areas, such as Antarctica and Greenland. The first reason is the difference between the meshing techniques used in the two softwares. In *GEEC*, we use a homogeneous topography model with a resolution of 10 km, while for *Tesseroids*, the topography is modelled on a geographical grid where the grid size varies with the latitude. This leads to distortions of the tesseroid shapes from nearly rectangular at the equator to nearly triangular at the poles, which results in an inaccurate computation in the tesseroid approach (Grombein et al., 2013). Second, the geometry of the mass distribution and the computation points are on the sphere in the *Tesseroids* software, whereas they are given on the ellipsoid in *GEEC*. This results in larger differences in the mass-measurement distance at high latitudes. The high topographies in Antarctica and Greenland amplify these factors.

Beyond these differences due to global meshing, the discrepancy between *GEEC* and *Tesseroids* results can also be associated with the two different techniques used to model the local topography surface. To highlight this point, we compare the polyhedron and tesseroid approaches at a regional scale over the Himalaya of eastern Nepal for a computation height of 10 km (Fig. 8). We obtain local deviations up to 20 mGal and 60 E in high slope areas. Unsurprisingly, *GEEC* is more suitable to model a rugged topography: the *GEEC* triangular shape discretization results in smaller deviations from the actual geometry and less computation biases, compared to the rectangular shape discretization in *Tesseroids*.

This application validates the use of *GEEC* to compute gravity and gravity gradients at regional and global scales. Compared to rectangular prism and tesseroid approaches, *GEEC* gives consistent results but provides a more flexible way to preserve the roughness of the Earth's surface in topography modelling.

5. Conclusion

We present a new open-source tool *GEEC* (Gal Eötvös Earth Calculator) to perform forward modelling of gravitaty and gravity gradients of an irregular body mass discretized in polyhedra. Following Singh and Guptasarma (2001), we give new formulas for gravity gradients based on the analytical solutions of the expansion of the line integrals of a constant-density polyhedron body. *GEEC* applies triangle meshes as facets to compose the polyhedra.

This new Matlab-based software allows a detailed modelling of bodies with complex surfaces at any input model resolution. Several tests are performed to validate *GEEC* for various measurement heights and body mass sizes. They include (1) a local ground survey as typically performed for geophysical prospecting, (2) a global analysis of a spherical shell taking into account the curvature of the Earth and (3) an assessment of global and regional topography effects on satellite and airborne measurements. The results demonstrate the robustness of our approach and confirm that the mesh size required to achieve a targeted accuracy depends on both the size of the body mass and its distance to the measurement points. Although a regular meshing is suitable for high measurements heights (> 5 km) such as airborne surveys and satellite data, grid refinement is needed for low altitude measurements in the immediate vicinity of the computation point.

Compared to alternative approaches, the two main advantages of *GEEC* lie in the capacity (1) to preserve the complexity of the body mass geometries at all scales and (2) to compute gravity and gravity gradients for any measurement points regardless of the extent and irregularity of their spatial distribution, including varying altitudes. *GEEC* is then a well-suited method to develop in future works joint inversions of all type of gravity measurements from ground and airborne surveys as well as from satellite missions.

Acknowledgments

This work was supported by grants from Beasiswa Unggulan, ANR, and CNES TOSCA.

References

Cadio, C., Saraswati, A., Cattin, R., & Mazzotti, S. (2016). A new approach to assess isostatic compensation of topography in continental domain from GOCE gravity gradients. Geophysical Journal International, 207(2). https://doi.org/10.1093/gji/ggw281.

Chambodut, A., Panet, I., Mandea, M., Diament, M., Holschneider, M., & Jamet, O. (2005). Wavelet frames: An alternative to spherical harmonic representation of potential fields. Geophysical Journal International, 163(3), 875–899. https://doi.org/10.1111/j.1365-246X.2005.02754.x

Grombein, T., Seitz, K., & Heck, B. (2013). Optimized formulas for the gravitational field of a tesseroid. Journal of Geodesy, 87(7), 645–660. https://doi.org/10.1007/s00190-013-0636-1.

Guptasarma, D., and Singh, B. (1999). New scheme for computing the magnetic field resulting from a uniformly magnetized arbitrary polyhedron: Geophysics, 64, 70–74.

Hubbert, M. K. (1948). A line-integral method of computing the gravimetric effects of two-dimensional masses. Geophysics, 13(2), 215-225.

Jousset, P., Mori, H., Okada, H., 2003. Elastic models for the magma intrusion associatedwith the eruption of Usu Volcano, Hokkaido, Japan. J. Volcanol. Geotherm. Res. 125, 81–106.

Lee, W. H. K., & Kaula, W. M. (1967). A spherical harmonic analysis of the Earth’s topography. Journal of Geophysical Research, 72(2), 753–758. https://doi.org/10.1029/JZ072i002p00753.

Mader, K. (1951). Das Newtonsche Raumpotential prismatischer Körper und seine Ableitungen bis zur 3. Ordnung. Österr. Z. f, Vermessungswesen, Sonderheft, 11.

Nagy, D., Papp, G., & Benedek, J. (2000). The gravitational potential and its derivatives for the prism. Journal of Geodesy, 74(7–8), 552–560. https://doi.org/10.1007/s001900000116.

Okabe, M. (1979). Analytical expressions for gravity anomalies due to homogeneous polyhedral bodies and translations into magnetic anomalies. Geophysics, 44(4), 730-741.

Panet, I., Kuroishi, Y., & Holschneider, M. (2011). Wavelet modelling of the gravity field by domain decomposition methods: an example over Japan. Geophys. J. Int, 184, 203–219. https://doi.org/10.1111/j.1365-246X.2010.04840.x

Pavlis, N. K., Factor, J. K., & Holmes, S. A. (2007). Terrain-related gravimetric quantities computed for the next EGM. Proceedings of the 1st International Symposium of the International Gravity Field Service (IGFS), Istanbul, (January 2006), 318–323.

Pohánka, V. (1988). Optimum expression for computation of the gravity field of a homogeneous polyhedral body. Geophysical Prospecting, 36(7), 733-751.

Rummel, R., Yi, W., & Stummer, C. (2011). GOCE gravitational gradiometry. Journal of Geodesy, 85(11), 777–790. https://doi.org/10.1007/s00190-011-0500-0

Singh, B., & Guptasarma, D. (2001). New method for fast computation of gravity and magnetic anomalies from arbitrary polyhedra. Geophysics, 66(2), 521–526. https://doi.org/10.1190/1.144494.

Talwani, M., & Ewing, M. (1960). Rapid computation of gravitational attraction of three-dimensional bodies of arbitrary shape. Geophysics, 25(1), 203-225.

Talwani, M. (1998). Errors in the total Bouguer reduction. Geophysics, 63(4), 1125–1130. https://doi.org/10.1190/1.1444412

Tsoulis, D., & Stary, B. (2005). An isostatically compensated gravity model using spherical layer distributions. Journal of Geodesy, 78(7–8), 418–424. https://doi.org/10.1007/s00190-004-0404-3

Tsoulis, D., Novàk, P., & Kadlec, M. (2009). Evaluation of precise terrain effects using high-resolution digital elevation models. Journal of Geophysical Research: Solid Earth, 114(2). https://doi.org/10.1029/2008JB005639

Tsoulis, D. (2012). Analytical computation of the full gravity tensor of a homogeneous arbitrarily shaped polyhedral source using line integrals. Geophysics, 77(2), F1–F11. https://doi.org/10.1190/geo2010-0334.1

Uieda, L., Barbosa, V. C. F., & Braitenberg, C. (2016). Tesseroids: Forward-modeling gravitational fields in spherical coordinates. GEOPHYSICS, 81(5), F41–F48. https://doi.org/10.1190/geo2015-0204.1

Van Camp, M., de Viron, O., Watlet, A., Meurers, B., Francis, O. & Caudron, C. (2017). Geophysics from terrestrial time-variable gravity measurements. Reviews of Geophysics, 55, 938–992. https://doi.org/10.1002/2017RG000566.

Tables

Table 1. Gravity g_z and gravity gradient T_{zz} due to a 1 km thick spherical shell with a constant density ρ = 2670 kg m^{-3} above a reference sphere with a mean radius *R* = 6378.137 km. Analytical and numerical *GEEC* results are calculated at various computation altitude *h* ranging from 0 to 255 km. *GEEC* computation is performed with a mesh size of 5 and 150 km (see figure 7).

h (km)	Analytical Solution		*GEEC* solution			
			High Resolution (5 km)		Low Resolution (150 km)	
	g_z (mGal)	T_{zz} (mE)	g_z (mGal)	T_{zz} (mE)	g_z (mGal)	T_{zz} (mE)
On surface	223.895	701.960	223.880	494.187	223.036	358.943
2	223.825	701.630	223.821	649.811	222.999	369.583
5	223.615	700.641	223.614	699.869	222.884	401.080
10	223.265	698.998	223.265	698.996	222.670	450.898
255	207.076	624.369	207.076	624.369	207.029	624.230

Table 2. Computation time as a function of model resolution (see figure 8). The number of vertex of each model is included. All of the simulations in this study are performed using a computer with CPU Intel Xeon Processor E5, 3.20 GHz processor base frequency, with 8 cores.

Resolution (km)	Number of point	CPU time (s)
5	23611683	560.4783
10	5902922	142.8204
15	2623522	65.5157
20	1475732	33.2904
25	944469	20.5205
30	655882	12.5056
35	481873	8.4574
40	368935	6.5717
45	291504	4.8327
50	236119	3.9219
55	195140	3.0618
60	163972	2.6336
65	139716	2.2824
70	120470	1.9610
75	104943	1.6734
80	92235	1.3990
85	81703	1.2719
90	72878	1.1223
95	65408	1.0331
100	59031	1.0316
105	53543	0.8780
110	48786	0.7806
115	44637	0.7215
120	40995	0.6747
125	37781	0.6198
130	34931	0.5547
135	32391	0.5910
140	30119	0.5319
145	28078	0.4740
150	26237	0.4542

Figure

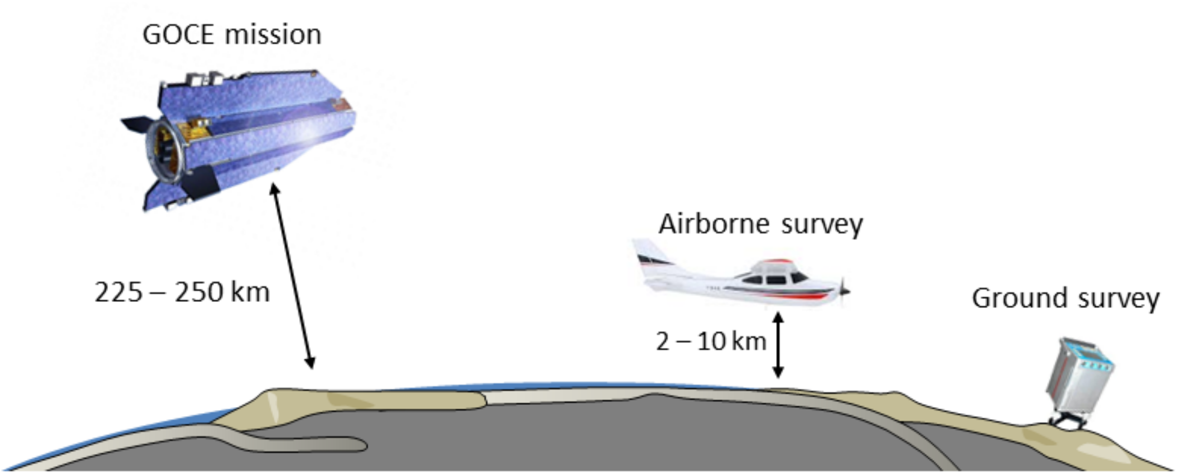

Figure 1. Classical gravity datasets from satellite missions, such as GOCE, to airborne and ground surveys. Together, these datasets can be used to assess density contrasts at depth and provide information at various scales from lithospheric structures to very local and shallow bodies.

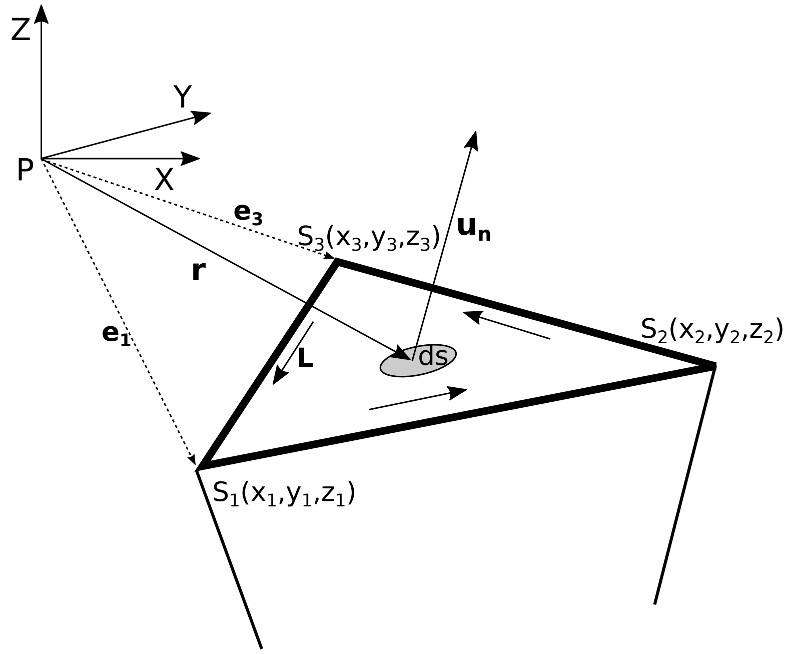

Figure 2. Polygonal surface in a right-handed Cartesian coordinate system and the scheme of the surface contribution computation. r is the distance between the observation point P and the element center. U_n is the unit outward normal vector of the surface element dS. The small solid arrows show the direction of the line integration around the edges, counter-clockwise from the outside.

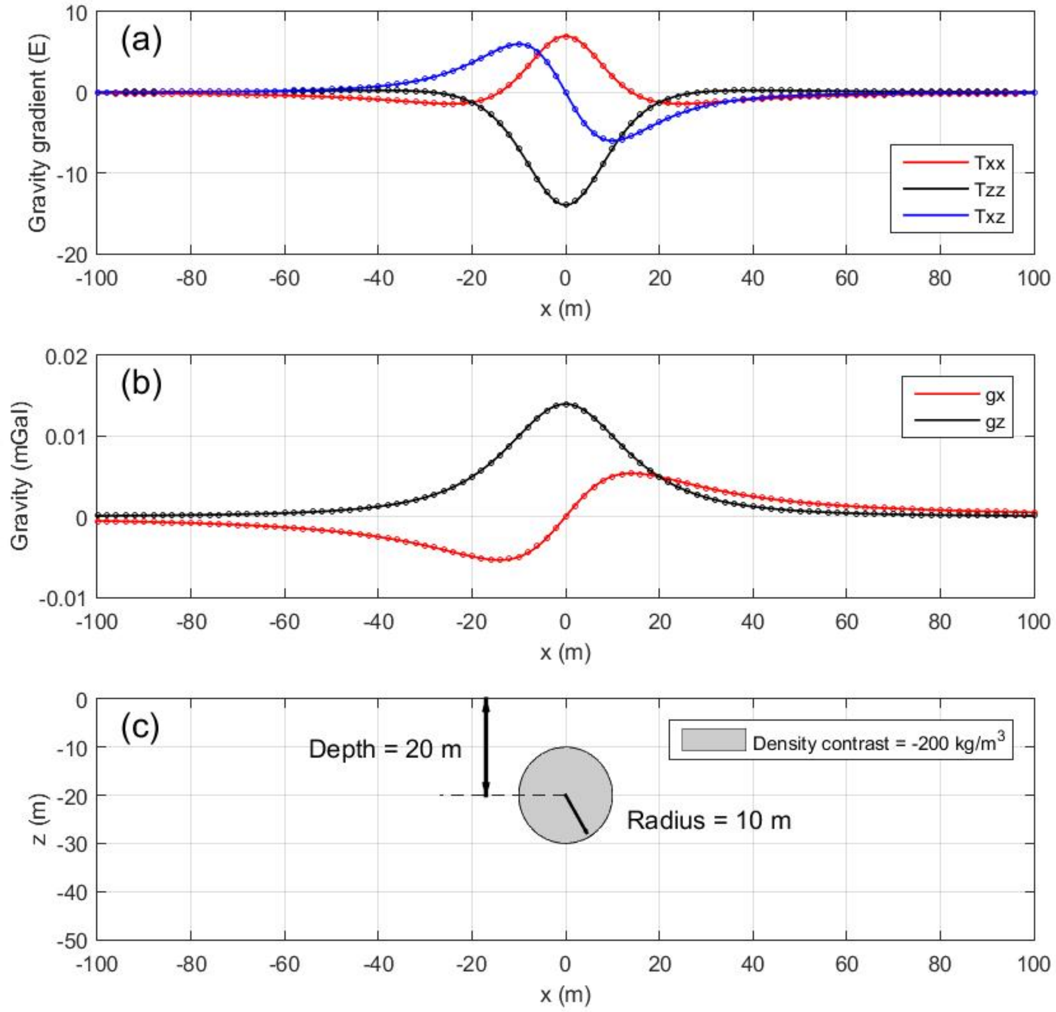

Figure 3. *GEEC* vs. theoretical analytical solutions for surface gravity and gravity gradients due to a buried sphere of anomalous density. (a) Gravity gradients from the theoretical (solid line) and *GEEC* (circles) solutions. (b) Gravity from the theoretical (solid line) and *GEEC* (circles) solutions. (c) Body mass geometry.

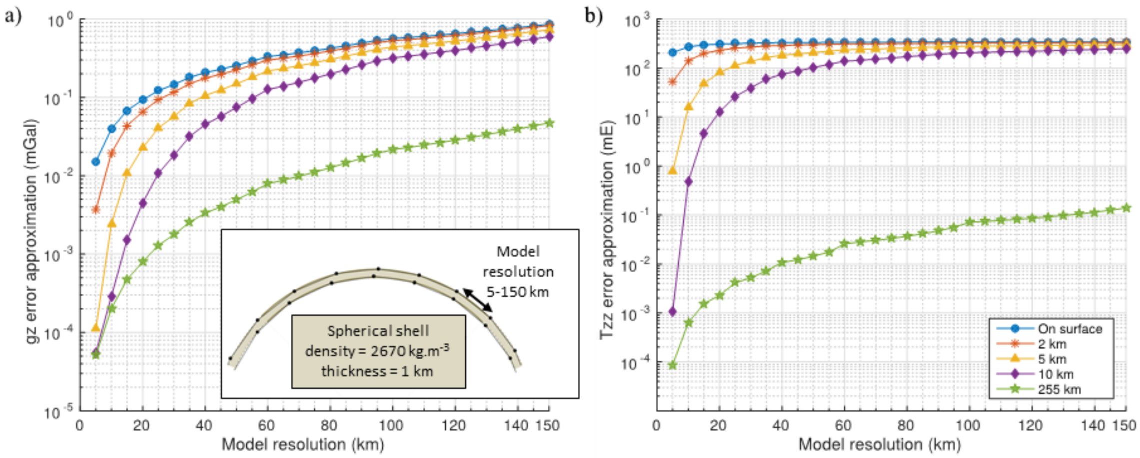

Figure 4. Relationship between height of gravity measurements and optimum mesh size (model resolution). Inset: Diagram of the model geometry used in *GEEC* to compute the gravity effect of a spherical shell with a constant density of 2670 kg.m^{-3} and a thickness of 1 km, corresponding to a plateau covering the whole Earth. (a) Error in g_z by *GEEC* computation relative to the analytical solution, as a function of the model resolution and the measurements height. (b) same as (a) for T_{zz} error.

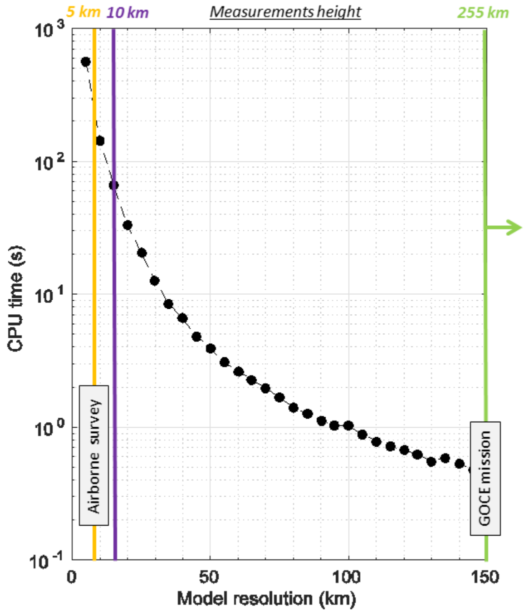

Figure 5. Relationship between CPU computation time, model resolution and measurement heights. Black circles are related to simulations performed using a computer with CPU Intel Xeon Processor E5, 3.20 GHz processor base frequency, with 8 cores and 16 threads per core (see table 2). Vertical color lines are associated with optimum model resolutions assuming an accuracy of 99.9% for the calculated gravity and gravity gradients. Color text gives measurement heights. Note that ground and low altitude airborne surveys require mesh resolutions smaller than 5 km.

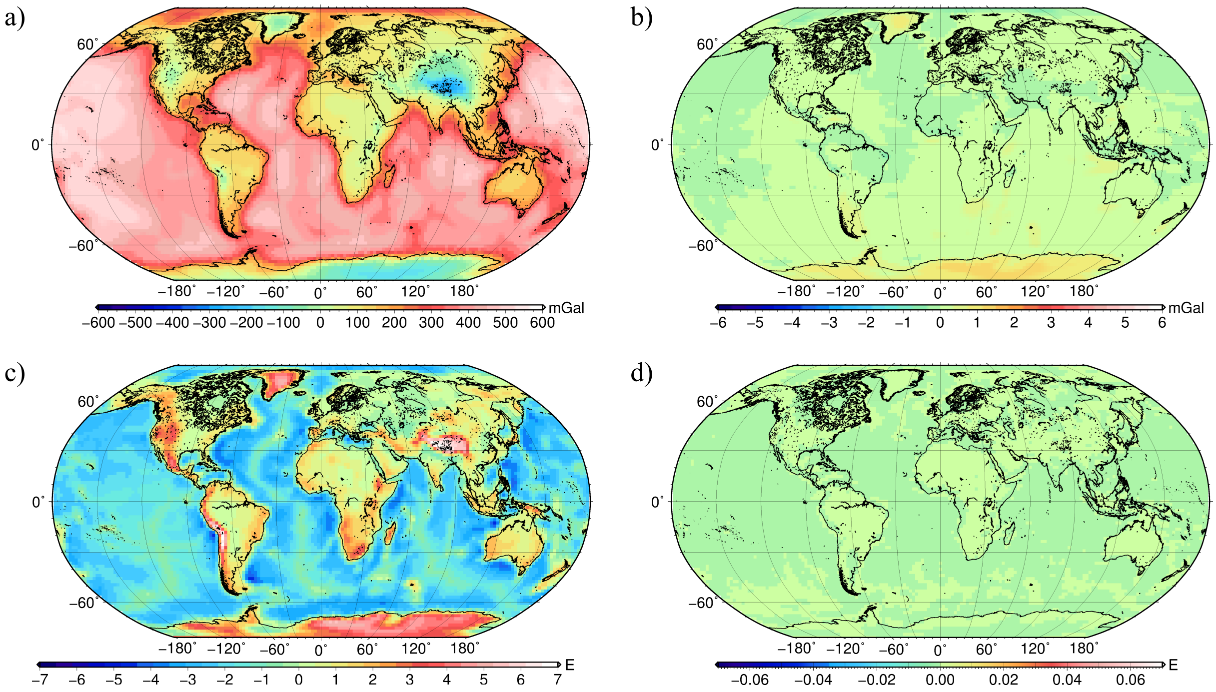

Figure 6. Comparison between *GEEC* and *Tesseroids* softwares. (a) and (b) Calculated g_z and T_{zz} due to global topography effect using *GEEC* at 255 km computation height with a model resolution of 10 km. Note that a positive mass contrast has a negative effect in vertical gravity in the ENU system. (c) and (d) Differences between *GEEC* and *Tesseroids* computations. Note the color scale, which represents 1 % of the color scale in (a) and (b).

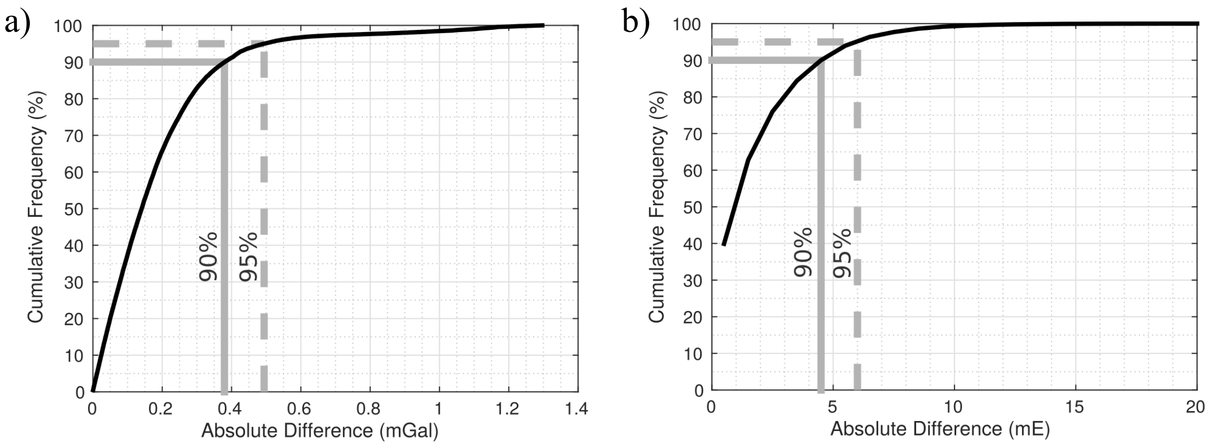

Figure 7. Cumulative frequency of the difference between *GEEC* and *Tesseroids* calculations of topography attraction in all gravity (a) and gravity gradients (b) components.

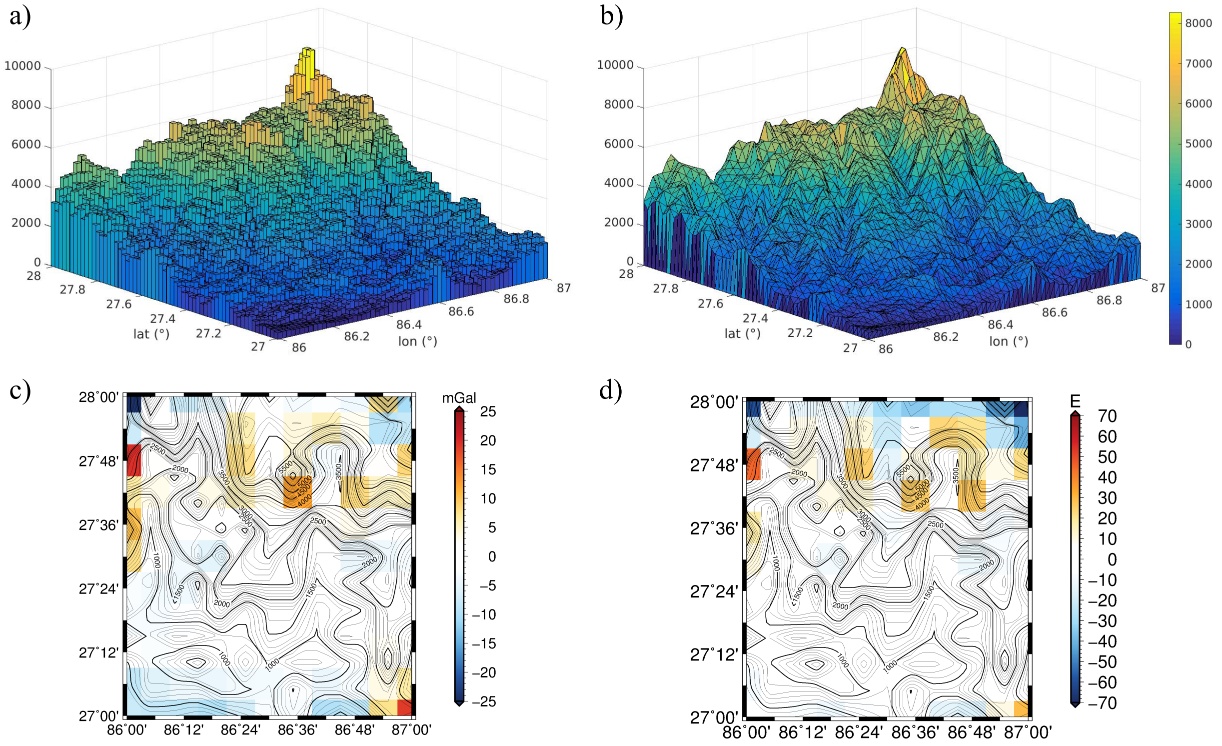

Figure 8. Effect of the discretization method in a rugged topographic surface, such as in the Himalayas of eastern Nepal. We consider an airborne survey at a constant altitude of 10 km . (a) Topographic surface discretization using prisms or tesseroids elements. (b) Same as (a) with a polyhedrons approach. (c) and (d) Difference in g_z and T_{zz} calculated from these two methods.

2.3. From GravProcess to GEEC

The first step of GEEC development is based on GravProcess, created by Cattin et al. (2015). GravProcess is a software that is dedicated to the processing of relative gravity measurements, including data corrections and network adjustments. One of its modules is aimed to perform terrain correction to estimate complete Bouguer anomaly. In the process of the creation and development of GEEC, we encountered some problems that made us enhance the code for a better and optimum computation of gravity and gravity gradients. A simplified scheme of the GEEC's evolutions from the beginning of the creation until the recent version is portrayed in Figure 2.1. This section is dedicated to describing the major improvements that have been made during the development of GEEC.

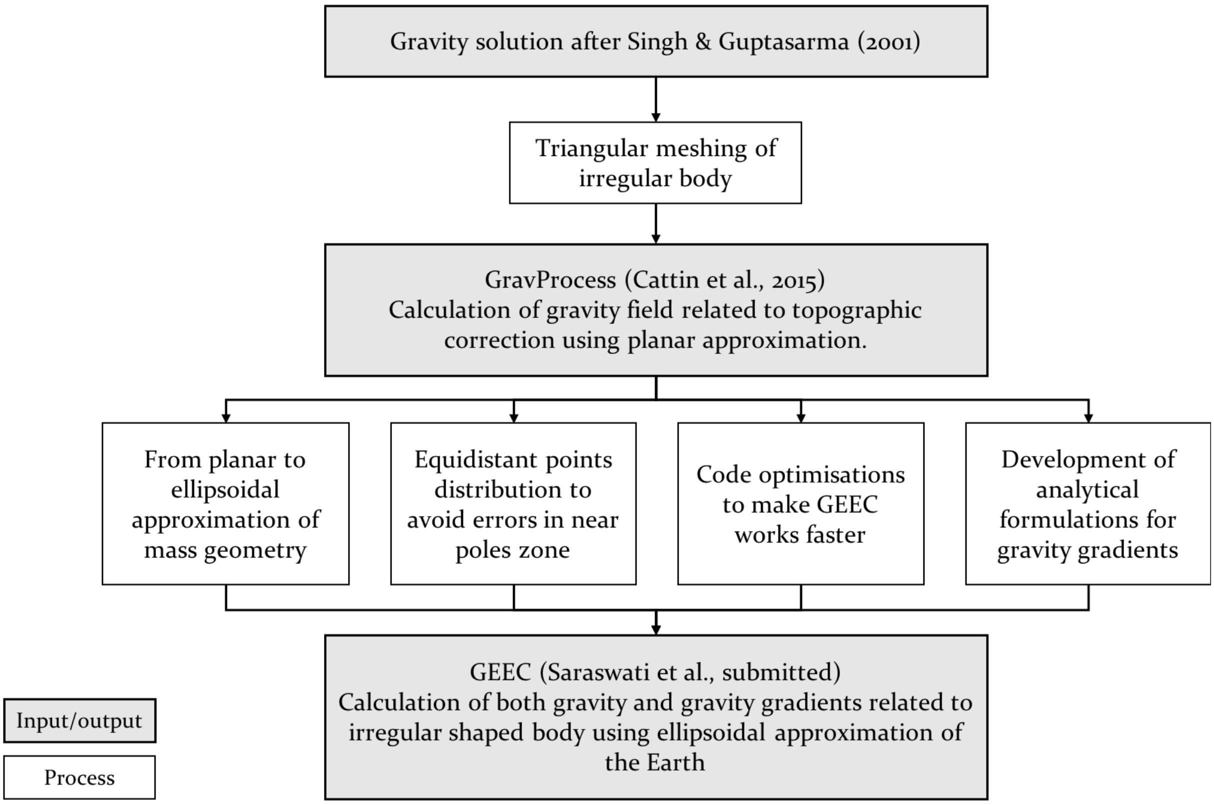

Figure 2.1: Flowchart of the improvements that have been made during GEEC development process.

2.3.1. From a Planar Approximation to the Ellipsoidal Model of the Earth

GEEC is developed by adapting the gravity forward modelling approach by Singh and Guptasarma (2001) to compute the gravity attraction of an irregular polyhedron with a uniform density. The geometry of a body mass is defined in a Cartesian coordinate system and carried out in the planar approximation. Dedicated to small-regional scale studies, the computation process to estimate the gravity field in GravProcess (Cattin et al., 2015) and thus in the very first version of GEEC was done in the planar field approximation.

However, for a large-regional study scale, the curvature of the Earth cannot be neglected, that is related to the unrealistic mass geometry (Figure 2.2) and its associated gravitational attractions. This problem has been addressed in the Hayford and Bowie (1912) system. For example, at a distance 22 km from the gravity station, the surface of the Earth drops 38 below tangent of the station (see Hammer (1939) table in Nowell (1999)), where the effect in the precision depends on the height variation. At this point, the use of spherical approximation in the gravity and gravity gradient forward modelling is a must.

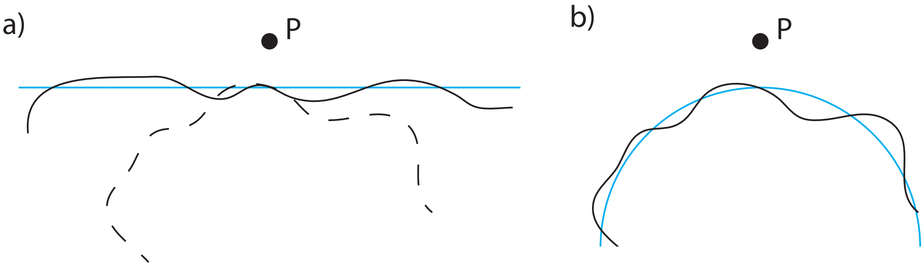

Figure 2.2: The comparison of the planar (a) and the spherical (b) approximation of a synthetic topography surface. The dashed lines represent real surface and the solid lines represent the modelled surface.

To deal with this problem, the geometry of the Earth-related mass model in GEEC is modelled in the ellipsoidal approximation. The computation in GEEC is executed in the local ENU (East, North, Up) Cartesian coordinate system. The available models of the Earth-related structure as well as the computation points that are normally defined in a geographic coordinate system are therefore transformed to the local ENU coordinate as well. The following sections will explain the processes in the coordinate transformations that are used in GEEC.

2.3.1.1. Geographic to 3D Cartesian Coordinates Transformation (and Inversely)

Digital terrain model, as an example of an Earth-related mass model, is usually defined in Geographic coordinate, where the position of the points is defined in longitude λ, latitude ϕ, and elevation h. In the GEEC computation process, these geographic coordinates must to be transformed into local ENU coordinates. To perform this transformation, firstly, the coordinates have to be transformed into a global 3D Cartesian system. The global 3D Cartesian coordinate system is defined with the origin located at the center of the Earth, the X-axis pointing the prime meridian, and the Z-axis pointing the North Pole (see Figure 2.3).

To transform the coordinate from geographic to 3D Cartesian system (X, Y, Z), the semi-major axis of the Earth a and its eccentricity e must be defined. The process to transform this coordinate is done by the following steps

$$\begin{aligned} X &= (N+h)(\cos\varphi\cos\lambda) \\ Y &= (N+h)(\cos\varphi\sin\lambda) \\ Z &= (N(1-e^2)+h)\sin\varphi \end{aligned} \tag{2.1}$$

where N is obtained by

$$N = \frac{a}{\sqrt{1-e^2\sin^2\varphi}} \tag{2.2}$$

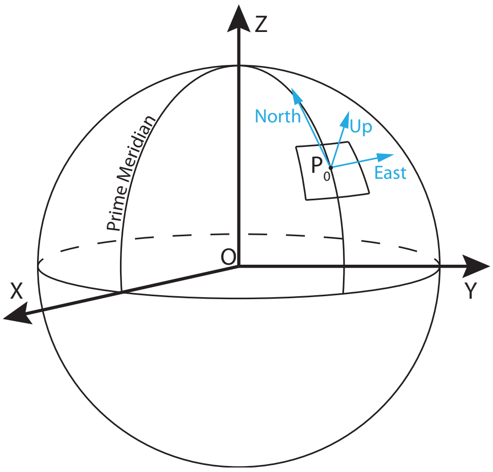

Figure 2.3: Cartesian (black axis) and local East-North-Up (blue axis) coordinate system.

This conversion from geographic to Cartesian coordinates is provided in GEEC in the function **ell2cart**.

Following Bowring (1976), the inverse coordinate transformation, from Cartesian to geographic coordinates, is given by

$$\begin{aligned} \lambda &= \tan^{-1}\frac{Y}{X} \\ \varphi &= \tan^{-1}\frac{Z+e'^2 b\sin^3\mu}{p-e^2 a\cos^3\mu} \\ h &= \frac{p}{\cos\lambda} - \frac{a}{\sqrt{1-e^2\sin^2\varphi}} \end{aligned} \tag{2.3}$$

where b is the semi-minor axis of the ellipsoid model and

$$p = \sqrt{X^2+Y^2} \tag{2.4}$$

$$\mu = \tan^{-1}\frac{aZ}{bp} \tag{2.5}$$

$$e'^2 = \frac{e^2}{1-e^2} \tag{2.6}$$

The transformation from Cartesian to geographic coordinates is provided in GEEC in the function **cart2ell**.

2.3.1.2. Geographic to Local Cartesian East-North-Up Coordinates Transformation

Like has been mentioned, the calculation in GEEC is performed using the Earth model as an ellipsoid model to calculate gravity and gravity gradients in the local ENU Cartesian system. In the local ENU Cartesian system, the point of origin is defined at a local point P_0 (see Figure 2.3), commonly is set at the measurement, with three Cartesian axes in the local East, North, and Up (ENU) directions. To transform the input coordinate from Geographic to local ENU coordinates, it can be done as following:

$$\begin{bmatrix} E \\ N \\ U \end{bmatrix} = M \times \begin{bmatrix} dX \\ dY \\ dZ \end{bmatrix} \tag{2.7}$$

where M is the rotation matrix of the point of origin (λ_0, φ_0)

$$M = \begin{bmatrix} \sin\lambda_0 & \cos\lambda_0 & 0 \\ -\sin\varphi_0\cos\lambda_0 & -\sin\varphi_0\cos\lambda_0 & \cos\varphi_0 \\ \cos\varphi_0\cos\lambda_0 & \cos\varphi_0\sin\lambda_0 & \sin\varphi_0 \end{bmatrix} \tag{2.8}$$

and

$$\begin{aligned} dX &= X - X_0 \\ dY &= Y - Y_0 \\ dZ &= Z - Z_0 \end{aligned} \tag{2.9}$$

(X, Y, Z) is the coordinate of the transformed point in the global 3D Cartesian coordinate system and (X_0, Y_0, Z_0) the 3D Cartesian coordinate of the point of origin in the ENU system using eq. (2.1). This function is provided in GEEC in **ell2enu**.

2.3.2. The Use of Equidistant Point Distribution

The coordinate of the existing global Earth models, e.g. Digital Terrain Model (DTM), crust model, are normally defined in a gridded dataset where the resolution is uniform in its longitudinal and latitudinal spacing. However, the actual size of a grid cell varies with the latitude and the shape of the grid is distorted from nearly rectangle to a nearly triangle as a function of the latitude (Figure 2.4). The tesseroid and prism approaches suffer from those problems that leads to the increase of the computation error on the near-pole zone (cf. Grombein et al., 2013; Uieda et al., 2016).

To deal with these problems, a triangle mesh with an uniform metric resolution can be a solution. From Figure 2.4, it can be seen that the distribution of the points all over the sphere surface is nearly uniform. This regularity in the resolution leads to the uniformity of the calculation precision. Although GEEC allows the computation using any point distribution, I suggest to use an iso-distance points dataset rather than a geographically gridded one.

In GEEC, the process to produce the iso-distance point distribution of a sphere utilizes the concept of the golden ratio and the golden angle that I adapt from Carlson (2011).

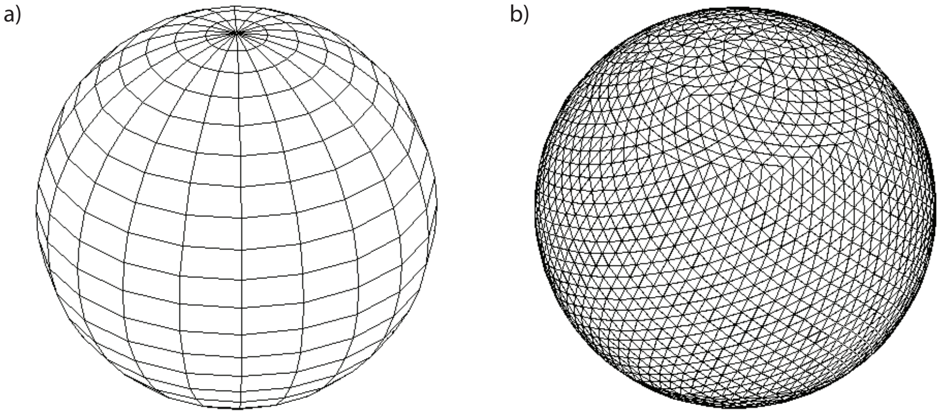

Figure 2.4: Gridded (a) and equidistant (b) point distribution.

The golden ratio and the golden angle can be obtained by

$$\text{golden ratio} = \frac{1+\sqrt{5}}{2} \tag{2.10}$$

$$\text{golden angle} = 2\pi\left(1 - \frac{1}{\text{golden ratio}}\right) \tag{2.11}$$

To discretize the surface of a sphere, I need to define the resolution of the mesh to obtain the number of the points n. For each point i, the longitude λ and the latitude φ, in radian, is obtained as following

$$\begin{aligned} \lambda_i &= (i-1) \times \text{golden angle} \\ \varphi_i &= \frac{\pi}{2} - \cos^{-1}\frac{1-2(i-1)}{n-1}, i \in \{1,2,3,...,n\} \end{aligned} \tag{2.12}$$

The point with i=1 is the point located at the North Pole. The elevation of these points is obtained by interpolating the input grid, e.g. DTM. GEEC provides the creation of this equidistant mesh in the routine **createequidistanttopo.m**.

2.3.3. Making GEEC Faster

The original algorithm of GEEC, based on the algorithm by Singh and Guptasarma (2001) included numerous iterations during the computation. This made the computation process demanding high resources of CPU, which implies to the inefficient computation time. Many improvements had been applied to GEEC to be more time and resource saving, including

- Transforming the replaceable looping parts into the form of matrix operation that is well suited for Matlab programming language.
- Adapting the computation algorithm to be specified for the computation using the triangle mesh as the representation of the geometry of the mass.

For comparison, Figure 2.5 shows the evolution of the computation process required by GEEC as a function of the resolution of the mass model from the first version (v.2016) to the latest version (v.2018). The size of the model is as large as the Earth, with a radius of 6 378.137 km. For the first version, an extravagant demand of the memory resource during the computation prevented the calculation over a whole globe, thus the mass model was limited with a spherical cap of 60°. After improvements and modifications of the code, the second and the latest versions of GEEC are enable to compute a whole Earth with reasonable time versus memory requirements, e.g., a computation of gravity and gravity gradient effects a whole Earth with a resolution of 20 km is done in 30 seconds.

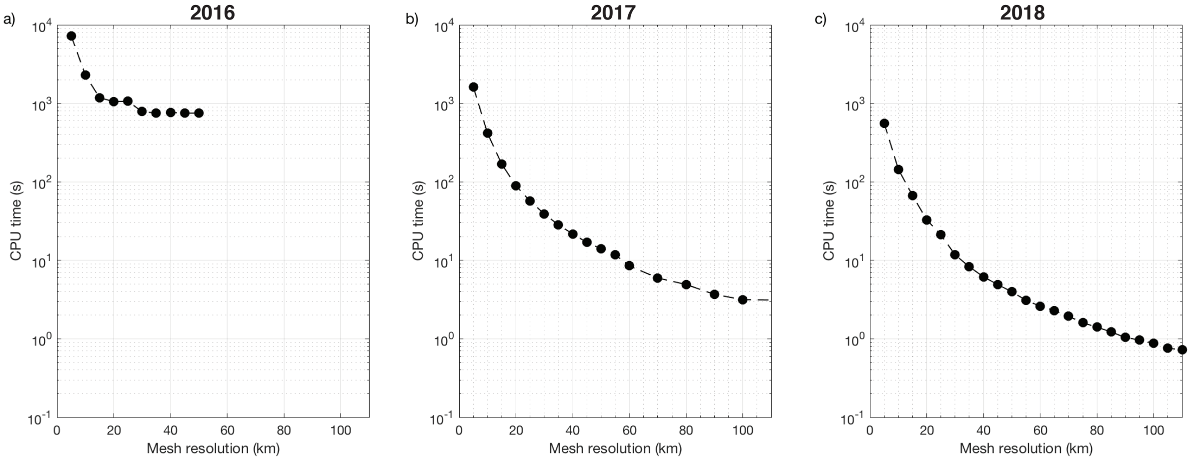

Figure 2.5: The evolution of the CPU time that is required in GEEC computation as a function of the model resolution. In the first version (made in 2016) (a), the spherical cap is limited at 60° due to the huge resource requirement in the computation. For the second (v.2017) (b) and the last (v.2018)(c) version, the calculation are performed using a whole sphere with the same size as the Earth.

2.3.4. Analytical Solution to Obtain the Gravity Gradients of an Irregular Polyhedron

As explained in the Chapter 1, gravity gradients may be obtained by dividing the difference of a pair of gravity values with the same vector direction by the distance between those observation points along a i-axis, like has been expressed in eq. (1.23). This method is valid if the distance between those points is small ($d \to 0$).

To evaluate this approach, I compute the gravity gradients of a spherical shell with a mass density ρ = 2,670 kg m^{-3} with a constant thickness 1 km above a reference sphere with a mean radius a = 6 378.137 km. The altitude of the computation varies between the surface (h = 1 km) and 255 km. The error is approximated using the difference between the GEEC's results and the analytical solution for a spherical shell (cf. Grombein et al., 2013).

This method is robust and applicable, but it still produces a remarkable noise (Figure 2.6a), especially at the satellite altitude (starry-green line). This noise is produced because the smaller the distance between points, the better approximation of the derivative, but the higher noise due to the computing precision.

To avoid this noise and make the computation more precise, I then enhanced the computation process by developing the gravity solution using the line-integral approach by Singh and Guptasarma (2001) to produce an analytical solution to calculate the gravity gradients of a polyhedron. The details of the formula are described in the associated paper (included in the end of this chapter).

This novel solution results in a better accuracy and stability in the computation especially at the satellite altitude (see Figure 2.6). The noise for the test at the altitude of satellite is no longer exist. It is because the noise which is larger than the precision is successfully removed by the novel analytical solution of gravity gradients. This improved algorithm is also more time-saving than the previous solution, e.g. for a computation using a resolution of 10 km, the latest version is ∼300 seconds faster than the second version (compare the CPU time of Figure 2.5c and 2.5b).

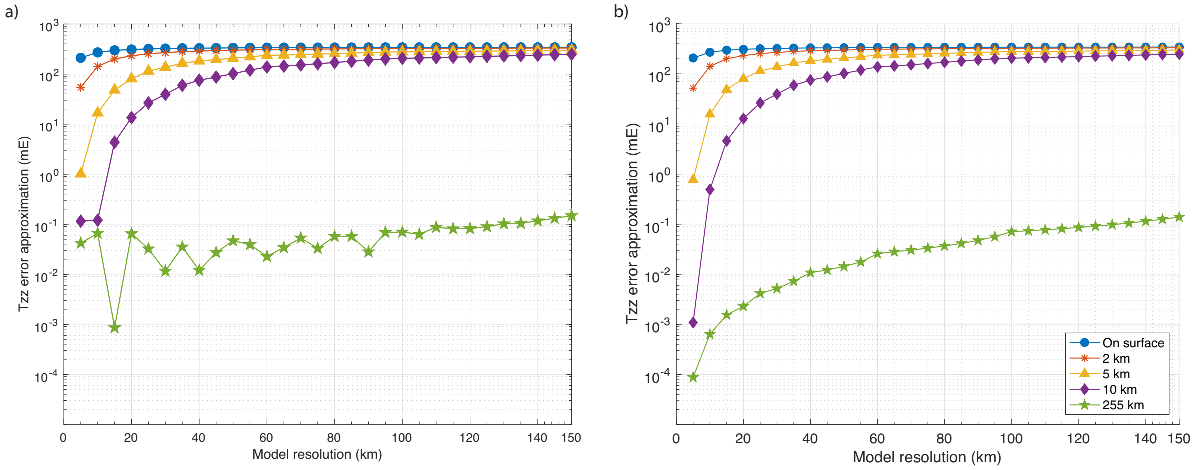

Figure 2.6: Comparison of the vertical gravity gradient by GEEC of the previous version (a) and the recent version (b). The use of eq. (1.23) to obtain gravity gradients in the previous version causes a larger noise, notably for the results at satellite altitude, than the use of the analytical solution.

2.4. Additional Information for the Implementation of GEEC

2.4.1. Technical Specification

All of the creation, development, running, and debugging process of GEEC is performed on a workstation with a Intel Xeon CPU E5-1680 v3 @ 3.20 GHz, containing 8 cores with 16 threads per core, 128 GB of RAM, and 500 GB of SSD in a UNIX operating system.

GEEC is written in the Matlab 2014b version. Because GEEC works under the Matlab environment, GEEC can be run on any operating system as long as a Matlab with the same or newer version is installed in the system. By taking advantage of the Matlab Parallel Toolbox, the computation time of GEEC can be enhanced, especially where GEEC is installed in a workstation or a cluster with a plenty amount of cores and threads.

2.4.2. Additional Functions in GEEC

The main function of this software is called **geec**. The details of the **geec** function and the required input and the output are given in the associated article.

Throughout the process, GEEC is developed to be adaptable for various applications, from the computation of a simple to a more complex mass geometry, from the ground to the satellite altitude of computation points, and from local to global scales of applications. To fulfill those necessities, beside the main function **geec**, GEEC also provides several functions depending to the type of application,

1. Functions **geec_topo** and **geec_topo_io** are the functions that are dedicated specifically to the computation of the topography effect. The computation is done in the ellipsoidal approximation. An option to set the extent of the computed topography is provided in these functions. In the **geec_topo_io**, GEEC introduces a scheme using two domains defined by two angles ψ_i and ψ_o, which correspond to the inner and outer spherical distance limit, respectively. User can combine two DTMs with different resolution and define the inner and the outer extent of each DTM, illustrated in Figure 2.7. The program to launch these functions are **launch_topo** and **launch_topo_io**.
2. For a simple geometry or a small size of the mass in the planar field, the function **geec_flat** is provided. An example to launch this function and to manage the input and output files is also provided in **launc_geec_flat.m** script.

2.4.2.1. Underdeveloped function

An underdeveloped function to perform a computation of a body mass with a lateral density variation is in the current process of development. Some objects that can be computed using this function such as a subducting slab and mantle layer below oceanic crust.

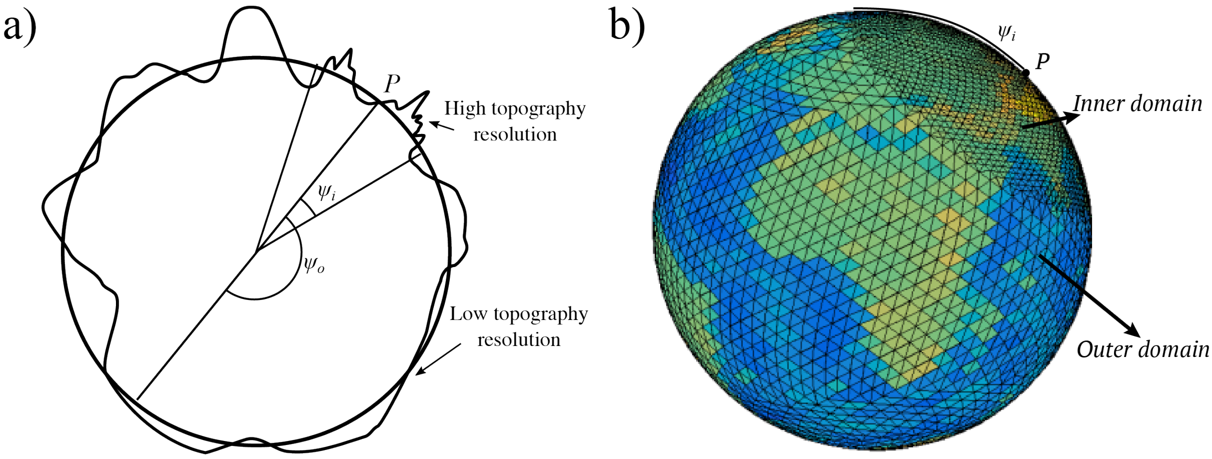

Figure 2.7: (a) Scheme of inner and outer domains in **geec_topo_io** around computation point P limited with the inner extent and outer extent, ψ_i and ψ_o, respectively, to optimize the use of high topography resolution within the near zone and less for the distant one. (b) The mesh illustration of inner and outer domains.

2.5. Conclusion

This chapter presents the development of GEEC (Gal Eötvös Earth Calculator), a Matlab-based computation tool to perform gravity and gravity forward modeling of an irregular shape body mass. Following Singh and Guptasarma (2001), new analytical formulas to calculate gravity gradients in the line-integral solutions have been developed.

GEEC applies triangle mesh as facets to compose the geometry of a polyhedra, which allows us to model in detail a body mass with a complex geometry regardless of its coordinates spatial distribution.

The use of GEEC for gravity and gravity gradient forward modelling offers the following advantages:

- Easy to use.
- Robust.
- Suitable for the computation effect of any mass geometry regardless of the scale of the object and the spatial distribution of the mass model.
- Supports the computation at any altitude and any spatial distribution regardless of the extent of the measurements points. This allows joint approaches combining satellite, airborne, and ground gravity and gravity gradients datasets.
- Its flexibility with any scale and spatial distribution of the measurement points as well as the geometry of the body mass makes GEEC as a all-in-one tool that allows whole processing, from the computation to the visualization in a single application.
- The use of parallel computation allows time-saving. GEEC is also ready to be launched in a large cluster for a better performance of computation.

Many applications can be realized by using GEEC. In this thesis, presented in the Chapter 3, GEEC is used to test the role of the spherical truncation distance ψ in the topographic correction of ground measurements, airborne surveys, and satellite missions for regional geodynamic application. In the Chapter 4, GEEC is used to calculate the synthetic models of a subducting slab and also the topography correction of the GOCE observation datasets on the Izu-Bonin-Mariana subduction zone.

Chapter 3

Optimum Topographic Gravity and Gravity Gradients Reduction for Regional Geodynamical Studies

3.1. Introduction

In the solid Earth, gravity is commonly used in combination with topography at commensurate resolution to elucidate the structures and dynamics of the Earth at depth. Estimation of the topography contribution in the gravity-related field is an important step in the analysis of gravitational data (Lemoine et al., 1997), in particular to develop topography-gravity transfer functions for the studies of isostasy (Watts, 2001) and dynamic topography (Burov and Diament, 1995; Cadio et al., 2016) or to perform topographic reductions as the first order correction to decipher the residual signal due crustal or lithospheric structures (Álvarez et al., 2012; Bouman et al., 2016). Since topography has a major effect in the Earth's total gravity field, the estimation of topography effect must be done carefully.

Concurrently with the availability of gravity and gravity gradient measurements with unprecedented resolution (cf. Chapter 1), high-resolution topography data also become available on global and regional scales from satellite missions (e.g., ETOPO01, GEBCO, SRTM, ALOS or Pléiades) with a spatial resolution up to ∼0.5 m as well as ground-based and airborne LiDAR (cf. Vaze and Teng, 2007). These new gravity, gravity gradient, and topography datasets require optimum topography modelling technique in order to preserve the data accuracy and precision, and to open the door for new global and regional geodynamic applications (e.g., Cadio et al., 2016; Panet et al., 2014).

Several methods exist to determine the topography gravitational effect, that can be classified in frequency domain technique (spherical harmonic modelling (e.g., Lee and

Kaula, 1967; Balmino et al., 2012; Hirt et al., 2012)) and space domains technique (including rectangular spherical prisms or tesseroids (Grombein et al., 2013; Uieda et al., 2016) approach, analytical solutions for rectangular prisms approach (Mader, 1951; Nagy et al., 2000), and polyhedron approach (cf. Okabe, 1979; Singh and Guptasarma, 2001)). In this study, I use the approach of gravity and gravity gradients forward modelling using the method of irregular polyhedron that has been implemented in GEEC (Gal Eötvös Earth Calculator) (Chapter 2). Beside its advantages about the flexibility with the mass model and the spatial distribution of the measurement points, it allows us to model the variations of topography surface in detail.

The Importance of Distant Topography

The entire Earth topography contributes to the gravitational attraction in gravity or gravity gradient measurements. The distance over which the topography effect must be considered, i.e. the topography truncation distance, in the gravity analysis remains debated (Talwani, 1998; Szwillus et al., 2016). To show how the topography effect varies as a function of the truncation distance, we calculate the gravity value due to the topography masses located within truncation distances $0° < \psi < 180°$ and compare them with the absolute value of Earth topography effect (i.e. the value where the entire Earth topography is considered). The computation is performed on a 10°×10° global grid at altitudes of 0, 10 and 255 km using the DTM2006.0 global topography model (Pavlis et al., 2007). Figure 3.1 shows the average value of gravity as a function of truncation distance ψ at each altitude.

For studies that consider the gravity variation in absolute value, topography must be included to a distance of ∼110° in order to reach 90% of the global value (Figure 3.1a). However, the irregularities of the Earth surface lead to a strong dispersion of the ψ distribution to obtain 90% of accuracy (Figure 3.1b). For applications that require a high accuracy ($\leq$ 1 mGal), a distance $\psi > 170°$ is necessary, which in practice nearly corresponds to a global (ψ=180°) computation.

Computation of the effect of global topography can easily be performed at satellite altitudes (higher than 255 km), for which a relatively low topography resolution can be used (see Chapter 2). In contrast, computation of topography effect at near Earth surface (such as ground and airborne survey altitudes) requires the use of a high-resolution topography. Moreover, the ground and airborne surveys are usually applied for studies at local or regional scale, for which a global-scale computation can be impractical.

Geodynamic studies at local and regional scales are commonly based on the analysis of relative spatial variations in the gravity anomalies, i.e. only differences between values across the region matter, while the absolute value is ignored. The distance between stations is then a key parameter that controls the optimal truncation distance to perform the topography correction (Talwani, 1998). For measurements at the same location, the truncation errors cancel each other regardless of the truncation distance. Beyond this obvious case, when the survey stations are close together, the relative measurements are mostly sensitive to topography irregularities surrounding each station because the errors

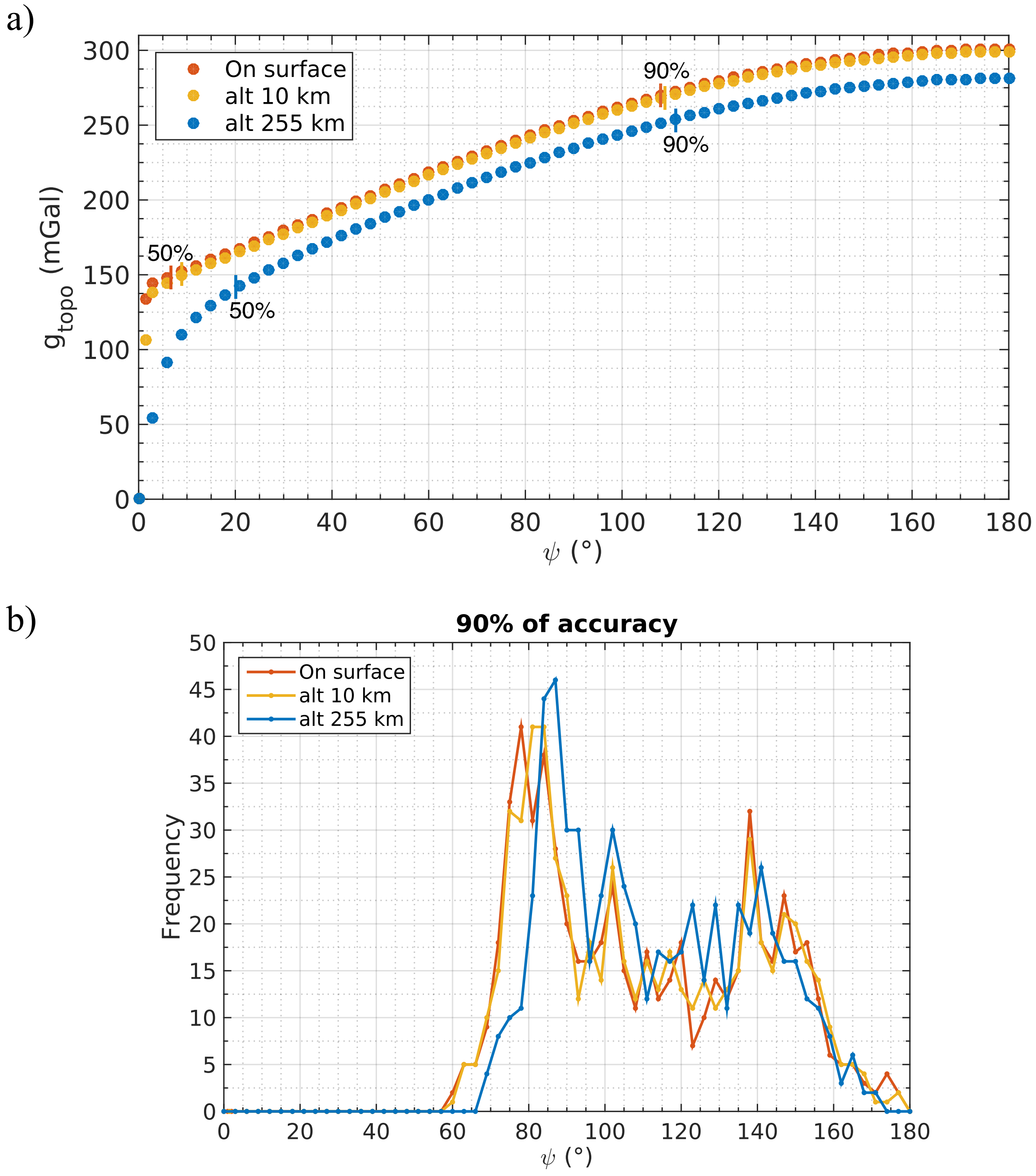

Figure 3.1: a) Average gravity effect of the topography masses located at a distance ψ of the computation point, at various altitudes (colors). Values at $\psi = 180°$ represent the effect of the global topography. The percentage of the gravity with topography extent ψ compared to the global effect (ψ=180°, true total contribution) is mentioned in the figure. (b) Distribution of the minimum distance ψ_t necessary to achieve 90% of the global topography effect (i.e., 90% accuracy) for all computation points.

caused by ignoring distant topography are similar.

The determination of the topography truncation distance depends on:

1. the altitude of the survey,
2. the size of survey area,
3. the roughness of regional topography, and
4. the organization of topography masses around the survey area.

Nowadays, several methods used to define the truncation distance for topographic corrections are usually based on:

1. an "empirical" distance of 1.5° (ca. 167 km) around the measurement point (Hayford and Bowie, 1912; Bullard, 1936) that is widely used for topographic correction of ground gravity surveys, notably for local to regional applications. However, this traditional method could be inappropriate for current developments of gravity surveys, particularly for the application on a large scale with high precision and for topography effect estimation at higher measurement altitude (e.g. airborne and satellite measurement) (Szwillus et al., 2016). This Bullard's distance is also reported to be too small for the application on a zone with a strong variation of topography roughness (Talwani, 1998; Mikuška et al., 2006)
2. at larger scales, set of trials and estimations of the obtained errors compared to the signal of interest. This method demands plenty of trials, thus it is very time consuming.
3. spectral analysis based on Parker (1973)'s frequency domain formulation in Kass and Li (2008), that is applicable for airborne gradiometry only. This method is rather simplistic because it does not account for the full range of spectral content in the topography and because it was tested on a very few specific area.
4. geostatistical analysis of local topography by Jekeli (2013). But this method is only valid for vertical gravity gradient.

To sum up, the existing methods to determine the truncation distance are developed for specific applications and do not answer to the question of the optimal distance for regional geodynamical studies.

This study is focused on the following questions: what is the optimum truncation distance to obtain the desired accuracy for application of ground, airborne, and satellite gravity and gravity gradient measurements at local and regional scales? And is it possible to define a systematic approach?

To answer those questions, I quantify the errors caused by neglecting distant topography masses on end-members region in terms of topography variation, which include (1) the Himalaya (with strong topography variation), (2) the Pacific region (with smooth topography (bathymetry) variation, and (3) the Southeast Pacific region with smooth topography variation within the zone and the presence of major topography around the zone (i.e. Andes Cordillera). This quantification of errors is applied for ground, airborne, and satellite altitudes of measurements.

This chapter starts with the presentation of the method that we use to evaluate the errors due to neglecting the topography beyond a given distance. The variation of relative errors in gravity and gravity gradients due to the variation of global topography will be demonstrated. Although the results exhibit a complex pattern due to the irregular distribution of Earth major topography structures, a straightforward relationship between truncation distance and the dimension of the zone is successfully extracted for application at regional scale. A guideline about of how far the truncation distance which must be considered to obtain the standard precision in geodynamic applications at local and regional scale is also presented.

Using a specific application on a gravity measurement profile across Eastern Nepal, this study illustrates the importance of an optimum truncation distance for geodynamical study to avoid any misinterpretation. Comparison of the results from this study with the previous study by Jekeli (2013) is also discussed in the end of the discussion.

3.2. Method

We investigate the relationship between the truncation distance ψ_t and the distance d between two stations P and Q (Figure 3.2) by calculating the relative difference in truncation errors between each station:

$$\sigma g(\psi_t, d) = \Big|[g_{topo}(\psi = 180°) - g_{topo}(\psi = \psi_t)]_P - [g_{topo}(\psi = 180°) - g_{topo}(\psi = \psi_t)]_Q\Big| \tag{3.1}$$

where $[g_{topo}(\psi = 180°) - g_{topo}(\psi = \psi_t)]$ is the difference in vertical attraction between the global topography effect ($\psi = 180°$) and the truncated topography effect ($\psi = \psi_t$). This difference thus represents the attraction due to masses beyond the truncation distance ψ_t , i.e. the error of ignoring topography beyond this distance. The difference in truncation errors between stations P and Q ($\sigma g(\psi_t, d)$) is a measure of the precision in the relative gravity anomalies between these points.

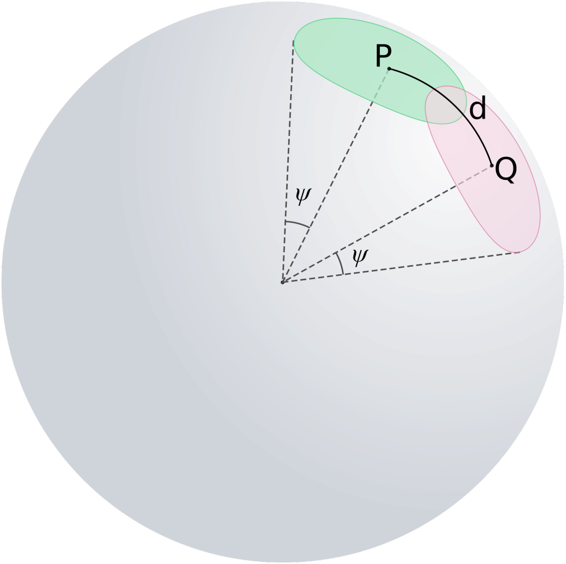

Figure 3.2: Scheme to evaluate the optimal truncation distance ψ to perform topography correction for a regional application. P and Q are two gravity stations (black dots) located at the limits of the survey area and separated by a distance *d*.

This approach is applied on three regions; The first region (77°-97°E, 18°-38°N) includes the Tibetan Plateau, the Himalayan belt and northern India. It is characterized by major variations in the topography elevation profile. The second one (105°- 125°W, 15°- 35°N) is in the Pacific Ocean, with smoother surface (bathymetry) variations. And the third one (95°-75°W, 15°-35°S) is in the south-eastern Pacific Ocean with a smooth surface (bathymetry) variation but with the existence of the Andes Cordillera as a major structure nearby. For those area, I calculate the gravity and gravity gradients effect of topography masses in continental and oceanic domains varying the truncation distance ψ_t from 0.1° to 180°.

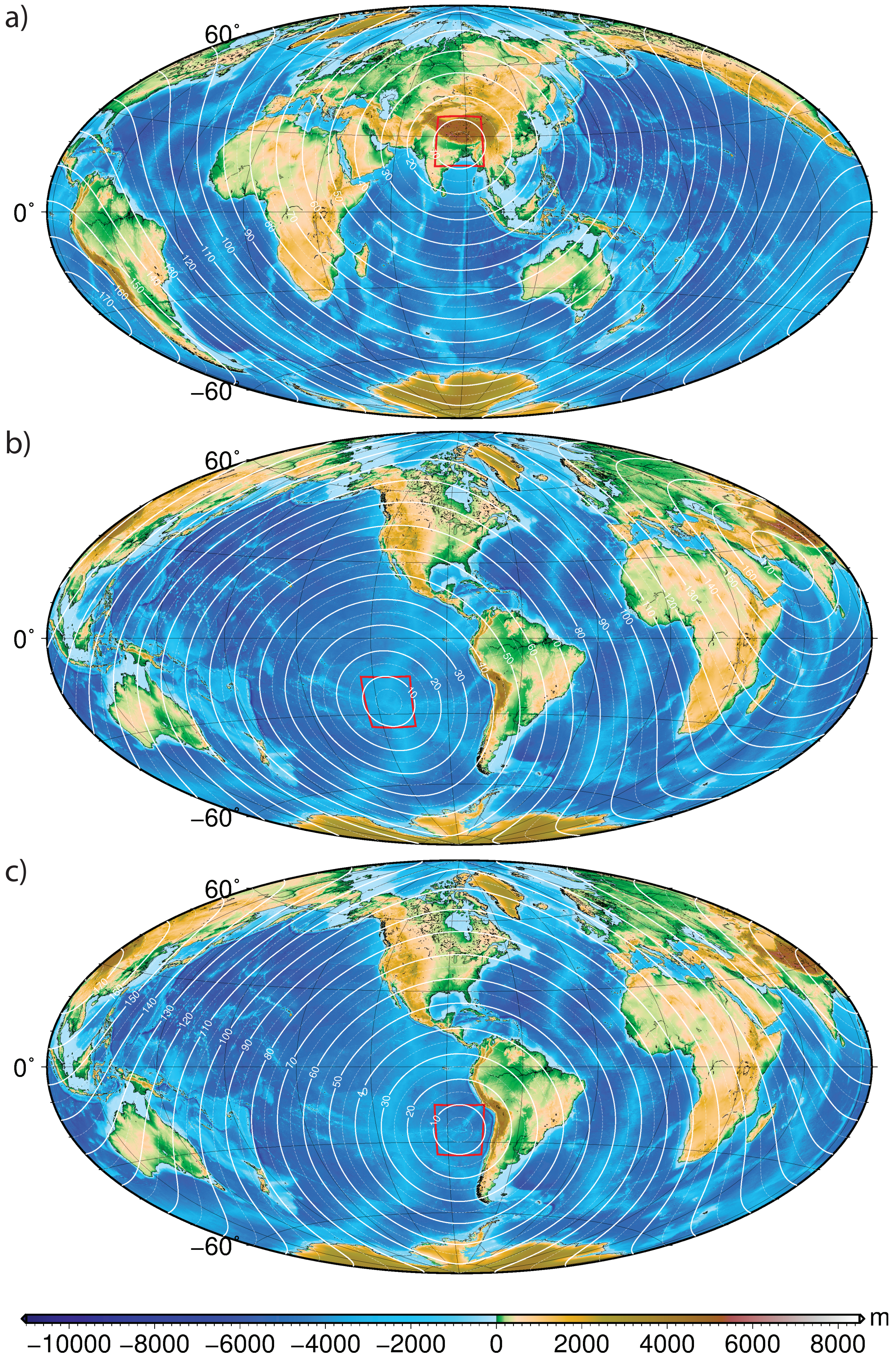

Figure 3.3: The test regions in the Himalaya (a), mid-Pacific (b), and southeastern Pacific (c) (red squares). White lines represent iso-distances from the tested regions.

The calculations are performed by using the DTM2006.0 topographic data (Pavlis et al., 2007) with a resolution of 10 km. The topography model is decomposed in two bodies: a rock layer for masses above sea level with a density $\rho_c = 2670$ kg m^{-3} and a water layer for masses below sea level with a density $\rho_w = 1000$ kg m^{-3}. Using the crustal density as the reference density, it gives a density contrast for the ocean of -1670 kg m^{-3}. The measurement points are set on the ground (altitude h+20 cm on the continents and h=20 cm on the oceans to ensure that the measurements for gravity gradient are outside the source), at mid altitude (10 km), and satellite altitude (255 km). The spatial distribution of measurement points is set with a spacing grid 0.2°×0.2°.

The pairs of stations are constructed by performing *2-combination* among the existing points within the regions. To ensure the representativeness of the results, I select the combinations of ψ_t and d that contain more than 100 pairs, thus the pairs with $d > 21°$ are excluded from the later procedures and analysis in this study (Figure 3.4).

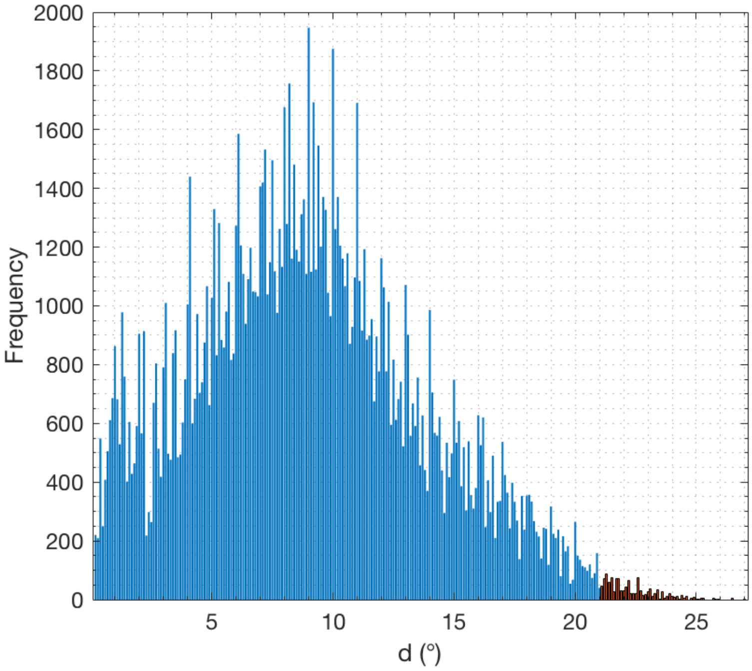

Figure 3.4: The number of pairs as a function of interstation distance d. To provide representative results, I select the d with n-pairs > 100. From the histrogram, the interstation distance d in this study is $d \leq 21°$ (in blue bars) and the data beyond $d = 21°$ are excluded (in red bars).

We want to provide a truncation value that is representative of an order of magnitude in the precision of the correction. Figure 3.5 demonstrates that the distribution of $\sigma g(\psi_t, d)$ at each combination of truncation distance ψ and interstation distance d does not extend very far to the high value (standard deviation or 90^{th} percentile is close to the mean). Although the distributions are not perfectly Gaussian, they are not extremely skewed, i.e. the mean and median are very close and the distributions are not far from being symmetrical. Therefore, the mean of the distribution is a good first-order estimator to represent the results.

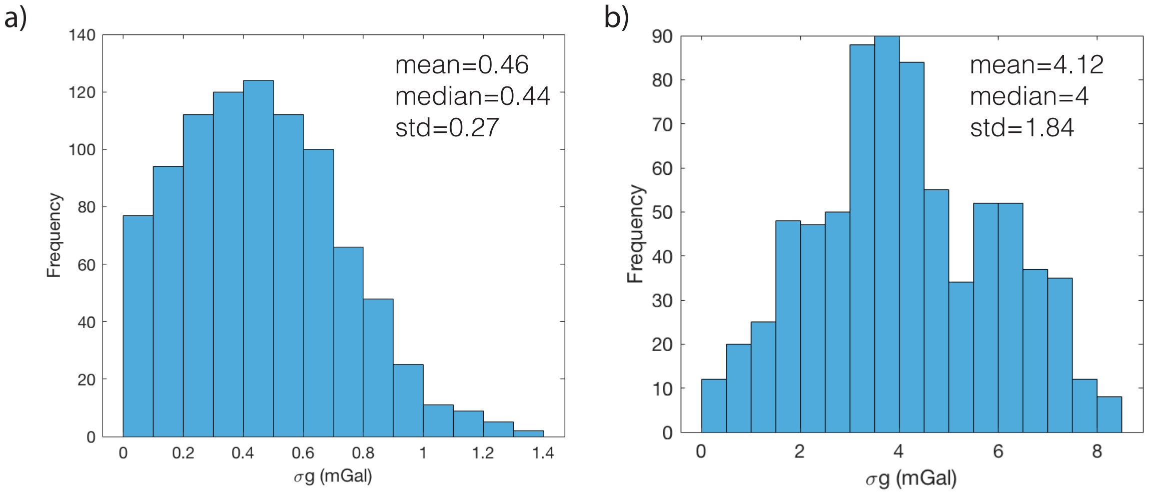

Figure 3.5: Histogram of $\sigma g(\psi_t, d)$ distribution at $(d = 2°, \psi_t = 15°)$ (a) and $(d = 15°, \psi_t = 30°)$ on Himalaya case as the sample points to view the distribution of $\sigma g(\psi_t, d)$.

3.3. Results

3.3.1. Gravity relative error due to global topography variation

Figure 3.6 shows the relative truncation error $\sigma g(\psi_t, d)$ as a function of interstation distance d and truncation distance ψ_t, calculated on topography surface on Himalaya (a), Pacific Ocean (b), and southeast Pacific Ocean close to Andes Cordillera (c). The results at other computation altitudes, 10 km and 255 km, can be found in Appendix B. The relative truncation error $\sigma g(\psi_t, d)$ exhibits a complex pattern for all three areas, that is associated to the topography variation within the zone and the irregularities of topography variation beyond the survey zones.

As expected, the maximum errors (over 10 mGal) are associated with small truncation distance ($\psi_t \leq 10°$) and large interstation distances ($d \geq 5°$). Errors for small truncation distances are larger for the Himalaya area (over 50 mGal), confirming the major effects of the topography roughness in local and regional corrections, which is not for the Pacific Ocean cases with a smoother topography (bathymetry) (with errors $\sigma g(\psi_t, d)$ around 5-10 mGal).

For pairs of stations that are separated by a large interstation distance ($d > 5°$) suffer from the topography variation in far-field. For example, the effect of Greenland for the Himalaya case results the errors with $\sigma g(\psi_t, d) > 5$ mGal (Figure 3.6). The effect of Greenland is weaker on the Pacific zone because the distance of Greenland from the tested zone in Pacific is further than the one on Himalaya.

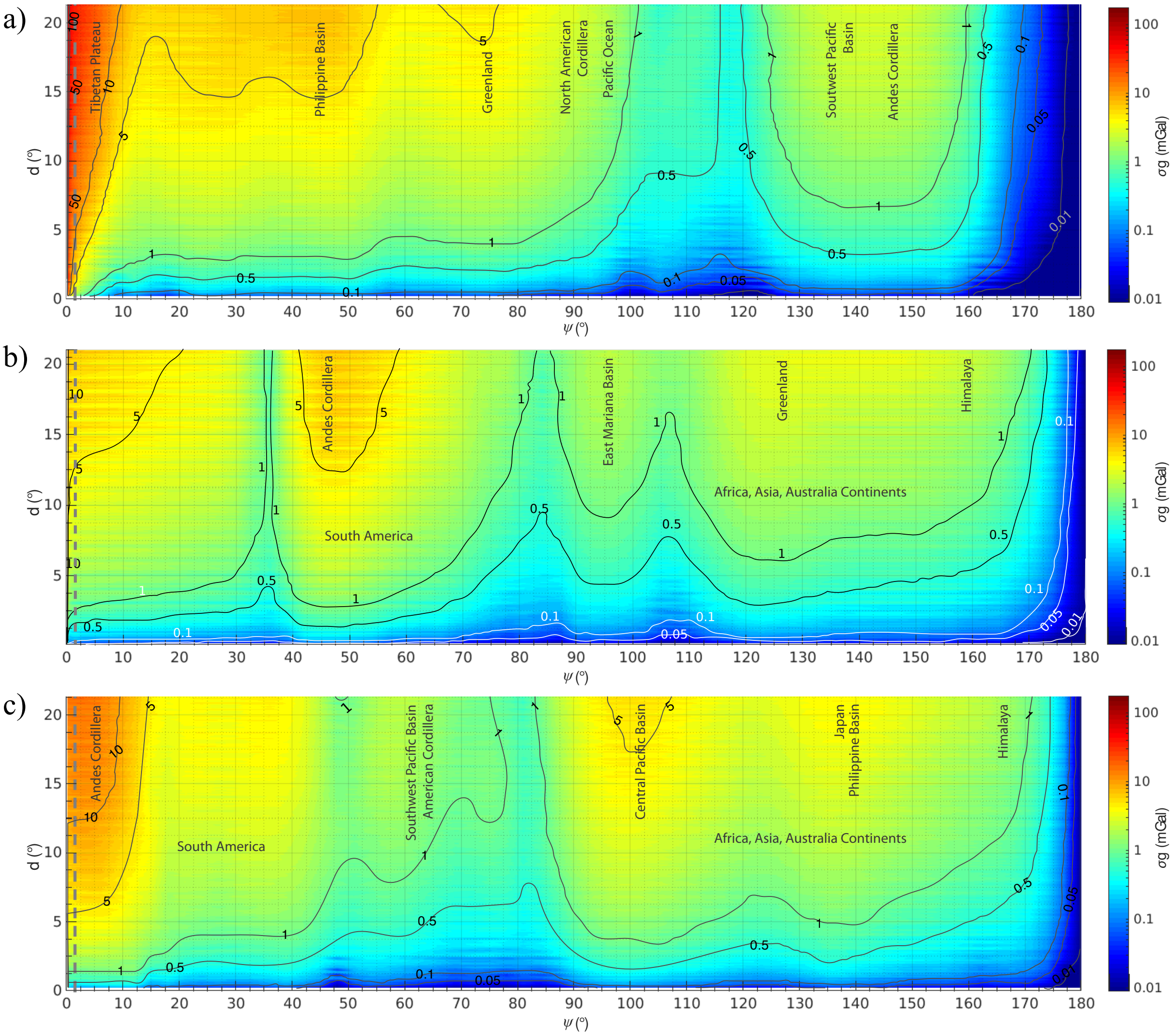

Figure 3.6: The difference in topography correction (differential error) $\sigma g(\psi_t, d)$ between to two points in the region, as a function of their distance d and the topography correction truncation ψ (cf. Figure 3.2), for Himalaya (a), Pacific (b), and Southeast Pacific (c) zones, respectively. The dashed grey line marks the ψ=1.5°, corresponding to the standard truncation distance (Bullard, 1936). The differential effect of major continental and oceanic masses are labeled (see Figure 3.3).

3.3.2. Gravity gradient relative error due to global topography variation

To investigate the relative truncation errors in gravity gradient, I use the same evaluation method, as written in eq. (3.1), by replacing the vertical gravity with vertical gravity gradient and implement it on the same areas (Figure 3.3). The results for ground measurement are illustrated in Figure 3.7. For the results at other computation altitudes, 10 km and 255 km, it can be found in Appendix B.

As expected, errors for Himalaya region for small truncation distance ($\psi_t \leq 5°$) are

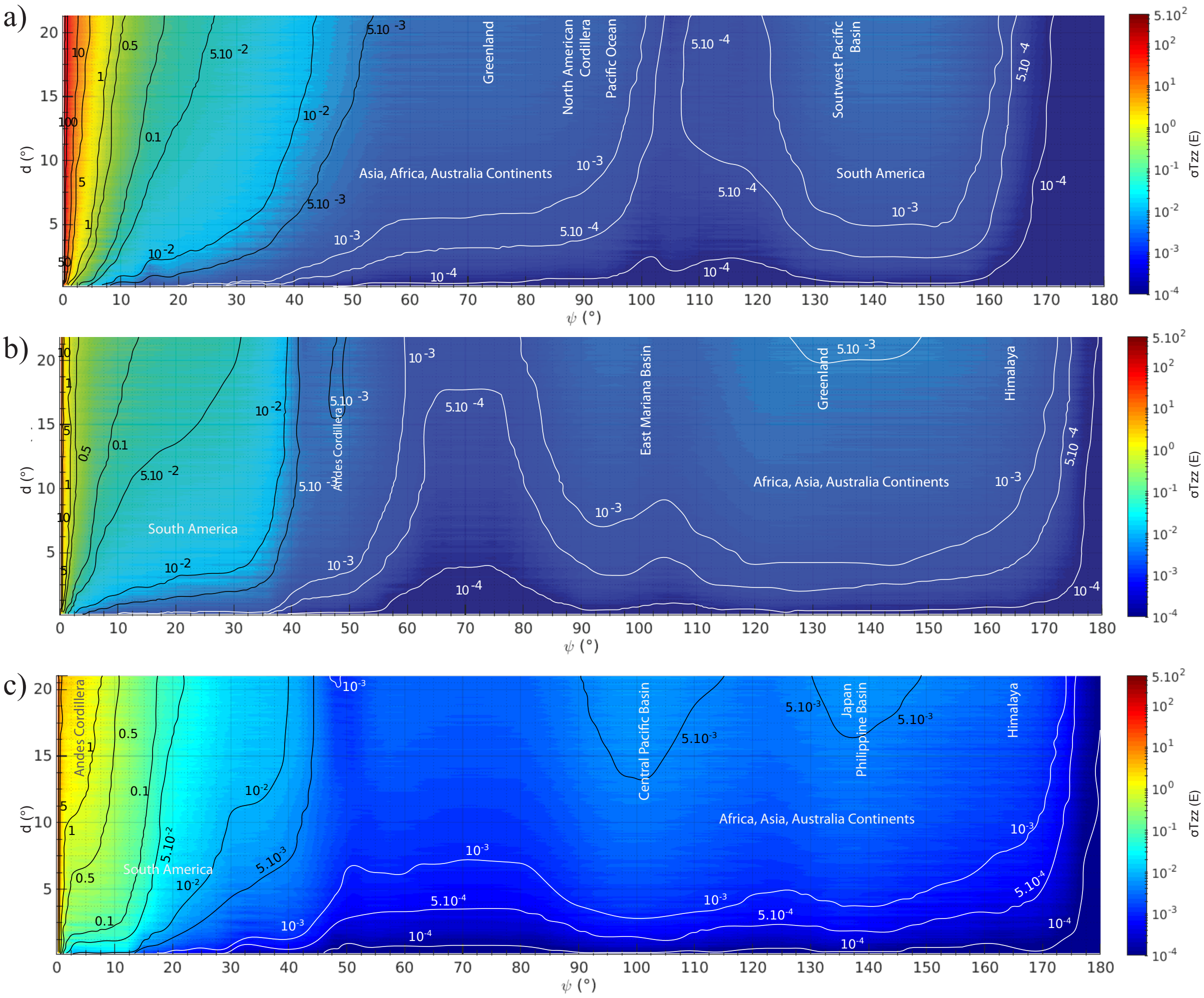

Figure 3.7: The difference in topography correction (differential error) in gravity gradient $\sigma T(\psi_t, d)$ (in Eötvös) between two points in the region, as a function of their distance d and the topography correction truncation ψ (cf. Figure 3.2), for Himalaya (a), Pacific (b), and Southeast Pacific (c) zones, respectively. The differential effect of major continental and oceanic masses are labeled (see Figure 3.3).

larger than in the Pacific regions, with relative truncation errors ($\sigma T(\psi_t, d)$) up to 100 E for the Himalaya area (Figure 3.7a) and up to 10 E for both Pacific cases (Figure 3.7b and c), confirming the major effect of topography variation within the zone. The variation of relative gravity gradient truncation errors associated with small truncation distance ($\psi_t \leq 10°$) decrease more steeply than the relative gravity truncation error in Figure 3.6. The gravity gradient errors $\sigma T(\psi_t, d)$ produced by distant major structures is better than 5 mE, thus represents a smaller error percentage than gravity errors $\sigma g(\psi_t, d)$ (see Figure 3.6 and Figure 3.7 for comparison). It confirms that gravity gradient is less sensitive to the far-field variation than gravity.

From those explanations above, there is a complex interaction between truncation distance ψ, scale of the zone (that is interpreted as the interstation distance d in this study), and spatial distribution of Earth topography to estimate the relative gravity and gravity gradient truncation errors, $\sigma g(\psi_t, d)$ and $\sigma T(\psi_t, d)$ respectively, that is mainly due to the variation of Earth topography around the globe and its relative distance to the zone of interests.

3.3.3. Topography effect at local and regional scale

3.3.3.1. Relative gravity truncation error

For this part of application, we are interested for the application in local and regional scale. Let us assume that for a geodynamic application at local scale, the dimension of the zone d does not exceed 2° and the required precision is 1 mGal. For application at regional scale, it is defined with a maximum dimension of 20° and a required precision of 10 mGal (e.g., Cattin et al., 2001). The standard precision of each scale of application is considered based on the spatial variation of gravity within the zone; for a local scale, normally the gravity is not highly varied (not exceeding hundreds mGal), thus it requires a higher precision that the one at regional scale (where the gravity variation can be more than hundreds mGal). By using this condition, we can magnify Figure 3.6 and focus on $\psi \leq 30°$.

At the first order of approximation, the results in Figure 3.8 exhibit a common characteristic: by applying $\psi_t = d$, the precision obtained ranges between 1-10 mGal, with values around 5 mGal. Surely, the variations of errors are specific for each zone and at each altitude of computation, for example for the result on Himalaya at satellite altitude where errors reach 30 mGal at $d \leq 8°$. But this relation between ψ and d is representative enough to be applied as a general idea.

As shown in the previous section, this condition depends strongly to the detail of the topography variation within and around the zone and also the altitude of the computation. In more detail, our results suggest three types of distributions for the relative truncation error at local scale (Figure 3.8),

- For Himalaya, errors $\sigma g(\psi_t, d) \geq 30$ mGal at satellite altitude and $\sigma g(\psi_t, d) \geq 5$ mGal for ground and airborne surveys are associated with truncation distances $\psi_t \leq$ 2°, mainly caused by the variation of the regional topography. To reduce this error, the truncation distance must be larger than the interstation distance ($\psi_t > d$).
- For the Pacific Ocean example, the smooth topography (bathymetry) surface results in relative truncation errors lower than 1 mGal with $\psi_t \leq 2°$. An exception for the result at satellite altitude, where the required truncation distance is 6.5° to ensure this precision.
- For the Southeast Pacific case, the presence of major structure in the vicinity (i.e. Andes Cordillera) obliges us to set apply the truncation distances ψ_t larger than 12°, 13°, and 15° to obtain errors ≤1 mGal for ground, airborne, and satellite surveys, respectively.

For applications at local scale, to make sure that the errors are less than 1 mGal, we suggest to use a truncation distance of 15°.

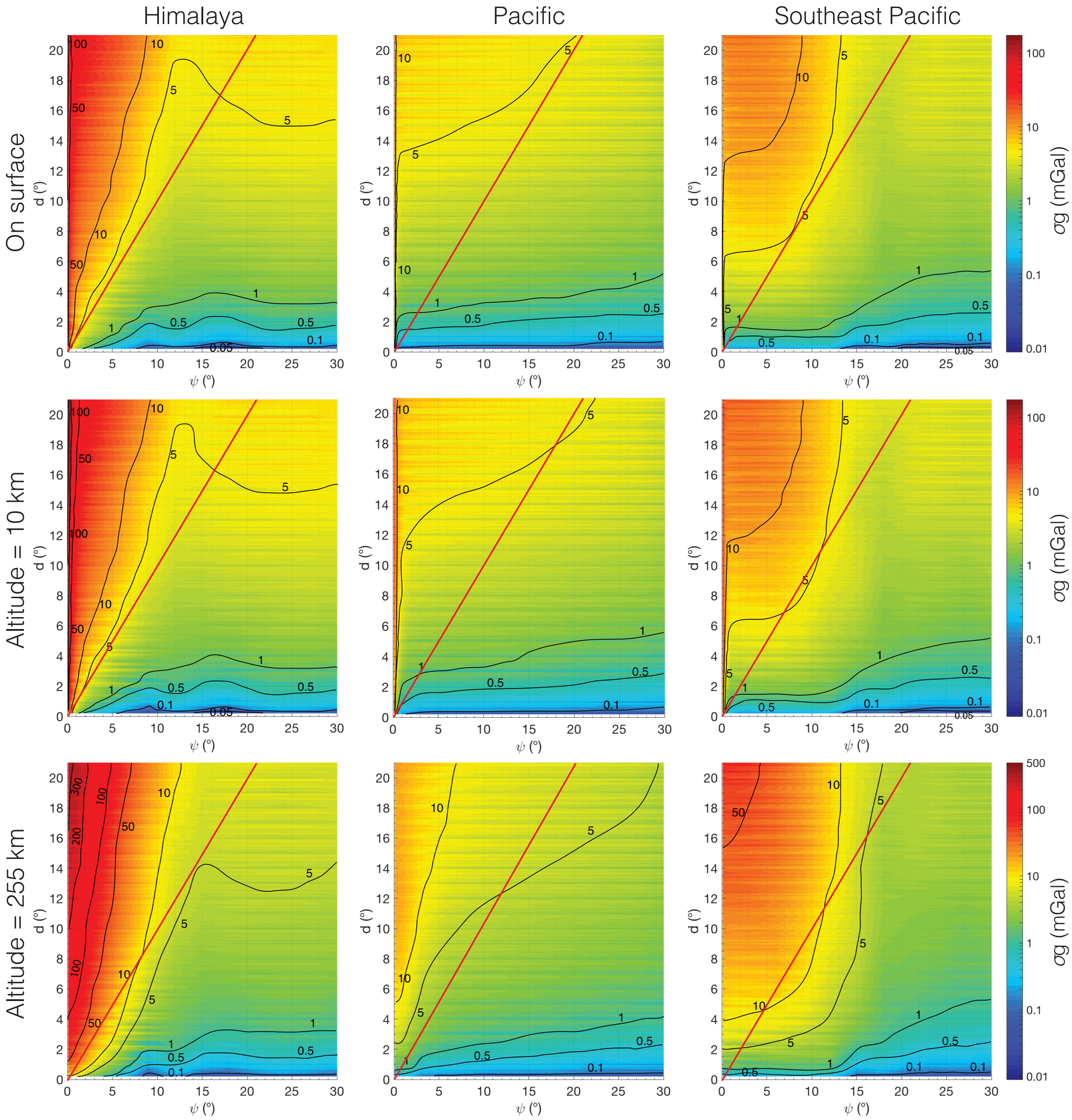

Figure 3.8: The difference in topography correction (differential error) $\sigma g(\psi_t, d)$ between to two points in the region, as a function of their distance d and the topography correction truncation ψ (cf. Figure 3.2), for Himalaya (left), Pacific (middle), and Southeast Pacific (left) zones at different altitude of acquisition, on the topography surface (top), at altitude 10 km (middle), and at altitude 255 km (bottom). The red line indicates a linear function $\psi_t = d$.

The effect of ignoring topography beyond a truncation distance ψ_t is more important as the increase of survey altitude, which demonstrates that far-field effects have a stronger influence on satellite altitude than on ground or airborne altitude (Szwillus et al., 2016). For example, Himalaya case requires a minimum truncation distance of 8.5°, 8.8°, and

12.5° to obtain errors ≤10 mGal at ground, mid-altitude, and satellite altitude, respectively. The presence of long topography wavelength around the Southern Pacific case necessitate to extent the minimum truncation distance to 8°, 8.5°, and 13° for ground, mid-altitude, and satellite altitude of surveys, respectively, to obtain 10 mGal of relative truncation errors. The required truncation distance to obtain 10 mGal of precision is summarized in Table 3.1. Errors of 10 mGal follow a quasi-linear combinations between d and ψ_t for all tested areas and at all tested altitudes.

The cases above are fixed with a precision of 10 mGal for regional case. We can expand the truncation distance ψ_t that have been mentioned above if we want to have a better precision. If the expected precision is few mGal, it will be necessary to include a whole global topography ($\psi_t = 180°$).

3.3.3.2. Relative gravity gradient truncation error

For relative gravity gradient truncation errors, the evaluation is done by using the precision of gradiometry at each measurement altitude as the threshold: 1 E for ground and mid-altitude surveys (see Chapter 1, Lane (2004),Jekeli (2013)) and 10 mE at satellite altitude (Rummel et al., 2011). The errors are decreasing as the measurement altitude increases since the observed gravity gradient is also decreasing as the increase of the measurement altitude (see Chapter 2 and Bouman et al. (2013)). The majority of errors variation for truncation distance ψ_t ≤40° is following a quasi-linear combinations between d and ψ_t (Figure 3.9).

The results in Figure 3.9 shows remarkable outcomes; for the estimation of topography effect in term of gravity gradient at ground and airborne altitudes with 1 E of precision, it can be fulfilled using $\psi_t \geq 8.5°$. For the estimation at satellite altitude, a precision of 10 mE can be achieved by using $\psi_t \geq 40°$.

The details of the minimum truncation distance ψ_t that is required for geodynamic applications at local and regional scale for all acquisition altitudes are given in Table 3.1.

Table 3.1: Estimated minimum truncation distance ψ_t in the assessment of topography contribution for geodynamic application at local and regional scales.

Scale	Region	Gravity			Gravity Gradient		
		Ground	Airborne	Satellite	Ground (1 E)	Airborne (1 E)	Satellite (10 mE)
Local (1 mGal) $d = 2°$	Himalaya	7°	7°	12.5°	2.75°	3°	4.5°
	Pacific	0.4°	1°	6.5°	0.75°	0.8°	9°
	Southeast Pacific	12.5°	13°	**15°**	0.8°	0.85°	17.5°
Regional (10 mGal) $d = 20°$	Himalaya	8.5°	8.8°	12.5°	7.5°	**8.5°**	**40°**
	Pacific	0.2°	0.5°	6°	1.6°	1.75°	39°
	Southeast Pacific	8°	8.5°	**13°**	6.5°	7°	35°

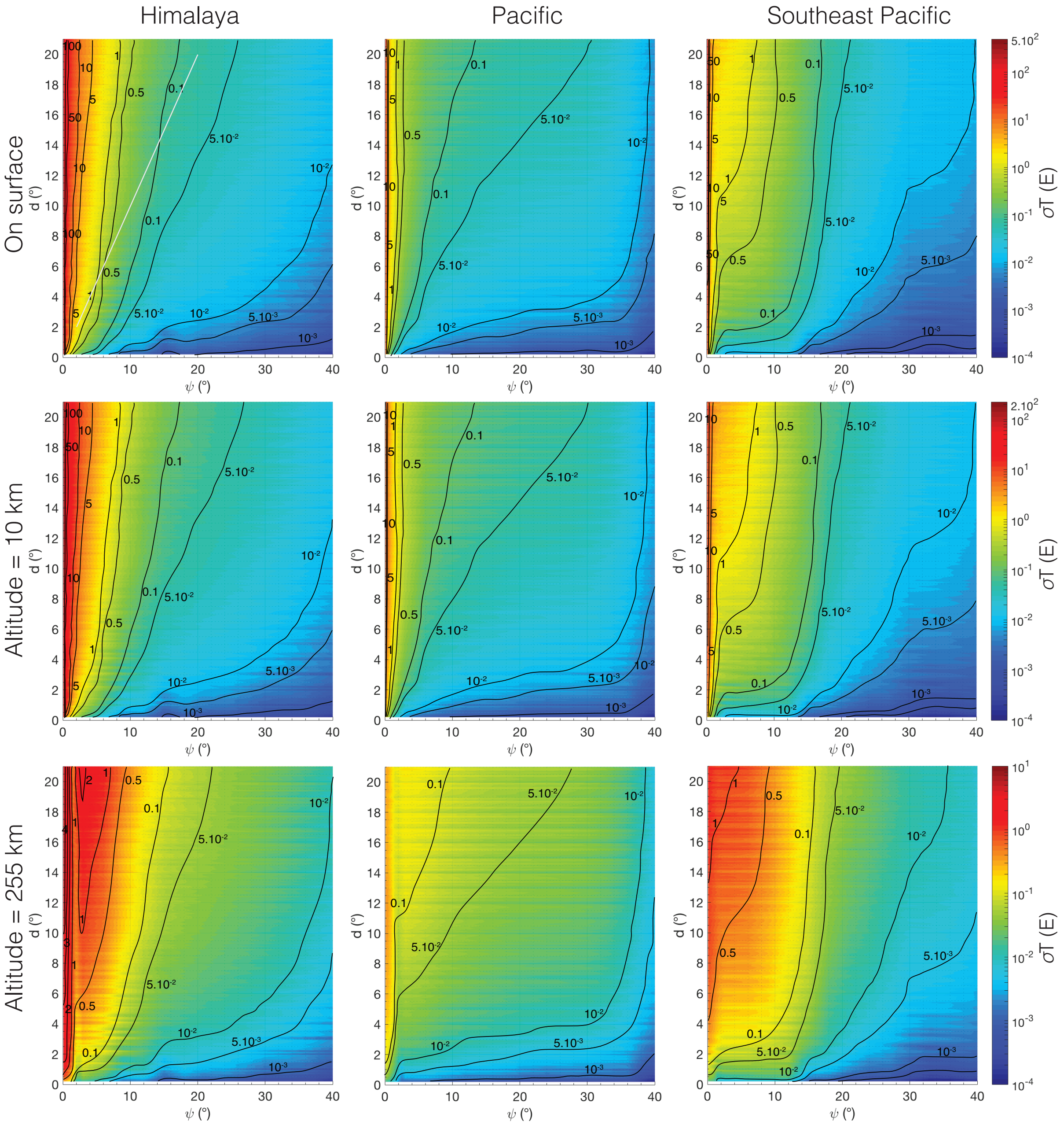

Figure 3.9: The difference in topography correction (differential error) $\sigma T(\psi_t, d)$ (in Eotvoš) between two points in the region, as a function of their distance d and the topography correction truncation ψ (cf. Figure 3.2), for Himalaya (left), Pacific (middle), and Southeast Pacific (left) zones at different altitude of acquisition, on the topography surface (top), at altitude 10 km (middle), and at altitude 255 km (bottom).

3.4. Discussion

The topographic contribution on ground surveys is classically calculated using the Bullard (1936) approach, that takes into account the effect of topography within a distance of 1.5° from measurements. However, as demonstrated in the previous section, this truncation distance is not adequate to be applied for current developments of gravity surveys, particularly for the application on a rugged region and/or at a large dimension of study area (larger than several tens of kilometers). Moreover, with the high accuracy of present gravimeters, it should be better if it is followed by a commensurate precision in gravity data processing. Like has been mentioned in the previous section, the results exhibit that a truncation distance ψ_t of 15° is suggested to ensure the relative truncation error is less than 1 mGal.

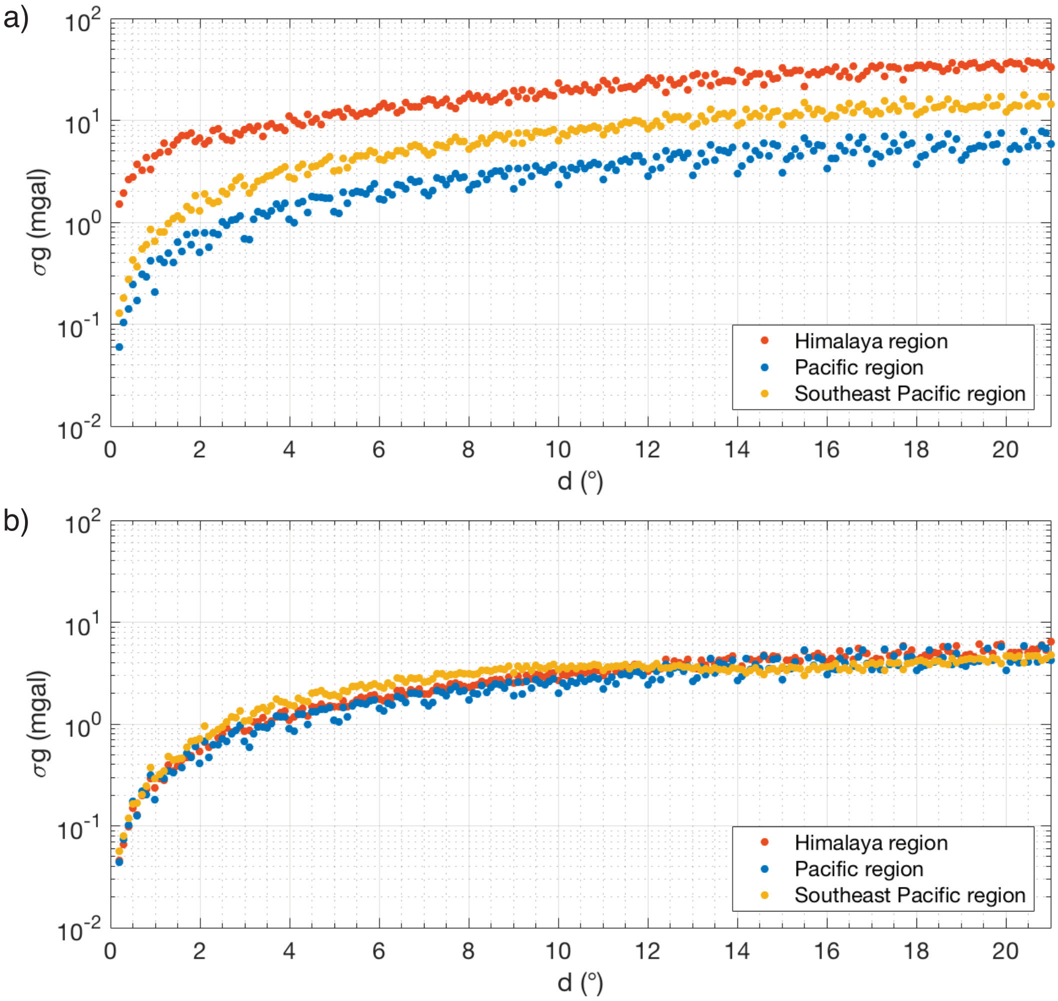

Figure 3.10: Differential error in the topography gravity corrections ($\sigma g(\psi_t, d)$) as a function of the extent of the survey zone (d) for topography corrections truncated at $\psi_t = 1.5°$ (a) and $\psi_t = 15°$ (b) for the Himalayan (red dots), Pacific (blue dots), and Southeast Pacific (yellow dots) regions.

Figure 3.10a shows the relative truncation error as a function of the interstation distance for the standard truncation distance of 1.5°. In the case of the Himalayan strong topography variations, the average error quickly rises above a few mGal for relatively short interstation distances (ca. 1° or 111 km). Average errors up to 40 mGal can be reached for interstation distances over ca. 15°. The smooth topography of the Pacific zone gives lower errors from 0.06 mGal to 10 mGal. The Southeast Pacific case with the presence of major structure in the vicinity of the zone gives errors from 0.1 mGal to 22 mGal. In comparison with the standard 1.5°, a truncation distance of $\psi_t = 15°$ significantly reduces the relative truncation errors in three example regions (Figure 3.10b). The average errors remain below ca. 10 mGal for all distances, and drop to less than 1 mGal for the common dimension of local ground-based surveys ($d \leq 2°$).

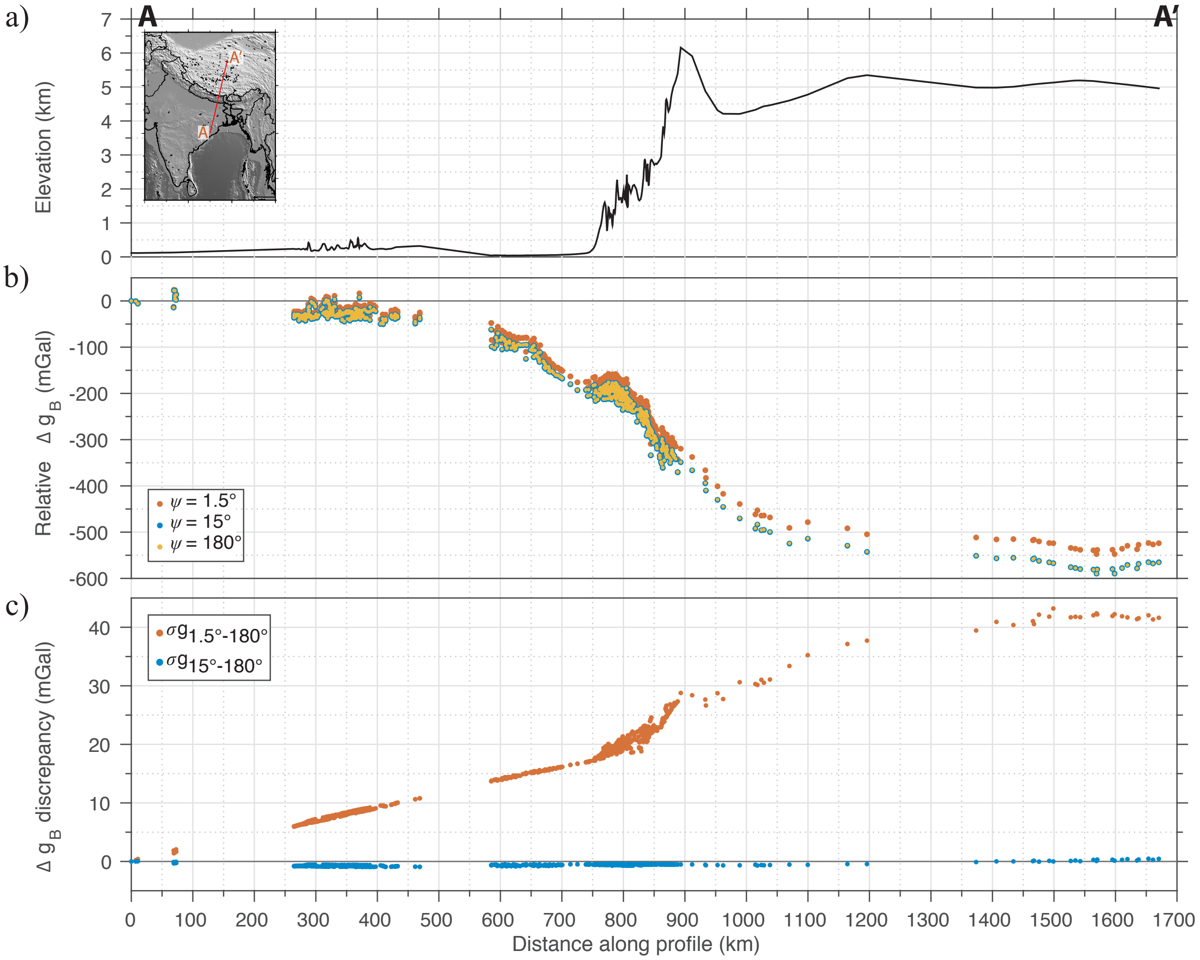

Figure 3.11: Example of the effect of the topography correction truncation along an India - Himalaya - Tibet profile (Berthet et al., 2013). (a) Topography along the profile (cf. insert). (b) Bouguer anomaly, relative to the point at distance 0 km, after terrain corrections with truncation distances $\psi_t = 1.5°$ (red), $\psi_t = 15°$ (blue), and $\psi_t = 180°$ (global topography, yellow). (c) Differences in Bouguer anomaly (i.e., differences in topography corrections) between $\psi_t = 1.5°$ and $\psi_t = 180°$ (red dots) and $\psi_t = 15°$ and $\psi_t = 180°$ (blue dots).

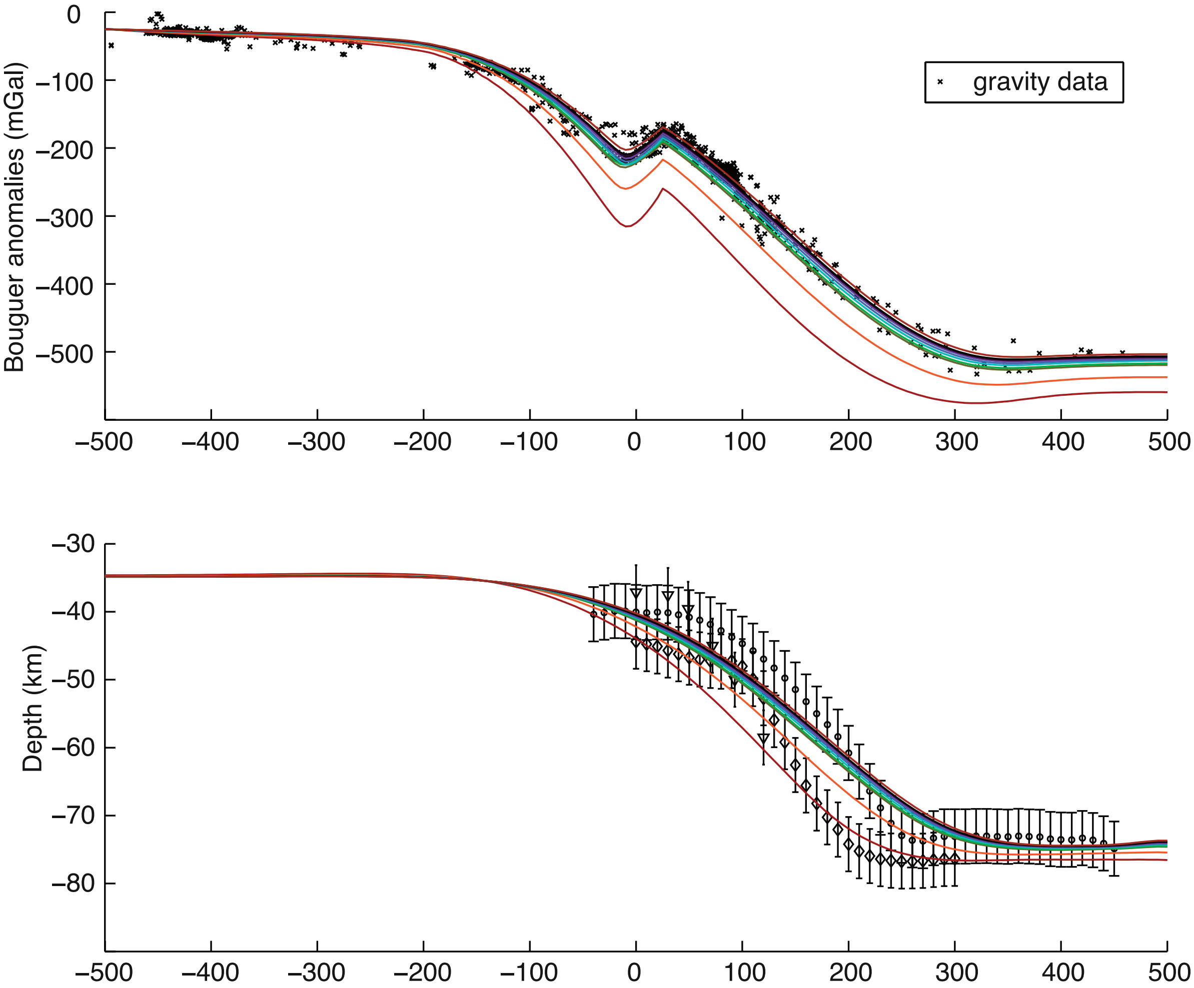

Figure 3.12: The variation of Bouguer anomaly (top) and its associated Moho geometries model (bottom), extracted from Berthet et al. (2013) as an example of the misinterpretation due to the relative errors in terrain corrections.

This effect is illustrated on a gravity anomaly profile across India - eastern Nepal - China used to assess the Indian Plate geometry beneath the Himalayas (Berthet et al., 2013). We use uncorrected gravity data (Bureau Gravimétrique International - BGI database, Sun, 1989; Cattin et al., 2001; Tiwari et al., 2006; Berthet et al., 2013) to compute Bouguer anomalies for three truncation distances of 1.5° (standard correction), 15°, and 180° (global correction). The Bouguer anomalies are translated to an arbitrary reference at the profile origin to analyse the relative variations (Figure 3.11b). Compared to the global correction, Bouguer anomalies based on the standard $\psi_t = 1.5°$ show deviations up to 45 mGal over the profile length (1700 km). Such long wavelength error can result in misinterpretation of about ten of kilometres in the geometry of the underthrusted Indian Plate and its effective elastic thickness (see Berthet et al., 2013) (Figure 3.12). In contrast, the topography reduction using a truncation distance of 15° yields relative errors smaller than 1 mGal along the whole profile (Figure 3.11c).

Our results demonstrate that a global correction of the topography effect is not required for ground-based relative gravity surveys for local and regional geodynamic applications, but the standard correction distance of 1.5° can lead to significant errors and misinterpretations. We then favour the use of a truncation distance $\psi_t = 15°$ to ensure a precision of 1 mGal in relative regional studies.

Considering that the roughness of topography is not homogeneous over the Earth's surface, it seems difficult to define a general solution to deal with the topography truncation distance. For gravity gradiometry, an algorithm based on a geostatistical analysis of the local topography by Jekeli (2013) could be an interesting method to tackle this problem. Nevertheless, this method seems to underestimate the far-field topographic effect. For example, on a rugged topography zone with the points separated at 50 km, Jekeli (2013) suggests $\psi_t \geq 0.43°$ to obtain a relative error less than 1 E, which is much smaller than the ψ_t derived from this study ($\psi_t \geq 1.5°$). For our result in the Pacific region, a truncation distance of 0.4° (~44 km) is needed to obtain the same relative error.

3.5. Conclusion and Perspective

Estimation of gravitational effects due to the variation of Earth topography is essential in gravity data analysis. This chapter underlines the importance of the optimum topography truncation distance as an essential parameter to assess topography effect for gravity and gravity gradient application in geodynamics at local, regional, and global scale.

This study confirmed that the precision in estimating the gravitational effect of Earth topography is mostly controlled by the truncation distance over which the topography is considered. The relation among relative errors, dimension of a study area, and the extent of topography is complex due to the irregularities of topography variations on the Earth surface. But by quantifying the relative truncation errors from end-members regions in terms of topography roughness: the Himalaya region with strong topography roughness and the Pacific region with smooth topography roughness and also a region on the Southeast Pacific that represents a zone with smooth topography within the zone but is completed with major topography structures in the vicinity, this study allows to create a guideline to determine the optimal truncation distance as a function of study scale.

From the tests that have been performed in this study, we show that:

- For the application of gravity or gravity gradients using the **absolute value of gravity-related field variation** that require a high precision (i.e. better than 1 mGal), the estimation of topography must be done using **global topography** ($\psi_t = 180°$). This type of application is widely used in the application of satellite gravity field observations.
- For the application at **global scale**, the computation of topography effect must be done by considering the **global topography**.
- In general, the use of truncation distance that is equal with the dimension of a zone

($\psi_t = d$) ensures precision in the range of 1-10 mGal (Figure 3.13). It is sure that the variations of errors are specific for each zone and at each altitude of computation. But this relation is representative enough to be applied as a general idea.

- At regional scale of gravity application ($d \leq 20°$), the use of $\psi_t = 15°$ ensure the gravity relative error less than 1 mGal at all tested altitudes.
- For topography effect in term of gravity gradient at regional scale, using the accuracy of the instruments as the threshold (1 E for the measurement on ground and airborne surveys and 0.01 E for satellite observations), the precision of 1 E on ground and airborne survey altitude can be obtained by using a truncation distance $\psi_t = 8.5°$. Whilst for topography effect at satellite altitude with a precision of 0.01 E, it can be obtained using $\psi_t = 40°$.

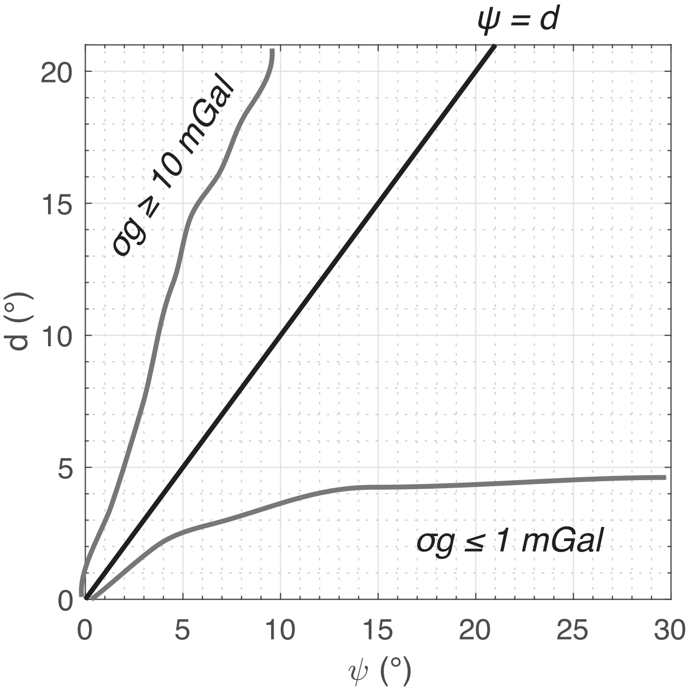

Figure 3.13: Distribution of relative gravity errors σg due to neglecting the effect of topography beyond truncation distance ψ as a function of dimension of the zone d. The use of $\psi = d$ ensure the precision between 1 and 10 mGal for application at regional scale.

The roughness of local topography and the presence of major structures around the zone play a major effect to define the optimum topography extent. A systematic study to estimate the optimum topography extent as a function of topography roughness seems to be important to be developed. By using a synthetic topography with a controlled topography roughness, a direct relation among the scale of study, topography roughness, and altitude of measurement and the associate relative errors could be obtained.

Chapter 4

Detailed Subduction Slab Geometry, What is Really Constrained from GOCE Observations?

4.1. Introduction

Subduction zone is one of the most interesting geological objects in our planet where intensives geodynamic process occur. Over the past decades, tremendous advances to explain the structures at depth have been gained from seismological, geochemical and geological data interpretation, mineral physics experiments and numerical modelling. The seismic tomography provides an image of the global three-dimensional internal structure through maps of fast and slow seismic anomalies, which delineate the geometry of plates sinking into the mantle (cf. Obayashi et al., 2009; Koulakov et al., 2011; Zhao et al., 2012). However, converting seismic velocities into densities is not straightforward, as it depends on temperature and chemical composition and are strongly affected by phase changes that influencing each other (Karato and Karki, 2001). Hence, we need further information to interpret the seismic signal in terms of density variations versus other physical processes.

The Gravity field and steady-state Ocean Circulation Explorer (GOCE) aimed to determine the static gravity field of the Earth (Rummel et al., 2002; Johannessen et al., 2003). GOCE gravity gradients have already been used for various regional applications (cf. Fuchs et al., 2013; Bouman et al., 2014; Alvarez et al., 2015; Cadio et al., 2016) as well as in global scale (cf. Panet et al., 2014). Since GOCE gravity gradients is sensitive to mass variation in 3D, it can be an efficient tool to characterize the geometry of a slab that can provide new insights with respect to traditional seismic and tomographic models.

One of the major challenges of modern Earth sciences is the understanding the geometry of the subduction, that is important in the studies of seismic hazard (e.g., Zhao et al., 2017; Gao, 2018). GOCE have been successfully used to illustrate the presence subducting lithosphere, like have been presented by Panet et al. (2014). Beyond detecting the presence of a slab, there is an open question about whether GOCE observations are capable of explaining the geometry of a slab in more detailed.

This study is performed to investigate the degree of constraint that can be brought by GOCE observations on the geometry of a subducting slab, including its density distribution, borders, dip angle, its lateral variation, and the evidence of slab tear. The investigations are started using synthetic models to provide preliminary insights for further investigations in the Izu-Bonin-Mariana (IBM) zone as the study area. All calculations in this investigation are performed using GEEC.

This chapter presents as the following:

- First, I present the processes in the first approach using synthetic slab models to give preliminary insights about the gravity gradients signatures related to the detailed structure of a slab, seen at satellite altitude. I apply GEEC to calculate the gravity gradient effects of given mass bodies that contain specific imposed geometry properties, including the variations on density distribution, dip angle, and its lateral variation. The gravity gradients due to the variation of slab dimensions and the modelled slab tear are also assessed.
- Then, the obtained results using synthetic models are presented. The estimations of which properties of detailed slab geometry that are theoretically detectable by GOCE observations are described. These results are used as the benchmark for the analysis of the real GOCE observations on the IBM zone.
- The properties of the used datasets, including the GOCE observations and the bathymetry as well as the crustal model, are presented. Details about GOCE data corrections applied in this study are also described.
- The confrontations of the results from synthetic modelling and the others obtained from GOCE data processing on the IBM case are then explained.
- The discussion about the detailed properties of slab geometry that can be constrained by GOCE observations are presented. It is then followed by the discussion about the requirement in global crustal dataset that can be used to assess properly the detailed structure of slab geometry.

4.2. Synthetic modeling

Gravity gradients signal over a subduction zone is often not straightforward to be deciphered. The existence of various structures in the zone together may create an intricate spatial distribution of gravity gradients within the zone. Therefore, before applying into a real subduction case as IBM, some test scenarios using several synthetic models of slab are performed to provide preliminary insights into the gravity gradients signal due to the slab's excess weight and to evaluate the associated signals to the geometry of the slab: its borders and the variation of the subduction angle. The computations using these synthetic models are performed at the altitude of 255 km, similar to the mean altitude of GOCE (Rummel et al., 2011).

As explained above, the Izu-Bonin-Mariana (IBM) subduction system will be used as a study case. Therefore, in the followings, the dimension of the synthetic slab model is adapted to the dimension of the IBM subduction. The dimension of the subducting slab (Figure 4.1) is extending 10° from X = 0° to to the south and 45° to the north to simulate the continuation of the subduction to the Kuril-Kamchatka subduction system in the north.

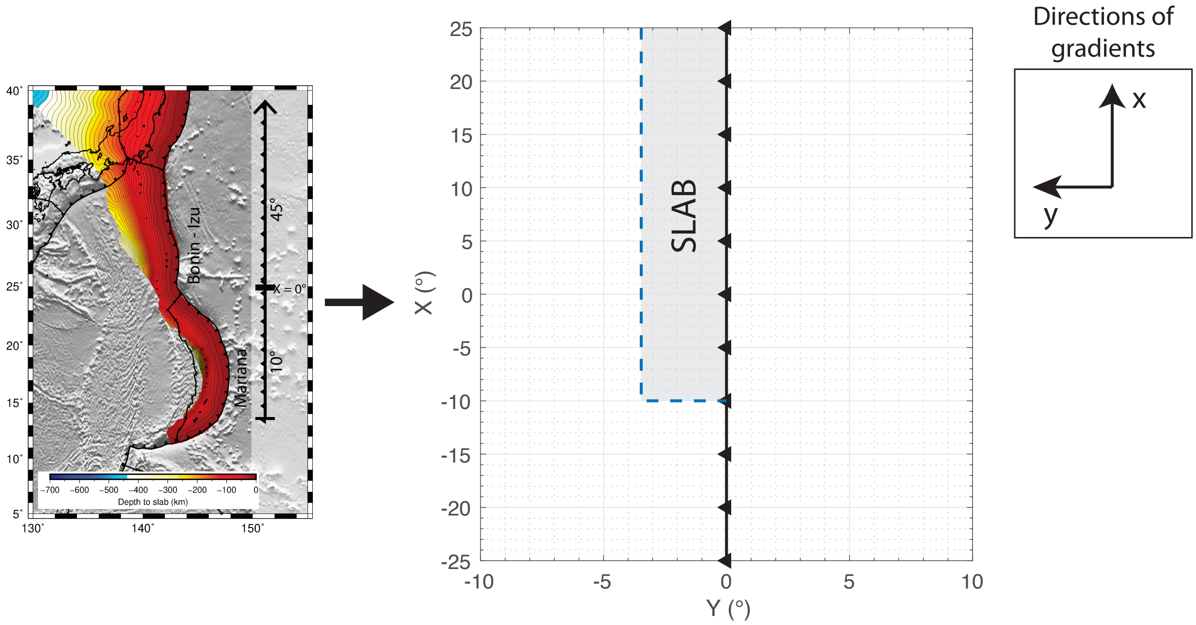

Figure 4.1: Reference for the dimensions of the synthetic slab adapted to the IBM case, with 10° on the south part and 45° on the north part (from X=0°). The contours in the left figure show the depth of the slab interface, after Hayes et al. (2012). The trench is marked with triangled line and the border of the slab is shown with the dashed line. The direction of gravity gradients is shown in the right figure.

Before I present the results from synthetic modelling, please note that the x-direction is positive to the north, which is parallel to the modelled trench. The y-direction is positive westward, which is perpendicular to the modelled trench. The z-direction is upward. In general, each component of gravity gradients is unique and sensitive to:

- T_{xx} is sensitive to west-east structure orientation
- T_{xy} is sensitive to the corners of structures
- T_{xz} is sensitive to lateral variations of structures with west-east orientation
- $T_{yy}$is sensitive to north-south structure orientation
- T_{xz} is sensitive to lateral variations of structures with north-south orientation
- T_{zz} is sensitive to radial variations

The details of each component's characteristics can be found in Chapter 1 Section 1.3.

4.2.1. Density Distributions of Slab Model

The interface of the slab models lies in a depth of 3 km below the surface (depth = 0 km) with 100 km thick and 700 km long. The slab as the source of the anomaly is divided into several finite mass bodies, including lithospheric mantle in the asthenosphere layer, oceanic crust body in the lithospheric mantle, and a chunk of oceanic crust in the asthenosphere layer, symbolized as A, B, and C in the Figure 4.2, respectively. The applied density anomaly $\Delta\rho$ is $\Delta\rho_A = +80$ kg m^{-3} for the layer A, $\Delta\rho_B = -500$ kg m^{-3} for the layer B, and $\Delta\rho_C = -420$ kg m^{-3} for the layer C. Those bodies are integrated differently on each model. On the first model, the simplest model, the only source of the anomaly is the subducting lithospheric mantle in the asthenosphere layer (Figure 4.2a). The presence of the oceanic crust with a thickness of 7 km in the lithospheric mantle as a source of anomaly is integrated in the second model (Figure 4.2b). In the third model, the subducting oceanic crust is assumed to dive into the asthenospheric layer (Figure 4.2c). Those models are performed to find the closest "naive" slab model for later than be adapted into the real case. All calculations of slab synthetic models are performed using GEEC. The parameters for spherical approximation is following GOCE's reference ellipsoid (see Section 4.3.2. and Table 1.1 in Chapter 1).

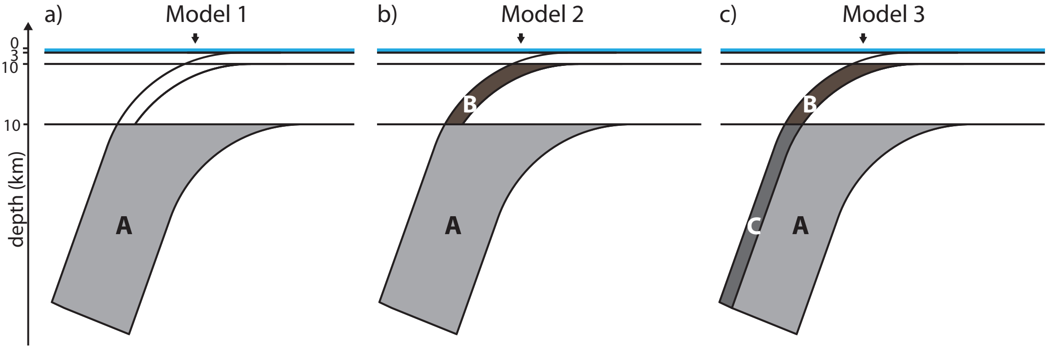

Figure 4.2: Schematic representation of the "naive models" of subducting plate. The small triangle indicates approximately the location of the trench.

Here, I assume a slab geometry with a constant dip θ of 55°, applies to all three models (Figure 4.2). The obtained gravity gradients are shown in Figure 4.3 (Slab model 1 - Figure 4.3 left, model 2 - Figure 4.3 middle, and model 3 - Figure 4.3 right).

According to the models considered, the calculated of gravity gradients show large differences. Unsurprisingly the highest amplitudes of gravity gradients in all components are obtained with model 1, because only a positive density contrast that is considered (Table 4.1). The integration of oceanic crust layer(s) with negative density contrast in the model 2 and 3 causes the diminution of the signal. The presence of oceanic crust in the lithospheric layer reduce the T_{yy} and T_{zz} signal up to ~650 mE (compare result from model 1 and model 2). The presence of oceanic crust in the asthenospheric layer adds the diminution up to ~600 mE also in T_{yy} and T_{zz}. More interestingly are the results show that negative density contrast that is related for oceanic crust generates short wavelength signals on the both sides of the trench (Figure 4.3, model 2 and 3).

The anomalies in T_{xy} and T_{xz} components could be related to the southern border of the slab. The signal due to the slab edge is described in more detail in Section 4.2.4.

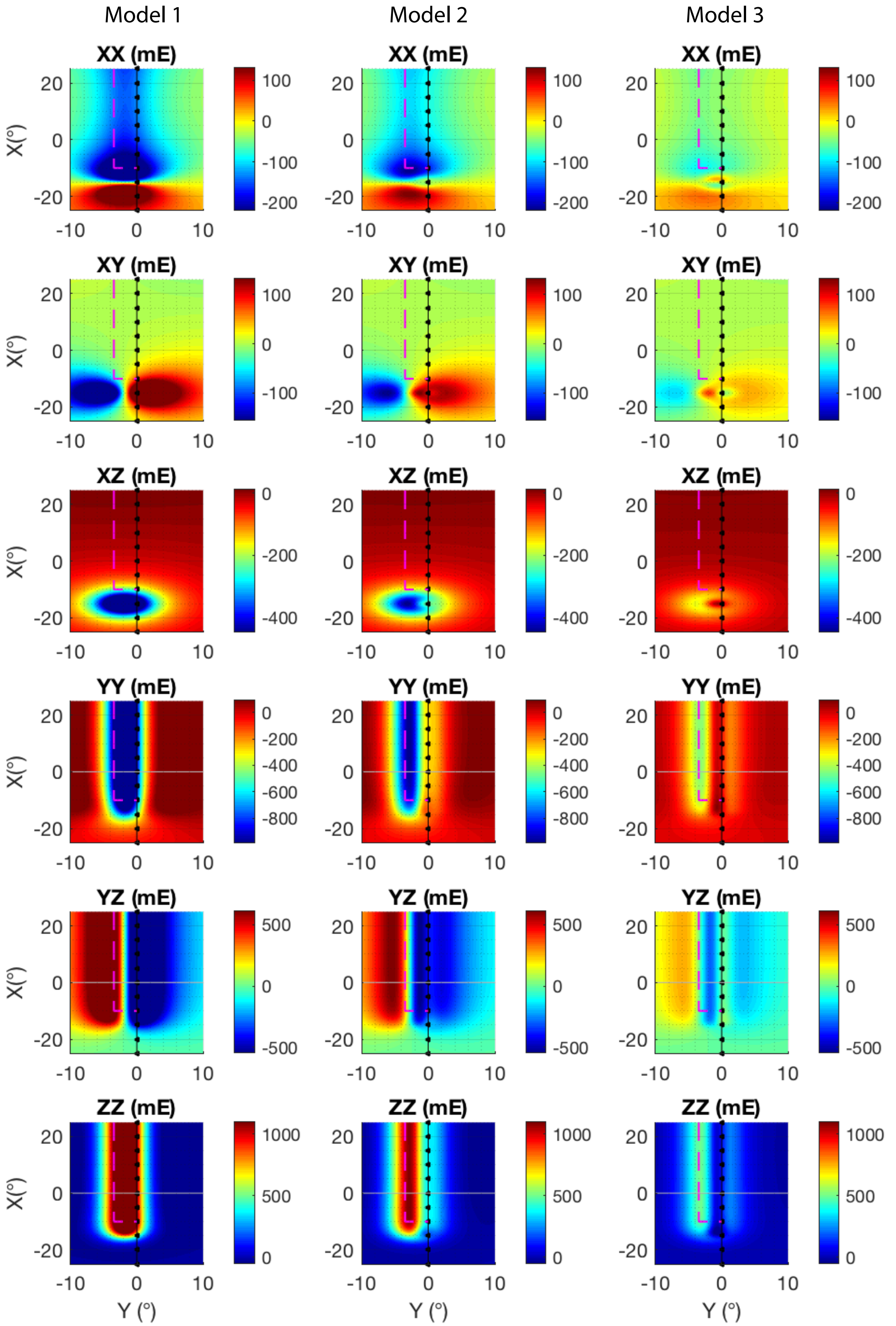

Figure 4.3: Gravity gradients response (in mE) of the synthetic slab model 1 (left), model 2 (middle), and model 3 (right) at 255 km of altitude. The triangle-line indicates the location of the trench. The dashed line show the border of the slab.

In in Figure 4.4, I present the value of components T_{zz}, T_{yy}, and T_{yz} of Figure 4.3 along a profile perpendicular to the trench (along the Y axis) (gray line in Figure 4.3) that exhibit the most remarkable signal variation comparing to the other components. The position of the peak in T_{zz} and T_{yy} may indicate the position of the center of the mass. Whilst in T_{yz}, the peaks may indicate the termination of a slab. However, it is quite difficult to be deduced. The termination of the slab is located at hundreds of kilometers depth, hence the wavelength of the resulted signal too long to be interpreted.

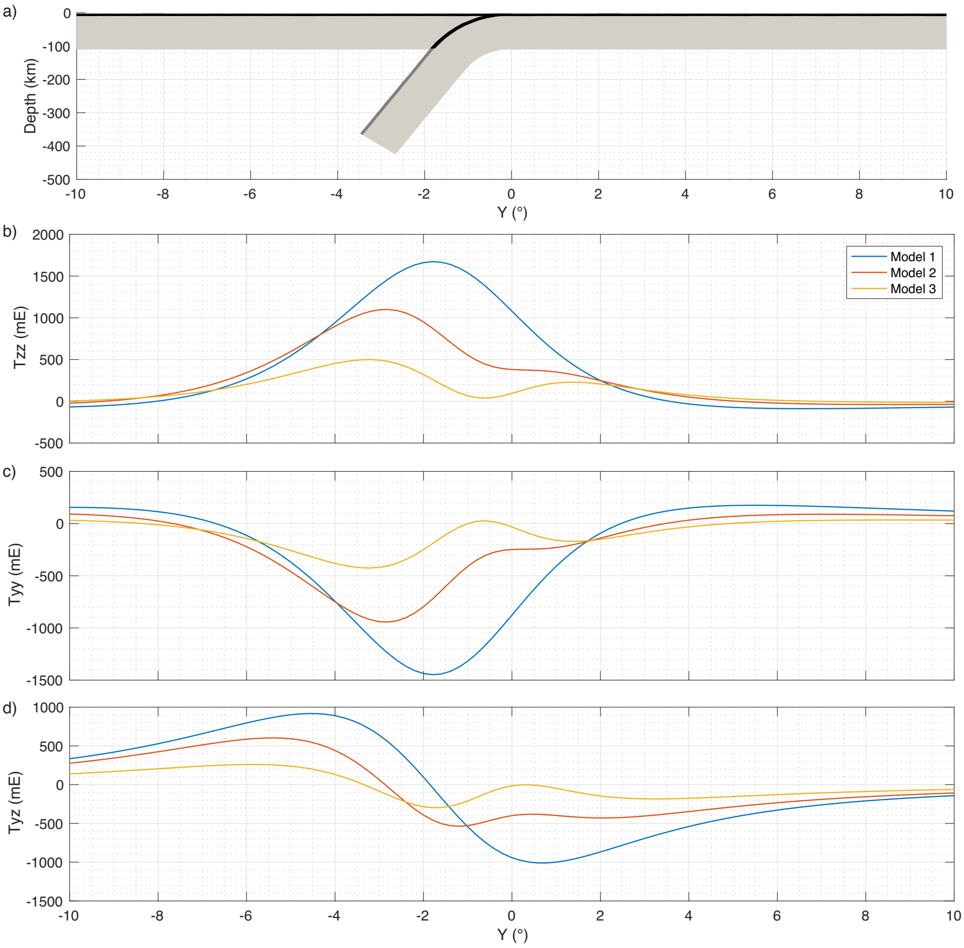

Figure 4.4: Variation of T_{zz}, T_{yy}, and T_{yz} of a profile perpendicular to the trench (along Y-axis) of different slab models (see Figure 4.2). The location of the profile is indicated with gray line in Figure 4.3.

As shown in Figure 4.4, the first model results in a single positive peak along the profile of T_{zz} and a negative trough for T_{yy}. When crustal layer is taken into account as in the case of the model 2 and model 3, its negative effect creates a through along the profile of Tzz and a crest for T_{yy} with a wavelength $\sim$4°with $\sim$250-300 mE of amplitude. These wavelength and amplitude of the oscillation are superior to the highest spatial resolution and precision of GOCE, 100 km and 10 mE, respectively. Therefore, these signal properties are theoretically detectable by GOCE. Since the location of the center of the anomalous mass is shifted, the location of the crest on T_{zz} profile (the trough for T_{yy}) is also shifted $\sim$1° away from the trench.

Table 4.1: Extremity of signal amplitude of each slab model of the profiles in Figure 4.4.

Component	Max. Amplitude (mE)		
	Model 1	Model 2	Model 3
T_{zz}	1673	1100	499
T_{yy}	-1448	-943	-425
T_{yz}	916	602	260

For T_{yz}, the slab model 1 creates a simple long wavelength along the profile perpendicular to the trench. While for the model 2 and model 3, the variation from a positive to a negative anomalous mass along the profile leads to a double oscillations with a wavelength of ∼4°and ∼250-300 mE of amplitude in T_{zz} and T_{yy}. The maximum amplitude along the profiles of each component in Figure 4.4 are given in Table 4.1.

In the following, we assume that model 1 is too simple to mimic the reality properly. Thus we only consider models 2 and 3 to study the effect of slab geometry that is reflected in gravity gradients.

Summary:

- The excess mass related to a slab produces a positive signal in T_{zz} and negative in T_{yy} with a magnitude greater than 500 mE and a total wavelength of ∼8° perpendicular to the trench. Thus, the presence of the slab is detectable by GOCE.
- Gravity gradients are sensitive enough to the distribution of anomalous density in the slab. The oscillation is produced due to the presence of negative anomalous body, that is related to the oceanic crust in the upper mantle, with a wavelength ∼4°. The presence of negative density contrast in the astenopheric layer reduces T_{zz} up to 600 mE.

4.2.2. Gravity gradients response to the dip variation

The variation of subduction angle or dip of the slab can lead to signal variations, both in the spatial distribution and its amplitude. For the comparison, here I calculate the gravity gradients correspond to the effect of a slab with a constant dip 45°, 55°, 60°, 80°, and 85°. Figure 4.5 shows the variation of T_{zz}, T_{yy}, and T_{yz} along the same profile. The results from each tested dip are displayed with different line colors.

Our results suggest that a dip angle variation from 45° to 85° can lead to a gradient change up to ∼200 mE in T_{zz} and T_{yy} components. A steeper slab produces weaker gravity gradients (see Table 4.2). It could be related to the position of the anomalous mass, a slab with a small dip is located closer to the surface. This can also be explained by the distance between the slab with respect to the measurement position.

However, it is difficult if we estimate a small dip variation. For example, with 5° of variation, the variation produced in T_{zz} is "only" ∼30 mE. By considering the noise in the observation, this signal variation can be in the limit of detection. However, if we have a larger dip variation, e.g. 10°, the variation in T_{zz} can reach ∼75 mE, that has a bigger

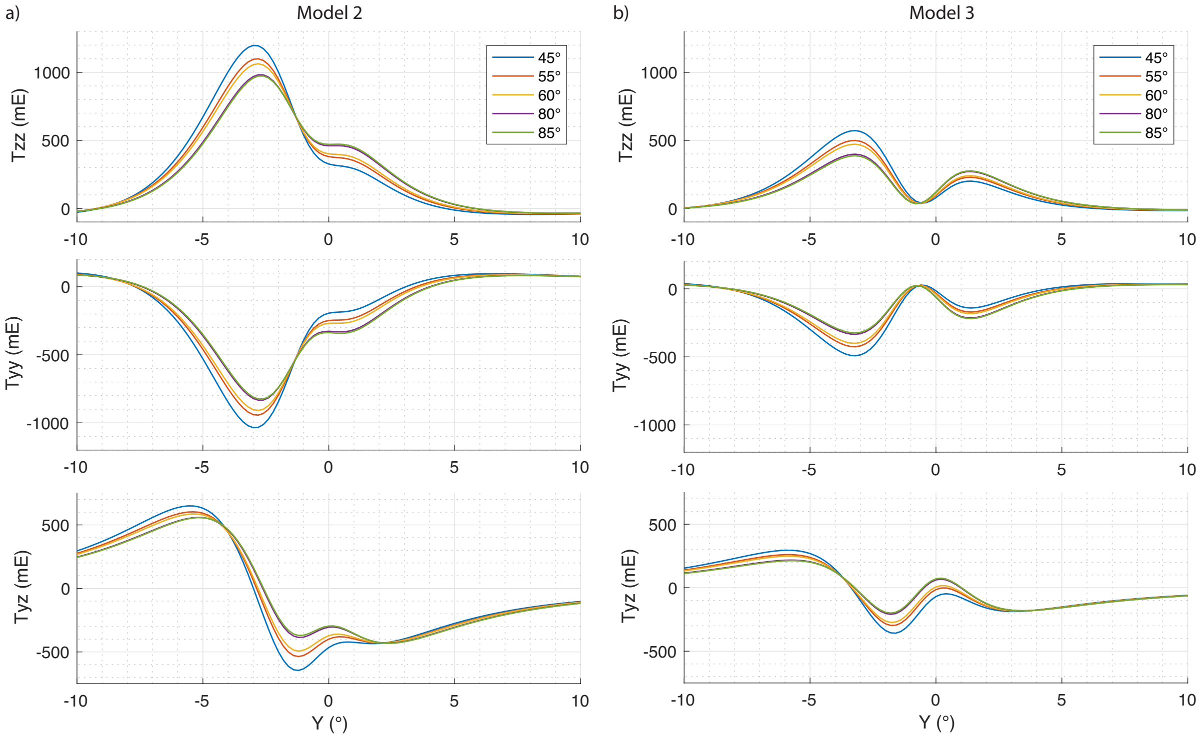

Figure 4.5: Profile as a function of the subduction angle, shown by the different colors, in T_{zz}, T_{yy}, and T_{yz} along the profile at X=0 of the slab model 2 (a) and model 3 (b).

chance to be detected in GOCE observations.

The variation of the dip also affects the geometry of the anomalous mass; the steeper the dip of a slab is, the closer the termination of a slab is to the trench. This observation is illustrated by the shift of the positive peak of T_{yz} toward the trench. However, this shift is small enough ($\sim 0.5°$), even with a comparison between angle dip 45°and 85°.

Summary:

- The variation of gravity gradients associated to the variation of dip $\geq$10° is possible to be detected in GOCE observation, with a magnitude of $\geq$75 mE. Any dip variations with $\Delta\theta \leq$10° produces a weak enough T_{zz} variations (e.g., $\sim$30 mE for $\Delta\theta = 5°$) that could lead to any misinterpretation if we consider also the noise in the data.

4.2.3. Gravity gradients response to the lateral variation of dipping angle

In the following study, the variation of the gravity gradients due to a lateral variation of the subduction angle is tested. In a case where there is an abrupt change of the dip parallel to the trench, a slab tearing could be happened. First, to avoid the effect due to the limit of the slab, the dimension of synthetic slab model is then set to be 45° of length

Table 4.2: Maximum amplitude of T_{zz} resulted from the variation of subduction dip of slab model 2 and 3.

Component	Dip (°)	Max. Amplitude (mE)	
		Model 2	Model 3
T_{zz}	45	1198	572
	55	1100	499
	60	1063	472
	80	982	398
	85	973	387
T_{yy}	45	-1035	-492
	55	-943	-425
	60	-909	-400
	80	-833	-334
	85	-825	-324
T_{yz}	45	650	295
	55	603	260
	60	587	248
	80	559	217
	85	557	213

of both sides of the "slab tear".

For the case of IBM slab, some studies have shown that there is a dip variation parallel to the trench (cf. Stern et al., 2004; Cruciani et al., 2005; Miller et al., 2005; Oakley et al., 2008; Jaxybulatov et al., 2013). Here, following Cruciani et al. (2005), I consider a dip angle along Izu-Bonin is ~55° and along Mariana slab is ~85° (Figure 4.6). The abrupt change of subduction angle is located at X=0°. Here, I use, as a reference, a model with a constant dip angle of 85°, where there is no lateral variation of subduction angle. Another test using a dip variation 85°-45° is also performed to see the gravity gradients effect where the lateral variation of the subduction angle is larger.

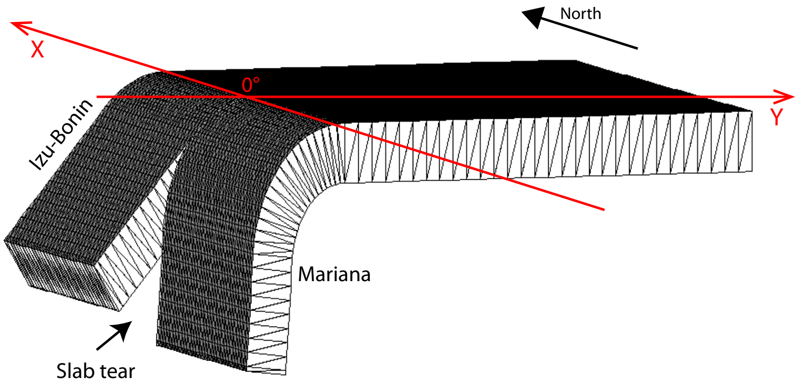

Figure 4.6: A 3D model of slab tear scheme due to an abrupt change of subduction angle for the case of IBM subduction.

The six components of gravity gradients calculated at the satellite altitude (255 km) is shown in Figure 4.7, using slab model 2 (a) and slab model 3 (b), with a dip variation of 85°-85° (left) as the reference, 85°-55° (middle), and 85°-45° (right). I present also the results of each component of gravity gradient along a X-profile parallel to the trench (Figure 4.8) that is indicated in the white line in Figure 4.7.

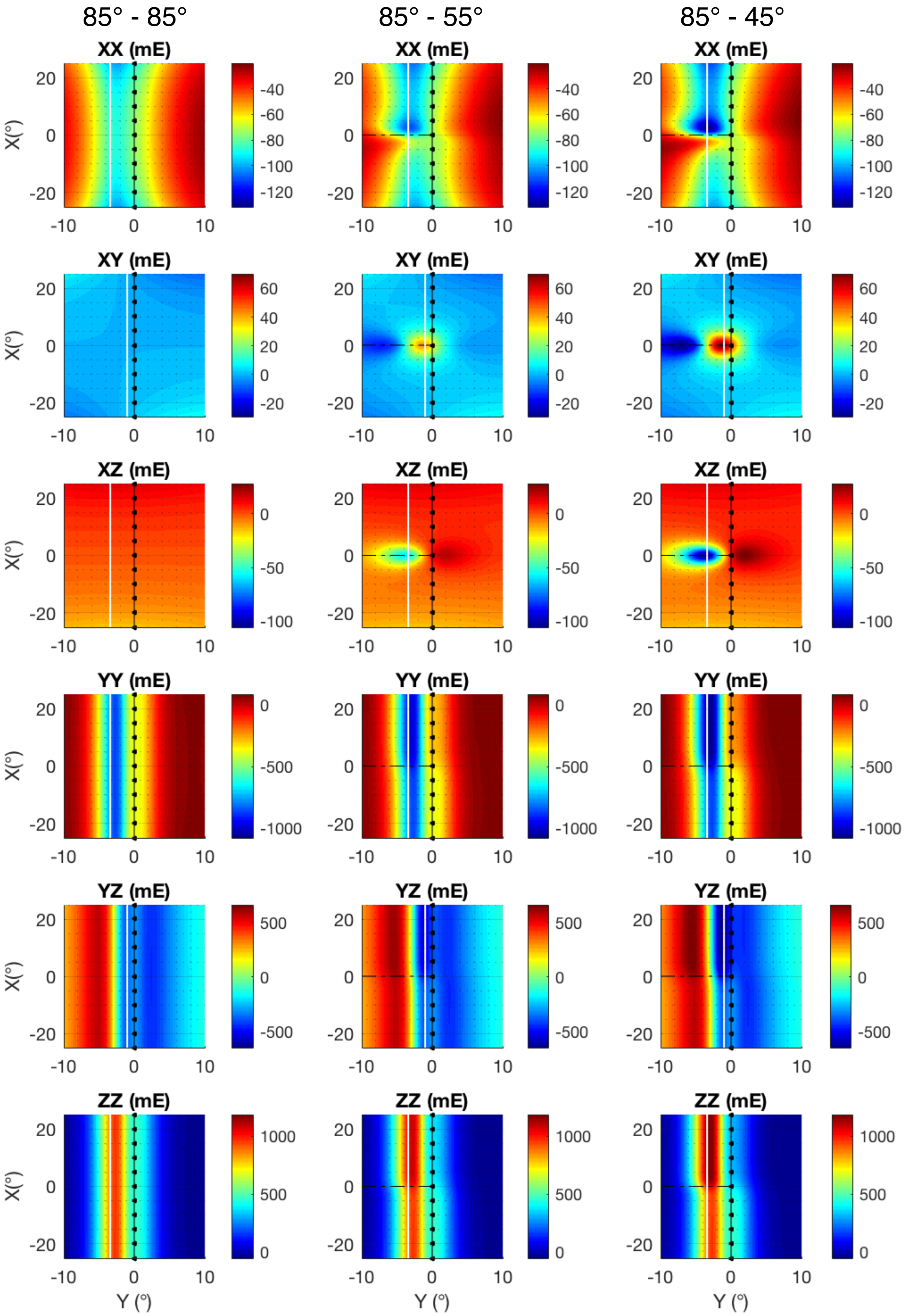

Figure 4.7a: Gravity gradients effect of slab model 2 using an infinite dimension of a slab (45°-45° on the both sides), with a lateral dip variation of 85° - 85° (left), 85° - 55° (middle), and 85° - 45° (right).

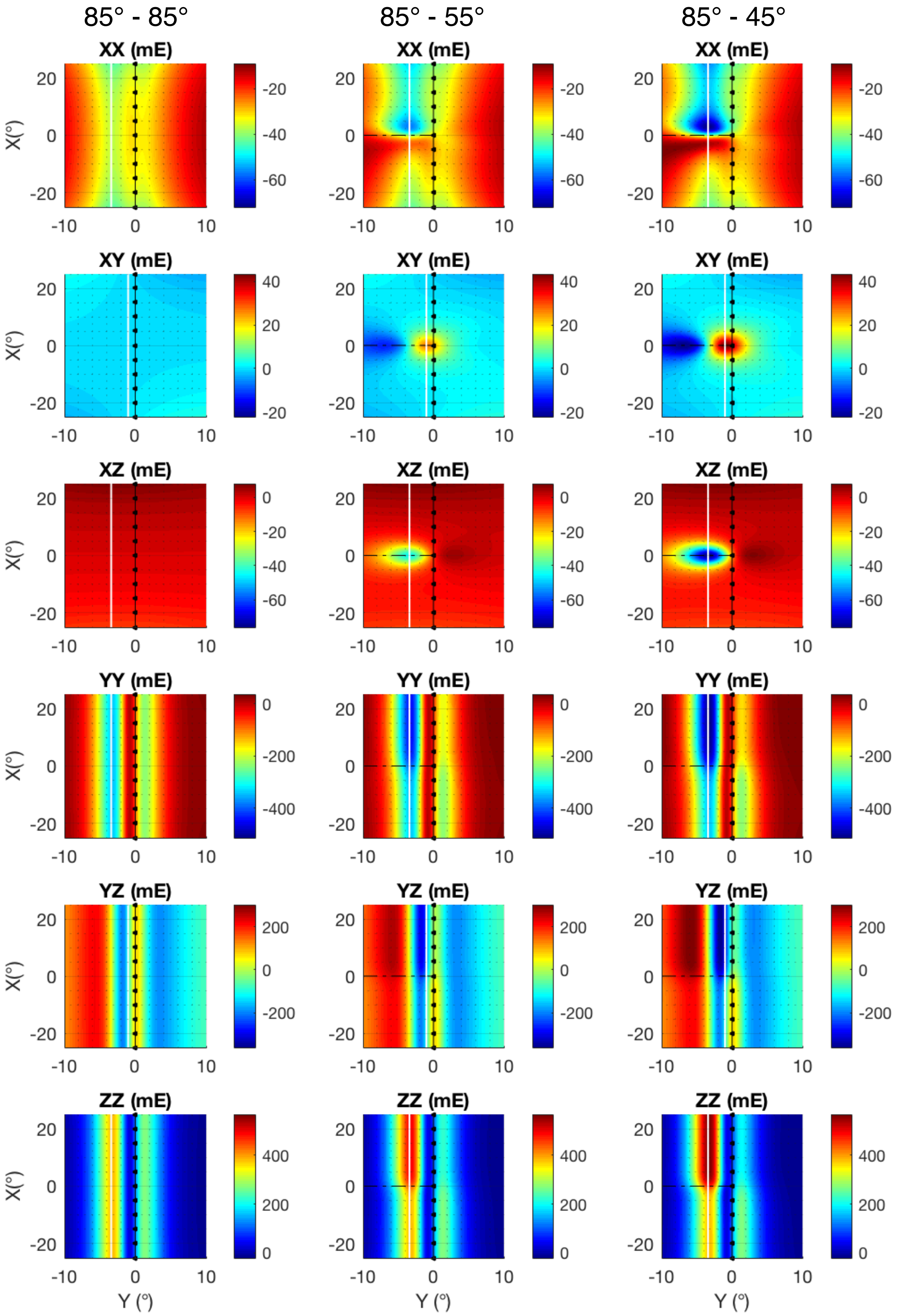

Figure 4.7b: Gravity gradients effect of slab model 3 using an infinite dimension of a slab (45°-45° on the both sides), with a lateral dip variation of 85° - 85° (left), 85° - 55° (middle), and 85° - 45° (right).

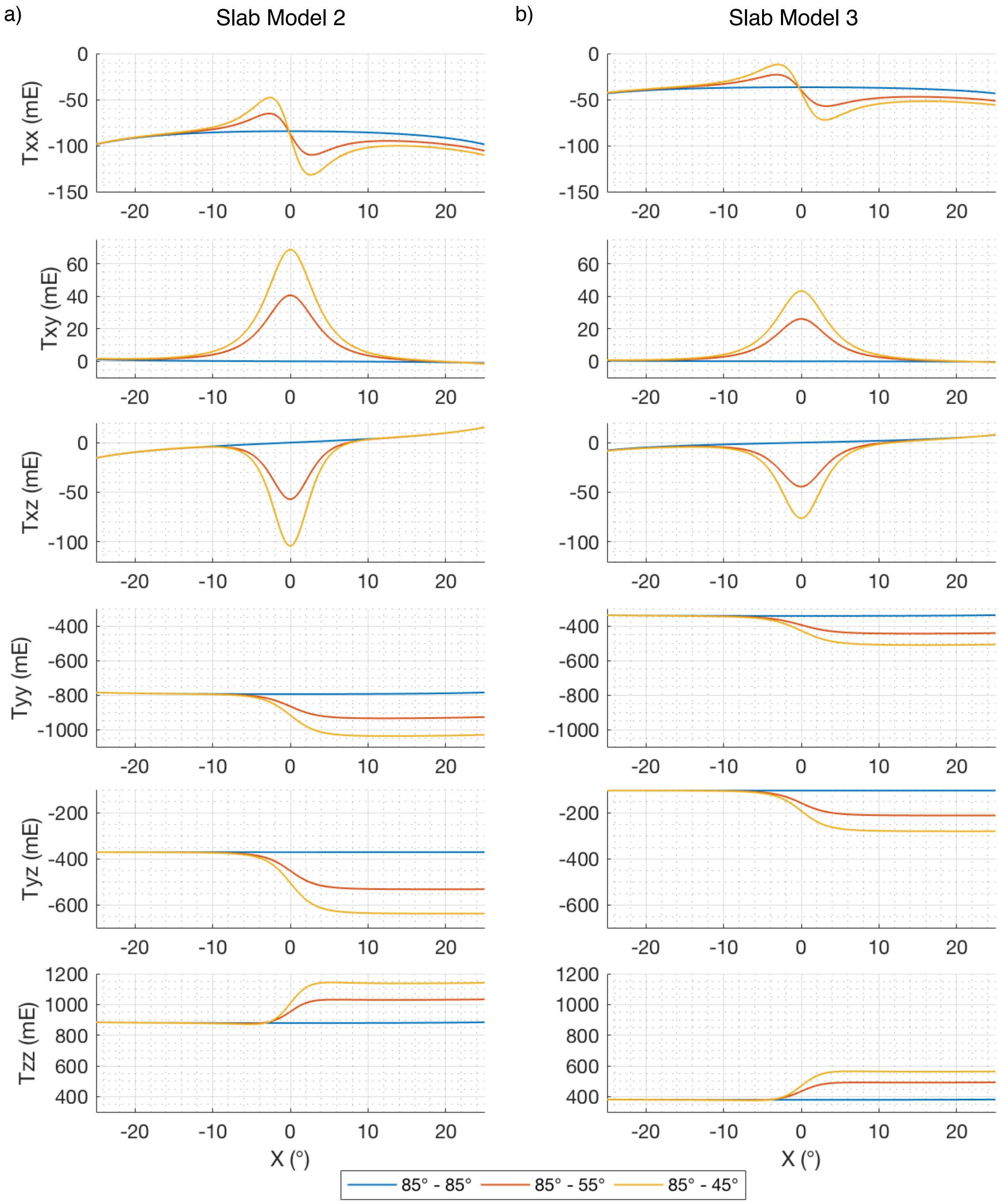

Figure 4.8: The gravity gradients effect due to the dip variation of the slab where the dimension of the slab is set in infinity using a slab model 2 (a) and model 3 (b).

Models 2 and 3 give similar patterns, as previously explained. The magnitude using slab model 2 is stronger than slab model 3 involving a large portion of crust. Each component of gradient provides unique response to the lateral variation of the subduction angle. The responses of each component are summarized in Table 4.3. As expected, since the dimension of the slab model is large (90°), the signal along the profile where there is no lateral variation is quasi-constant. Our results suggest that the gravity gradient components that can be used to localize where the subduction angle changes abruptly are T_{xx}, T_{xy}, and T_{xz} where the X-direction is parallel to the trench. The other components, T_{yy}, T_{yz}, and T_{zz}, can be used to analyze if there is any lateral variation along the subduction by regarding its signal variations parallel to the trench.

Table 4.3: Description of the gravity gradients' responses to the lateral variation of slab's subduction angle (based on Figure 4.7).

	No lateral variation of subduction angle	**With lateral variation of subduction angle**
T_{xx}	Consists of a signal with a wavelength more than 50° with a variation of ±15 mE along the profile	There is an oscillation due to the lateral variation of subduction angle; the middle point between the crest and the trough coincides with the location of the tear.
T_{xy}	The signal along the profile is almost constant with a variation of ∼2 mE	A positive anomaly is produced around the tear, the crest of the anomaly lies where the subduction angle changes abruptly
T_{xz}	Consists of a signal with a wavelength more than 50° with a variation of ±15 mE along the profile	A negative anomaly is produced around the tear, the trough of the anomaly lies where the subduction angle changes abruptly
T_{yy}	The signal along the profile is almost constant with a variation of ∼9 mE	The signal increases where the subduction angle decreases (negative)
T_{yz}	The signal along the profile is almost constant with a variation of ∼0.5 mE	The signal is stronger where the subduction angle decreases (negative)
T_{zz}	The signal along the profile is almost constant with a variation of ∼5 mE	The signal is stronger where the subduction angle decreases (positive)

The maximal magnitude of gravity gradient variations due to the lateral variation of slab geometry is summarized in Table 4.4 in the column 45°-45° (infinite plate). As expected, by comparing the resulted variations of 85°- 55° and 85°- 45°, a larger angle variation leads to a stronger gravity gradients variations, varies at each component (17 mE in T_{xx}, 28 mE in T_{xy}, -47 mE in T_{xz}, -103 mE in T_{yy}, -106 mE in T_{yz}, 112 mE in T_{zz}). For the case of IBM zone, with a lateral variation of 85°- 55°, the variation of T_{yz} along the profile is the largest among the other components. The obtained results in T_{yy}, T_{yz}, and T_{zz} show gravity gradients varies over 100 mE, that is theoretically detectable in GOCE observation.

As preliminary results, it appears that tear due to an abrupt change of subduction that happens locally produces anomaly with a wavelength larger than 5° (∼550 km) in T_{xx}, T_{xy}, and T_{xz} components (see also Table 4.4). This wavelength is larger than the minimum resolution of GOCE (i.e. 100 km) (Rummel et al., 2011). The magnitude of the anomaly due lateral variation of dip 85°- 55° is about 14-19 mE in T_{xx}, while it is stronger in T_{xy} (26-41 mE) and T_{xz} (44-57 mE), depend on the model 2 or 3. Theoretically, with this wavelength and magnitude, these anomalies are detectable in GOCE observation.

Summary:

- Slab's lateral dip variation of 85°- 55°, like for the case of IBM, is theoretically detectable in GOCE observation, with T_{yy}, T_{yz}, and T_{zz} variations are greater than 140 mE.
- The location of the tear could be detected in GOCE observation, particularly using T_{xz} component that shows 44-57 mE of anomaly with a wavelength of 5.6°. However, this condition is limit enough to be applied in the real case when we consider the presence of noise in the data.

Table 4.4: Amplitude and the resolution (half wavelength λ)of gravity gradients due to the lateral variation of slab dip where the value is relative to the value corresponds to the slab model without slab variation (dip variation 85°-85°) as the reference. The dimension of the slab model: 45°-45° for an infinite model and 10°-45° for the dimension similar to the IBM.

	Dip Variation	**Component**	**Amplitude (mE)**		**1/2λ (°)**	
			45°- 45°	**10°- 45°**	**45°- 45°**	**10°- 45°**
Slab Model 2	85°- 55°	T_{xx}	19	19	5.2	5.2
		T_{xy}	41	41	7.8	7.7
		T_{xz}	-57	-57	5.6	5.6
		T_{yy}	-142	-142	-	-
		T_{yz}	-161	-161	-	-
		T_{zz}	152	152	-	-
	85°- 45°	T_{xx}	37	37	5.2	5.2
		T_{xy}	69	69	7.4	7.3
		T_{xz}	-104	-104	5.4	5.4
		T_{yy}	-245	-245	-	-
		T_{yz}	-267	-267	-	-
		T_{zz}	264	264	-	-
Slab Model 3	85°- 55°	T_{xx}	14	14	5.6	5.6
		T_{xy}	26	26	8	8
		T_{xz}	-44	-44	6.6	6.6
		T_{yy}	-104	-104	-	-
		T_{yz}	-108	-108	-	-
		T_{zz}	113	113	-	-
	85°- 45°	T_{xx}	25	25	5.6	5.6
		T_{xy}	43	43	7.6	7.6
		T_{xz}	-76	-76	6.2	6.2
		T_{yy}	-170	-170	-	-
		T_{yz}	-177	-177	-	-
		T_{zz}	186	186	-	-

4.2.4. The Effect of The Slab Edge

In the previous models, I used a slab with a dimension of 45° to the north and 45° to the south from the location of the "slab tear". However, for the case of IBM zone, the dimension along Mariana subduction is ~10°. In the following test, we examine the effect of the border of a slab to the gravity gradients and how it affect the signal due to the slab tear.

The obtained results show that the slab edge produces ~125 mE and and ~10° of wavelength in T_{xx}, T_{xy}, and T_{xz} (Figure 4.9 and Figure 4.10). Compared to the previous results, this signal is stronger than the one due to slab tear, except for T_{xy} and T_{xz} which can locally exhibit similar amplitude. The negative anomalous body related to the subducting oceanic crust results in oscillation with a shorter wavelength (~3°) coincide with the location of the slab edge.

Using the results from slab model with no lateral dipping variation (85°- 55°) as the reference, the signal residual due to the tear slab still have the similar wavelength and magnitude compared to the previous test (using an infinite dimension of slab).

Summary:

- The slab edge produces ~125 mE and and ~10° of wavelength in T_{xx}, T_{xy}, and T_{xz} components, but it is mostly remarkable in T_{xz} component. This signal is large enough to be detected using GOCE observations.
- The location of the signal peak in T_{xy} and T_{xz} along a profile parallel to the trench coincides with the location of the slab edge.

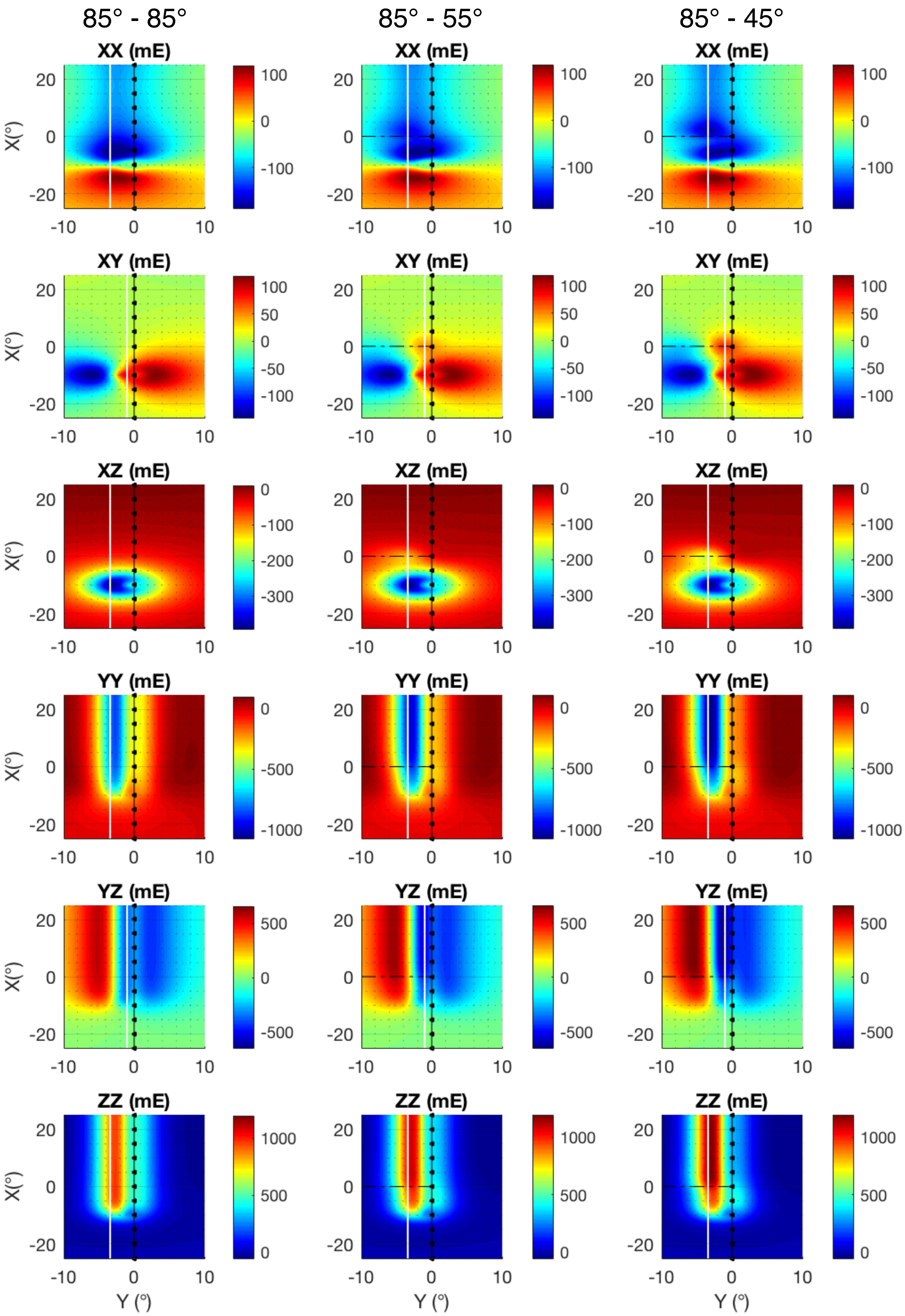

Figure 4.9a: Gravity gradients effect of slab model 2 using a dimension of slab on the IBM zone (10° on the south - 45° on the north), with a lateral dip variation of 85° - 85° (left), 85° - 55° (middle), and 85° - 45° (right).

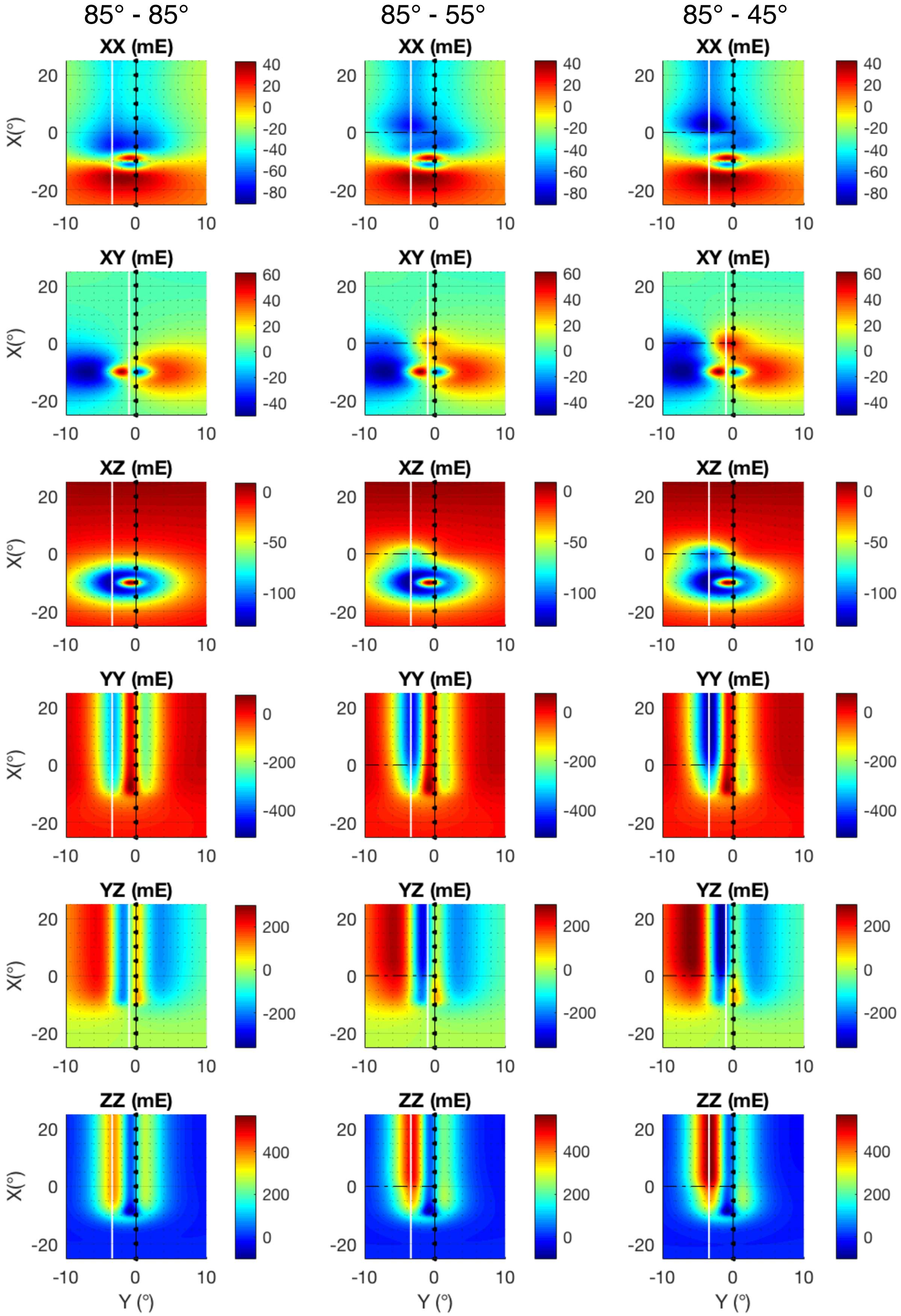

Figure 4.9b: Gravity gradients effect of slab model 3 using a dimension of slab on the IBM zone (10° on the south - 45° on the north), with a lateral dip variation of 85° - 85° (left), 85° - 55° (middle), and 85° - 45° (right).

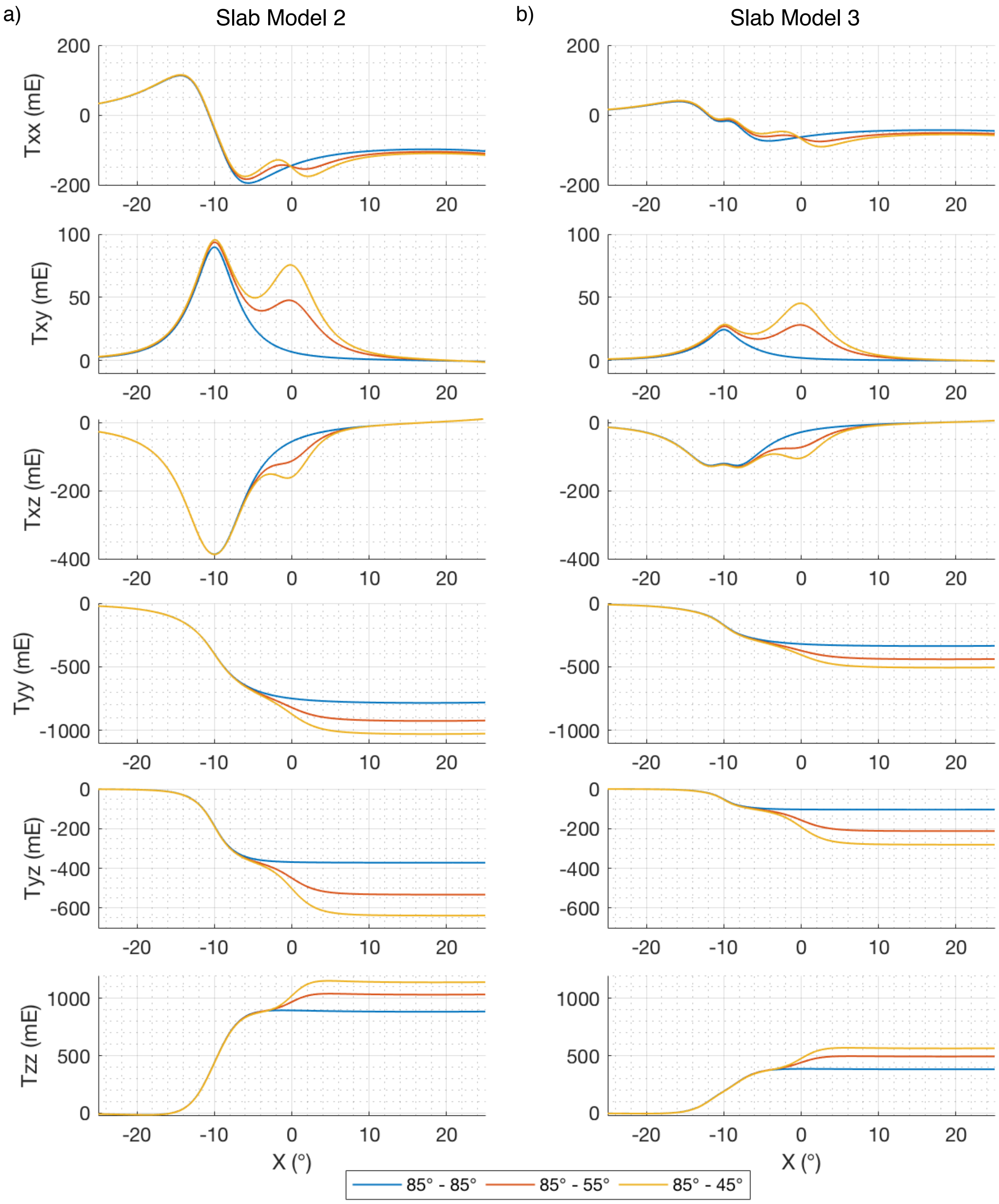

Figure 4.10: Profiles as a function of the subduction angle, shown by the different colors, in T_{zz}, T_{yy}, and T_{yz} along the profile at X=0 of the slab model 2 (a) and model 3 (b), with a dimension of the slab is 10° on the south and 45° on the north.

4.2.5. Summary of The Synthetic Tests

Our first approach using synthetic models of slab allows us to evaluate the gravity gradients related to the structure of the slab, including its density distribution, its edge, and its subudction angle. From the results above, the density distribution model of a slab matters to the spatial distribution and the magnitude of gravity gradients. The presence of crustal anomalies in the subducting slab appears as a major parameter that controls both amplitude and wavelength of gradients. The presence of crustal anomalies in the astenopheric layer reduces T_{zz} up to 600 mE. The oscillation is produced due to the presence of negative anomalous body, that is related to the oceanic crust in the upper mantle, with a wavelength $\sim$4°. This suggests that a good knowledge of the geometry of the oceanic crust is essential for signal reduction and to assess the detailled geometry of a slab.

This geometry of a subducting slab depends to its subduction angle, and gravity gradients at satellite altitude are sensitive enough to this parameter. The spatial distribution of gravity gradients is shifted towards the trench due as a function of the dip. The signal of gravity gradients is stronger for a slab with a lower subduction angle since the position of the subducting slab is closer to the surface than a steeper one. The variation of gravity gradients associated to the variation of dip $\geq$10° is possible to be detected in GOCE observation, with a magnitude of $\geq$75 mE. Any dip variations with $\Delta\theta \leq 10°$ produces a weak enough T_{zz} variations (e.g., $\sim$30 mE for $\Delta\theta = 5°$) that could lead to any misinterpretation if we consider also the noise in the data.

Lateral variation of subduction angle of a slab theoretically can be detected by gravity gradients at GOCE altitude. In the tests above, the signal associated with the dipping change of 30° has a magnitude more than 140 mE in T_{yy}, T_{yz}, and T_{zz}.

Tests above also show that the location where the dip changes abruptly can also be estimated by regarding the peak of T_{xz} with 44-57 mE of signal anomaly and a wavelength of 5.6°. However, this condition is limit enough to be applied in the real case when we consider the presence of noise in the data. The location where the dip angle changes is only detectable where the dip changes abruptly, that is not a common case in the subduction.

The slab edge produces $\sim$125 mE and and $\sim$10° of wavelength in T_{xx}, T_{xy}, and T_{xz} components, but it is mostly remarkable in T_{xz} component. This signal is relatively stronger than the one resulted from a slab tear. The signal due to the slab edge is strong enough to be detected using GOCE observations.

From the results above, GOCE measurements are capable to provide important information to constrain slab geometry, including edge and dip angle. However, the detection of second-order features as lateral variation of dip angle appears quite delicate. Lateral dip variation of a slab is could be detected using GOCE observations if only the variation of dip is large enough (e.g. $\Delta\theta \geq 30°$) and the change is abrupt. For a smoother lateral variation, it may be difficult to be assessed.

For the implication to a real case, the results from this synthetic test can be used where the gravity gradients signal that we have is the signal residual associated to a subducting slab only. Some proper corrections and reductions of gravity gradients datasets thus have to be performed to attain this kind of residual to extract the information of the structure of a subducting slab from gravity gradients signal. The next sections will discuss about an application on the IBM zone, including the correction and reduction processes of GOCE datasets.

4.3. Application to Izu-Bonin-Mariana (IBM) Subduction Zone

4.3.1. Izu-Bonin-Mariana: Geodynamical context

The Izu-Bonin-Mariana (IBM) arc system is a tectonic-plate convergent boundary, formed as a result of the Pacific plate subducting beneath the Philippine Sea plate. Subduction began in the Izu-Bonin-Mariana convergent margin circa 50 Ma (Taylor, 1992; Cosca et al., 1998). It extends ∼3 400 km along the trench from the south of Tokyo, Japan to northern Yap, creates a nearly south-north oriented structure (see Figure 4.11). The Sofugan Tectonic Line at ∼29°30'N separates the Izu and Bonin segments, while the boundary between the Bonin and Mariana segments is defined by the northern end of the Mariana Though back-arc basin at ∼23°N. The age of the subducting oceanic lithosphere is younger in the north than in the south, varied about 130 - 170 million years old (Müller et al., 2008).

The trench as the eastern boundary of the arc system varies from ∼11 km deep in the Challenger Deep to a shallow part with a deep less than 3 km where the Ogasawara Plateau joins the subduction system. The Ogasawara Plateau itself is a igneous seamount chain which is Jurassic in age, that is younger than the surrounding material on the Pacific plate (Miller et al., 2004). From bathymetry profile, this plateau is ∼5 km higher than the surrounding sea floor. The presence of the Ogasawara Plateau causes the bend around the contact zone between Izu-Bonin and Mariana trenches, as proposed by Jaxybulatov et al. (2013).

Subducting oceanic crust along the Izu-Bonin Trench is ∼6 km thick. While on the east of the Mariana Trench, the oceanic crustal thickness varies between 5.3 to 7 km with the presence of numerous seamounts with 2 to 3 km of height (Oakley et al., 2008). On the subducted plate, the crustal thickness is less constant, moreover due to the presence of the ridges and volcanic arc on the bakc-arc system. Some profiles obtained from reflection/refraction seismic surveys by previous studies ((e.g., Takahashi et al., 2007, 2008, 2009) give a crustal thickness ranging from 17 km to 20 km on the volcanic arc and the ridges and 6 km to 10 km for the other structures (basins and the fore-arc).

Some previous study have been performed to understand the geometry of IBM subduction (cf. van der Hilst and Seno, 1993; Cruciani et al., 2005; Stern et al., 2004; Miller et al., 2004, 2005; Hayes et al., 2012; Jaxybulatov et al., 2013). The results of those

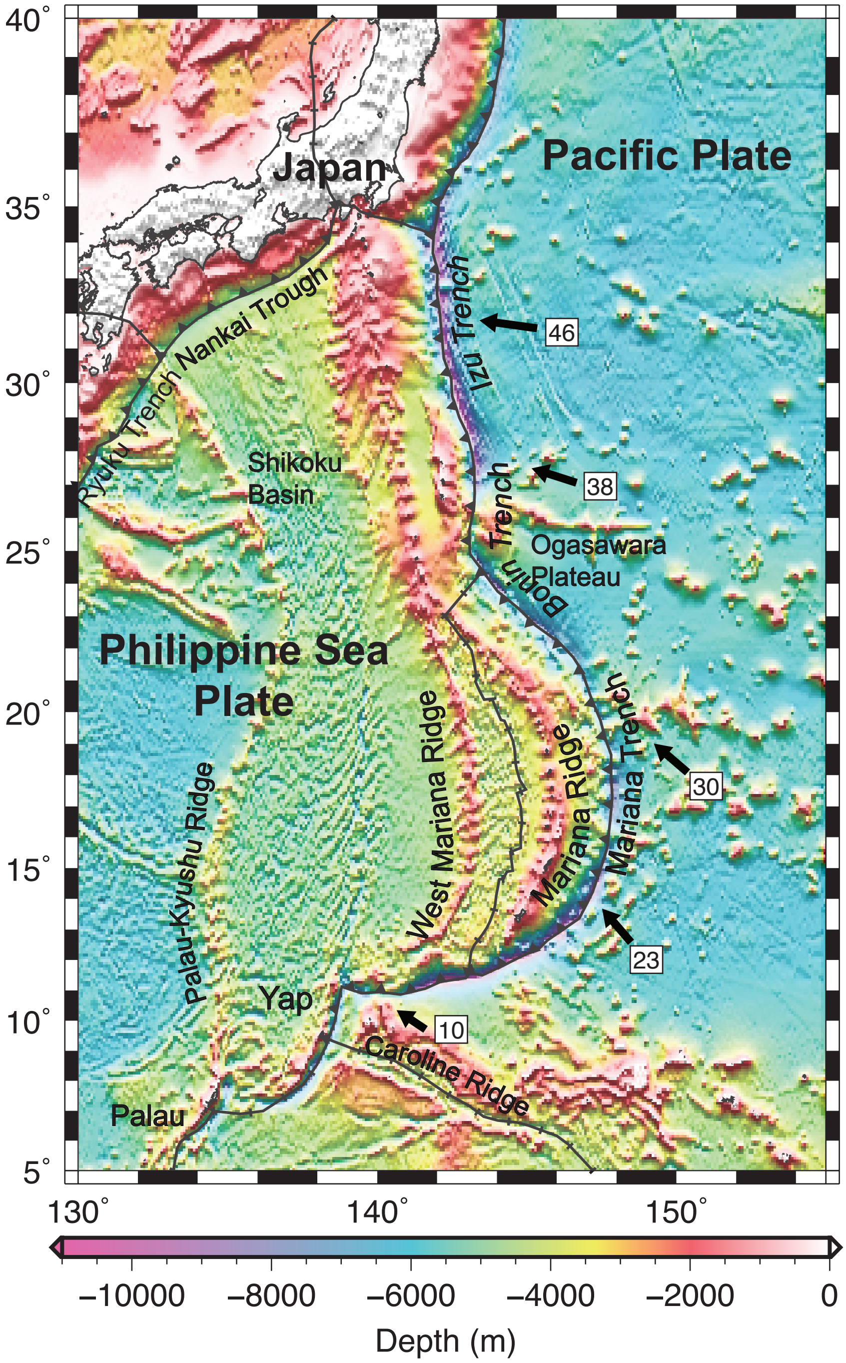

Figure 4.11: Izu-Bonin-Mariana (IBM) subduction zone. The color represent the bathymetry from GEBCO (Weatherall et al., 2015). Triangle lines show the trenches and the fenced lines shows the troughs. The arrows indicate the direction of the plate movement. Numbers in the white box indicate the relative plate motion (mm/yr).

studies agrees that there are lateral variations of subduction angle that is steeper on the south (Mariana) and less steep on the north (Izu-Bonin), with various proposed dip angle variations. The location of seimicity on IBM zone is presented in Figure 4.12a to illustrate the lateral variation of the subduction. In this study, I adapt the subduction angle proposed by Cruciani et al. (2005) with a variation of 85° on the south and 55° on the north. Some proposed models by Miller et al. (2004, 2005) and Zhao et al. (2017) illustrate the evidence of slab tear on IBM subduction. Those models are prensented in Figure 4.12b-d.

IBM presents an outstanding example for this study, for several reasons:

- It is a well-studied zone in term of geophysical observations.
- The structures on the IBM zone are large enough, so it is observable for gravity gradients at satellite altitude. The subduction system is ∼3 400 km long, with ∼ 1 200 km of Izu-Bonin part and the rest related to Mariana part.
- IBM major structures are elongated in south-north direction, therefore it is suitable for gravity gradient analysis using the horizontal components.
- The IBM arc system is a good example of an intra-oceanic convergent margin. Because this arc system is far from any continent, it is not affected by the large volume of sediments due to the accretion. As a consequent, a relatively thin sedimentary cover makes it much easier to study the arc structure.
- Several studies have reported that there are lateral variations of subduction angle that is steeper in the southern part (Mariana) and less steep on the northern part (Izu-Bonin) with a variation of ∼30°. This variation could be large enough to be assessed using GOCE observations.

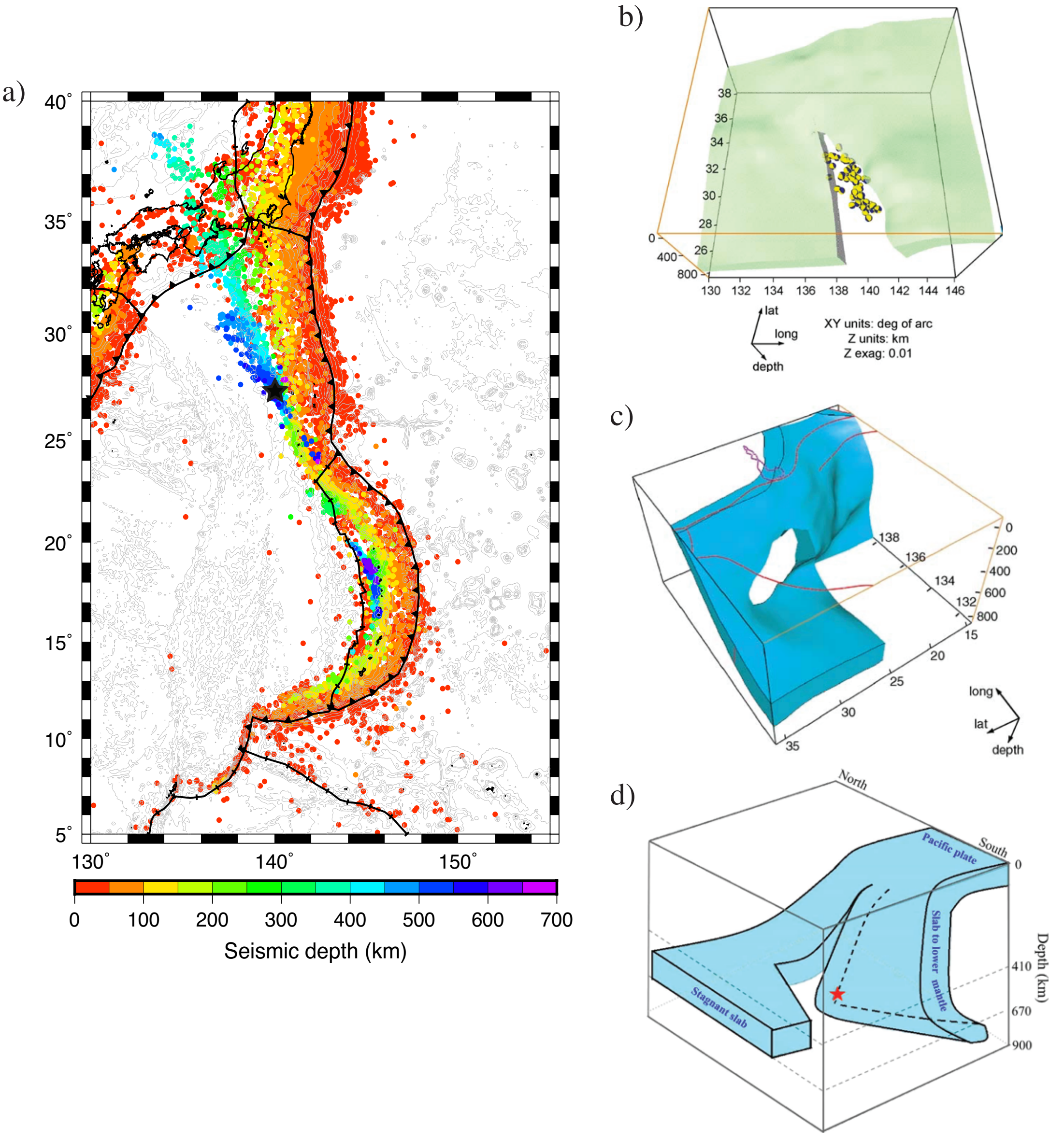

Figure 4.12: (a) Seismicity of the study region from the reprocessed International Seismological Centre (ISC) catalogue (Storchak et al., 2013). Some proposed slab tear geometries by Miller et al. (2004) (b), Miller et al. (2005) (c), and Zhao et al. (2017) (d). The location of the red star in figure (d) is indicated in figure (a) with a black star.

4.3.2. GOCE gravity gradients - Level 2

The data used in this study are the GOCE gravity gradients of level-2 product **EGG_TRF_2**. This type of datasets has been externally calibrated and corrected to gravity gradients due to temporal gravity variations by the GOCE High Processing Facility (HPF) (see Gruber et al., 2010b,a). This dataset contains the gravity gradients in the Local North Oriented Frame (LNOF), that is a local Cartesian reference system with a right-handed North-West-Up frame with the X-axis pointing North, the Y-axis pointing West, and the Z-axis pointing Up. The information that is provided in EGG_TRF_2 dataset include GPS time (in second), position of the data in geocentric coordinate (longitude, latitude, and radius from geocenter), gravity gradients in LNOF (in s^{-2}), estimation of gravity gradients error of each component (in s^{-2}), and its flags for outliers.

In this study, the EGG_TRF_2 dataset is used with a data period from 04-August-2013 until 19-October-2013. The data points are dense enough for the studied area and this is the period where the GOCE satellite was located at the lowest altitude (∼230 km) than the periods before, thus a stronger signal is expected. The variation of the GOCE altitude in that period over the IBM zone is shown in Figure 4.13. With this altitude of measurement, like has been mentioned in the Section 1.2., the effective spatial resolution of GOCE data is around 80 - 100 km.

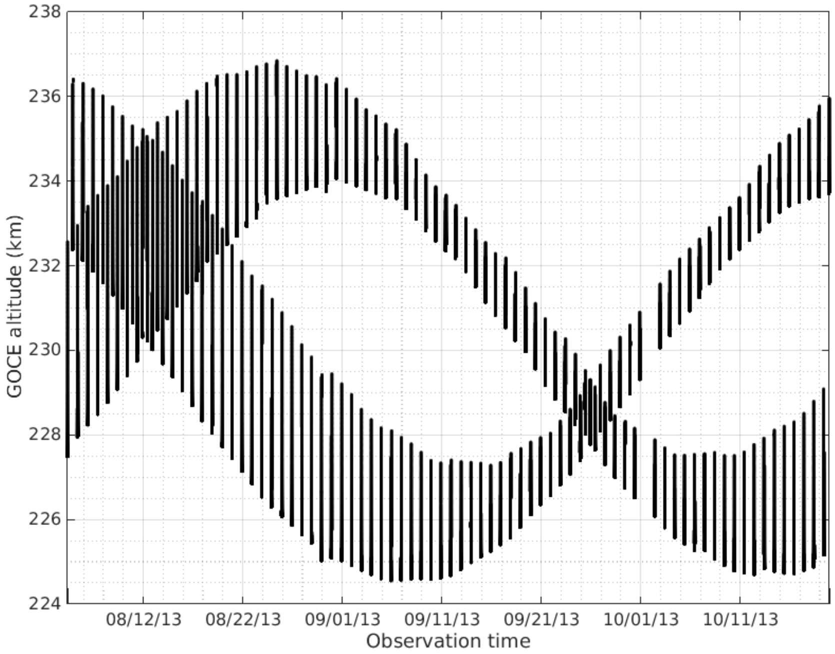

Figure 4.13: GOCE altitude variation during the used dataset's period of observation. The GOCE data have been selected for the region around the Izu-Bonin-Subduction zone.

In GOCE EGG_TRF_2 dataset, the gravity gradients T_{xx}, T_{yy}, T_{zz}, and T_{xz} are determined with high accuracy, whereas the T_{xy} and T_{yz} are less accurate (Bouman et al., 2013). Hence, the T_{xy} and T_{yz} components were therefore treated using EIGEN-05C and

EIGEN-05S as the a-priory static gravity field models (Gruber et al., 2010b). GOCE gravity gradients during selected observation period on IBM zone are shown in Figure 4.14. The statistical properties of the estimated error σ of each GOCE gravity gradient component is shown in the Table 4.5.

Table 4.5: Statistical properties of the uncertainty σ of each component of GOCE observation data.

Components	Min (mE)	Max (mE)	Mean (mE)	Std (mE)
T_{xx}	8	8	8	0
T_{yy}	9	10	9	1
T_{zz}	11	12	11	0
T_{xy}	3	4	4	0
T_{xz}	10	10	10	0
T_{yz}	4	4	4	0

For the computation of gravity field quantities, reference ellipsoid GRS80 system is used (ESA, 2010). The defining constants are mentioned in Table 1.1. in the Chapter 1.

4.3.3. GOCE data processing

GOCE measures the total attraction of the Earth graviational field, which contains the attraction from the figure of the Earth (normal shape), topography, and other variations at depth. The estimation of gravity gradients signal associated to the structure of a slab is done by analyzing the signal residual of gravity gradients. To that aim, from along orbit GOCE TRF data, an anomaly map of gravity gradients at satellite altitude on the study zone is built with respect to an Earth reference spheroid model. Data reductions, including reduction of topography-bathymetry effect is then performed.

The gravity gradients in this study are maintained at the GOCE altitude, therefore noise amplification resulting from the downward continuation to the Earth's surface can be avoided. All of the estimations of gravity gradients for data reduction processes are performed by using a forward modelling method by GEEC. This gives us an advantage to do the calculations of any type of body mass at the original position of GOCE along orbit dataset.

4.3.3.1. GOCE Coordinate Transformation

GOCE TRF datasets are provided in geocentric coordinate, defined in longitude λ, latitude φ, and radial distance r from the center of the Earth. Calculation in spherical approximation in GEEC is carried out in geographic coordinate system. Hence a coordinate transformation of GOCE TRF datasets is needed.

To transform geocentric to geographic coordinate system, firstly we convert the geo-

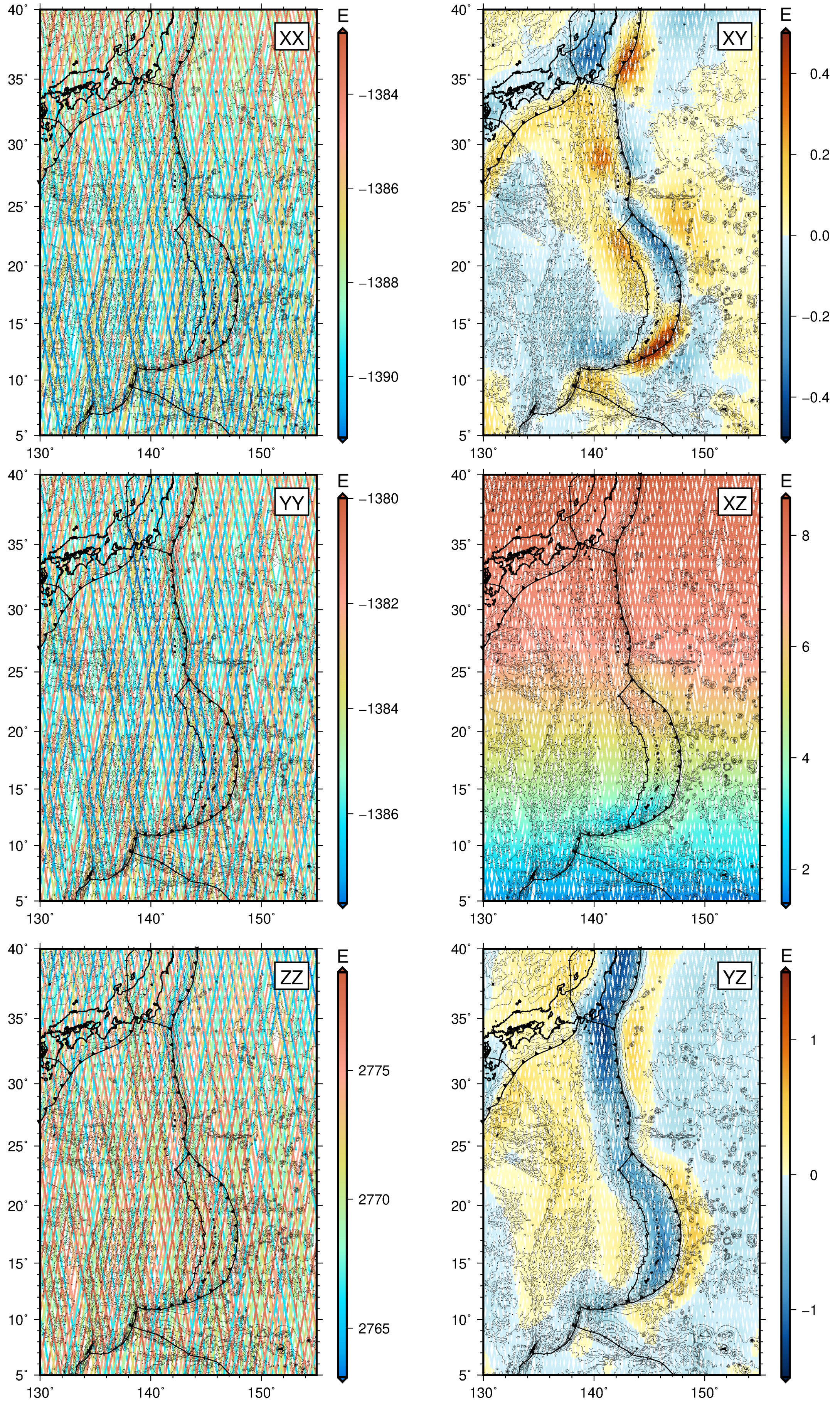

Figure 4.14: Gravity gradients from GOCE observation along GOCE orbit track on the IBM zone.

centric coordinate to 3D Cartesian system,

$$\begin{aligned} X &= r\left(\cos\varphi\cos\lambda\right) \\ Y &= r\left(\cos\varphi\sin\lambda\right) \\ Z &= r\sin\varphi \end{aligned} \tag{4.1}$$

then followed by the transformation from 3D Cartesian to geographic system using eq. (2.3) - (2.6) (described in Chapter 2).

4.3.3.2. Correction of Normal Gravity Gradients

Gravity gradients measured by GOCE comprise the gravitational attraction of the entire Earth. Therefore, we have a really strong gravity gradients signal. Since the total attraction of the Earth is really strong, the variations of GOCE altitude along its orbit (Figure 4.13) leave a visible trail of gravity gradient variations, around 7-8 E in T_{xx}, T_{yy} and around 15 E in T_{zz}. Components T_{xx}, T_{xz}, T_{yy}, and T_{zz} are also dominated by the gravity gradients variation along latitude due to the flattening of the Earth, whilst T_{xy} and T_{yz} are free from that factor (Chapter 1). To obtain anomaly maps of the studied region, the signal due to the normal shape of the Earth must be removed.

I calculate the effect of normal Earth in gravity gradients term by using eq. (1.30) - (1.34) in Section1.4. Then it is followed by using the matrix rotation in eq. (1.45) to transform the obtained normal gravity gradients to the LNOF reference system. I use the spheroid GRS80 as the normal Earth reference, like mentioned in the GOCE High Processing Facility (HPF) standard (ESA, 2010). The parameters of GRS80 are mentioned in Table 1.1. (Chapter 1). The obtained results for normal T_{xx}, T_{xz}, T_{yy}, and T_{zz} can be found in Figure 4.15.

The regional anomaly maps of IBM zone can be found in Figure 4.16. The effect due to the normal shape of the Earth and Earth's sphericity are removed. The obtained anomalies reflect irregularities in the distribution of mass and its interface deflections with respect to the reference model.

Similar to conventional gravity anomaly maps, the anomaly of gravity gradients at satellite altitude show remarkable details mainly related to the Earth's topography and bathymetry features that are reflected with short-wavelength anomalies (see also Figure 4.11). T_{zz} exhibits negative anomalies (-1 E) with $\sim$1°of wavelength along the trench, where the bathymetry is deep, and positive anomalies (0.5-1 E) along the island arc and Japan. In T_{yy}, a component that is sensitive to the east-west variation, the trench along IBM arc is marked with positive anomaly ($\sim$1 E). Along island arc and Japan, T_{yy} shows negative anomaly ($\sim$1 E). The southern part of Mariana arc, which is elongated east-west, is marked with negative anomaly ($\sim$1 E) in T_{xx} component.

The signal that is related to topography variations is still dominant in Figure 4.16. To be able analyze gravity gradients signal associated with the mass below the surface, topography correction will be needed.

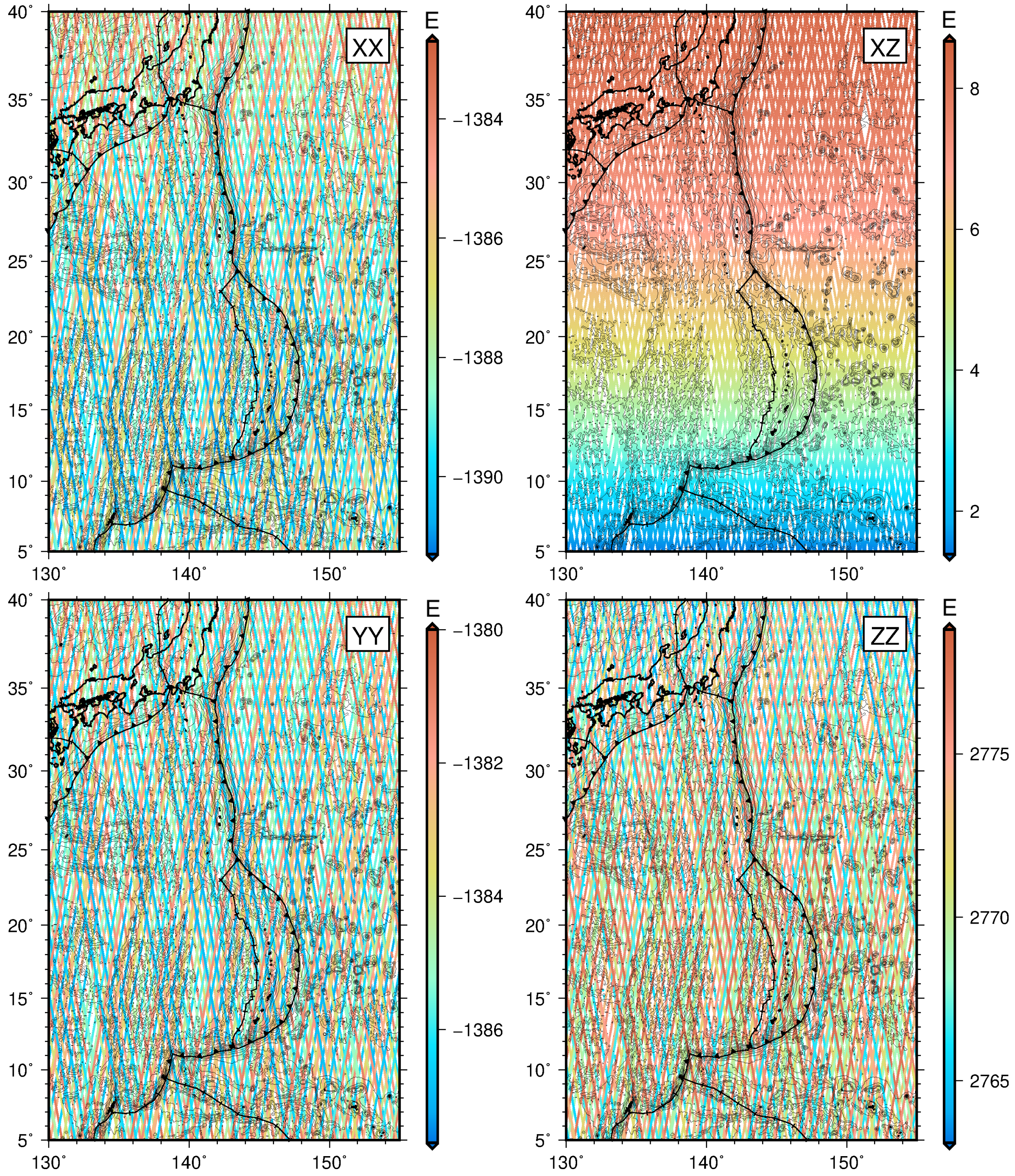

Figure 4.15: Gravity gradients of normal ellipsoid along GOCE orbit track on the IBM zone.

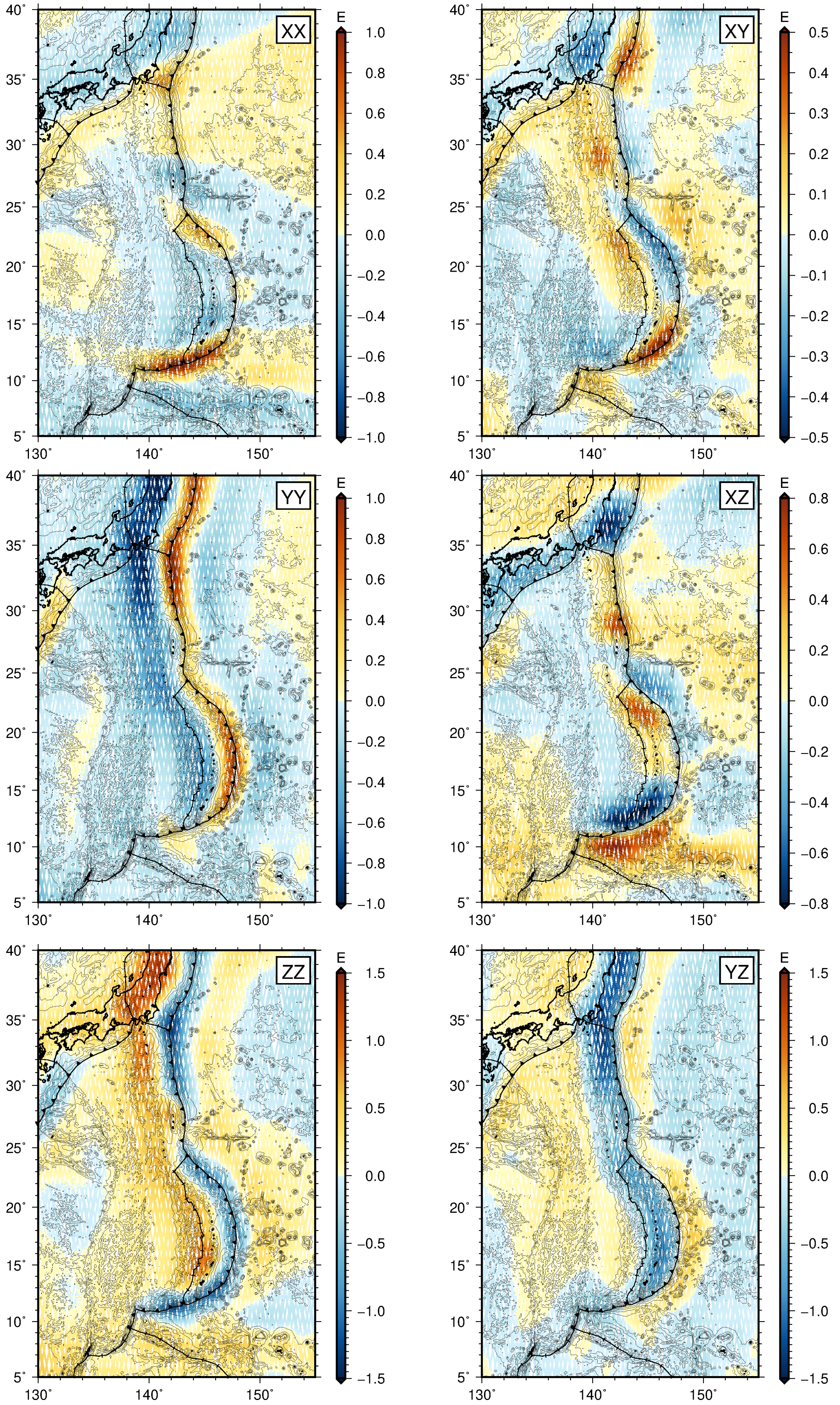

Figure 4.16: Gravity gradients disturbance along GOCE orbit track on the IBM zone.

4.3.3.3. Topography Correction

The Earth's topography has a major contribution to the variation of Earth gravitational field after the normal shape of the Earth and its flattening and rotation (see Figure 1.8). As been discussed in Chapter 3, for geodynamics application at satellite altitude using absolute value of gravity gradients, the use of global topography dataset is required.

Topography effect combines the positive effect of the mass excesses above a specified reference surface, e.g. ellipsoid or geoid, and the negative effect of mass deficit below this reference surface. Gravity gradients due to the topography effect is normally composed in a short wavelength. Topographic correction of gravity gradients field observations is performed in order to remove the effect of the mass on the Earth surface, therefore the residual that we obtain only reflect remaining subsurface features.

Topography and bathymetry dataset that is used in this study is GEBCO 2014 gridded bathymetric dataset that contains a global 30 arc-second interval grid for ocean and land (Weatherall et al., 2015; GEBCO, 2014). Data sources in GEBCO 2014 consists of regional seafloor mapping contributions, bathymetric soundings, and version 2.0 of the SRTM30 for land area.Altimetry bathymetry is used for completing the data where there is no bathymetry measurement on that area, which is not for the case of IBM zone. This dataset was then processed using GEEC sub-routines to obtain a global equidistance dataset with a resolution of 10 km for later to be used in topography effect computation. Topography and bathymerty map on the IBM zone is shown in Figure 4.11.

The vertical datum of GEBCO is mean sea level. Digital Terrain Model (DTM) height adjustment was then performed to bring the topography-bathymetry surface in respect to the ellipsoid of reference (GRS80) using the geoid height (or undulation) N as determined from EGM96 geopotential model. This height adjustment is carried out in order to avoid the indirect effect caused by different vertical reference level (Talwani, 1998).

Topography effect is computed at GOCE along orbit data position. The topography model is decomposed in two bodies: rock layer for masses above sea level with a density $\rho_r = 2670$ kg m^{-3} and water layer for masses below sea level with a density $\rho_r = 1030$ kg m^{-3}. Using a crustal density $\rho_r = 2800$ kg m^{-3} as the reference below sea level, the density anomaly for ocean layer is -1670 kg m^{-3}.

The topography effect on the IBM zone is shown in Figure 4.17. The excess mass above mean sea level (msl) in Japan are marked with positive anomaly ($\sim$2 E) in T_{zz}. Water bodies below msl produce negative anomalies on the oceanic domain, vary up to -5 E in T_{zz}. Along the island arc, the T_{zz} shows anomalies approximately -0.1 to 0 E, that is weaker than its surrounding due to its shallower bathymetry profiles. The island arc and Japan with higher bathymetry-topography profiles comparing to its eastern-western bathymetry features results in negative anomalies in T_{yy} (between -1 and 0 E). In T_{xx}, the deep trench on the southern part of Mariana arc ($\sim$11°N results in strong positive anomalies ($\sim$3 E). T_{xx} around the Ogasawara plateau, located around 142°-144°E; 27°N, is weaker than the trenches on its northern and southern part. This plateau is $\sim$4 000 m higher than its surrounding.

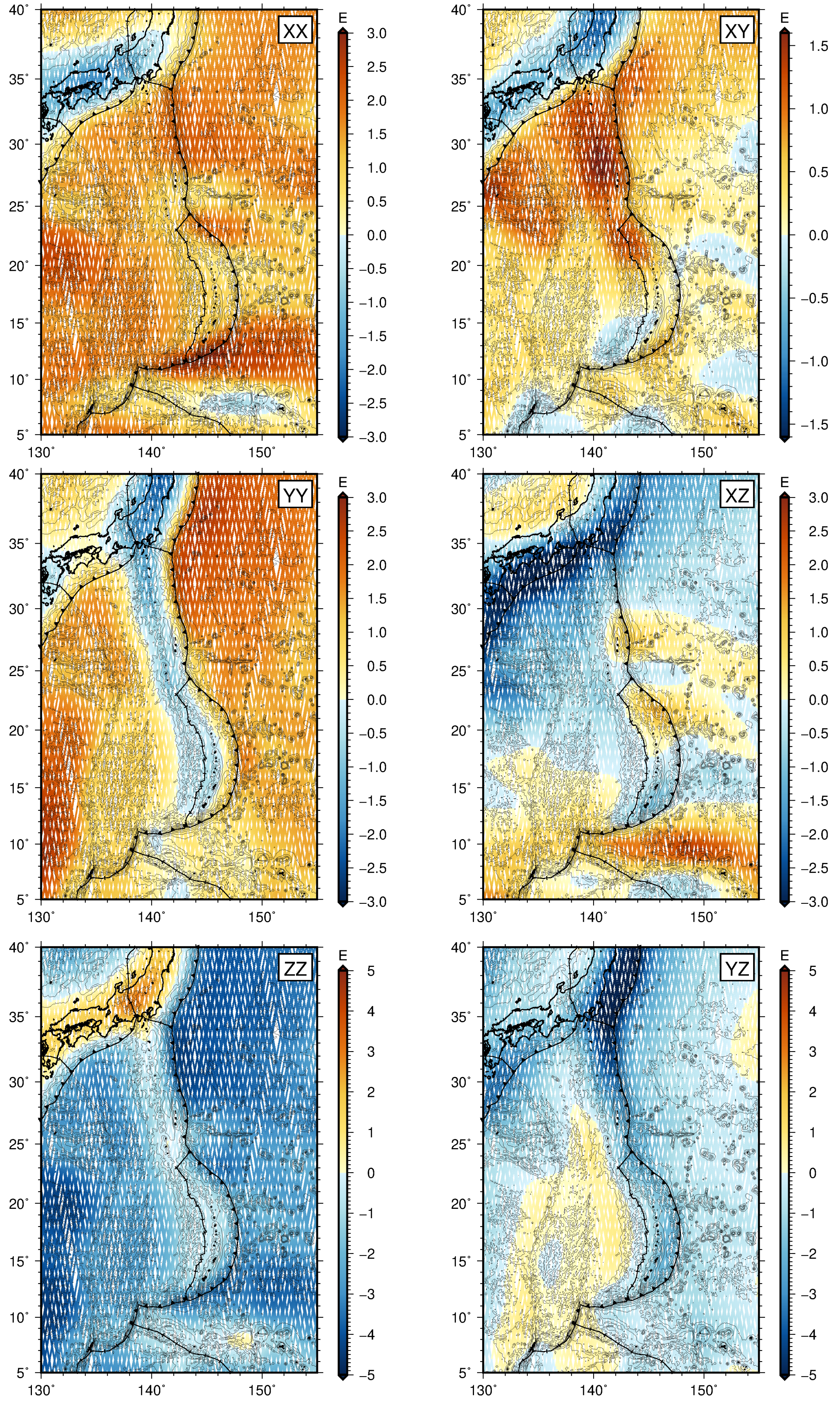

Figure 4.17: Topography and bathymetry effect along GOCE's track observation over the IBM zone.

If we compare the gravity gradients due to the topography effect (Figure 4.17) and the anomaly of gravity gradients after normal correction (Figure 4.16), the signal due to the topography effect is stronger and the distributions of the signals are different. This could be an indication if the gravity gradients in Figure 4.16 are not only related to topography, but also related to other sources, e.g., slab or mantle variation. To find out, the topography effect is removed from the gravity gradients anomaly. The results of this correction are shown in Figure 4.18.

The small wavelength signal associated with the topography variation is removed, yet they are still containing complex spatial distribution of gravity gradients. After the topography effect correction, gravity gradient distribution in T_{zz} shows positive anomalies over the oceanic domain (up to 5 E) and negative around Japan (∼-1.5 E). This could indicate the evidence of thinner and denser oceanic crust that contributes to positive anomaly and the presence of crustal root beneath Japan with negative anomaly contribution.

The island arc is marked with a weak positive anomaly (∼0.5 E) in T_{zz}, that is weaker than its surrounding. This could be related to the presence of thicker crustal layer along the arc that provides negative contribution to gravity gradients signal. T_{yy} highlights positive gradient anomaly with a wavelength of 1° along the IBM back-arc system. It coincides to the weak positive signal in T_{zz}, as been mentioned before.

To investigate whether we can see the signature of the slab in the gravity gradients that have been corrected to the normal shape and the topography effect, I trace 2 profiles across Izu (profile A), Bonin (B), and Mariana arc (profile C) to see the variation of T_{zz}, T_{yy}, and T_{yz} along the profile (Figure 4.19). These profiles mimic the profile that we used in the synthetic modelling (Figure 4.4) in order to assess the signal due to the presence of the slab. These three gravity gradient components are chosen since they exhibit the most remarkable variation along the profile perpendicular to the trench (see Section 4.2.1.).

If we compare the signal residual in T_{zz}, T_{yy}, and T_{yz} after the topography effect correction along the profile (Figure 4.19-red line) and the one resulted from the synthetic tests (Figure 4.4), the profiles of gradients in the IBM case are closer to the slab model 3 (where the crustal anomaly remains in the slab to a depth of asthenosphere layer), notably in T_{yz}. However, the wavelength and the amplitude of the oscillation on the profile from IBM case are much stronger than the one resulted from synthetic models, more negatives up to 2 E inT_{zz} and more positives up to 2 E in T_{yy}. This could be an indication of the presence of other source that contributes in producing this strong signal, positive in T_{yy} and negative in T_{zz}, for example.

One of the possible sources is crustal root or crustal thickening. Crustal root results in negative anomaly in T_{zz} component (cf. Cadio et al., 2016). From the crustal models resulted from tomography inversion by Takahashi et al. (2007) and Takahashi et al. (2009) (Figure 4.20), we can see that there is crustal thickening below the volcanic arcs and the ridges. The gravity gradients that are obtained from synthetic modelling does not consider the presence of crustal layer above the slab. Thus, to extract the signal due to the slab, the effect of this crustal layer should be removed.

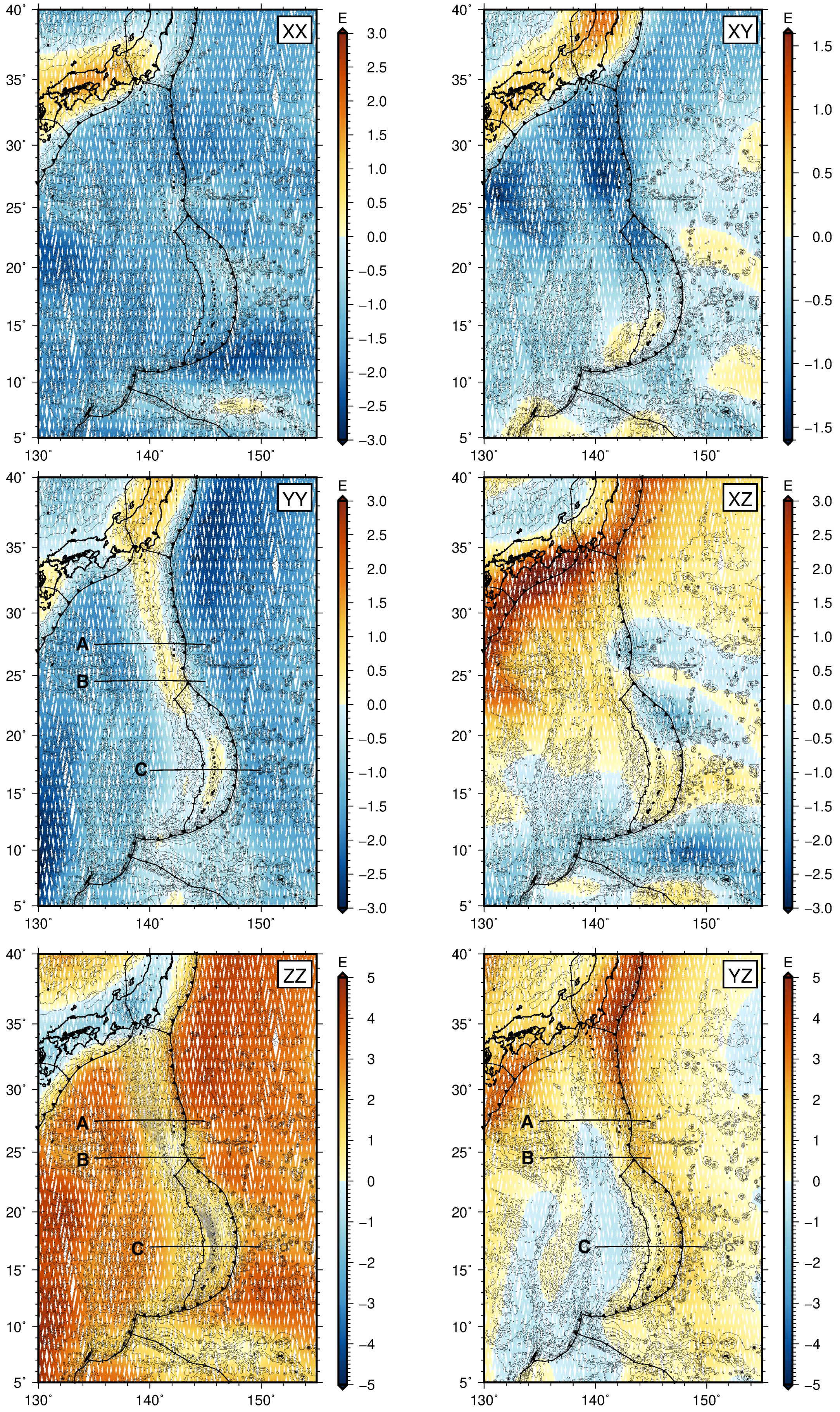

Figure 4.18: Residual of gravity gradients after topography and bathymetry effect reduction on the IBM zone.

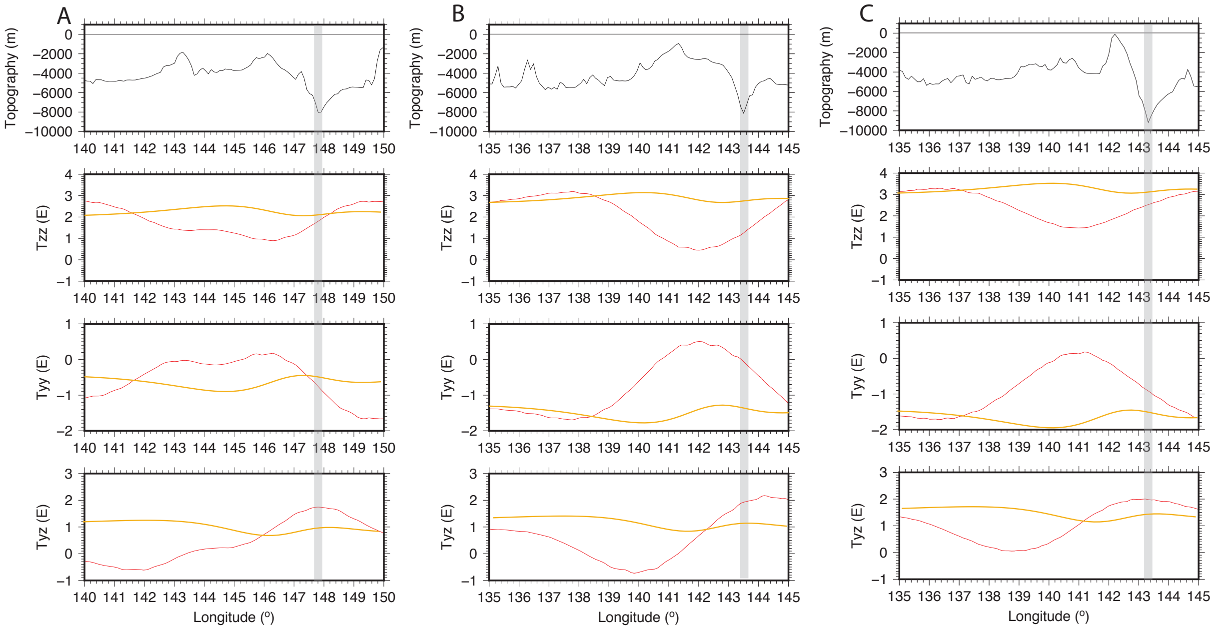

Figure 4.19: Topography profile and T_{zz}, T_{yy}, and T_{yz} components of gravity gradients after topography reduction along profiles A, B, and C that are elongated perpendicular to the trench (red line). The yellow line is the effect of the slab that is obtained using synthetic models (Section 4.2.). The location of the profiles is indicated in Figure 4.17.

4.3.3.4. Crustal Effect Reduction

Until this step, the results from gravity gradients data reductions show that topography reduction only is not enough to decipher the structure of a subducting slab. The presence of crustal layer still has a significant effect on the residual gravity gradients.

Until today, the availability of global crustal model is not as sophisticated as global topography model. Global crustal model datasets that are available right now is limited to crust 1.0 (Laske et al., 2013) and GEMMA (Reguzzoni and Sampietro, 2015) with a grid resolution of 1° and 30’ respectively. However, between those two available datasets, only crust 1.0 that is independent to the gravity dataset, whilst GEMMA is constructed based on the inversion of GOCE data. Like has been discussed by Szwillus et al. (2016) and also in Chapter 3, a truncated topography and crustal model for gravity gradients analysis at satellite altitude could lead to errors. So, until this manuscript writing, crust 1.0 dataset is the best crustal model that I can use.

The Moho depth in global crustal model crust 1.0 is based on 1° × 1 ° averages of an updated database of crustal thickness data from active source seismic and receiver function studies (Laske et al., 2013). The sediment and crustal structures in crust 1.0 model are predicted from globally averaged data from active seismic method and deep drilling profiles. In case where there is no seismic measurement available, the crustal structure is predicted by a generalization to similar tectonic and geological setting.

Figure 4.21 shows the Moho depth from crust 1.0 model on IBM zone. In crust 1.0 model, the Moho depth along the IBM back-arc system is approximately less than 10 km,

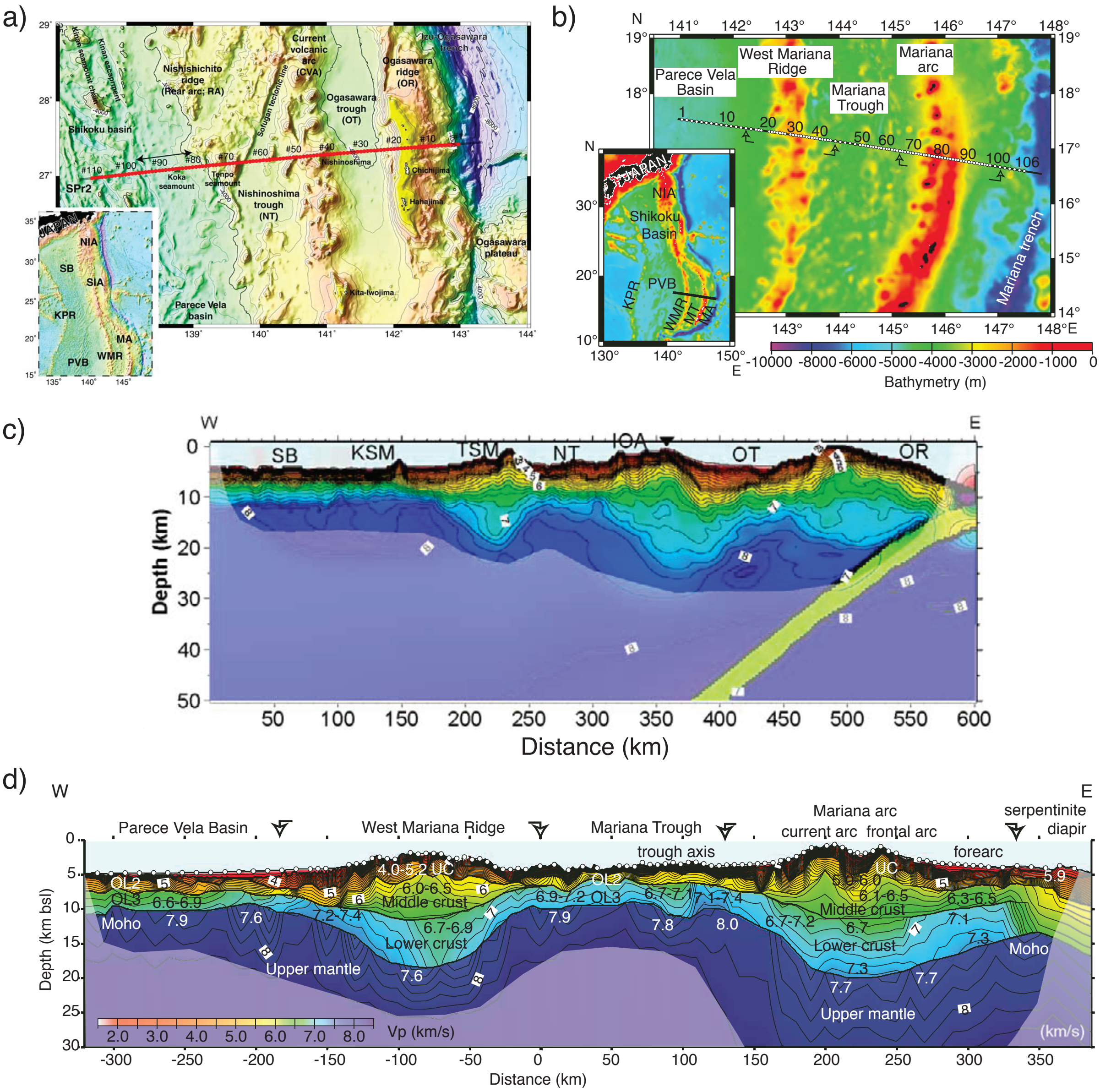

Figure 4.20: Velocity model of Izu and Mariana back-arc system. Bathymetry map of Izu (a) and Mariana (b) back-arc system. Inset shows the profile superimposed on bathymetry of entire Izu-Bonin- Mariana arc, and locates Parece Vela Basin (PVB), West Mariana Ridge (WMR), Mariana Trough (MT), Northern Izu arc (NIA), Kyushu Palau ridge (KPR), Mariana arc (MA), and Mariana Trench. The seismic profile at each zone is indicated by red line in (a) and black line in (b). (c) shows the final velocity model of Izu back-arc system from seismic tomography inversion in Takahashi et al. (2009), while (d) shows the final model for Mariana back-arc system by Takahashi et al. (2007).

contrary to the profile of velocity model by Takahashi et al. (2007) and Takahashi et al. (2009) that illustrate of crustal thickening along the islands and volcanic arc as parts of the back-arc system. The comparison Moho depth along the same profiles (Figure 4.21 in red lines) from crust 1.0 model and tomographic inversion results in Takahashi et al.

(2007) and Takahashi et al. (2009) is illustrated in Figure 4.22. The difference between those models can reach up to 25 km of depth in certain location, particularly below the Mariana and Ogasawara arcs and ridges.

Figure 4.23 show the gravity gradients effect due to the global crustal layer by crust 1.0. The estimation of crustal effect is performed by applying a contrast density of 500 kg m^{-3} between crustal and mantle layer. The obtained results do not reflect the presence of thick arc crust on the back-arc. The inadequate accuracy of crust 1.0 model does not allow us to obtain the gravity gradients due to the crustal layer with an adequate precision. As a consequence, with the current availability and precision of crustal model datasets, estimation of slab structure is difficult to be achieved.

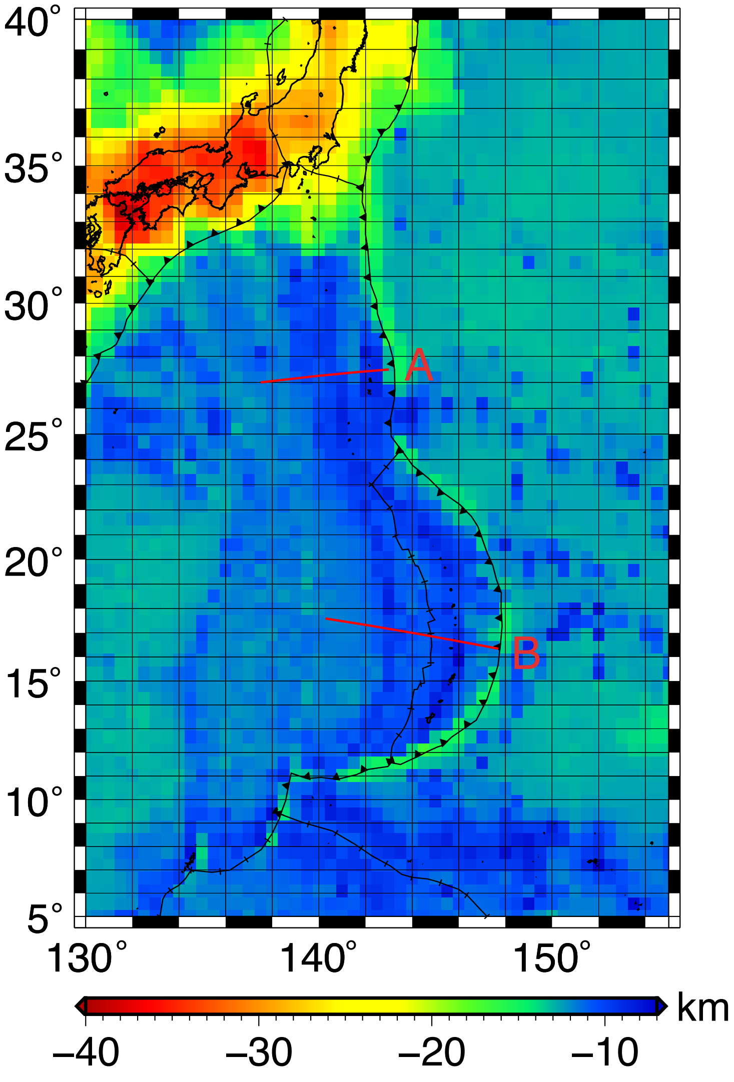

Figure 4.21: Moho depth crust1.0 (Laske et al., 2013)

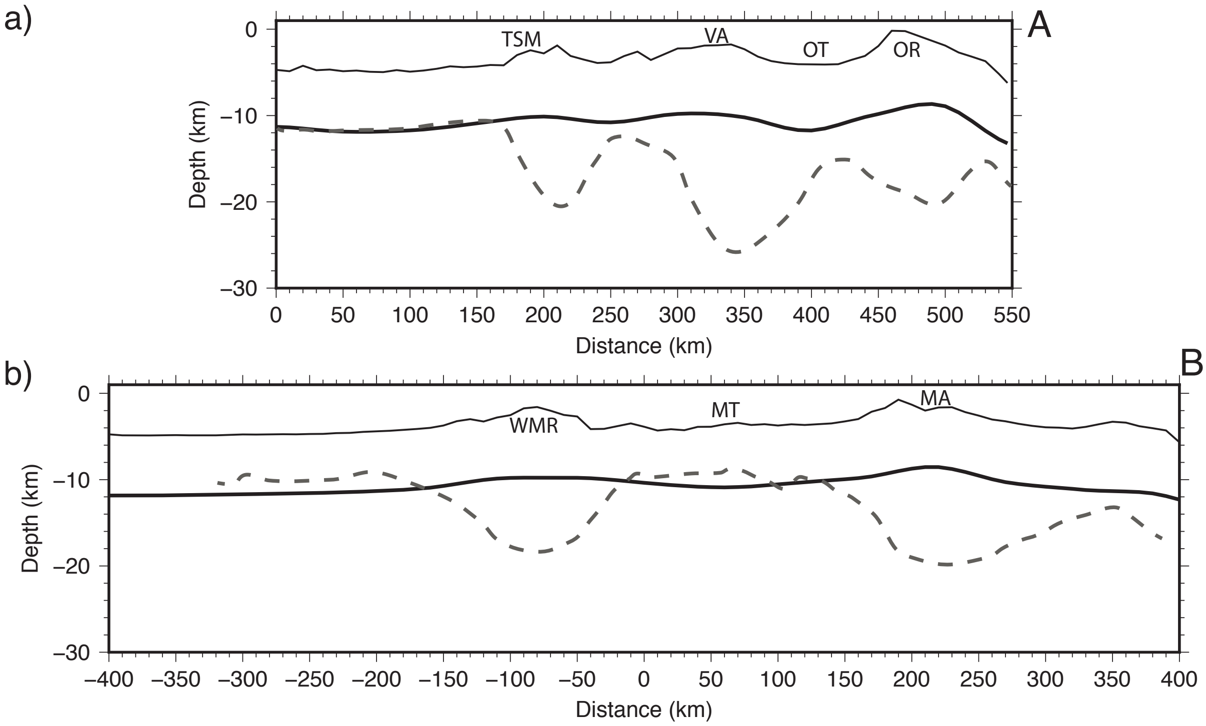

Figure 4.22: Comparison of Moho depth along profiles in Figure 4.20 between the model from crust 1.0 (Laske et al., 2013) and the tomographic inversion result after Takahashi et al. (2009) along profile A (a) and Takahashi et al. (2007) along profile B (b). The location of the profile is indicated in Figure 4.21. The profile from crust 1.0 is shown in black-bold line, whilst the results from Takahashi et al. (2009) and Takahashi et al. (2007) are in dashed-gray line. Bathymetry variation along the profiles is also provided in thin-black line. TSM: Tenpo Seamount, VA: Volcanic Arc, OT: Ogasawara Trough, OR: Ogasawara Ridge, WMR: West Mariana Ridge, MT: Mariana Trough, MA: Mariana Arc.

4.4. Discussion

Can we estimate the detailed geometry of a slab using GOCE dataset?

This is the question that we are trying to answer in this study. Although from the tests using synthetic model, we can decipher the second-order structures of a slab by regarding the gravity gradients spatial distribution, the application on a real geodynamic case results in different outcome. Based on GOCE data processing in this study, the answer of this question is difficult to be reached.

To be able to assess gravity gradients associated to a slab, a high precision of computation method and correct estimation of topography and crustal effect has to be done. To do so, the calculations are performed using GEEC. Validation processes in Chapter 2 shows

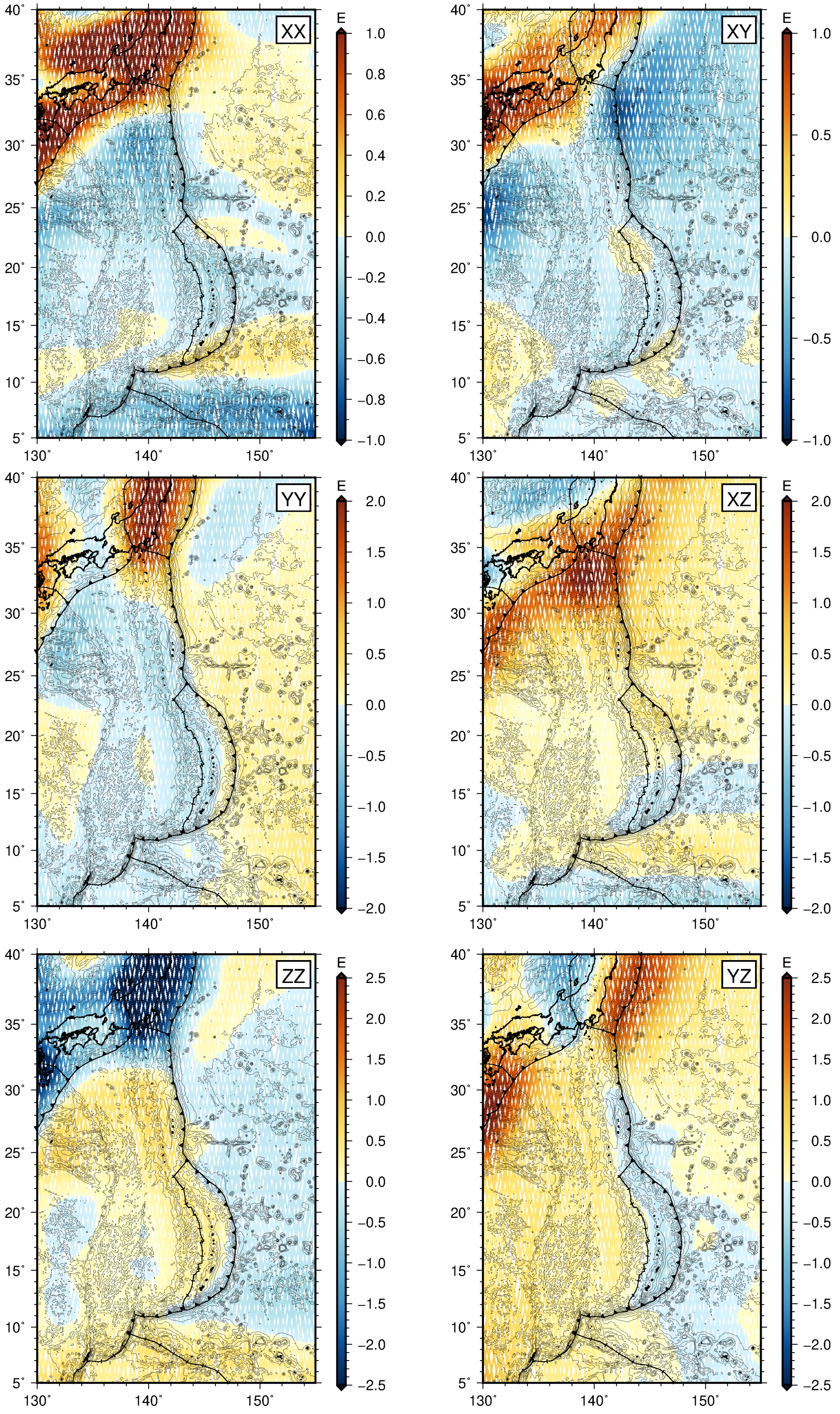

Figure 4.23: Gravity gradients of crust effect from global crustal model crust 1.0 on the IBM zone by Laske et al. (2013).

that GEEC is able to perform gravity gradient forward modelling with high precision.

GOCE dataset accuracy is better than 10 mE, that is good enough to extract the gravity gradient information due to the slab geometry (see Section 4.2.5.). Topography correction is performed by using a high-resolution dataset (GEBCO 2014) where the produced gravity gradients errors is less than the accuracy of GOCE dataset (Chapter 2). The crust model that is used in this study has a low resolution (i.e. 1°) and the discrepancy of its Moho depth on the IBM area can reach up to 25 km compared to the model from local geophysical observations. A poor estimation of crustal effect thus is the main source of the error.

Crustal model accuracy and its implication to the gravity gradients at satellite altitude

Lastly, we assess errors due to the Moho depth uncertainties using the crustal model crust 1.0 by Laske et al. (2013)). First, we impose on the Moho depth a constant offset of 1 km and 5 km (illustrated in Figure 4.24) and calculate its associated gravity gradients. The computation is performed at the position of GOCE measurements in the IBM study case. The discrepancies between the resulted gravity gradients from the reference model and from the offset models are then assumed as the errors. This approach show that the obtained errors in diagonal components are in skewed distribution (Figure 4.25a and c). With a constant offset of 1 km in the Moho depth model, errors in T_{zz} are approximately -120 mE, while errors in T_{xx} and T_{yy} are around 60 mE (Table 4.6). The errors obtained with a crust model with a constant offset of 5 km are greater than the one with 1 km offset, approximately -713 mE in T_{zz} and 300-400 mE in T_{xx} and T_{yy} components. While in the off-diagonal components, the obtained errors are quasi-normally distributed with a median value around 1-3 mE for the results using 1 km offset and 15-75 mE for the results using 5 km offset. This may indicate that the off-diagonal components are less sensitive to the depth variation than the diagonal components.

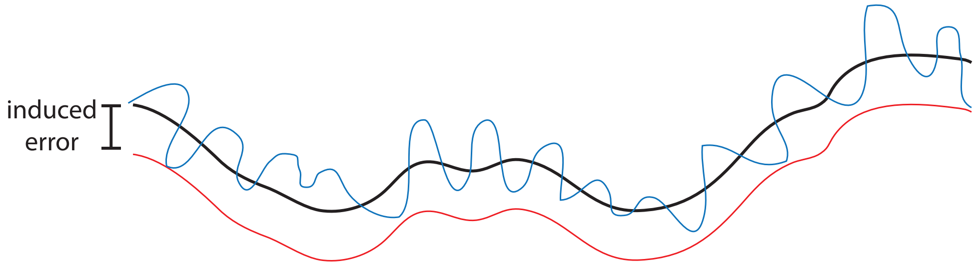

Figure 4.24: Scheme of how the variations of Moho depth are applied to the crust model. The black line illustrates the reference Moho depth. The red line illustrates the resulted variations after imposing a constant offset. The blue line illustrates the resulted Moho depth after adding random errors.

Second, we assume a normally distributed random offset with a range of 1 km and 5 km. By introducing these offsets to the crustal model, the results show that the error distributions in the diagonal components of gravity gradients follow the normal distribution of the imposed errors (Figure 4.25b and d). They also exhibit larger errors than the ones in the off-diagonal components, consistent with the results of the previous test. The largest error is obtained in T_{zz} with ~63 mE from a crust model with a precision of 1 km and ~369 mE from a crust model with 5 km of precision. Other statistic values can be found in Table 4.6. The errors obtained from random noise are approximately half times smaller than the errors obtained from a constant offset. It may indicate that the combination of positive and negative errors that related to the imposed depth acts as a counterbalance to the gravity gradients signature.

By considering the accuracy of GOCE observations, the errors obtained from a crustal model with 5 km of uncertainties are superior to the gravity gradients signatures in the synthetic tests (see Section 4.2.) to assessing the presence of the slab, the density distribution of a slab, and to estimate the slab edge (Table 4.7). The estimation of slab dip angle and its lateral variation cannot be performed using a crustal model with 5 km of accuracy because the errors (Table 4.6) are superior to the gravity gradients associated to those slab geometry properties.

With the use of a crustal model with 1 km of accuracy, the errors associated to the uncertainty of the crustal model is 80% lower than the errors obtained from 5 km of crustal model's uncertainty. Therefore, we can assess several more detailed properties of slab geometry (Table 4.7), but still very limited for certain slab properties. For the estimation of slab dip angle, the precision that we can obtain by using a 1 km of uncertainty is not better than 20°, when it is 10° if there is no additional error from crustal effect. Detection of lateral dipping variation and the location where it changes is very limited for a $\Delta\theta \geq 40°$. Any variation below that is very difficult to be detected. To be able to assess the lateral variation in more detail, the use of crustal model with an accuracy better than 1 km is required.

Table 4.6: Gravity gradients errors due to the precision of a crustal model.

Gradients	Constant offset error (mE)				Random error (mE)			
	-1 km		-5 km		±1 km		±5 km	
	median	std	median	std	median	std	median	std
T_{xx}	60	17	371	293	30	27	185	111
T_{xy}	0	6	15	269	0	14	3	61
T_{xz}	3	18	15	361	3	30	-6	128
T_{yy}	60	15	342	374	30	26	177	118
T_{yz}	0	18	-75	491	-1	30	-29	136
T_{zz}	-120	26	-713	572	-63	43	-369	186

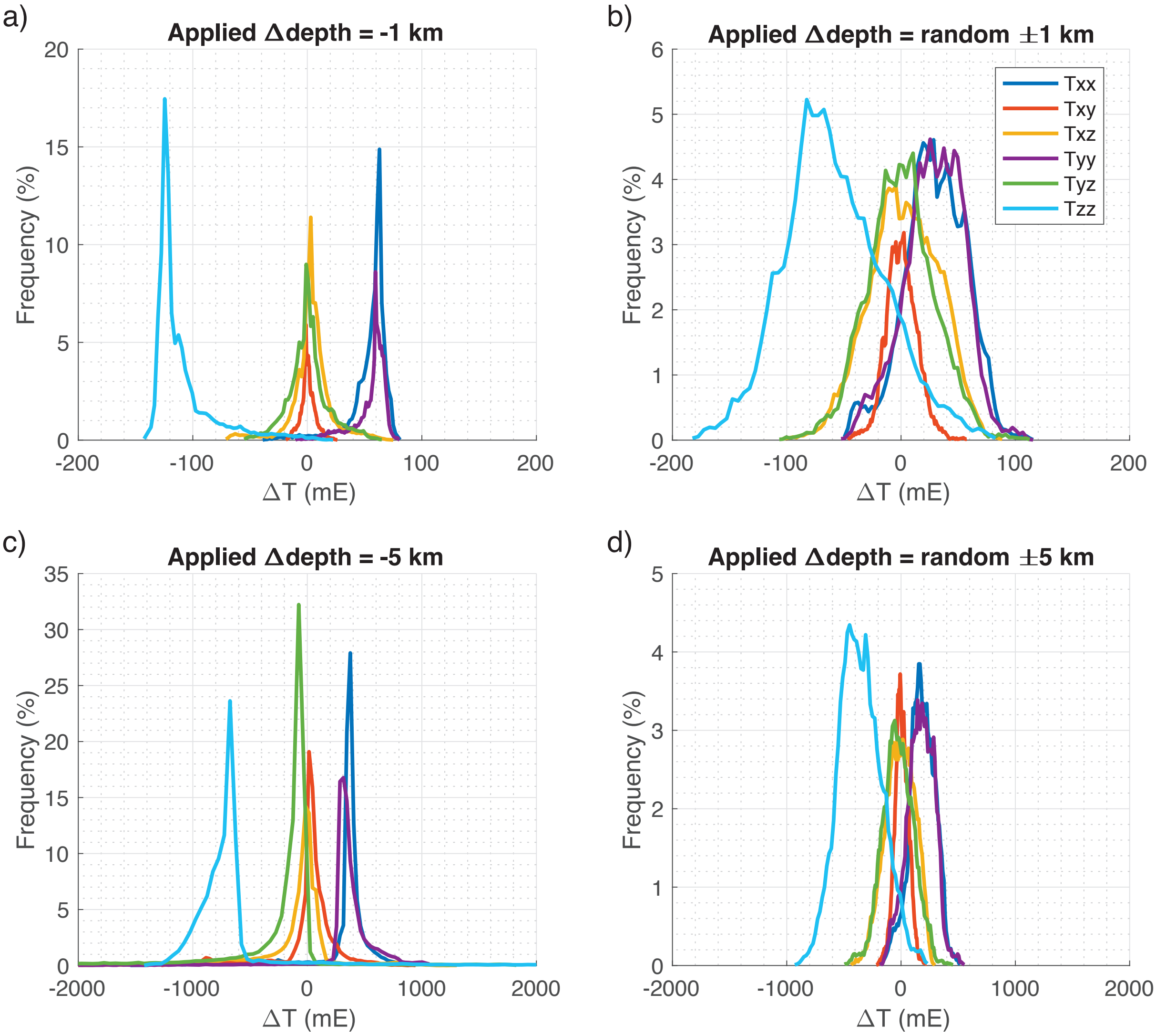

Figure 4.25: Gravity gradient errors due to the error of crustal model.

Table 4.7: Assessment of crustal model accuracies to estimate the detailed properties of slab geometry. The associated gravity gradient signatures are based on synthetic tests in Section 4.2. The errors due to the uncertainties in crustal model for each component are summarized in Table 4.6. (✓-detectable, ×-undetectable).

.	Slab Properties	Magnitude (mE)	Gradients	Notes	Crustal model uncertainties	
					5 km	1 km
0 order						
	The presence of subducting slab	600-1100	yz, yy, zz	Model 2	✓	✓
		260-500	yz, yy, zz	Model 3	✓	✓
1st order						
	Density distribution of a slab	600, 500, 350	zz, yy, yz	Between model 2 and 3	✓	✓
	Slab edge	400	xz	Model 2	✓	✓
		125	xz	Model 3	×	✓
	Slab dip angle	70	yy, zz	$\sigma\theta = 10°$	×	limited to $\sigma\theta \geq 20°$
2nd order						
	Lateral variation of slab dipping angle	104-113	yy, yz, zz	$\Delta\theta = 30°$	×	limited to $\Delta\theta \geq 40°$
		170-186	yy, yz, zz	$\Delta\theta = 40°$	×	✓
	Location of where the slab dip changes	14-44	xx, xy, xz	$\Delta\theta = 30°$	×	×
		25-76	xx, xy, xz	$\Delta\theta = 40°$	×	very limited

4.5. Conclusion

In this chapter, I present some approaches that I did in attempt to see if we can extract the detailed information about the structure of a slab, including the distribution of density in the slab, slab border, dip angle, and its lateral dip variation, using gravity gradients at satellite altitude.

The tests using synthetic models of subduction show that the gravity gradients are sensitive enough to assess the density distribution in the slab, with a variation of 350-600 mE in T_{yz}, T_{yy}, and T_{zz} and with a wavelength of 8°. The slab edge results in the variation greater than 125 mE in T_{xz} with a wavelength of $\sim$10°. Estimation of dip angle of a slab could be performed with a precision no better than 10° by assessing the variations in T_{yy} and T_{zz}. Lateral dip variation of a slab is also possible to be detected. The lateral dip variation of more than $\Delta\theta \geq 30°$ results a variation $\sim$100 mE in T_{yz}, T_{yy}, and T_{zz} components. The location where the dip changes abruptly can be estimated using T_{xx}, T_{xy}, and T_{xz} components, where it produces 14-40 mE of anomaly with a wavelength of 5-7°. The obtained gravity gradients anomaly associated with these detailed structures are superior than GOCE accuracy (10 mE) and spatial resolution (100 km) (cf. Gruber et al., 2010b; Drinkwater et al., 2003). The results from synthetic models are therefore promising.

Horizontal gravity gradient components are normally less used than the vertical gravity gradient in gravity gradients applications. The tests using synthetic models in this study highlight that the horizontal components, that are sensitive to the limit and lateral variation of geometry of a structure, can also provide useful information to constrain the detailed geometry of a structure.

I then applied this approach using GOCE gravity gradients in Izu-Bonin-Mariana (IBM) zone. This zone is chosen because the geometry is relatively simple and elongated in the south-north orientation that is suitable to test the usefulness of horizontal gradients. This zone is also a convergence zone between oceanic plates, thus I can avoid any transition between oceanic-continental plate and the geometry of the subduction is not perturbed by the presence of accretion prisms.

However, in the application to a real subduction case, extracting gravity gradients information due to the subduction geometry is not straightforward. Panet et al. (2014) have shown that it is possible to detect the presence of an ancient slab in depth by using GOCE data. However, this study in IBM zone exhibits that to perform a second-order structure detection, particularly the lateral variation along the subduction, is difficult to be achieved. Performing an optimum calculation to estimate the effects of a body mass is required, and having a high resolution and high precision dataset of both topography and crustal model is mandatory.

This study is unsuccessful to decipher the information about the second-order detailed geometry of a subducting slab using GOCE gravity gradients dataset. The main reason that could be invoked is the accuracy and the spatial resolution of the available crustal models that remains too low and thus it introduces and additional error to the residuals of gravity gradients.

To be able assessing the density distribution of a slab and the slab edge, a global crustal model with 5 km of accuracy is required. Whilst for assessing the dip of a slab and its extreme lateral dip variation, a global crustal model with an accuracy 1 km is required. To estimate the location of slab lateral variation, a global crustal model with an accuracy better than 1 km is mandatory.

This study also provides guidance for the development of satellite missions or other Earth's gravity observation. GOCE's altitude still seems too high to assess the detailed geometry of lithospheric structures. By descending the altitude of acquisition, the magnitude of the signal could be amplified by avoiding the noise due to the data downward continuation.

Performing a joint interpretation of gravity and gravity gradients datasets from various altitudes of acquisition, i.e. ground measurement, airborne survey, and satellite mission could also be a solution. The signal associated to crustal and slab effect can be distinguished using wavelength properties at each dataset.

Conclusions and Perspectives

Scientific Context

Nowadays, the scientific community has as its disposal a unique gravity and gravity gradient dataset with unprecedented accuracy and spatial resolution. This new dataset enhances our knowledge of the Earth gravitational field at various scales and wavelengths; small wavelengths are inferred from ground survey whereas medium to long wavelengths are documented from airborne and satellite measurements. In parallel with gravimetry, the improvement of digital elevation model obtained from satellite observations, such as Pléiade, also provides more detailed information about Earth's structure geometry. Together, these novel datasets provide a great opportunity to better understand the Earth's structures and dynamics at local, regional, and global scales.

To optimize the use and the interpretation of these high-quality datasets, the proper techniques in the gravity data processing should be used, hence the quality of the data can be maintained. This thesis consists of a series of studies aiming to improve the precision in the chain of gravity and gravity gradients data processing for geodynamics studies, in particular, to perform joint approaches combining ground, airborne, and satellite gravity-related datasets.

To realize this aim, several attempts have been made. I started with the development a computation code GEEC that is capable to compute precisely both the gravity and gravity gradients effects of any mass body, regardless of its geometry and its distance from measurements. Next, I presented a first application dedicated to the assessment of optimal parameters required to calculate topography effects which is an essential step for the interpretation of gravity-related data. In this study, I paid a special attention to control parameters, such as DEM resolution or topography truncation distance for local, regional, and global applications. In the last chapter, I applied GEEC to the Izu-Bonin-Mariana subduction zone to assess the degree of details in lithospheric structure images that can be deciphered from GOCE measurements.

Results

In this thesis, I developed a dedicated code to calculate the gravitational effect of Earth body mass at various scales, local to global scale, at various altitudes, from ground, airborne, and satellite measurements, named GEEC (Gal Eötvös Earth Calculator). GEEC is a novel Matlab-based computation tool to calculate the gravity and gravity gradients effect of an irregular mass body based on a the analytical solution of the expansion of line integrals of a polyhedron body. Following gravity solution by Singh and Guptasarma (2001), I developed a new formula of gravity gradients that is implemented in GEEC's algorithms. Beside for topography effect estimations, GEEC is also able to calculate the gravitational effects of other bodies, both in spherical approximation that is highly recommended for Earth-related studies and also in planar approximation for a simple mass geometry.

GEEC is easy to use, including all processes from computation to visualization of the obtained result. Beside of its simplicity, the application of GEEC for gravity and gravity gradients forward modelling offers other advantages:

- GEEC deals with body mass in various scales regardless of its geometry, in other words, it has a high capacity to preserve the complexity of the body mass geometries at all scales.
- GEEC supports the computation at any altitude and any spatial distribution of measurement points regardless of the extent of the study area. This allows joint approaches combining datasets obtained from satellite, airborne, to ground surveys.
- In gravity or gravity gradients processing, GEEC can serve as a all-in-one tool to accomplish gravitational data correction, data reductions, and forward model in stochastic methods.
- High numerical precision in Matlab makes a robust computation process.
- GEEC allows parallel computation that provides an efficient computation time.

Validation processes in local, regional, and global scales confirm the robustness of GEEC's performance where the resolution of the model, that depends on both size of the body mass and its distance from the measurement point, controls strongly the accuracy of the results.

The contribution of this thesis for geodynamics lies in two parts. Firstly, I investigate the importance of distant topography and its consequences to the precision of topography correction. Topography has a major contribution in the Earth gravitational attraction, therefore the estimation of topography effects must be carefully considered in the processing of gravity data, especially in areas with rugged topography or at large-scale studies.

This study confirmed that the precision in estimating the gravitational effect of Earth topography is mostly controlled by the truncation distance of which the topography is considered. The classical distance of 1.5°, proposed by Bullard (1936), is confirmed in this study to be too narrow for regional application and also for zones with high topography variations. By quantifying the relative truncation errors from end-members regions in terms of topography roughness within and around the zones, this study allows to create a guideline to determine the optimal truncation distance as a function of dimension of study area to assess the topography effect.

Our results suggest that the use of global topography in the estimation of topography effect is mandatory for the following types of application:

- Gravity and gravity gradient applications at global scale.
- For the analysis of the spatial variation of gravity and gravity gradients in its absolute value, regardless of its scale of application. Application using satellite observation datasets can be categorized in this case.
- For high-accuracy gravity studies that require a very high precision in the estimation of topography effect (better than 1 mGal and 10 mE).

For studies at local and regional scales that are based on the analysis of relative spatial variations of gravity-field, i.e. only differences between values accross the region matter while the absolute value is ignored, truncated topography at a specific distance can be adequate. From this study,

- At the first order of approximation, by using the dimension of the zone d as the topography truncation distance ψ_t, i.e. $\psi_t = d$, it ensures to obtain topography effect with a precision between 1 and 10 mGal, with 5 mGal in average.
- At regional scale of gravity application, where the dimension is smaller than 20°, the use of 15° of truncation distance ensures to obtain a precision of $\sim$1 mGal. This truncation distance applies to all measurement altitudes.
- In gravity gradient applications at regional scale, the topography effect with a precision of 1 E for ground and airborne altitude can be obtained using a truncation distance of $\geq$8.5°. While for gravity gradient at satellite altitude that requires a precision of 0.01 E, it can be fulfilled by using a truncation distance of $\geq$40°.

For the second application in this thesis, I addressed the issue: Are GOCE observations relevant to obtain a detailed image of the structure of a slab, including its detailed geometry and lateral variation? The accuracy and spatial resolution of GOCE, 10 mE and 100 km respectively, are used as the threshold in this study to assess which properties of slab geometry that can be detected by GOCE observations.

Resulted gravity gradients modelling using synthetic slab model, computed at GOCE mean altitude (255 km), exhibit that the presence of the slab can be easily detected by GOCE observations. The excess mass related to the slab generates positive anomaly in T_{zz} with a magnitude of 1100 mE and a wavelength of $\sim$10°, negative anomaly in T_{yy} with a same magnitude and wavelength as T_{zz}, and in T_{yz} with a half-wavelength of 5° and an amplitude of $\sim$500 mE.

By analyzing the gravity gradients responses to the variations of more detailed properties of the slab geometry, our results demonstrate that:

- Gravity gradients are sensitive to the density distribution of a subducting slab. The presence of crustal layer with negative density contrast on a slab generates lower magnitude at all gravity gradient components with a variation of $\leq$ 600 mE, notably for T_{yy}, T_{yz} and T_{zz} components. The presence of this negative density contrast also generates oscillations with a shorter wavelength (~4°) along a profile perpendicular to the trench.

- The subduction edge is most noticeable in T_{xz} component with negative anomaly with a magnitude of $\geq$125 mE and ~10° of wavelength, where x-direction is parallel to the trench.

- Estimation of slab dipping angle is possible to be performed using GOCE, with precision no better than 10°. The difference of 10° of slab dip produces ~75 mE of variation in T_{zz} and T_{yy}.

- Lateral variation of slab dipping angle produces remarkable signal variation that can be detected by GOCE, particularly in T_{yy}, T_{yz}, and T_{zz} components. Lateral variation with $\Delta\theta \geq 30°$ produces variations with magnitude >100 mE in T_{yy}, T_{yz}, and T_{zz}.

The slab properties that mentioned above, such as the density distribution of a slab, the slab edge, the slab dipping angle, and its lateral dipping variation is theoretically can be detected by GOCE observations.

But, it is difficult to locate where the slab dip changes using GOCE observations, especially when there is a presence of crustal layer on the upper part of the subducting slab. The most remarkable anomaly is resulted in T_{xz} with a magnitude of <76 mE and with ~6.5° of half-wavelength. Theoretically, these signal properties are detectable by GOCE. However, if the presence of noise in the real observations is also taken into account in the analysis, this detailed structure property is difficult enough to be interpreted.

However, the results from synthetic models are only applicable to a real case if the effects of mass layers above the slab, i.e. topography-bathymetry and crustal structure, are properly removed. In the application to the Izu-Bonin-Mariana (IBM) subduction zone, topography and bathymetry effects are successfully removed. However, due to the low spatial resolution and accuracy of the available global crustal model, the crustal effect are not successfully removed thus the residual of gravity gradients is still interfered by the presence of crustal effect. Therefore, the residual gravity gradients signal cannot properly explain the detailed structures of IBM slab, such as the border of the slab, the slab dip angle, and its lateral variation. This study underlines the importance to use global Earth mass model, including topography, bathymetry, and crustal model, with a high accuracy and spatial resolution in order to interpret the second-order of slab geometry, for example the location of slab tear.

Our results suggest that to be able to assess the first-order properties of the slab geometry using GOCE observations, including slab edge, its density variation, and slab dip, the reduction of crustal effect requires a global crustal model with an accuracy of 1 km. While for assessing the second-order properties of the slab geometry, such as its lateral dip variation and the location where the dip angle change, the use of global crustal model with an accuracy better than 1 km is mandatory.

Perspectives

During this thesis, I showed that the precision during the chain of gravity-related data processing is essential for the interpretation in geodynamics studies. Factors that play an important role to achieve the expected precision include (1) the computation techniques itself, (2) the accuracy and the spatial resolution of gravity data, and (3) the properties of the used Earth mass model (in this case is topography and crust models), including its spatial resolutions, truncation distances or spatial extents, and accuracies.

I showed that GEEC is capable to encompass most essential steps in the chain of gravity-related data processing, including gravity correction and reduction processes as well as in the stochastic process as a part of the process to interpret the results. In order to make GEEC more advanced, flexible, and time-saving, particularly for computation of topography correction, a systematic study about the role of the truncation distance, the resolution of digital terrain model, the altitude of measurement and the morphology, in term of roughness of topography of a zone is now required. This can be achieved using synthetic topography morphology based on the use of well-known parameters, such as Hurst exponent (e.g., Candela et al., 2009; Persson, 2015). By completing this task and developing an automation algorithm to be implemented in GEEC, an adaptive discretization of triangle mesh that constructs the polyhedron can be achieved.

The approaches to assess the detailed geometry properties of a slab in this study are performed using static models of a slab without taking into account the dynamic aspects at depth. For future works, this aspects could be considered in the modelling to better understand the gravity gradient signatures related to the subducting slab.

The case study of Izu-Bonin-Mariana zone also underlines the necessity of well-constrained mass geometry model to perform a precise data processing and to obtain results that are interpretable. Crustal model construction with a high-accuracy and spatial resolution is thus required to better constrain mass variations at depth, including its detailed geometry properties. Geophysical studies and data merging of seismic tomography inversion results are then highly encouraged. A combination of gravity-related datasets at various altitudes also can be a solution, where the effect of Earth crust and other masses at depth, such as a subducting slab, can be separated by considering the different wavelengths of gravity or gravity gradients (spectral analysis).

As demonstrated in this study, the gravity gradient signatures related to the lateral variation of a subducting plate is relatively weak, only slightly superior to the accuracy of GOCE dataset. This aspect limits the use of GOCE dataset at its original altitude to detect and to localize second-order geometry properties of a slab. These results highlight the interest to measure the Earth's gravity gradients field at a lower altitude than GOCE's. For example, installing an atomic interferometry absolute gravimeter on a balloon that flights up to 40 km of altitude in the framework of HEMERA Project coordinated by the French space agency CNES (Centre National d'Etúdes Spatiales) (HEMERA H2020, 2018) could be envisaged for future works to produce a stronger gravity response with a better spatial resolution.

Although the gravity gradients from GOCE mission appears inadequate to constrain the details of a slab structure properties, they allow the detection of deep mass variations at a large scale (e.g., Panet et al., 2014) as well as the structure properties in the first order (i.e. border of a subducting plate, slab dipping variation, and density distribution model), as shown in Chapter 4. This aspect could be developed in future works to open a perspective about detection of slab termination using gravity gradients data. For example, this approach should be applicable to delineate the geometry of Yakutat terrane in southeastern Alaska that can be related with the seismicity of the zone (cf. Mazzotti and Hyndman, 2002; Eberhart-Phillips et al., 2006; Worthington et al., 2012). Detection of the geometry of an anomaly source or to delineate the segmentation of seismicity on a subduction zone (cf. Song and Simons, 2003) by using tensor deconvolution method (e.g., Beiki, 2010; Mikhailov et al., 2007) could be also considered in the analysis of gravity gradients signal in future works.

Lastly, the algorithm established in this thesis to calculate the gravity effect is based on the solution by Singh and Guptasarma (2001). This solution is also adapted to calculate the 3D magnetic field of a polyhedron source. Hence, in a near future, algorithms to calculate the magnetic field of an anomalous body will be also integrated in GEEC to support the study of the contribution of magnetic data, from SWARM satellite mission for example.

Appendices

Appendix A

Compensation degree of Airy isostasy derived from topography and satellite gravity gradient

In the beginning of my thesis, I participated in the production of paper by Cadio et al. (2016). This method highlight the importance of topography contribution in the geodynamical processes.

Geophysical Journal International

Geophys. J. Int. (2016) **207,** 645–654
Advance Access publication 2016 August 10
GJI Geodynamics and tectonics

doi: 10.1093/gji/ggw281

A new approach to assess isostatic compensation of topography in continental domain from GOCE gravity gradients

Cécilia Cadio,[1] Anita Saraswati,[1] Rodolphe Cattin[1] and Stéphane Mazzotti[1,2]

[1] *Géosciences Montpellier, Université de Montpellier and CNRS UMR* 5243, *CC*060 *Place E. Bataillon, F*-34095 *Montpellier Cedex* 05, *France. E-mail: cecilia.cadio@gm.univ-montp2.fr*
[2] *School of Earth and Ocean Sciences, University of Victoria, PO Box* 3065 *STN CSC, Victoria, BC V*8*W*3*V*6, *Canada*

Accepted 2016 July 25. Received 2016 July 21; in original form 2016 January 26

SUMMARY

Estimating how topography is maintained provides insights into the different factors responsible for surface deformations and their relative roles. Here, we develop a new and simple approach to assess the degree of isostatic compensation of continental topography at regional scale from GOCE gravity gradients. We calculate the ratio between the radial gradient observed by GOCE and that calculated from topography only. From analytical and statistical formulations, simple relationships between this ratio and the degree of compensation are obtained under the Airy–Heiskanen isostasy hypothesis. Then, a value of degree of compensation at each point of study area can be easily deduced. We apply our method to the Alaska-Canada Cordillera and validate our results by comparison with a standard isostatic gravity anomaly model and additional geophysical information for this area. Both our GOCE-based results and the isostatic anomaly show that Airy–Heiskanen isostasy prevails for the Yukon Plateau whereas additional mechanisms are required to support topography below the Northwest Territories Craton and the Yakutat collision zone.

Key words: Numerical approximations and analysis; Satellite geodesy; Gravity anomalies and Earth structure; Continental margins: convergent; North America.

1 INTRODUCTION

An important question in geodynamics, especially for continental domains, is to distinguish the part of the topographic signal isostatically compensated by either crustal roots (Airy–Heiskanen model) or lateral density variations (Pratt–Hayford model) from the one associated with lithosphere rigidity (Vening-Meinesz model; Watts 2001) and present-day mantle convection (Braun 2010; Flament *et al*. 2013). Topography variations are associated with gravity anomalies for which the amplitude is not only related to mass anomalies at the surface but also to compensating masses at depth. Indeed, the spatial variations of gravity are directly related to the density anomalies located in both the crust and mantle. Joint analysis of topography and gravity data can thus help identify the isostatic component from the dynamic one in the topographic signal, and gives an estimate of their contribution (Hager *et al*. 1985; Watts 2001; Cadio *et al*. 2012).

Owing to space gravity missions, unprecedented high-quality data are now available on the entire Earth surface and improve considerably our knowledge of gravity field (Tapley *et al*. 2005). In particular, the GOCE mission (Gravity Field and Steady-State Ocean Circulation Explorer; Drinkwater *et al*. 2003) allows the study of features as small as 80 km in continental orogens (Hirt *et al*. 2012; Bruinsma *et al*. 2014), often characterized by a sparse spatial coverage of available ground gravity data due to high reliefs. Such resolution is made possible by the low altitude (~255 km) of the GOCE satellite, which does not provide measurements of the gravity field but of its variations in the three spatial directions (Rummel *et al*. 2011). Beyond the resolution improvement compared to previous space gravity missions, GOCE gravity gradients are also much more sensitive to the spatial structure and directional properties of the attracting masses than classical observation of gravitational intensity (Mikhailov *et al*. 2007).

These satellite gravity gradients constitute a new class of observations that requires the development of new methods in order to extract information. In solid Earth geophysics, analyses of GOCE gravity gradients have been mainly developed to address the global Earth's internal structure at crustal (Reguzzoni *et al*. 2013), lithospheric (Bouman *et al*. 2015) and mantle (Panet *et al*. 2014) level. At a regional scale, GOCE gravity data have been used to identify geological structures (Álvarez *et al*. 2012; Mariani *et al*. 2013; Shin *et al*. 2015).

Here, we propose a new and simple approach to assess the mechanism and degree of isostatic compensation in a given region using GOCE gravity gradients. We use analytical and statistical formulations to compute the degree of topography compensation under the Airy–Heiskanen isostasy hypothesis. This allows identifying areas for which this hypothesis is valid and those requiring different or additional compensation mechanisms. Thus, our approach provides complementary information to usual analysis of the geoid to

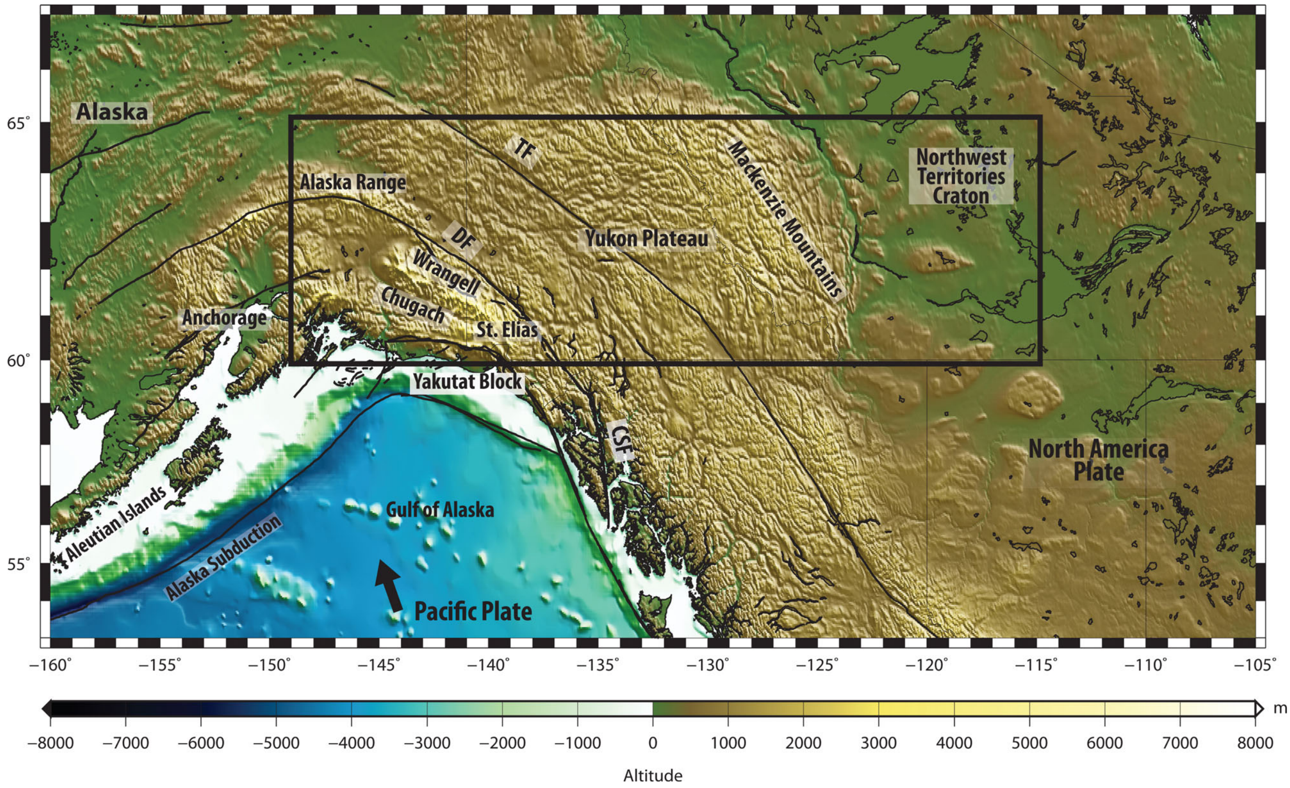

Figure 1. Topography of the NW American cordillera. Thin black lines show some of the primary faults for reference (DF, Denali Fault and TF, Tintina Fault). The arrow indicates the motion of the Pacific Plate relative to North America. The black box marks the study area.

elevation ratio used to estimate the apparent compensation depth of a specific topographic structure (Chase *et al*. 2002; Cadio *et al*. 2012). Also, on continental areas, the gravity gradients measured from the GOCE satellite provide a homogeneous coverage of higher resolution than previously available gravity data. This improvement in resolution is in part related to the technique of differentiation. GOCE gravity gradients are thus better suited to study continental structures at the regional scale. Beyond this benefit, the new approach allows us to interpret a new kind of data defined in different spatial directions. Although we focus on the radial gravity gradient in this study, our method can constitute a basis to explore the others components.

We test our method over the NW America orogen (Fig. 1), which is associated with the accretion of allochthonous blocks carried by the Pacific plate in the corner of the Gulf of Alaska (e.g. Lahr & Plafker 1980; Plafker *et al*. 1994). The study area extends from the Yakutat collision zone along the continental margin to the Canadian Craton, spanning the entire Alaska-Canada Cordillera. The topography pattern, the crustal thickness and the isostatic compensation mode are well defined in most of this region and vary significantly (Lewis *et al*. 2003; Hasterok & Chapman 2007; Mazzotti *et al*. 2008), making this area particularly well adapted to validate our method.

In the following, we present our approach to estimate the degree of the local isostatic compensation of the topography in continental domains at regional scale. First, we explain the methodology from which the degree of compensation is deduced. We introduce the GOCE gravity gradients and present the formulations obtained for a synthetic model. Next, we apply our approach to the NW America orogeny. Finally, we discuss the results in terms of isostatic and dynamic topography in the region.

2 METHODS

In our approach, the degree of compensation α is estimated from GOCE measurements. First, we calculate the ratio β between the radial gradient observed by GOCE and that modeled from topographic contribution only. Next, using a simple cylinder model, we obtain a relationship between α and β under the Airy–Heiskanen isostasy hypothesis. In this way, a degree of compensation can be deduced at each point of the study area.

2.1 GOCE and topography gravity gradients

The European Space Agency's GOCE mission provides data with unprecedented global resolution (Bruinsma *et al*. 2014). GOCE directly measures, on a ∼255-km-altitude orbit, the six components of the Earth's gravity gradient tensor (T_{xx}, T_{yy}, T_{zz}, T_{xy}, T_{yz}, T_{zx}) corresponding to the first spatial derivatives of the gravity in three directions (Rummel *et al*. 2011):

$$T_{ij} = \frac{\partial g_i}{\partial j} = \frac{\partial g_j}{\partial i} = T_{ji}. \qquad (1)$$

The GOCE High-level Processing Facility (Fuchs & Bouman 2011) expresses the gradients in the Local North Oriented Frame (LNOF). In this right-handed North-West-Up frame, the radial gradient T_{zz} gives an isotropic view of masses whereas the others derivatives underline masses orthogonal to the differentiation directions.

In this study, we use the gravity gradient grid at 255 km above the WGS 84 reference ellipsoid established by Bouman *et al*. (2016). The gradients are given in the LNOF frame with a resolution of 0.2 deg. The grid combines the GOCE gradients measured during the period from 2010 February 1 to 2013 November 11 for the small and intermediate scales (<700 km) and GRACE (Gravity Recovery

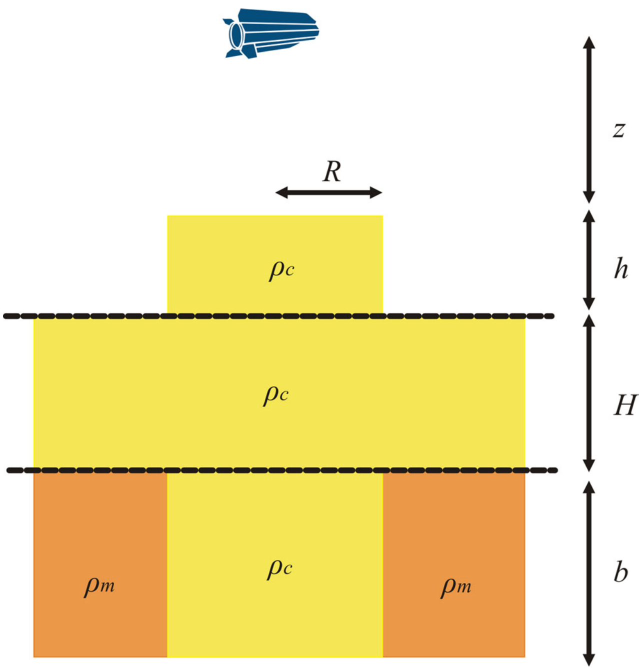

Figure 2. Cylinder model of the topography with its compensation following the Airy–Heiskanen isostatic model with R, the radius of the cylinder, h the elevation, H the hydrostatic equilibrium crustal thickness, b the thickness of the crustal root, ρ_c the crustal density and ρ_m the mantle density. The satellite is at altitude $z + h = 255$ km above the ellipsoid.

and Climate Experiment) data for longer wavelengths. Based on satellite data only, it therefore provides a precision over the whole Earth of 0.01–0.06 E (Eötvös, with $1\ \mathrm{E} = 10^{-9}\ \mathrm{s}^{-2}$) for the T_{zz} component (Panet *et al.* 2014). In the following, we consider the signal as significant when its amplitude is above 0.05 E.

The gravity gradient due to topography is given by the GeoExplore project (Grombein *et al.* 2013, 2014; Bouman *et al.* 2016). The topographic contribution is estimated from the spherical harmonic model RWI_TOPO_2012, complete to degree and order 1800 (Grombein *et al.* 2014). In this model, the DTM2006.0 topography (Pavlis *et al.* 2007) is decomposed into three layers corresponding to rock, water and ice masses with density values of 2670, 1000 and 920 kg m^{-3}, respectively.

2.2 Synthetic model

2.2.1 Model parameters

We evaluate the contribution of a partially or totally compensated topography in the radial component of the gravity gradient tensor from synthetic models. We assume a local isostatic compensation following the Airy–Heiskanen model in which the topography is accommodated by variations in Moho depth, the crust having a constant density (Fig. 2). The gravitational signal of a compensated topography is thus related to both the topographic mass excess and the crustal root mass deficit. In order to derive simple analytical expressions, we approximate a given topography and the associated crustal root as a superimposition of two cylinders separated by a distance H corresponding to a reference crust (Fig. 2). Parameters of this model correspond to the cylinder density, height and radius. The density value is the crustal density ρ_c for the topography and the crust–mantle density contrast $\Delta\rho = \rho_c - \rho_m$ for the root. The thickness b of the root is calculated from the height h of the topography:

$$b = -\alpha \frac{\rho_c}{\Delta\rho} h, \tag{2}$$

where α is the degree of compensation. For $\alpha = 1$, the topography is totally compensated in the Airy–Heiskanen hypothesis, whereas $\alpha > 1$ and $\alpha < 1$ are associated with an over- and undercompensated topography, respectively. The two cylinders having the same radius R, a model is thus described by a set of six independent parameters: $(\alpha, \rho_c, \Delta\rho, h, R, H)$.

2.2.2 Gravity and gravity gradient

The vertical component of the gravitational attraction Δg due to the two-cylinder model can be analytically calculated above the centre of the cylinder as (e.g. Turcotte & Schubert 2002):

$$\Delta g = \Delta g_{\mathrm{topo}} + \Delta g_{\mathrm{crustal\ root}} \tag{3}$$

where

$$\Delta g_{\mathrm{topo}} = 2\pi G \rho_c \left(h + \sqrt{z^2 + R^2} - \sqrt{(z+h)^2 + R^2} \right)$$

$$\Delta g_{\mathrm{crustal\ root}} = 2\pi G \Delta\rho \times \left(b + \sqrt{(z+h+H)^2 + R^2} - \sqrt{(z+h+H+b)^2 + R^2} \right) \tag{4}$$

with G the gravitational constant (Table 1) and z the distance above the upper surface of the topography cylinder (Fig. 2). Here, to be consistent with GOCE data, the measurement point is held at altitude $z + h = 255$ km above the ellipsoid.

As the GOCE gravity gradient is the first vertical derivative of Δg, the analytical radial component T_{zz} is derived from eqs (3) and (4):

$$\mathrm{T}_{zz} = \frac{\partial \Delta g}{\partial z} = \frac{\partial \Delta g_{\mathrm{topo}}}{\partial z} + \frac{\partial \Delta g_{\mathrm{crustal\ root}}}{\partial z} = T_{zz_{\mathrm{topo}}} + T_{zz_{\mathrm{crustal\ root}}} \tag{5}$$

where

$$T_{zz_{\mathrm{topo}}} = 2\pi G \rho_c \left(\frac{z}{\sqrt{z^2 + R^2}} - \frac{z+h}{\sqrt{(z+h)^2 + R^2}} \right)$$

$$T_{zz_{\mathrm{crustal\ root}}} = 2\pi G \Delta\rho \left(\frac{z+h+H}{\sqrt{(z+h+H)^2 + R^2}} - \frac{z+h+H+b}{\sqrt{(z+h+H+b)^2 + R^2}} \right). \tag{6}$$

The ratio β between the total gradient T_{zz} and the topography gradient $T_{zz_{\mathrm{topo}}}$ is:

$$\beta = \frac{T_{zz}}{T_{zz_{\mathrm{topo}}}} = \frac{T_{zz_{\mathrm{topo}}} + T_{zz_{\mathrm{crustal\ root}}}}{T_{zz_{\mathrm{topo}}}} = 1 + \frac{T_{zz_{\mathrm{crustal\ root}}}}{T_{zz_{\mathrm{topo}}}}. \tag{7}$$

2.2.3 Relationships between α and β

In order to derive a relationship between the degree of compensation (α) and the total to topography gradient ratio (β), we assume *a priori* information on ρ_c, $\Delta\rho$, h, R and H, with value ranges that

Table 1. Definitions of parameters and their values. The ranges for the Alaska-Canada Cordillera are in italic. α_{min} and α_{max} are the upper and lower bounds of the reference model in Fig. 3.

Parameters	Definition	Value and range
G	Gravitational constant	6.67×10^{-11} m^3 kg^{-1} s^{-2}
ρ_c	Crustal density	2600–2900 kg m^{-3}
ρ_{c_max}	Highest value for α_{max}	2900 kg m^{-3}
$\Delta\rho$	Crust–mantle density contrast	−700–300 kg m^{-3}
$\lvert\Delta\rho_{\mathrm{max}}\rvert$	Highest value for α_{max}	−700 kg m^{-3}
h	Elevation	10–4.5 × 10^3 m
h_{min}	Lowest value for α_{min}	10 m
h_{max}	Highest value for α_{max}	4.5 × 10^3 m
R	Cylinder radius	1–500 × 10^3 m
R_{min}	Lowest value for α_{max}	1 × 10^3 m
R_{max}	Highest value for α_{min}	500 × 10^3 m
H	Hydrostatic equilibrium crustal thickness	10–60 × 10^3 m
		25–40 × 10^3 m
H_{min}	Lowest value for α_{min}	25 × 10^3 m
H_{max}	Highest value for α_{max}	40 × 10^3 m
z	GOCE satellite altitude	250 × 10^3 m
α	Degree of compensation	
β	Ratio between GOCE gradients and its topographic contribution	

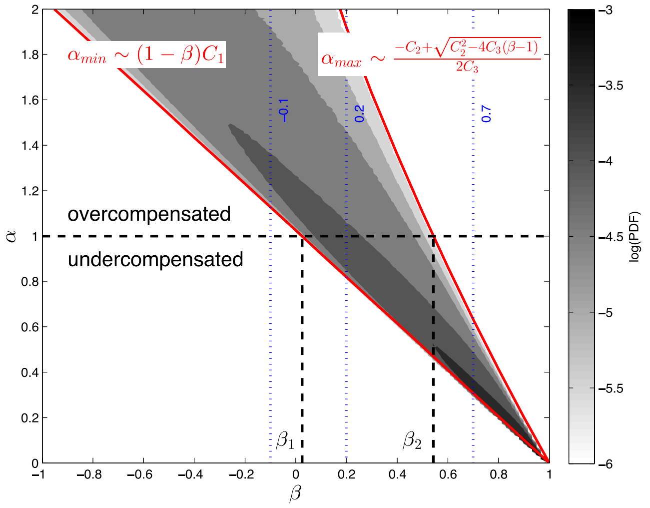

Figure 3. Relationship between the degree of compensation α and the ratio β. The grey colour scale gives the probability density associated with a collection of 10^8 models. Red lines give the lower and the upper bounds (α_{min} and α_{max}) for the degree of compensation. Independently of the model parameter values, the topography is systematically overcompensated (respectively, undercompensated) for ratio values of $\beta < 0.02$ (respectively, $\beta > 0.55$). The blue dotted lines give the location of profiles presented in Fig. 5.

correspond to continental regions (Table 1); each parameter set then corresponds to a (α, β) couple. We sample the potential combinations of this six-parameter space by randomly selecting 10^8 possible models using a uniform distribution for each parameter sampled from its *a priori* range (Table 1). This random selection is large enough to provide a quasi-systematic exploration of the parameter space with the associated (α, β) couples. The sample of 10^8 (α, β) couples is then analysed using a bivariate frequency histogram to derive a non-parametric statistical distribution, or probability density function (PDF), that describes the probability of occurrence of possible (α, β) couples for our *a priori* range of parameters.

The obtained PDF exhibits a clear relationship between the compensation degree α and gravity gradient ratio β (Fig. 3). Unsurprisingly, α and β are inversely correlated. A high degree of compensation involves a large-mass deficit at depth, which directly reduces the amplitude of the radial component T_{zz}. More interestingly, our calculations show that the lowest α values are bounded by a linear relationship between α and β, which corresponds to the lowest (h, H) and the highest R:

$$\alpha_{\mathrm{min}} \sim (1-\beta)\, C_1 \tag{8}$$

In contrast, the upper bound for α is given by a non-linear relationship with β, which corresponds to the highest (h, H, ρ_c, $|\Delta\rho|$) and the lowest R:

$$\alpha_{\mathrm{max}} \sim \frac{-C_2 + \sqrt{C_2^2 - 4C_3\,(\beta-1)}}{2C_3}. \tag{9}$$

Derivations of eqs (8) and (9), and constants C_1, C_2 and C_3 are given in Appendix. Using the parameter ranges given in Table 1, the topography is overcompensated ($\alpha > 1$) for $\beta < 0.02$, whereas $\beta > 0.55$ is associated with an undercompensated ($\alpha < 1$) topography (Fig. 3).

We test the influence of each individual parameter by varying their value independently from the others, so that all the topographic deformations observed on the Earth's surface, in terms of amplitude, spatial extent and density contrasts, are considered. Fig. 4 shows how the relationships between α and β associated with eqs (8) and (9) evolve as functions of ρ_c, $\Delta\rho$, h, R, H and z. α_{min} varies only slightly and is mainly influenced by the highest R and the lowest H. In contrast, α_{max} is much more sensitive to parameter values, especially to the highest h, H and $\Delta\rho$. The sensitivity is weaker with the lowest R and z. Both relationships are weakly dependent on ρ_c.

In order to estimate a degree of compensation α for a given ratio β (derived from GOCE and topography data), we calculate likelihood distributions of α for all values of β (discretized every 0.01) on the basis of their joint probability distribution (Fig. 3). Fig. 5 shows examples of such α likelihood distributions for three β values. These distributions can be characterized by a maximum and half-width (values at $\frac{1}{2}$ maximum probabilities, Fig. 5), which are used in the following to quantify the degree of compensation α by its most-likely value and an associated uncertainty (α, α_l and α_u; Fig. 6).

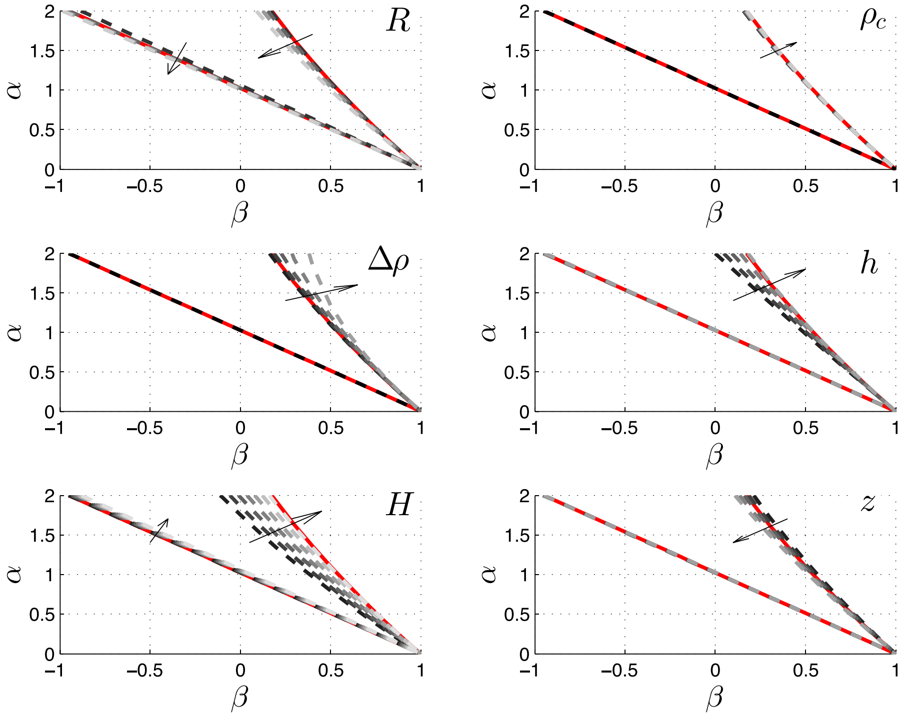

Figure 4. Sensitivity of the compensation degree ($\alpha_{\max}$ and $\alpha_{\min}$) to model parameters. Parameters set: cylinder radius R, crustal density ρ_c, crust–mantle density contrast $\Delta\rho$, elevation h, reference crustal thickness H and satellite elevation z. Parameter ranges: $R_{\min} \in [25; 100\ \text{km}]$, $R_{\max} \in [250; 1000\ \text{km}]$, $\rho_c \in [2600; 2900\ \text{kg m}^{-3}]$, $\Delta\rho \in [-700; -300\ \text{kg m}^{-3}]$, $h_{\min} \in [0; 1\ \text{km}]$, $h_{\max} \in [1; 5\ \text{km}]$, $H_{\min} \in [10; 25\ \text{km}]$, $H_{\max} \in [30; 60\ \text{km}]$ and $z \in [230; 270\ \text{km}]$. The grey colour scale (dashed lines) and associated black arrows indicate an increase in the parameter value. The red lines are associated with the data collection presented in Fig. 3.

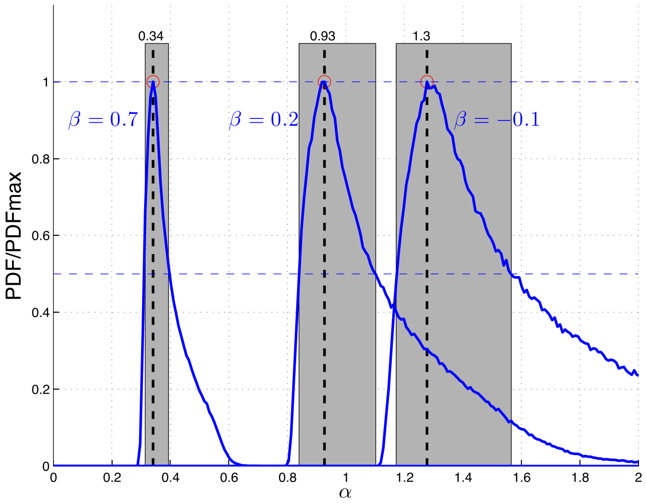

Figure 5. Example of probability density of α for three different values of β (*cf.* Fig. 3). The red circles correspond to the obtained maximum. The most likely value of 'alpha' is given by the number above the red circles. The grey areas represent the range of possible 'alpha' values (uncertainty) for a selected threshold of 50 per cent probability.

3 APPLICATION TO THE ALASKA-CANADA CORDILLERA

3.1 Elevation, crust thickness and isostatic state

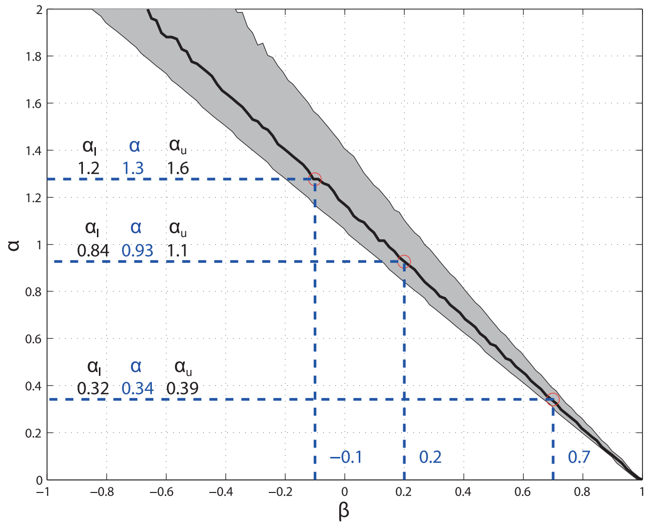

Figure 6. Transfer function between β and α. Black is the most likely α. Grey envelop is associated with the α uncertainties. The red circles are associated with the three different values of β presented Fig. 5. Blue text gives the value of β and α. Black text gives the lower (α_l) and upper (α_u) limit of α.

On the basis of its first-order topography and geology, we can subdivide the NW America orogen area into three domains: (1) the Yakutat collision zone, (2) the Yukon Plateau and (3) the Northwest Territories Craton (Fig. 1). The collision front, including the Alaska Range and the St Elias–Chugach–Wrangell Mountains, comprises high and steep mountains located at the northern boundary of the Yakutat block (Fig. 1) and is associated with an intense seismicity (Doser & Lomas 2000; Mazzotti *et al.* 2008). The average elevation in this region is ~2500 m, with highs up to 6000 m in the Alaska Range and St Elias Mountains. These ranges are inferred to result from a series of subduction and collision processes, including the present-day underthrusting of the Yakutat block. The crustal thickness is not well resolved for a large part of this area. Nevertheless, the isostatic anomaly map established by Barnes *et al.* (1994) shows that this region is not in Airy–Heiskanen equilibrium and the topography is undercompensated. A deep support related to the mantle dynamics around the edge of the Pacific slab could be expected in such context (Mazzotti *et al.* 2008).

The Yukon Plateau has an average elevation of ~1000 m with little relief (Fig. 1) and a consistent crustal thickness of ~35 km (Erdmer *et al.* 2001; Rasendra *et al.* 2014). At its easternmost part, it is delimited by the Mackenzie Mountains, which rise to an elevation of ~2000 m. Although located 600–800 km northeast of the Yakutat collision, these mountains are affected by a strong seismicity and mark the transition between the backarc active Cordillera and the stable Canadian Shield (Mazzotti *et al.* 2008). Strain transfer across the whole Cordillera is made possible by a hot lithosphere (Mazzotti & Hyndman 2002). Isostatic equilibrium prevails for most of this region (Lewis *et al.* 2003).

Finally, lowlands and lakes, with an average elevation of ~300 m and a crust of 35 km thickness (Cook *et al.* 1999), characterize the Northwest Territories Craton (Fig. 1). This region is associated with a cold and thick lithosphere, similar to the Canadian Shield, which contributes to the regional isostatic equilibrium (Lewis *et al.* 2003).

3.2 GOCE results

The GOCE radial gravity gradient T_{zz} over the Alaska-Canada Cordillera reflects at first order the topography (Figs 7a and b). The radial gradient displays a significant signal over the topography highs with a maximal magnitude of 0.8 E in the St. Elias–Wrangell Mountains. Minimal values are observed over the eastern lowlands where the signal varies slowly. The Mackenzie Mountains, which culminate at ~2000 m, are associated with the higher signal in the Yukon plateau region.

We show the calculated topography gradient $T_{zz_{\text{topo}}}$ in Fig. 7(c). $T_{zz_{\text{topo}}}$ displays a pattern close to GOCE observations but with higher amplitudes (*cf.* maximal of 2.6 E over the St Elias–Wrangell Mountains). This significant difference in amplitudes between observations and predictions points out the existence of a process reducing the gravitational effect of topography, such as local isostatic compensation by crustal thickness variations, which we can assess simply and efficiently by estimating a degree of compensation. Fig. 7(d) shows the spatial distribution of the gravity gradient ratio β. We distinguish the three different domains: the eastern lowlands with $\beta < -0.3$, the Yukon Plateau with $-0.3 \leq \beta \leq 0.3$ and the northwest highlands with $\beta > 0.3$.

The corresponding degree of compensation is obtained from the transfer function between β and α established in Section 2.2.3 and is shown in Fig. 8. The transfer function is adapted to our study area using *a priori* information available on the reference crustal thickness H (Table 1). The uncertainty range of the degree of compensation, α_l and α_u (Fig. 6), is represented in Figs 8(c) and (d). The three maps show a gradual increase of the degree of compensation under the Airy–Heiskanen hypothesis from the collision front to the stable craton area. α is significantly higher than 1 in the Eastern lowlands, indicating that the region is overcompensated. The Yukon Plateau area, characterized by α values varying between 0.7 and 1.2, is close to the isostatic equilibrium. Finally, associated with $\alpha < 0.7$, topography highs in the Alaskan forearc and Yakutat collision zone are only partially compensated.

3.3 Discussion

In order to validate the approach, we ensure the consistency between our results deduced from GOCE observations and the isostatic gravity anomalies derived from the WGM2012 global model based on terrestrial measurements and GRACE satellite data (Bonvalot *et al.* 2012). These isostatic anomalies are obtained by subtracting to the Earth Gravitational Model 2008 (EGM2008; Pavlis *et al.* 2008) the gravitational effect of the topography and its low-density root according to the Airy–Heiskanen model with a reference crust thickness of 30 km. Thus, a negative (positive) isostatic anomaly indicates an over (under) compensation of reliefs whereas a zero isostatic anomaly reflects a topography perfectly compensated.

We first apply a 200 km high-pass filter to WGM2012 isostatic anomalies to obtain a similar wavelength content as for our satellite-based analysis. Second, we correct the WGM2012 isostatic anomaly to account for the difference in crustal thickness reference (30 km for WGM2012 versus 35 km in our analysis tuned to regional seismic data). This correction, calculated using eqs (2) and (4) to account for topography variations, corresponds to about 0–10 mGal depending on local topography. The resulting WGM2012 isostatic anomaly shows a good general agreement with the degree of compensation derived from GOCE observations (Fig. 9 versus Fig. 8). Both our GOCE-based results and the ground-based WGM2012 isostatic anomaly show that Airy–Heiskanen isostasy prevails for the Yukon Plateau whereas additional mechanisms are required to support topography below the Northwest Territories Craton and the Yakutat collision zone.

For the Northwest Territories region, our analysis and the isostatic anomaly map indicate an overcompensated topography, that is, that the actual crustal root is greater than the isostatic root predicted by the Airy–Heiskanen model (Figs 8 and 9). However, seismic data indicate that crustal thickness under this region is similar to that of the Yukon Plateau (~33–35 km; Cook *et al.* 1999; Erdmer *et al.* 2001; Rasendra *et al.* 2014) and corresponds to isostatic equilibrium with the Plateau elevation (~1 km). Thus, the overcompensated signature and the support of the low topography are not associated with simple Airy–Heiskanen isostasy. As shown by Lewis *et al.* (2003) and Hasterok & Chapman (2007), thermal isostasy is likely the primary support mechanism due to the presence of a thick and cold lithosphere below the Craton. Near-sea level elevation regions (0–200 m), such as the Canadian Craton, have indeed a wide range of crustal thicknesses (25–55 km) and a simple relation between these two quantities is difficult to establish (Zoback & Mooney 2003). This implies a significant contribution of a cooler and denser lithospheric mantle to reach the isostatic equilibrium in these areas.

In contrast with the Craton, the Yakutat collision system to the west is isostatically undercompensated: crustal thickening resulting from the collision between the Yakutat block and the American continent does not completely compensate the St Elias and Chugach Mountains elevation (Figs 8 and 9). Our approach indicates the existence of additional mechanisms that support the topography in the collision zone: (1) the continental lithosphere could be rigid enough to partially maintain these reliefs. However, the collision zone is characterized by large deformation and faults, which can highly reduce the rigidity of lithosphere, as shown by the low effective elastic thickness (<20 km) obtained over the region (Kirby & Swain 2009). Moreover, the Alaska-Canada Cordillera is located in a recent backarc region characterized by a hot, thin and weak lithosphere (Hyndman *et al.* 2005). (2) Alternatively, asthenospheric mantle dynamic processes could contribute to topography support, such as sublithospheric erosion by small-scale convection (Cadio

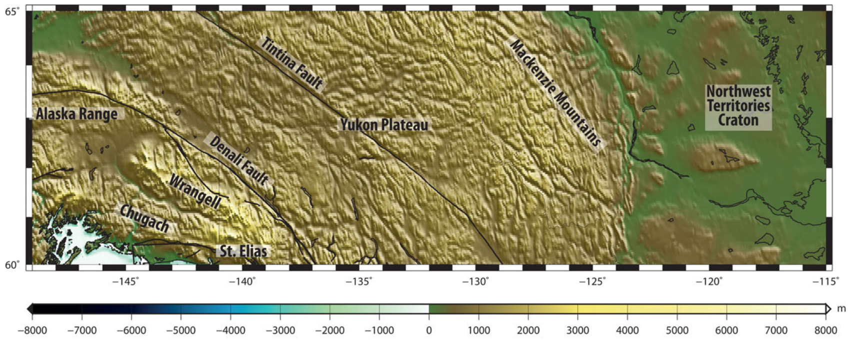

(a) Topography

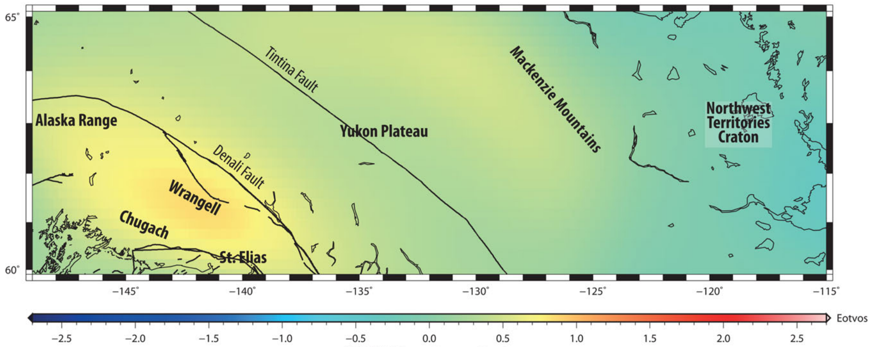

(b) GOCE gravity gradients

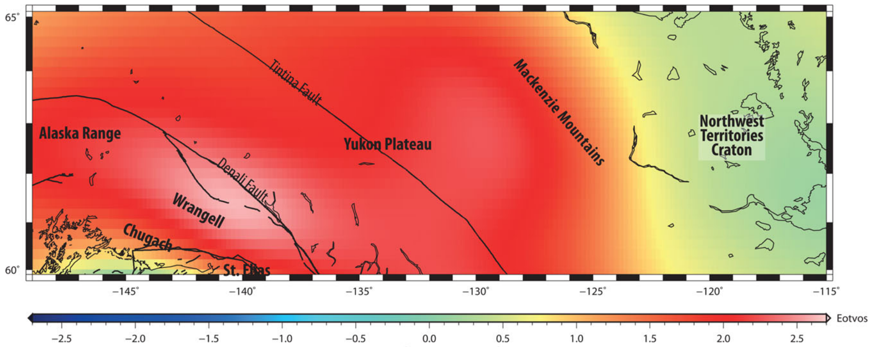

(c) Topography gravity gradients

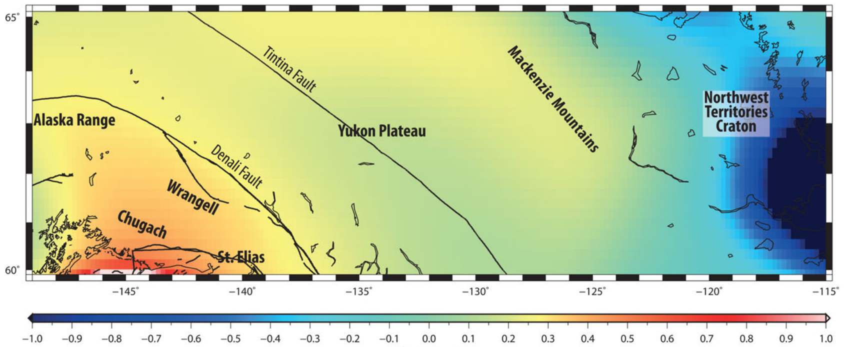

(d) Ratio β

Figure 7. (a) Topography, (b) the GOCE radial gravity gradient T_{zz}, (c) the uncompensated topographic contribution $T_{zz\ \mathrm{topo}}$ and (d) the ratio β over the Alaska-Canada Cordillera.

et al. 2012). Mantle flow associated with the edge of the Yakutat slab could also contribute to dynamic topography. Thus, our approach could allow the identification of dynamic topography in this region and provide an estimate of its minimal contribution. The comparison between observed and synthetic gravity gradients derived from numerical modeling of subduction process could bring further constraints on the slab dynamics at the collision front.

4 CONCLUSIONS

The approach developed here evaluates the degree of the local isostatic compensation of the topography, under the Airy–Heiskanen hypothesis, in continental region. This simple method only requires knowledge of the radial GOCE gradient and its topographic contribution, data available on the entire Earth's surface. Consequently, our approach can be easily applied to any continental region and

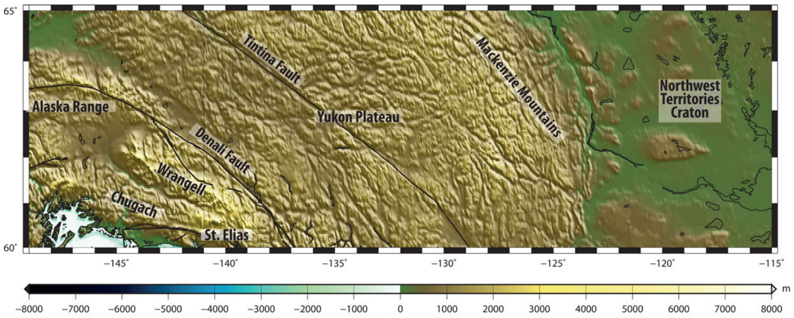

(a) Topography

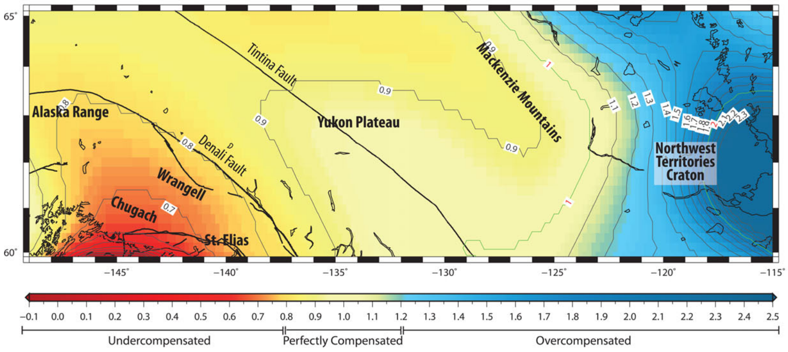

(b) α

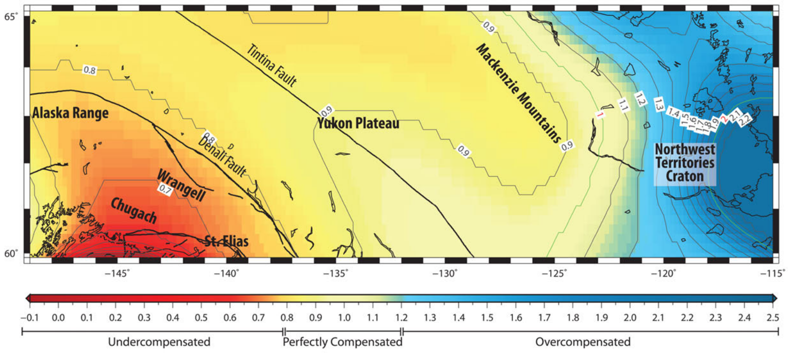

(c) α_l

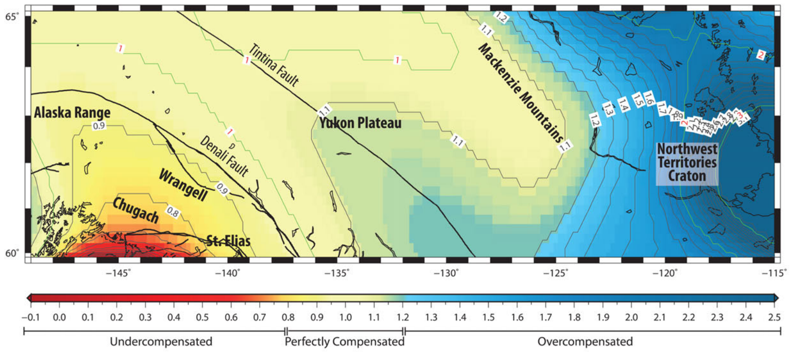

(d) α_u

Figure 8. (a) Topography, (b) the degree of compensation α and (c) its estimated range α_l and (d) α_u over the Alaska-Canada Cordillera.

can integrate independent constraints on parameters specific to each region. It can be also adapted to oceanic domain, allowing the study of subduction zones. Finally, the gravity gradient tensor holds complementary information in other components, which can be used in future studies.

Our application on the NW America orogen confirms the presence of additional mechanisms in the topography support, involving thermal isostasy, lithosphere rigidity and probably mantle dynamics. This approach provides constraints on the maximal (minimal) potential isostatic (dynamic) topography and associated with independent data (seismic velocity, seismicity, surface heat flow, etc.) can bring additional information on the Moho depth, on thermal or mechanical lithospheric variations, and on deeper mantle processes.

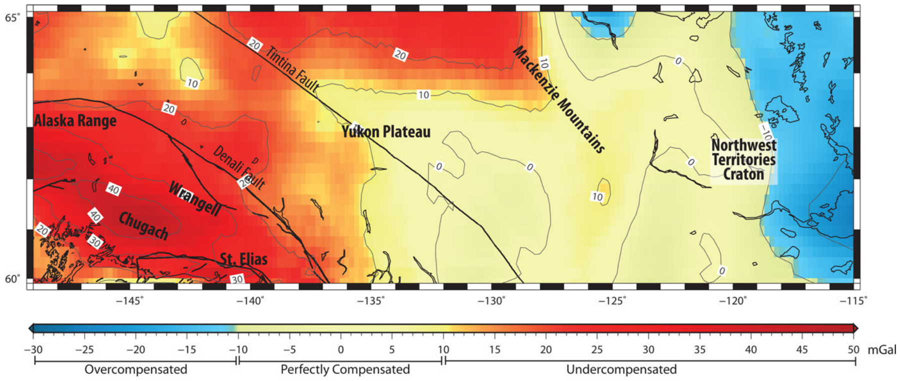

Figure 9. Isostatic gravity anomalies derived from the WGM2012 global model (Bonvalot *et al.* 2012) smoothed with a 200 km high-pass filter and corrected to account for the difference in crustal thickness reference (30 km for WGM2012 versus 35 km in our analysis tuned to regional seismic data).

ACKNOWLEDGEMENTS

We are grateful to two anonymous reviewers for critical and constructive comments on the manuscript. This study was supported by French 'Agence Nationale de la Recherche' grant ANR-12-CHEX-0004-01 (DefDyCor) and by the 'Centre National d'Etudes Spatiales' (CNES—TOSCA science committee). We wish to thank Elisa Dagnaud for her assistance in administration.

REFERENCES

Álvarez, O., Gimenez, M., Braitenberg, C. & Folguera, A., 2012. GOCE satellite derived gravity and gravity gradient corrected for topographic effect in the South Central Andes region, *Geophys. J. Int.,* **190**(2), 941–959.

Barnes, D.F., Mariano, J., Morin, R.L., Roberts, C.W. & Jachens, R.C., 1994. Incomplete isostatic gravity map of Alaska, in *The Geology of Alaska,* Vol. G-1 (plate 9, scale 1:2 500 000), eds Plafker, G. & Berg, H.D., Geological Society of America, Geology of North America.

Bonvalot, S. *et al.*, 2012. *World Gravity Map*, Commission for the Geological Map of the World. BGI-CGMW-CNES-IRD, Paris.

Bouman, J. *et al.*, 2015. GOCE gravity gradient data for lithospheric modeling, *Int. J. Appl. Earth Obs.,* **35**(A), 16–30.

Bouman, J., Ebbing, J., Fuchs, M., Sebera, J., Lieb, V., Szwillus, W., Haagmans, R. & Novak, P., 2016. Satellite gravity gradient grids for geophysics, *Sci. Rep.,* **6,** 21050, doi:10.1038/srep21050.

Braun, J., 2010. The many surface expressions of mantle dynamics, *Nat. Geosci.,* **3,** 825–833.

Bruinsma, S.L., Förste, C., Abrikosov, O., Lemoine, J.-M., Marty, J.-C., Mulet, S., Rio, M.-H. & Bonvalot, S., 2014. ESA's satellite-only gravity field model via the direct approach based on all GOCE data, *Geophys. Res. Lett.,* **41,** 7508–7514.

Cadio, C., Ballmer, M., Panet, I., Diament, M. & Ribe, N., 2012. New constraints on the origin of the Hawaiian swell from wavelet analysis of the geoid to topography ratio, *Earth planet. Sci. Lett.,* **359–360,** 40–54.

Chase, C.G., Libarkin, J.A. & Sussman, A.J., 2002. Colorado Plateau: geoid and means of isostatic support, *Int. Geol. Rev.,* **44,** 575–587.

Cook, F.A., van der Velden, A.J. & Hall, K.W., 1999. Frozen subduction in Canada's Northwest Territories: lithoprobe deep lithospheric reflection profiling of the western Canadian shield, *Tectonics,* **18,** 1–24.

Doser, D.I. & Lomas, R., 2000. The transition from strike-slip faulting to oblique subduction in southeastern Alaska from seismological studies, *Tectonophysics,* **316,** 45–65.

Drinkwater, M.R., Floberghagen, R., Haagmans, R., Muzi, D. & Popescu, A., 2003. GOCE: ESA's first Earth Explorer Core mission, in *Earth Gravity Field From Space: From Sensors to Earth Sciences, Space Sci. Ser. ISSI,* Vol. 17, pp. 419–432, eds Beutler, G.B. *et al.*, Kluwer.

Erdmer, P., Cook, F., Clowes, R., Snyder, D., Evenchick, C., van der Velden, A. & Hall, K., 2001. Some geological constraints on Cordilleran structure imposed by Line 3 reflections-MacMillan Pass to White Pass, in *Slave-Northern Cordillera Lithospheric Evolution Transect and Cordilleran Tectonics Workshop,* Lithoprobe Report 79, pp. 54–55, Compilers Cook, F. & Erdmer, P.

Flament, N., Gurnis, M. & Müller, R.D., 2013. A review of observations and models of dynamic topography, *Lithosphere,* **5,** 189–210.

Fuchs, M. & Bouman, J., 2011. Rotation of GOCE gravity gradients to local frames, *Geophys. J. Int.,* **187,** 743–753.

Grombein, T., Seitz, K. & Heck, B., 2013. Optimized formulas for the gravitational field of a tesseroid, *J. Geodesy,* **87**(7), 645–660.

Grombein, T., Luo, X., Seitz, K. & Heck, B., 2014. A wavelet based assessment of topographic isostatic reductions for GOCE gravity gradients, *Surv. Geophys.,* **35**(4), 959–982.

Hager, B., Clayton, C., Richards, M., Comer, R. & Dziewonski, A., 1985. Lower mantle heterogeneity, dynamic topography and the geoid, *Nature,* **313,** 541–545.

Hasterok, D. & Chapman, D.S., 2007. Continental thermal isostasy: 2. Application to North America, *J. geophys. Res.,* **112,** B06415, doi:10.1029/2006JB004664.

Hirt, C., Kuhn, M., Featherstone, W.E. & Göttl, F., 2012. Topographic/isostatic evaluation of new-generation GOCE gravity field models, *J. geophys. Res.,* **117,** B05407, doi:10.1029/2011JB008878.

Hyndman, R.D., Currie, C.A. & Mazzotti, S., 2005. Subduction zone backarcs, mobile belts, and orogenic heat, *GSA Today,* **15**(2), doi:10:1130/1052-5173.

Kirby, J. & Swain, C., 2009. A reassessment of spectral TE estimation in continental interiors: the case of north america, *J. geophys. Res.,* **114**(B8), 1978–2012.

Lahr, J.C. & Plafker, G., 1980. Holocene Pacific–North America plate interaction in southern Alaska: implications for the Yakataga seismic gap, *Geology,* **8,** 483–486.

Lewis, T.J., Hyndman, R.D. & Flück, P., 2003. Heat flow, heat generation, and crustal temperatures in the northern Canadian Cordillera: thermal control of tectonics, *J. geophys. Res.,* **108**(B6), doi:10.1029/2002JB002090.

Mariani, P., Braitenberg, C. & Ussami, N., 2013. Explaining the thick crust in paraná basin, brazil, with satellite GOCE gravity observations, *J. South Am. Earth Sci.,* **45,** 209–223.

Mazzotti, S. & Hyndman, R.D., 2002. Yakutat collision and strain transfer across the northern Canadian Cordillera, *Geology,* **30,** 495–498.

Mazzotti, S., Leonard, L.J., Hyndman, R.D. & Cassidy, J.F., 2008. Tectonics, dynamics, and seismic hazard in the Canada-Alaska cordillera, in *Active Tectonics and Seismic Potential of Alaska,* Vol. 179, pp. 297–319, eds Freymueller, J.T., Haeussler, P.J., Wesson, R.L. & Ekstrom, G., Geophys. Monograph Series, American Geophysical Union.

Mikhailov, V., Pajot, G., Diament, M. & Price, A., 2007. Tensor deconvolution: a method to locate equivalent sources from full tensor gravity data, *Geophysics,* **72**(5), 61–69.

Panet, I., Pajot-Metivier, G., Greff-Lefftz, M., Métivier, L., Diament, M. & Mandea, M., 2014. Mapping the mass distribution of Earth's mantle using satellite-derived gravity gradients, *Nat. Geosci.,* **7,** 131–135.

Pavlis, N.K., Factor, J.F. & Holmes, S.A., 2007. Terrain-related gravimetric quantities computed for the next EGM, in *Proceedings of 1st international symposium of the IGFS: Gravity Field of the Earth,* Special Issue, Vol. 18, pp. 318–323.

Pavlis, N.K., Holmes, S.A., Kenyon, S.C. & Factor, J.F., 2008. An earth gravitational model to degree 2160, in *EGU General Assembly 2008 (EGM'08),* Vienna, Austria, April 13–18.

Plafker, G., Moore, J.C. & Winkler, G.R., 1994. Geology of the southern Alaska margin, in *The Geology of Alaska,* Vol. G1, pp. 389–449, eds Plafker, G. & Berg, H.C., Geological Society of America, Geology of North America.

Rasendra, N., Bonnin, M., Mazzotti, S. & Tiberi, C., 2014. Crustal and upper mantle anisotropy related to fossilized transpression fabric along the Denali Fault, northern Canadian Cordillera, *Bull. seism. Soc. Am.,* **104**(4), 1964–1975.

Reguzzoni, M., Sampietro, D. & Sansò, F., 2013. Global Moho from the combination of the CRUST 2.0 model and GOCE data, *Geophys. J. Int.,* **195,** 222–237.

Rummel, R., Yi, W. & Stummer, C., 2011. GOCE gravitational gradiometry, *J. Geod.,* **85,** 777–790.

Shin, Y.H. *et al.*, 2015. Moho topography, ranges and folds of Tibet by analysis of global gravity models and GOCE data, *Sci. Rep.,* **5,** 11681, doi:10.1038/srep11681.

Tapley, B. *et al.*, 2005. GGM02—an improved Earth gravity model from GRACE, *J. Geod.,* **79,** 467–478.

Turcotte, D. & Schubert, G., 2002. *Geodynamics,* 2nd edn, Cambridge Univ. Press.

Watts, A.B., 2001. *Isostasy and Flexure of the Lithosphere,* Cambridge Univ. Press.

Zoback, M.-L. & Mooney, W.D., 2003. Lithospheric buoyancy and continental intraplate stresses, *Int. Geol. Rev.,* **45,** 95–118.

APPENDIX: MATHEMATICAL FORMULATIONS BETWEEN α AND β

Using the function of real $f(x) = \frac{x}{\sqrt{x^2+R^2}}$ eq. (6) can be written as

$$\begin{aligned} T_{zz_{\text{topo}}} &= 2\pi G\rho_c\left(f(z) - f(z+h)\right) \\ T_{zz_{\text{crustal root}}} &= 2\pi G\Delta\rho\left(f(z+h+H) - f(z+h+H+b)\right). \end{aligned} \tag{A1}$$

The function *f* being infinitely differentiable, it can be approximated by using a finite number of terms of its Taylor series with $(x, y) \in \mathbb{R}^2$:

$$f(x+y) = f(x) + yf'(x) + \frac{y^2}{2!}f''(x) + \cdots + \frac{y^n}{n!}f^{(n)}(x) + \cdots. \tag{A2}$$

Compared to z, H and R the elevation h is always small. Hence, two cases can be considered to simplified eq. (7). First assuming that the crustal root b is also small the first two terms of eq. (A2) can be used to simplify eqs (6) and (7)

$$\begin{aligned} T_{zz_{\text{topo}}} &\sim -2\pi G\rho_c hR^2\left(z^2+R^2\right)^{-\frac{3}{2}} \\ T_{zz_{\text{crustal root}}} &\sim 2\pi G\Delta\rho hR^2\left((z+h+H)^2+R^2\right)^{-\frac{3}{2}}. \end{aligned} \tag{A3}$$

The ratio β between the observed gravity gradient T_{zz} and $T_{zz_{\text{topo}}}$ is then

$$\beta = \frac{T_{zz}}{T_{zz\ \text{topo}}} = \frac{T_{zz_{\text{topo}}} + T_{zz_{\text{crustal root}}}}{T_{zz_{\text{topo}}}} = 1 + \frac{T_{zz_{\text{crustal root}}}}{T_{zz_{\text{topo}}}} \sim 1 - \alpha\left(\frac{z^2+R^2}{(z+h+H)^2+R^2}\right)^{\frac{3}{2}} \tag{A4}$$

which corresponds to a simple linear relationship between β and α

$$\begin{aligned} \alpha &\sim (1-\beta)C_1 \\ C_1 &= \left(\frac{z^2+R^2}{(z+h+H)^2+R^2}\right)^{-\frac{3}{2}}. \end{aligned} \tag{A5}$$

This equation can be used for small b only. Thus, it gives a lower bound for α. Note that for $\lim\limits_{R\to+\infty}(\alpha) = 1-\beta$.

For cases in which the crustal root b is comparable to z, H or R, the third terms of eq. (A2) cannot be neglected and $T_{zz_{\text{crustal root}}}$ becomes

$$T_{zz_{\text{crustal root}}} \sim 2\pi G\Delta\rho\left[-bR^2\left((z+h+H)^2+R^2\right)^{-\frac{3}{2}} + 3\frac{b^2}{2}R^2(z+h+H)\left((z+h+H)^2+R^2\right)^{-\frac{5}{2}}\right]. \tag{A6}$$

The ratio β is then

$$\begin{aligned} \beta &\sim 1 - C_2\alpha - C_3\alpha^2 \\ C_2 &= \left(\frac{z^2+R^2}{(z+h+H)^2+R^2}\right)^{\frac{3}{2}} = \frac{1}{C_1} \\ C_3 &= \frac{3\rho_c}{2\Delta\rho}h(z+h+H)\frac{\left[(z+h+H)^2+R^2\right]^{-\frac{5}{2}}}{(z^2+R^2)^{-\frac{3}{2}}}. \end{aligned} \tag{A7}$$

Thus, we obtain the following quadratic polynomial equation

$$C_3\alpha^2 + C_2\alpha + (\beta-1) \sim 0 \tag{A8}$$

which has for root ($\alpha > 0$)

$$\alpha \sim \frac{-C_2 + \sqrt{C_2^2 - 4C_3(\beta-1)}}{2C_3}. \tag{A9}$$

Appendix B

Relative errors due to topography truncation

Relative gravity truncation errors

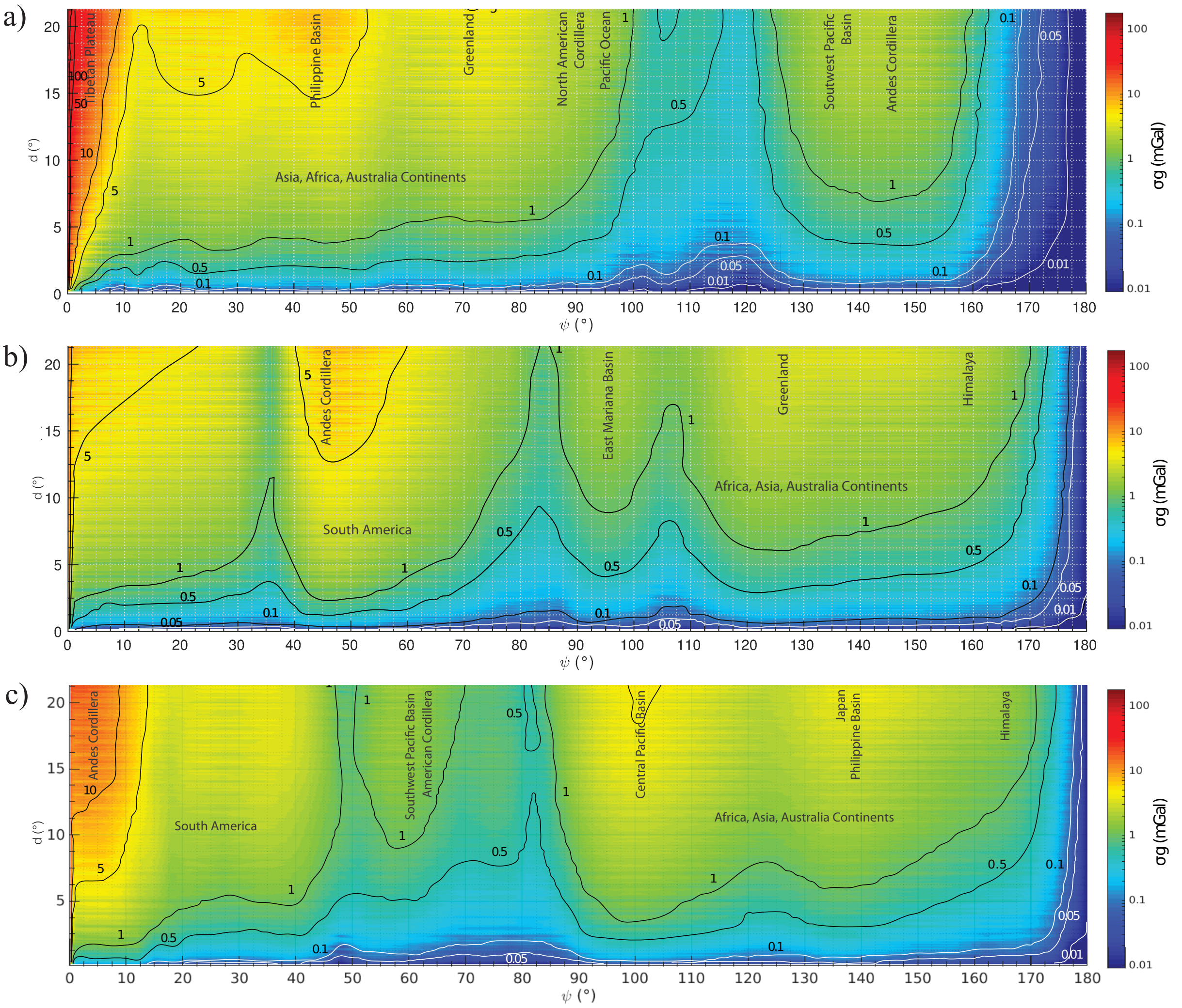

Figure B.1: Relative gravity error $\sigma g(\psi_t, d)$ at airborne altitude (10 km) between to two points in the region, as a function of their distance d and the topography correction truncation ψ (cf. Figure 3.2), for Himalaya (a), Pacific (b), and Southeast Pacific (c) zones, respectively. The dashed grey line marks the ψ=1.5°, corresponding to the standard truncation distance (Bullard, 1936). The differential effect of major continental and oceanic masses are labeled (see Figure 3.3).

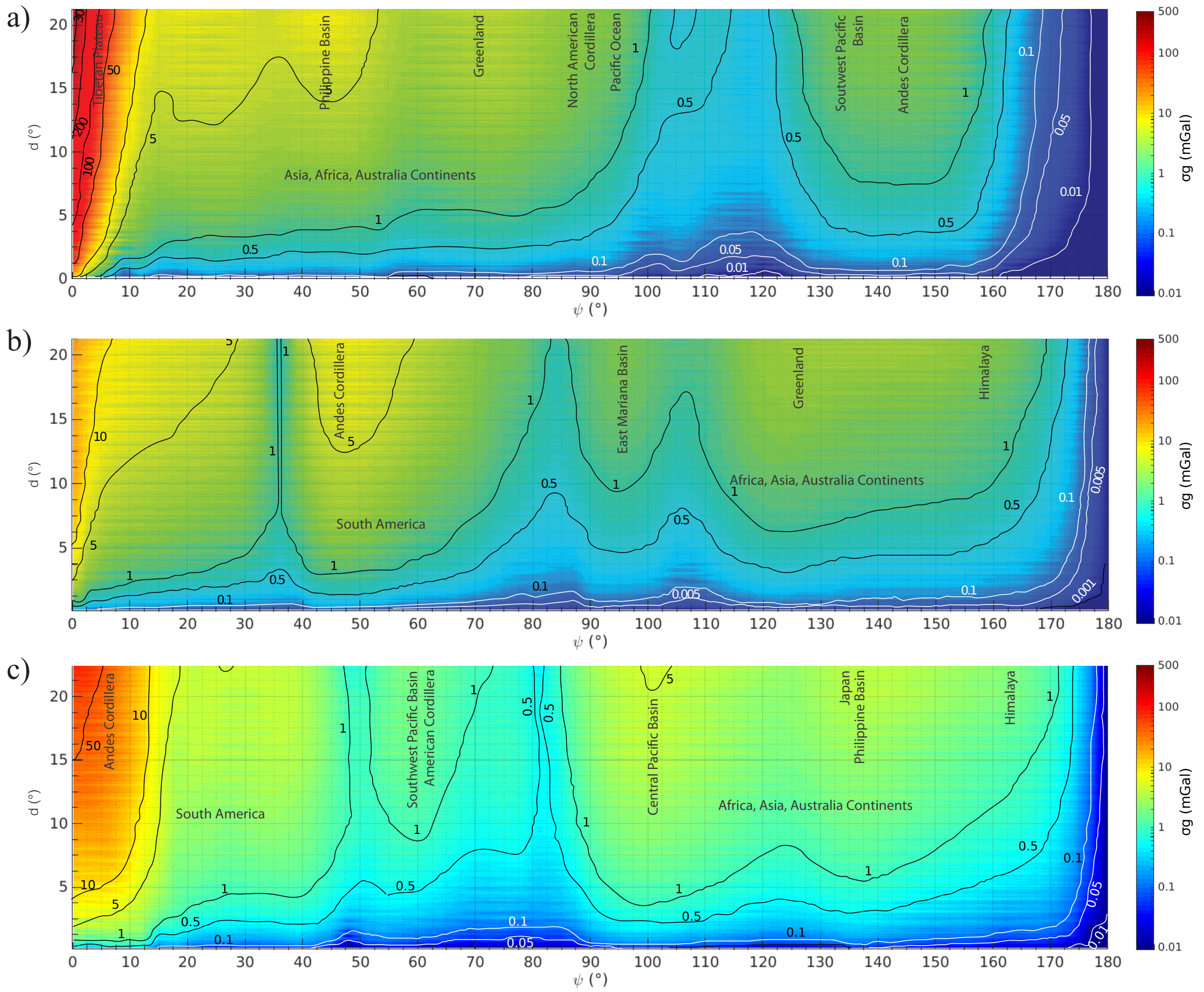

Figure B.2: Relative gravity error $\sigma g(\psi_t, d)$ at satellite altitude (255 km) between to two points in the region, as a function of their distance d and the topography correction truncation ψ (cf. Figure 3.2), for Himalaya (a), Pacific (b), and Southeast Pacific (c) zones, respectively. The dashed grey line marks the ψ=1.5°, corresponding to the standard truncation distance (Bullard, 1936). The differential effect of major continental and oceanic masses are labeled (see Figure 3.3).

Relative gravity gradient truncation errors

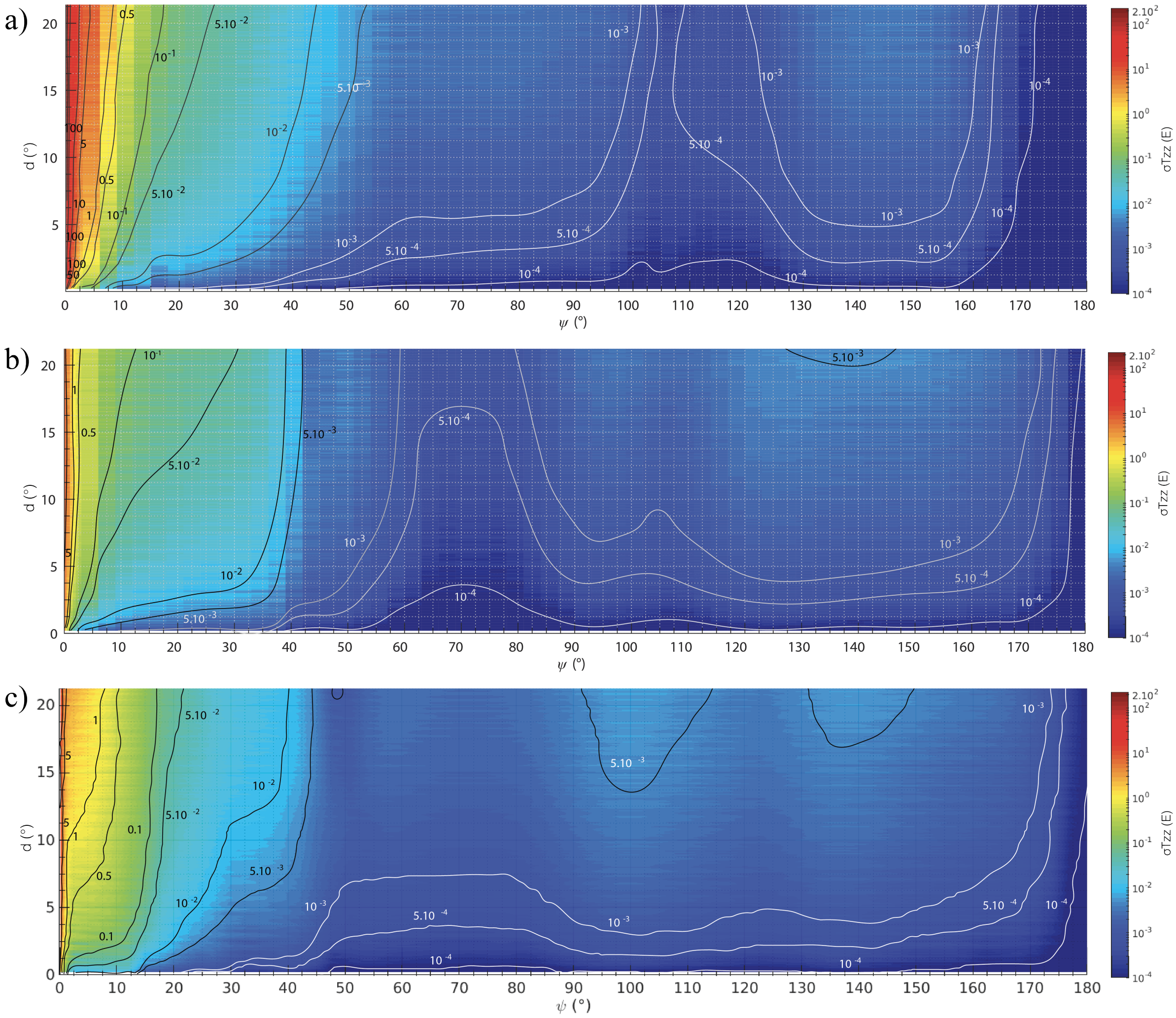

Figure B.3: Relative gravity gradient error $\sigma T(\psi_t, d)$ (in Eötvös) at airborne altitude (10 km) between two points in the region, as a function of their distance d and the topography correction truncation ψ (cf. Figure 3.2), for Himalaya (a), Pacific (b), and Southeast Pacific (c) zones, respectively. The differential effect of major continental and oceanic masses are labeled (see Figure 3.3).

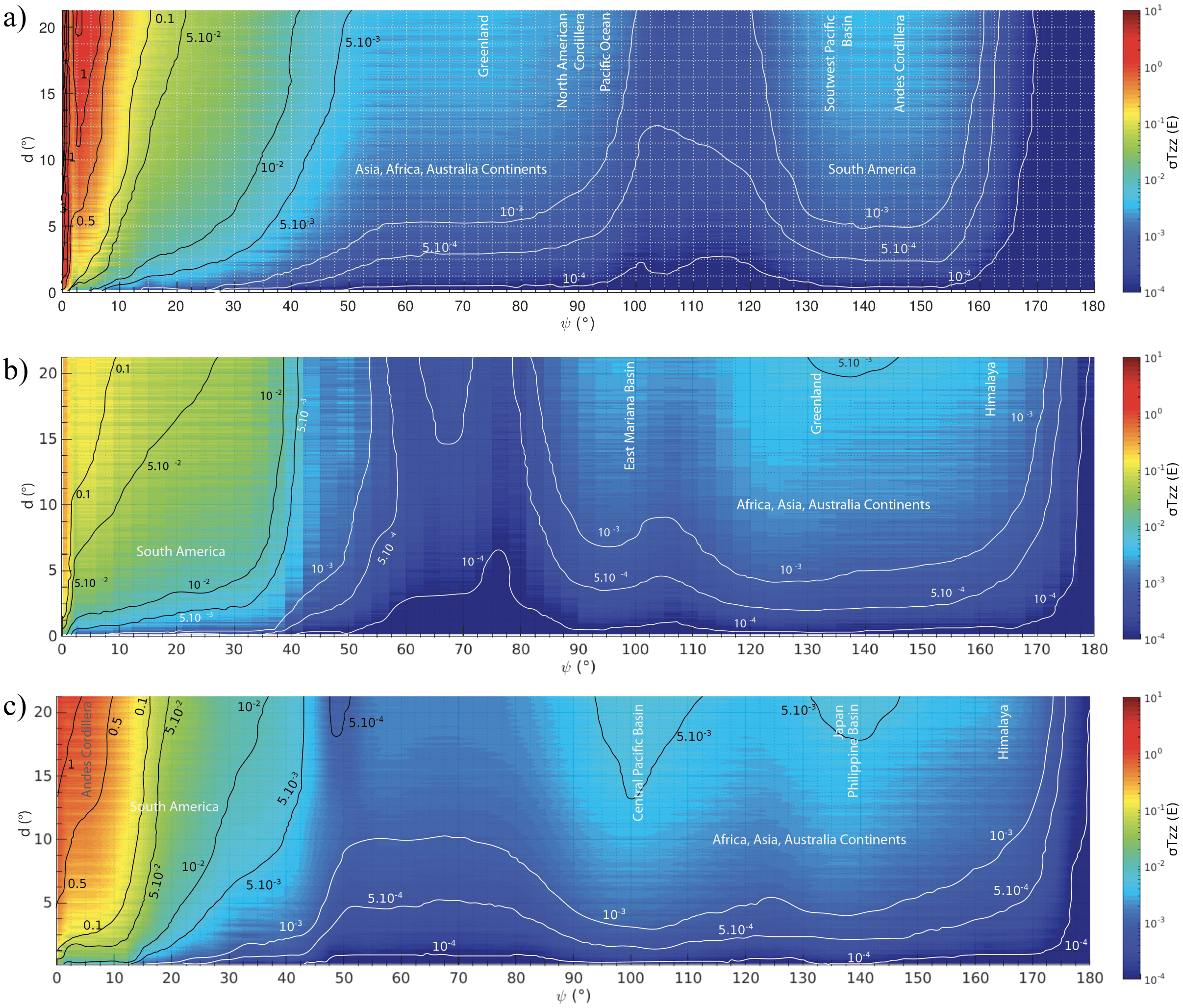

Figure B.4: Relative gravity gradient error $\sigma T(\psi_t, d)$ (in Eötvös) at satellite altitude (255 km) between two points in the region, as a function of their distance d and the topography correction truncation ψ (cf. Figure 3.2), for Himalaya (a), Pacific (b), and Southeast Pacific (c) zones, respectively. The differential effect of major continental and oceanic masses are labeled (see Figure 3.3).

Bibliography

Adam, C., Yoshida, M., Suetsugu, D., Fukao, Y., and Cadio, C. (2014). Geodynamic modeling of the South Pacific superswell. *Physics of the Earth and Planetary Interiors*.

Álvarez, O., Gimenez, M., Braitenberg, C., and Folguera, A. (2012). GOCE satellite derived gravity and gravity gradient corrected for topographic effect in the South Central Andes region. *Geophysical Journal International*, 190(2):941–959.

Alvarez, O., Gimenez, M. E., Martinez, M. P., Lince Klinger, F., and Braitenberg, C. (2015). New insights into the Andean crustal structure between 32Â° and 34Â°S from GOCE satellite gravity data and EGM2008 model. *Geological Society, London, Special Publications*.

Andersen, O. B. and Knudsen, P. (1997). Global gravity field from the ERS-1 and the geosat geodetic mission altimetry - The Mediterranean Sea. *European Space Agency, (Special Publication) ESA SP*.

Balmino, G., Vales, N., Bonvalot, S., and Briais, A. (2012). Spherical harmonic modelling to ultra-high degree of Bouguer and isostatic anomalies. *Journal of Geodesy*, 86(7):499–520.

Barnett, C. T. (1976). Theoretical Modeling of the Magnetic and Gravitational Fields of an Arbitrarily Shaped Three-Dimensional Body. *Geophysics*, 41(6):1353.

Barthelmes, F. (2018). *Global Models*, pages 1–9. Springer International Publishing, Cham.

Beiki, M. (2010). Analytic signals of gravity gradient tensor and their application to estimate source location. *GEOPHYSICS*.

Berthet, T., Hetényi, G., Cattin, R., Sapkota, S. N., Champollion, C., Kandel, T., Doerflinger, E., Drukpa, D., Lechmann, S., and Bonnin, M. (2013). Lateral uniformity of India Plate strength over central and eastern Nepal. *Geophysical Journal International*, 195(3):1481–1493.

Berthet, T., Ritz, J. F., Ferry, M., Pelgay, P., Cattin, R., Drukpa, D., Braucher, R., and Hetényi, G. (2014). Active tectonics of the eastern Himalaya: New constraints from the first tectonic geomorphology study in southern Bhutan. *Geology*.

Blakely, R. (1996). *Potential theory in gravity and magnetic applications.* Cambridge University Press.

Bonvalot, S., Le Moigne, N., Merlet, S., Desruelle, B., Lautier-Gaud, J., Menoret, V., and Vermeulen, P. (2016). The new Absolute Quantum Gravimeter (AQG): first results and perspectives. *EGU General Assembly 2016, held 17-22 April, 2016 in Vienna Austria, id. EPSC2016-11824*, 18.

Bouman, J., Ebbing, J., and Fuchs, M. (2013). Reference frame transformation of satellite gravity gradients and topographic mass reduction. *Journal of Geophysical Research: Solid Earth*, 118(2):759–774.

Bouman, J., Ebbing, J., Fuchs, M., Sebera, J., Lieb, V., Szwillus, W., Haagmans, R., and Novak, P. (2016). Satellite gravity gradient grids for geophysics. *Scientific reports*, 6(August 2015):21050.

Bouman, J., Fuchs, M., Ivins, E., van der Wal, W., Schrama, E., Visser, P., and Horwath, M. (2014). Antarctic outlet glacier mass change resolved at basin scale from satellite gravity gradiometry. *Geophysical Research Letters*, 41(16):5919–5926.

Bowring, B. R. (1976). Transformation from Spatial to Geographical Coordinates. *Survey Review*, 23(181):323–327.

Brockmann, J. M., Zehentner, N., Höck, E., Pail, R., Loth, I., Mayer-Gürr, T., and Schuh, W. D. (2014). EGM-TIM-RL05: An independent geoid with centimeter accuracy purely based on the GOCE mission. *Geophysical Research Letters.*

Bullard, E. C. (1936). Gravity Measurements in East Africa. *Philosophical Transactions of the Royal Society of London. Series A, Mathematical and Physical Sciences*, 235(757):445–531.

Burov, E. and Diament, M. (1996). Isostasy, equivalent elastic thickness, and inelastic rheology of continents and oceans. *Geology.*

Burov, E. B. and Diament, M. (1995). The effective elastic thickness (Te) of continental lithosphere: what does it really mean? *Journal of Geophysical Research.*

Cadio, C., Ballmer, M. D., Panet, I., Diament, M., and Ribe, N. (2012). New constraints on the origin of the Hawaiian swell from wavelet analysis of the geoid to topography ratio. *Earth and Planetary Science Letters.*

Cadio, C., Saraswati, A., Cattin, R., and Mazzotti, S. (2016). A new approach to assess isostatic compensation of topography in continental domain from GOCE gravity gradients. *Geophysical Journal International*, 207(2).

Candela, T., Renard, F., Bouchon, M., Brouste, A., Marsan, D., Schmittbuhl, J., and Voisin, C. (2009). Characterization of fault roughness at various scales: Implications of three-dimensional high resolution topography measurements. *Pure and Applied Geophysics.*

Carlson, C. (2011). How I Made Wine Glasses from Sunflowers.

Cattin, R., Martelet, G., Henry, P., Avouac, J. P., Diament, M., and Shakya, T. R. (2001). Gravity anomalies, crustal structure and thermo-mechanical support of the Himalaya of Central Nepal. *Geophysical Journal International*, 147(2):381–392.

Cattin, R., Mazzotti, S., and Baratin, L. M. (2015). GravProcess: An easy-to-use MATLAB software to process campaign gravity data and evaluate the associated uncertainties. *Computers and Geosciences*, 81:20–27.

Chambodut, A., Panet, I., Mandea, M., Diament, M., Holschneider, M., and Jamet, O. (2005). Wavelet frames: An alternative to spherical harmonic representation of potential fields. *Geophysical Journal International*, 163(3):875–899.

Chanard, K., Avouac, J. P., Ramillien, G., and Genrich, J. (2014). Modeling deformation induced by seasonal variations of continental water in the Himalaya region: Sensitivity to Earth elastic structure. *Journal of Geophysical Research: Solid Earth*.

Chen, T. and Dransfield, M. (2016). Gravimetry and gravity gradiometry technologies at CGG Multi-Physics. In *2016 Airborne Gravimetry for Geodesy Summer School*.

Christensen, A. N., Dransfield, M. H., and Van Galder, C. (2015). Noise and repeatability of airborne gravity gradiometry. *First break*, 33(4):55–63.

Cosca, M., Arculus, R., Pearce, J., and Mitchell, J. (1998). 40Ar/ 39Ar and K-Ar geochronological age constraints for the inception and early evolution of the Izu-Bonin - Mariana arc system. *The Island Arc*, 7(3):579–595.

Crossley, D., Hinderer, J., and Riccardi, U. (2013). The measurement of surface gravity. *Reports on Progress in Physics*, 76(4):046101.

Cruciani, C., Carminati, E., and Doglioni, C. (2005). Slab dip vs. lithosphere age: No direct function. *Earth and Planetary Science Letters*.

Damiani, T. M. and Youngman, M. A. (2011). GRAV-D General Airborne Gravity Data User Manual. *Version*, 1.

Debs, J. E., Mcdonald, G., Close, J. D., Robins, N. P., Hardman, K. S., and Altin, P. A. (2013). From apples to atoms: Measuring gravity with ultra cold atomic test masses. *Preview*, 164:30–33.

Dransfield, M. (2010). Advances in airborne gravity gradiometry at Fugro Airborne Surveys. In *EGM 2010 International Workshop*.

Dransfield, M. H. and Lee, J. B. (2004). The FALCON® airborne gravity gradiometer survey systems. *Abstracts from the ASEG-PESA Airborne Gravity 2004 Workshop*.

Drinkwater, M. R., Floberghagen, R., Haagmans, R., Muzi, D., and Popescu, A. (2003). GOCE: ESA's first earth explorer core mission. In *Space Science Reviews*, volume 108, pages 419–432.

Dubois, J., Diament, M., Cogné, J.-P., and Mocquet, A. (2011). *Géophysique*. Dunod.

Eberhart-Phillips, D., Christensen, D. H., Brocher, T. M., Hansen, R., Ruppert, N. A., Haeussler, P. J., and Abers, G. A. (2006). Imaging the transition from Aleutian subduction to Yakutat collision in central Alaska, with local earthquakes and active source data. *Journal of Geophysical Research: Solid Earth*.

ESA (2008). Constituents of 'g'.

ESA (2010). GOCE standards. *Doc. No.: GOTN-HPF-GS-0111*, (3).

Ferry, M., Le Roux-Mallouf, R., Ritz, J.-F., Berthet, T., Peyret, M., Vernant, P., Maréchal, A., Cattin, R., Mazzotti, S., and Poujol, A. (2014). Tri-stereo Pleiades images-derived digital surface models for tectonic geomorphology studies. *EGU General Assembly 2014, held 27 April - 2 May, 2014 in Vienna, Austria, id.16401*, 16.

Forsberg, R. and Olesen, A. V. (2007). Broad-band gravity field mapping by airborne gravity and GOCE. In *European Space Agency, (Special Publication) ESA SP*.

Forte, A. M. and Mitrovica, J. X. (2001). Deep-mantle high-viscosity flow and thermochemical structure inferred from seismic and geodynamic data. *Nature*.

Francis, O., Van Camp, M., van Dam T., T., Warnant, R., and Hendrickx, M. (2004). Indication of the uplift of the Ardenne in long-term gravity variations in Membach (Belgium). *Geophysical Journal International*.

Fuchs, M. J., Bouman, J., Broerse, T., Visser, P., and Vermeersen, B. (2013). Observing coseismic gravity change from the Japan Tohoku-Oki 2011 earthquake with GOCE gravity gradiometry. *Journal of Geophysical Research: Solid Earth*.

Gao, H. (2018). Three-dimensional variations of the slab geometry correlate with earthquake distributions at the Cascadia subduction system. *Nature Communications*.

GEBCO, I. (2014). GEBCO 2014 Grid.

Grombein, T., Luo, X., Seitz, K., and Heck, B. (2014). A Wavelet-Based Assessment of Topographic-Isostatic Reductions for GOCE Gravity Gradients. *Surveys in Geophysics*, 35(4):959–982.

Grombein, T., Seitz, K., and Heck, B. (2013). Optimized formulas for the gravitational field of a tesseroid. *Journal of Geodesy*, 87(7):645–660.

Gruber, T., Abrikosov, O., and Hugentobler, U. (2010a). GOCE standards. *Doc No: GO-TN-HPF-GS-0111*, (3).

Gruber, T., Rummel, R., Abrikosov, O., van Hees, R., and Others (2010b). GOCE level 2 product data handbook. Technical report, GO-MA-HPF-GS-0110.

Gruber, T., Visser, P. N., Ackermann, C., and Hosse, M. (2011). Validation of GOCE gravity field models by means of orbit residuals and geoid comparisons. *Journal of Geodesy*.

H. P. Elieff, S. and Sander, L. (2015). Results from SGL's AIRGrav airborne gravity system over the Kauring airborne gravity test site. *ASEG Extended Abstracts*, 2015(1):1.

Hager, B. H., Clayton, R. W., Richards, M. A., Comer, R. P., and Dziewonski, A. M. (1985). Lower mantle heterogeneity, dynamic topography and the geoid. *Nature*.

Hammer, S. (1939). Terrain Corrections for Gravimeter Stations.

Hannah, J. (2001). Airborne gravimetry: a status report. *Department of Surveying, University of Otago: Dunedin, New Zealand*.

Hayes, G. P., Wald, D. J., and Johnson, R. L. (2012). Slab1.0: A three-dimensional model of global subduction zone geometries. *Journal of Geophysical Research: Solid Earth*.

Hayford, J. F. and Bowie, W. (1912). *The Effect of Topography and Isostatic Compensation Upon the Intensity of Gravity*. Number 10. U.S. Coast and Geodetic Survey.

Heck, B. and Seitz, K. (2007). A comparison of the tesseroid, prism and point-mass approaches for mass reductions in gravity field modelling. *Journal of Geodesy*, 81(2):121–136.

HEMERA H2020 (2018). Hemera H2020 - Integrated access to balloon-borne platforms for innovative research and technology.

Hinderer, J., Crossley, D., and Warburton, R. J. (2015). Superconducting Gravimetry. In *Treatise on Geophysics: Second Edition*.

Hirt, C. (2016). Gravity Forward Modeling. In *Encyclopedia of Geodesy*, pages 1–5. Springer International Publishing, Cham.

Hirt, C., Kuhn, M., Featherstone, W. E., and Gtötl, F. (2012). Topographic/isostatic evaluation of new-generation GOCE gravity field models. *Journal of Geophysical Research: Solid Earth*, 117(5).

Hofmann-Wellenhof, B. and Moritz, H. (2005). *Physical geodesy*.

Jacob, T., Bayer, R., Chery, J., Jourde, H., Moigne, N. L., Boy, J. P., Hinderer, J., Luck, B., and Brunet, P. (2008). Absolute gravity monitoring of water storage variation in a karst aquifer on the larzac plateau (Southern France). *Journal of Hydrology*.

Jaxybulatov, K., Koulakov, I., and Dobretsov, N. L. (2013). Segmentation of the Izu-Bonin and Mariana slabs based on the analysis of the Benioff seismicity distribution and regional tomography results. *Solid Earth*.

Jekeli, C. (2013). Extent and resolution requirements for the residual terrain effect in gravity gradiometry. *Geophysical Journal International*.

Johannessen, J. (1999). Gravity Field and Steady-State Ocean Circulation Mission. Technical Report July, ESA.

Johannessen, J. A., Balmino, G., Le Provost, C., Rummel, R., Sabadini, R., Sünkel, H., Tscherning, C. C., Visser, P., Woodworth, P., Hughes, C. W., Legrand, P., Sneeuw, N., Perosanz, F., Aguirre-Martinez, M., Rebhan, H., and Drinkwater, M. R. (2003). The European gravity field and steady-state ocean circulation explorer satellite mission: Its impact on geophysics. *Surveys in Geophysics*.

Karato, S.-i. and Karki, B. B. (2001). Origin of lateral variation of seismic wave velocities and density in the deep mantle. *Journal of Geophysical Research: Solid Earth*.

Kass, M. A. and Li, Y. (2008). Practical aspects of terrain correction in airborne gravity gradiometry surveys. *Exploration Geophysics*.

Koulakov, I. Y., Dobretsov, N. L., Bushenkova, N. A., and Yakovlev, A. V. (2011). Slab shape in subduction zones beneath the Kurile-Kamchatka and Aleutian arcs based on regional tomography results. *Russian Geology and Geophysics*.

Kusche, J. and Schrama, E. J. (2005). Surface mass redistribution inversion from global GPS deformation and Gravity Recovery and Climate Experiment (GRACE) gravity data. *Journal of Geophysical Research: Solid Earth*.

Lane, R. (2004). Airborne Gravity 2004 proceddings. *Airborne Gravity 2004 - Abstracts from the ASEG-PESA Airborne Gravity 2004 Workshop*.

Larson, K. M. and Van Dam, T. (2000). Measuring postglacial rebound with GPS and absolute gravity. *Geophysical Research Letters*.

Laske, G., Masters, G., Ma, Z., and Pasyanos, M. (2013). Update on CRUST1.0 -A 1-degree Global Model of Earth's Crust. In *Geophysical Research Abstracts EGU General Assembly*.

Lee, W. H. K. and Kaula, W. M. (1967). A spherical harmonic analysis of the Earth's topography. *Journal of Geophysical Research*, 72(2):753–758.

Lemoine, F. G., Smith, D. E., Kunz, L., Smith, R., Pavlis, E. C., Pavlis, N. K., Klosko, S. M., Chinn, D. S., Torrence, M. H., Williamson, R. G., Cox, C. M., Rachlin, K. E., Wang, Y. M., Kenyon, S. C., Salman, R., Trimmer, R., Rapp, R. H., and Nerem, R. S. (1997). The Development of the NASA GSFC and NIMA Joint Geopotential Model. pages 461–469.

Mader, K. (1951). Das Newtonsche Raumpotential prismatischer Körper und seine Ableitungen bis zur 3. *Ordnung. Österr. Z. f, Vermessungswesen, Sonderheft*, 11.

Mazzotti, S. and Hyndman, R. D. (2002). Yakutat collision and strain transfer across the northern Canadian Cordillera. *Geology*.

Meinesz, F. A. V. (1928). *A formula expressing the deflection of the plumb-line in the gravity anomalies and some formulae for the gravity-field and the gravity-potential outside the geoid*. Koninklijke Nederlandsche Akademie van Wetenschappen.

Mikhailov, V., Pajot, G., Diament, M., and Price, A. (2007). Tensor deconvolution: A method to locate equivalent sources from full tensor gravity data. *GEOPHYSICS*.

Mikuška, J., Pašteka, R., and Marušiak, I. (2006). Estimation of distant relief effect in gravimetry. *Geophysics*, 71(6).

Miller, M., Gorbatov, A., and Kennett, B. (2005). Heterogeneity within the subducting Pacific slab beneath the Izu-Bonin-Mariana arc: Evidence from tomography using 3D ray tracing inversion techniques. *Earth and Planetary Science Letters*, 235(1-2):331–342.

Miller, M. S., Kennett, B. L., and Lister, G. S. (2004). Imaging changes in morphology, geometry, and physical properties of the subducting Pacific plate along the Izu-Bonin-Mariana arc. *Earth and Planetary Science Letters*.

Morgan, W. J. (1972). Deep Mantle Convection Plumes and Plate Motions.

Moritz, H. (1980). Geodetic reference system 1980. *Bulletin Géodésique*.

Müller, R. D., Sdrolias, M., Gaina, C., and Roest, W. R. (2008). Age, spreading rates, and spreading asymmetry of the world's ocean crust. *Geochemistry, Geophysics, Geosystems*, 9(4):n/a–n/a.

Nagy, D., Papp, G., and Benedek, J. (2000). The gravitational potential and its derivatives for the prism. *Journal of Geodesy*, 74(7-8):552–560.

NASA (1987). Geophysical and Geodetic Requirements for Global Gravity Field Measurements, 1987-2000. In *Report of a Gravity Workshop, Colorado Springs, CO*, page 45, Washington D.C. NASA Geodynamics Branc, Division of Earth Science and Applications.

Niebauer, T. (2015). Gravimetric Methods - Absolute and Relative Gravity Meter: Instruments Concepts and Implementation. In *Treatise on Geophysics: Second Edition*.

Niebauer, T. M., Sasagawa, G. S., Faller, J. E., Hilt, R., and Klopping, F. (1995). A new generation of absolute gravimeters. *Metrologia*, 32(3):159–180.

Nowell, D. A. (1999). Gravity terrain corrections - an overview. *Journal of Applied Geophysics*.

Oakley, A. J., Taylor, B., and Moore, G. F. (2008). Pacific Plate subduction beneath the central Mariana and Izu-Bonin fore arcs: New insights from an old margin. *Geochemistry, Geophysics, Geosystems*.

Obayashi, M., Yoshimitsu, J., and Fukao, Y. (2009). Tearing of stagnant slab. *Science*.

Okabe, M. (1979). Analytical expressions for gravity anomalies due to homogeneous polyhedral bodies and translations into magnetic anomalies. *GEOPHYSICS*, 44(4):730–741.

Panet, I., Chambodut, A., Diament, M., Holschneider, M., and Jamet, O. (2006). New insights on intraplate volcanism in French Polynesia from wavelet analysis of GRACE, CHAMP, and sea surface data. *Journal of Geophysical Research: Solid Earth*.

Panet, I., Kuroishi, Y., and Holschneider, M. (2011). Wavelet modelling of the gravity field by domain decomposition methods: an example over Japan. *Geophys. J. Int*, 184:203–219.

Panet, I., Pajot-Métivier, G., Greff-Lefftz, M., Métivier, L., Diament, M., and Mandea, M. (2014). Mapping the mass distribution of Earth's mantle using satellite-derived gravity gradients. *Nature Geoscience*, 7(2):131–135.

Parker, R. L. (1973). The Rapid Calculation of Potential Anomalies. *Geophysical Journal of the Royal Astronomical Society.*

Pavlis, N., Holmes, S., Kenyon, S., and Factor, J. (2008). An earth gravitational model to degree 2160: EGM2008. *presented at the 2008 General Assembly of the European Geosciences Union, Vienna, Austria, April 13-18.*

Pavlis, N. K., Factor, J. K., and Holmes, S. A. (2007). Terrain-related gravimetric quantities computed for the next EGM. *Proceedings of the 1st International Symposium of the International Gravity Field Service (IGFS), Istanbul*, (January 2006):318–323.

Persson, B. (2015). On the fractal dimension of rough surfaces. *NanoScience and Technology.*

Ramillien, G., Cazenave, A., and Brunau, O. (2004). Global time variations of hydrological signals from GRACE satellite gravimetry. *Geophysical Journal International.*

Reguzzoni, M. and Sampietro, D. (2015). GEMMA: An Earth crustal model based on GOCE satellite data. *International Journal of Applied Earth Observation and Geoinformation*, 35(PA):31–43.

Reigber, C., Jochmann, H., Wünsch, J., Petrovic, S., Schwintzer, P., Barthelmes, F., Neumayer, K.-H., König, R., Förste, C., Balmino, G., Biancale, R., Lemoine, J.-M., Loyer, S., and Perosanz, F. (2005). Earth Gravity Field and Seasonal Variability from CHAMP. In *Earth Observation with CHAMP*, pages 25–30. Springer-Verlag, Berlin/Heidelberg.

Rummel, R., Balmino, G., Johannessen, J., Visser, P., and Woodworth, P. (2002). Dedicated gravity field missions - principles and aims. *Journal of Geodynamics.*

Rummel, R., Yi, W., and Stummer, C. (2011). GOCE gravitational gradiometry. *Journal of Geodesy*, 85(11):777–790.

Sander, S., Argyle, M., Elieff, S., Ferguson, S., Lavoie, V., and Sander, L. (2005). The AIRGrav airborne gravity system. *CSEG Recorder.*

Sandwell, D. T., Müller, R. D., Smith, W. H., Garcia, E., and Francis, R. (2014). New global marine gravity model from CryoSat-2 and Jason-1 reveals buried tectonic structure. *Science.*

Sandwell, D. T. and Smith, W. H. (1997). Marine gravity anomaly from Geosat and ERS 1 satellite altimetry. *Journal of Geophysical Research B: Solid Earth.*

Sandwell, D. T. and Smith, W. H. (2009). Global marine gravity from retracked Geosat and ERS-1 altimetry: Ridge segmentation versus spreading rate. *Journal of Geophysical Research: Solid Earth.*

Sansò, F. and Sideris, M. G. (2013). The Forward Modelling of the Gravity Field. pages 3–71. Springer, Berlin, Heidelberg.

Sasagawa, G. S., Klopping, F., Niebauer, T. M., Faller, J. E., and Hilt, R. L. (1995). Intracomparison tests of the FG5 absolute gravity meters. *Geophysical Research Letters*, 22(4):461–464.

Seeber, G. (2003). *Satellite Geodesy.*

Seigel, H. O. (1995). *A Guide To High Precision Land Gravimeter Surveys.*

Singh, B. and Guptasarma, D. (2001). New method for fast computation of gravity and magnetic anomalies from arbitrary polyhedra. *GEOPHYSICS*, 66(2):521–526.

Song, T.-R. A. and Simons, M. (2003). Large trench-parallel gravity variations predict seismogenic behavior in subduction zones. *Science (New York, N.Y.)*, 301(5633):630–3.

Stern, R. J., Klemperer, S. L., and Fouch, M. J. (2004). An overview of the izu-bonin-mariana subduction factory. In *Geophysical Monograph Series.*

Stokes, G. G. (1849). On the variation of gravity on the surface of the Earth. *Trans. Camb. Phil. Soc.*, 8:672–695.

Storchak, D. A., Di Giacomo, D., Bondár, I., Engdahl, E. R., Harris, J., Lee, W. H. K., Villaseñor, A., and Bormann, P. (2013). Public release of the ISC-GEM global instrumental earthquake catalog (1900-2009). *Seismological Research Letters.*

Sun, W. (1989). Bouguer gravity anomaly map of the People's Republic of China. *Chin. Acad. Geoexplor., Beijing.*

Szwillus, W., Ebbing, J., and Holzrichter, N. (2016). Importance of far-field topographic and isostatic corrections forregional density modelling. *Geophysical Journal International*, 207(1):274–287.

Takahashi, N., Kodaira, S., Klemperer, S. L., Tatsumi, Y., Kaneda, Y., and Suyehiro, K. (2007). Crustal structure and evolution of the Mariana intra-oceanic island arc. *Geology.*

Takahashi, N., Kodaira, S., Tatsumi, Y., Kaneda, Y., and Suyehiro, K. (2008). Structure and growth of the Izu-Bonin-Mariana arc crust: 1. Seismic constraint on crust and mantle structure of the Mariana arc-back-arc system. *Journal of Geophysical Research: Solid Earth.*

Takahashi, N., Kodaira, S., Tatsumi, Y., Yamashita, M., Sato, T., Kaiho, Y., Miura, S., No, T., Takizawa, K., and Kaneda, Y. (2009). Structural variations of arc crusts and rifted margins in the southern Izu-Ogasawara arc-back arc system. *Geochemistry, Geophysics, Geosystems.*

Talwani, M. (1998). Errors in the total Bouguer reduction. *GEOPHYSICS*, 63(4):1125–1130.

Tapley, B. D., Bettadpur, S., Watkins, M., and Reigber, C. (2004). The gravity recovery and climate experiment: Mission overview and early results. *Geophysical Research Letters.*

Taylor, B. (1992). Rifting and the volcanic-tectonic evolution of the Izu-Bonin-Mariana arc. *Proceedings of the Ocean Drilling Program, Scientific Results.*

Tiberi, C., Diament, M., Déverchère, J., Petit-Mariani, C., Mikhailov, V., Tikhotsky, S., and Achauer, U. (2003). Deep structure of the Baikal rift zone revealed by joint inversion of gravity and seismology. *Journal of Geophysical Research: Solid Earth*, 108(B3).

Tiwari, V. M., Vyghreswara Rao, M. B. S., Mishra, D. C., and Singh, B. (2006). Crustal structure across Sikkim, NE Himalaya from new gravity and magnetic data. *Earth and Planetary Science Letters*, 247(1-2):61–69.

Torge, W. (1989). *Gravimetry.* W. de Gruyter.

Torge, W. (2001). *Geodesy.* Walter de Gruyter, Berlin.

Tscherning, C. C. (1976). Computation of the second-order derivatives of the normal potential based on the representation by a Legendre series. *Manuscripta geodaetica*, 1(1):71–92.

Tsoulis, D. (2012). Analytical computation of the full gravity tensor of a homogeneous arbitrarily shaped polyhedral source using line integrals. *Geophysics*, 77(2):F1–F11.

Tsoulis, D. and Stary, B. (2005). An isostatically compensated gravity model using spherical layer distributions. *Journal of Geodesy*, 78(7-8):418–424.

Uieda, L., Barbosa, V. C. F., and Braitenberg, C. (2016). Tesseroids: Forward-modeling gravitational fields in spherical coordinates. *GEOPHYSICS*, 81(5):F41–F48.

Van Camp, M., de Viron, O., Watlet, A., Meurers, B., Francis, O., and Caudron, C. (2017). Geophysics From Terrestrial Time-Variable Gravity Measurements.

van der Hilst, R. and Seno, T. (1993). Effects of relative plate motion on the deep structure and penetration depth of slabs below the Izu-Bonin and Mariana island arcs. *Earth and Planetary Science Letters.*

Vaze, J. and Teng, J. (2007). High Resolution LiDAR DEM - How good is it? *Modsim 2007: International Congress on Modelling and Simulation*, pages 692–698.

Verdun, J., Klingelé, E. E., Bayer, R., Cocard, M., Geiger, A., and Kahle, H. G. (2003). The alpine Swiss-French airborne gravity survey. *Geophysical Journal International.*

Watts, A. B. (2001). *Isostasy and flexure of the lithosphere.* Cambridge University Press, Oxford.

Weatherall, P., Marks, K. M., Jakobsson, M., Schmitt, T., Tani, S., Arndt, J. E., Rovere, M., Chayes, D., Ferrini, V., and Wigley, R. (2015). A new digital bathymetric model of the world's oceans. *Earth and Space Science*, 2(8):331–345.

Worthington, L. L., Van Avendonk, H. J., Gulick, S. P., Christeson, G. L., and Pavlis, T. L. (2012). Crustal structure of the Yakutat terrane and the evolution of subduction and collision in southern Alaska. *Journal of Geophysical Research: Solid Earth*.

Zhao, D., Fujisawa, M., and Toyokuni, G. (2017). Tomography of the subducting Pacific slab and the 2015 Bonin deepest earthquake (Mw 7.9). *Scientific Reports*.

Zhao, D., Yanada, T., Hasegawa, A., Umino, N., and Wei, W. (2012). Imaging the subducting slabs and mantle upwelling under the Japan Islands. *Geophysical Journal International*.

Abstract

Nowadays, the scientific community has at its disposal gravity and gravity gradient datasets with unprecedented accuracy and spatial resolution that enhances our knowledge of Earth gravitational field at various scales and wavelengths, obtained from ground to satellite measurements. In parallel with gravimetry, the advancement of satellite observations provides the community with more detailed digital elevation models to reflect the Earth's structure geometry. Together, these novel datasets provide a great opportunity to better understand the Earth's structures and dynamics at local, regional, and global scales. The use and interpretation of these high-quality data require refinement of standard approaches in gravity-related data processing and analysis. This thesis consists of a series of studies aiming to improve the precision in the chain of gravity and gravity gradient data processing for geodynamic studies. To that aim, we develop a tool, named GEEC (Gal Eötvös Earth Calculator) to compute precisely the gravity and gravity gradients effects due to any mass body regardless of its geometry and its distance from measurements (Saraswati et al, submitted). The gravity and gravity gradients effects are computed analytically using the line integral solution of an irregular polyhedron. The validations at local, regional, and global scales confirm the robustness of GEEC's performance, where the resolution of the model, that depends on both size of the body mass and its distance from the measurement point, control strongly the accuracy of the results. We present an application for assessing the optimum parameters in the computation of gravity and gravity gradients due to topography variations. Topography has a major contribution in Earth gravitational attraction, therefore the estimation of topography effects must be carefully considered in the processing of gravity data, especially in areas of rugged topography or in large-scale studies. For high-accuracy gravity studies at a global scale, the topography correction process must consider the topography effect of the entire Earth. But for local to regional applications based on relative variations within the zone, we show that truncated topography at a specific distance can be adequate. When using a truncation distance that equals with the dimension of the study area, errors 1-10 mGal are obtained. The use of 15° ensure a precision of 1 mGal. For gravity gradient, to obtain 1 E of precision, a truncation distance of 8.5° is required. To obtain 0.01 E of precision, the truncation distance must be set at 40°. Lastly, we approach the issue: Are GOCE measurements relevant to obtain a detailed image of the structure of a subducting plate, including its geometry and lateral variation? The results of gravity gradients forward modelling using synthetic slab models demonstrate that the detailed structures of slab geometry are detectable by gravity gradients at GOCE mean altitude (255 km). However, in the application to the real case of Izu-Bonin-Mariana subduction zone, the second-order geometric features of the subducting plate (e.g., slab tear) are difficult to be detected due to poor spatial resolution and accuracy of the currently available global crustal model. We show that to be able to assess the geometry of a slab in the second-order, the estimation of crustal effect using a global crustal model with an accuracy better than 1 km is mandatory.

Keywords : gravity field, space gradiometry (GOCE), numerical development, forward modelling, optimization, geodynamics

Résumé

La communauté scientifique dispose aujourd'hui de jeux de données gravimétriques et gradiométriques d'une précision et d'une résolution spatiale sans précédent. Ces données obtenues à partir de mesures au sol, d'acquisitions aériennes et d'observations satellitaires permettent d'améliorer notre connaissance du champ gravitationnel de la Terre à diverses échelles et longueurs d'onde. Les observations satellitaires fournissent également à la communauté des modèles numériques de terrain globaux de plus en plus détaillés qui permettent une meilleure prise en compte de la géométrie fine des structures géologiques. Ensemble, ces nouveaux jeux de données offrent une opportunité unique de mieux comprendre les structures et la dynamique terrestre aux échelles locale, régionale et globale. L'utilisation et l'interprétation de ces données de haute qualité nécessitent d'aller au-delà des approches standards en matière de traitement et d'analyse des données gravimétriques et gradiométriques. Focalisée sur des applications géodynamiques, cette thèse consiste en une série d'études visant à améliorer la précision dans la chaine de traitement et d'interprétation de ces données. Pour cela, un nouvel outil a été développé. Intitulé GEEC (Gal Eötvös Earth Calculator), il permet de calculer précisément les effets gravimétriques et gradiométriques dus à un corps massique, quelles que soient sa géométrie et sa distance aux mesures (Saraswati et al, submitted). Ces effets sont calculés analytiquement en utilisant la solution intégrale le long des arrêtes d'un polyèdre irrégulier. Les validations aux échelles locale, régionale et globale ont permis de quantifier les performances et la robustesse de GEEC. Nous montrons qu'il est possible de définir une emprise optimale assurant rapidité de calcul et précision des résultats, qui dépend à la fois de la taille du corps massique et de sa distance aux points de mesure. L'estimation de l'effet de la topographie doit être soigneusement pris en compte dans le traitement des données gravimétriques et gradiométriques, en particulier dans les zones de topographie accidentée ou dans les études à grande échelle. Dans un premier temps, nous montrons que, pour les études gravimétriques de haute précision, la correction des effets topographiques sur les données satellitaires nécessite d'utiliser une emprise globale. A l'inverse, une topographie tronquée sur une distance égale à la dimension de la zone étudiée peut être adéquate dans l'analyse de variations relatives à des échelles locales et régionales, générant des erreurs de 1 à 10 mGal sur les mesures relatives. Plus généralement, une distance de troncature de 15° assure une précision de 1 mGal. Dans le cas de données de gradient de gravité, une distance de troncature de 8,5° (resp. 40 °) est requise pour obtenir une précision relative d'environ 1 E (resp. 0,01 E). Dans la troisième partie de cette thèse, nous abordons le problème suivant : les données du satellite GOCE sont-elles pertinentes pour obtenir une image détaillée de la structure d'une plaque de subduction (slab), y compris de sa géométrie et des variations latérales ? L'analyse d'une série de modèles synthétiques de slab montre que les structures détaillées de la géométrie sont détectables par les données de gradient de gravité à l'altitude moyenne de GOCE (255 km). Cependant, l'application au cas réel de la zone de subduction d'Izu-Bonin-Mariannes montre que la détection des caractéristiques géométriques de second ordre (par ex. déchirure de slab) reste difficile, en raison de la faible résolution spatiale des données et, principalement, de la mauvaise qualité des modèles d'épaisseur de croûte actuellement disponible. Nous montrons que, pour pouvoir étudier les détails de géométrie d'un slab, modèle régional ou global d'épaisseur de croûte est nécessaire avec une précision supérieure à environ 1 km.

Mots-clefs : champ de pesanteur, gradiométrie spatiale (GOCE), développement numérique, modèle directe, optimisation, géodynamique